# Microstructural, Biomechanical and Biocompatibility Studies of Porous Ti-Nb-Zr Alloys Fabricated by Powder Metallurgy

A thesis submitted for the degree of Doctor of Philosophy (PhD)

by

**Eyyüp Murat Karakurt**

Department of Mechanical and Aerospace Engineering
College of Engineering Design and Physical Sciences
Brunel University London
Uxbridge, UB8 3PH, United Kingdom

June 2023

Supervision: Dr Yan Huang

# Abstract

This thesis presents a study on microstructural, biomechanical, and in vitro studies of Ti-Nb-Zr alloys fabricated by powder metallurgy with the space holder technique. This work aims to fabricate Ti-xNb (x:10, 20, and 30; at.%), Ti-20Zr (at.%) and Ti-xNb-10Zr (x: 10, and 20; at.%) alloys with different porosities used as a load-bearing implant that can mimic bone structure.

Microstructural analysis was performed by using various methods including scanning electron microscopy, energy dispersive spectroscopy, electron backscatter diffraction and X-ray diffraction. Corrosion performance was assessed via electrochemical polarisation tests, while mechanical behaviour was determined by uniaxial compressive tests. In vitro studies such as cell viability and proliferation, adhesion potential, and genotoxicity were examined by performing MTT assay, scanning electron microscopy, fibronectin adsorption, and plasmid-DNA interaction assay.

Results revealed that the alloys could be divided into low and highly porous categories, with porosities ranging from 21% to 29% and 43% to 58%, respectively. The alloys exhibited irregularly shaped open pores with a uniform pore size distribution, allowing for cell ingrowth.

Adding a space holder effectively adjusted the porosity characteristics of the alloys achieved. As foreseen, porosities dramatically diminished the mechanical performance of the alloys. The ultimate compressive strengths ranged from 618 MPa to 1376 MPa for low porous alloys and from 48 MPa to 356 MPa for highly porous alloys. Moreover, potentiodynamic polarisation revealed that the alloys had passivation behaviour, protecting against corrosion attacks in Hank’s Balanced Salt Solution.

Ti-xNb and Ti-xNb-10Zr alloys contained hcp α-Ti and bcc β-Ti phases with primary niobium phase, while Ti-20Zr alloys exhibited hcp α-Ti and distorted hcp α'-Ti phase structures.

Biological evaluations of the alloys studied met the biocompatibility criteria required for orthopaedic biomaterial use. Microscopic examination of L929 and Saos-2 cell lines increased cell adherence and proliferation at a high density due to migration of the pores.

## Acknowledgements

I wish to express my sincere appreciation to Dr Yan Huang for offering me the opportunity to pursue my PhD in BCAST at Brunel University London for the last four years. His support and guidance from the first day of the PhD journey to the completion of the project have taught me great lessons in my research.

I am truly indebted to the Republic of Türkiye Ministry of National Education for sponsoring my PhD studies. I am grateful to Yuksel Cetin from TUBITAK Marmara Research Centre (Genetic Engineering and Biotechnology Institute), Prof. Dr Mehmet Kaya from Namik Kemal University, Asst. Prof. Huseyin Demirtas from Karabuk University, and Omer Çakmak from Pohang University of Science and Technology (POSTECH).

I would like to sincerely thank Dr Ashley Howkins and Dr Lorna Anguilano for their kind support on electron microscopic analysis. I wish to thank Ms Sam Melvin, Ms Loredana Saccone, and Ms Aneta Walsh for their excellent technical support during my laboratory work. I also thank the members of BCAST.

Finally, I wish to express my appreciation to my dearest wife, Saniye Seyma, my son, Resit, and my daughter, Zeynep Inci for their support and encouragement during my PhD study. I owe my deepest gratitude to my mother and father, who provided me with their unconditional love and support throughout my study.

**Eyyüp Murat Karakurt**
Brunel University London
Uxbridge, United Kingdom
June 2023

# Contents

## List of Figures

# List of Tables

## Academic Studies & Scientific Activities

### Conference participation

- A Comprehensive Study on the Porosity Effect of Ti-20Zr Alloy Produced by Powder Metallurgy as a Biomaterial; International Conference on Biomedical Engineering and Medical Physics (ICBEMP 2020), London, United Kingdom, December 10-11, 2020.

- Effect of Zr Concentration on the Microstructure and Mechanical Performance of Porous Ti-Zr System by Powder Metallurgy; 6th International Conference on Materials Sciences and Nanomaterials (ICMSN 2022), London, United Kingdom, July 12-14, 2022.

- Evaluation of Biocompatibility of Porous Titanium- Niobium Alloys; The United Kingdom Society for Biomaterials (UKSB 2022), Sheffield, United Kingdom, June 27-28, 2022.

### Publications

- Karakurt, E. M., Huang, Y., Kaya, M., Demirtaş, H., and Çakmak, Ö. (2022). Effect of Zr Concentration on the Microstructure and Mechanical Performance of Porous Ti-Zr System by Powder Metallurgy. In Key Engineering Materials, 936, 25-31.

- Karakurt, E. M., Huang, Y., Kaya, M., Demirtas, H., Acikgoz, A., and Demircan, G. (2023). Effect of Relative Density on Microstructure, Corrosion Resistance and Mechanical Performance of Porous Ti–20Zr Alloys Fabricated by Powder Metallurgy. Arabian Journal for Science and Engineering, 2023, 1-11.

- Karakurt, E. M., Cetin, Y., Incesu, A., Demirtas, H., Kaya, M., Yıldızhan, Y., and Tosun, M. and Huang, Y. (2023). Microstructural, Biomechanical and Biocompatibility Studies of Titanium-Niobium-Zirconium Alloys Fabricated by Powder Metallurgy. Materials, 16, 4240.

## Nomenclature

A list of symbols is given with a brief description.

| | |
|---|---|
| $\varepsilon$ | General porosity ratio (%) |
| Å | Angstrom |
| m | Mass (g) |
| v | Volume ($cm^3$) |
| $\rho$ | Sintered (bulk) density ($g/cm^3$) |
| $\rho_o$ | Theoretical density ($g/cm^3$) |
| $\alpha$-Ti | The alpha titanium phase |
| $\alpha^{I}$-Ti | The martensitic alpha titanium phase |
| $\alpha^{II}$-Ti | The martensitic alpha titanium phase |
| $\beta$-Ti | The beta titanium phase |
| $\omega$-Ti | The omega titanium phase |
| µm | Micrometre |
| $R_p$ | Polarisation resistance ($\Omega/cm^2$) |
| $\beta_a$ | Anodic Tafel slope ($V\ dec^{-1}$) |
| $\beta_c$ | Cathodic Tafel slope ($V\ dec^{-1}$) |
| $I_{corr}$ | Corrosion density ($\mu A\ cm^{-2}$) |
| Ө | Diameter |
| N | Newton |
| Pa | Pascal |
| MPa | Megapascal |
| $C_2H_5OH$ | Ethanol |
| $Al_2O_3$ | Alumina |
| $ZrO_2$ | Zirconia or baddeleyite |
| $Ca_3(PO_4)_2$ | Tricalcium phosphate |
| $C_3H_4O_2$ | Polylactic acid |
| $ZrSO_4$ | Zirconium silicate |
| $NH_4HCO_3$ | Ammonium bicarbonate |
| NH3 | Ammonia |
| CO2 | Carbon dioxide |
| °C | Centigrade |

# Abbreviations

| | |
|---|---|
| BSE | Backscattered electron |
| SE | Secondary electron imaging |
| EBSD | Electron backscattered diffraction |
| XRD | X-ray diffraction |
| PBS | Phosphate buffered saline |
| SEM | Scanning electron microscope |
| EDS | Energy dispersive spectroscopy |
| Ti | Titanium |
| Nb | Niobium |
| Zr | Zirconium |
| SH | Space holder |
| Hcp | Hexagonal closed-packed structure |
| Bcc | Body centred-cubic structure |
| CP | Commercially pure |
| UCS | Ultimate compressive strength |
| EIS | Electrochemical impedance spectroscopy |
| HBSS | Hanks’ Balanced Salt Solution |
| Ms | Martensite–start temperature |
| PBS | Phosphate-buffered saline |
| UHMWPE | High molecular weight polyethylene |
| PMMA | Polymethylmethacrylate |
| PE | Polyethylene |
| SME | Shape memory effect |
| FN | Fibronectin |
| ISO | International organization for standardization |
| OD | Optical density |

1

# Chapter 1. Introduction

## 1.1 Background

Materials science is a multidisciplinary field that deals with the study of materials and their structures, properties, and behaviour under different conditions (Omran, 2020). It encompasses various branches of science such as physics, chemistry, and engineering to understand and develop new materials that can be used in various applications. Material science and biomaterials are interconnected areas of research (Zahir et al., 2022). In the beginning stage of biomaterials, the materials employed as biomaterials were standardly well-defined. However, biomaterials derived from materials employed in the manufacture of human medical or dental implants were not specifically designed for human applications. In addition, the histological examination was initially defined in animal models such as rabbits, rats, and hamsters. At that point, it was quite difficult to find alternatives to the current material options used in implantology. However, advanced in vitro studies provided opportunities for the development and production of new types of biomaterials. With this method, histological examinations of materials used as biomaterials can be performed much more practically and inexpensively compared to in vivo (González-Gualda et al., 2021).

Various material groups can be used as biomaterials fabricated from metal, polymer, and ceramic materials. Ease of fabrication, relatively low cost, and combination with superior mechanical performance have given metals a key role in implantology. In this regard, various metallic biomaterials such as titanium-based alloys, cobalt-chromium alloys, and stainless steel have been developed by scientists. Although titanium-based alloys have higher costs and more complex production processes compared to the above-mentioned material groups, they are widely used as biomaterial owing to their lower density, superior chemical stability and more acceptable mechanical performance and thus have been dominating the metallic biomaterials market. Ti-6Al-4V or Ti-6Al-7Nb alloys are the most preferred titanium-based alloys in hip and knee implants (nearly 60%) (Zahir et al., 2022). The key alloying elements aluminium and vanadium in the alloy may cause adverse influences in clinical practice. Vanadium ions released from Ti-6A-4V alloy may change the kinetics of the enzyme activity related to inflammatory responses. Aluminium may also lead to Alzheimer's disease through long-term implantation. This toxic issue must be addressed with the development of aluminium and vanadium-free titanium-based alloys. This is one of the motivations for the present work.

Ti-Nb-Zr alloys have recently been a focal point of interest in the development of advanced titanium-based implants. Both niobium and zirconium are biocompatible and their addition to titanium allows the control of both phase constituents and microstructures, and therefore mechanical properties (Mishchenko et al., 2020). In particular, β stabiliser niobium has been used for promoting the formation of the ductile β phase (Lin et al., 2019). Titanium alloys with a certain β phase have generally been preferred in implantology since they exhibit lower elastic modulus, more acceptable mechanical strength, and better biocompatibility than α titanium alloys. Zirconium is a neutral or weak β stabiliser when individually alloyed to titanium matrix. Its addition is mainly for improving strength, fracture toughness and wear resistance (Wu et al., 2022). In the Ti-Nb-Zr system to be developed in this study, the alloying element concentrations were designed to produce desired microstructures with both α and β phases. Powder metallurgy with space holder technique was considered the best manufacturing technology for producing titanium alloys with controlled porosity and was therefore selected in this thesis. (Angelo et al., 2022).

A biomechanical mismatch between the host bone and the orthopaedic biomaterial is a core issue of concern (Goncalves et al., 2020). The majority of metallic biomaterials may exhibit much higher mechanical performance than natural bone. Such a condition may lead to a reduction in bone mineral density or bone resorption over time, which is a known stress-shielding issue. This may increase healing time and even result in implant failure (Matuła et al., 2020). Using porous implant materials can be advantageous for implantology since their mechanical properties better match those of bone and thus can minimise the stress-shielding issue. Therefore, there is a delicate balance between the porosity and mechanical performances of the orthopaedic biomaterial.

One motivation for the introduction of pores into orthopaedic biomaterial is to generate a porous structure by mimicking the structure of human bone (Du et al., 2022). Titanium-based alloys with macro and micro pores can enhance the integration with human tissue when implanted. Some researchers have revealed that a porous structure can facilitate capturing the cellulose and increase the osseointegration features since it provides an adequate site for tissue healing, bone ingrowth, and blood and nutrient transport (Ha et al., 2022).

Biomaterials can be employed in various fields such as dental implants, drug delivery and surgery tool and load-bearing implants. One of the fastest-growing markets in biomaterial fields is orthopaedic biomaterials (load-bearing implants); its annual growth rate over the last ten years has been in the range of 7% to 15% (Industry Experts Inc., 2022). However, orthopaedic biomaterials may not efficiently meet the requirements of the patient. The commercial orthopaedic biomaterials on the market may have serious health implications. Especially most hip implants currently employed are insufficient in terms of mechanical performance, biocompatibility, and corrosion resistance. Therefore, it is essential to produce new-developed orthopaedic biomaterials with superior properties.

This work aims to overcome the drawbacks of the above-mentioned problems by producing binary and ternary Ti-Nb-Zr alloys with different porosities used as load-bearing implants that can mimic bone structure.

### 1.2. Research Objectives

The major objectives of this work are to:

- Fabricate stable, vanadium and aluminium-free porous titanium-based alloys used as orthopaedic biomaterial that can mimic the human bone.
- Give a detailed description of material properties and methodologies employed in this thesis to fabricate porous binary and ternary Ti-Nb-Zr alloys, and in vitro procedures.
- Study the role of niobium and zirconium found in titanium matrix.
- Examine the effect of general porosity on the microstructure and mechanical performance of the alloys produced by powder metallurgy combined with the space holder technique.
- Present and analyse the data collated from in vitro studies of the alloys, including cell viability and proliferation, adhesion potential, and genotoxicity.
- Understand the relationship between general porosity achieved and cell viability of the alloys.
- Make recommendations for future research in this field.

### 1.3 Outline of Thesis

After a sincere acknowledgement and an introduction of the research background, the previous literature is reviewed in Chapter 2 with a detailed overview of the previous theoretical studies on biomaterials, including the definition of the biomaterial, biomaterial concepts, and classification of biomaterials and problems with biomaterials, including bone structure. Also in Chapter 2, titanium and its alloys used as orthopaedic biomaterial are summarised and powder metallurgy combined with the space holder technique is reviewed. Chapter 3 describes the experimental procedures used and characterisation techniques in detail. In Chapter 4, the results of the material characterisations of Ti-Nb-Zr alloys achieved in this work are presented with microstructure observation of optical microscopy (OM), scanning electron microscopy (SEM), and energy dispersive spectroscopy (EDS), electron backscatter diffraction (EBSD) and phase identification (XRD). In Chapter 5, the role of general porosity and microstructure on mechanical properties (i.e., ultimate compressive strength, yield strength and elastic modulus) is presented, including orientation relationships between general porosity and stress of the alloys achieved. Chapter 6 covers the role of general porosity and composition in potentiodynamic polarisation analysis. In vitro studies such as cell viability and proliferation, adhesion potential, and genotoxicity were examined by performing MTT (3-[4,5-

dimethylthiazol-2-yl]-2,5 diphenyl tetrazolium bromide) assay, fibronectin adsorption, and plasmid-DNA interaction assay are presented in Chapter 7. The main conclusions and suggestions for future work are listed in Chapter 8.

# Chapter 2. Literature Review

## 2.1. Biomaterial

### 2.1.1. Definition of Biomaterial

The most accepted definition of a biomaterial is material designed to replace partially or fully the function of damaged or lost tissues, bones, or organs (Zhang and Williams, 2019). The primary characteristics of biomaterial are superior corrosion resistance, non-toxicity, and good biocompatibility. Biomaterials should not only be considered as implants or prostheses but can also be widely used in medical devices such as mechanical organs (extracorporeal devices) and diagnostic kits (Hudecki et al., 2019). An X-ray image of a modern implant is given in **Fig. 2.1** (Manam et al., 2017).

**Figure 2.1.** (a) knee implant: (b) ankle implant (Manam et al., 2017).

Biomaterials can be divided into three major groups based on the tissue's response or interaction: bioactive, bioinert, and bioresorbable.

Bioinert biomaterial can be defined as biomaterial that can establish a poor bond with the tissue without changing the structure of living tissue (see **Fig. 2.2.**). This type of biomaterial has minimal interaction with tissue when implanted. In this regard, the tissue tends to form a filamentous or fibrous capsule at the implantation site due to its contact with the biomaterial. The thickness of the fibrous capsule is based on the degree of bioinertness of the biomaterial used. At this point, the fibrous capsule may inhibit the biomaterial from interacting with the tissue. Therefore, better results can be achieved when the surface of bioinert biomaterial is coated with a film that can establish an active bond with the tissue. Some examples of bioinert biomaterials are titanium-based alloys, alumina ($Al_2O_3$), zirconia ($ZrO_2$) and polyethylene (PE) (Anas et al., 2023).

Bioactive biomaterial can be defined as biomaterial that can establish a strong bond with surrounding tissue such as skin, blood vessels and cartilage (see **Fig. 2.2.**) (Wang et al., 2023). Such biomaterials have high biological activity; thus, they can completely interact with the surrounding tissue. They can generate a biochemical bond with the tissue when implanted, which promotes the tissue adhering to the biomaterial surface; thus, integration between the bioactive biomaterial and tissue will be enhanced. For this reason, they can be generally used as a film for many types of biomaterials to improve the interaction between tissue and biomaterial (Anas et al., 2023). The most well-known example of bioactive biomaterial is hydroxyapatite. It is a synthetic mineral compound with a similar chemical composition to the mineral component of bone tissue. However, the structure and function of bone are far more complex due to the presence of living cells and collagen fibers, making bone a dynamic and adaptable tissue in the body. Its composition is almost the same as the composition of human bone, as seen in **Fig. 2.3.**

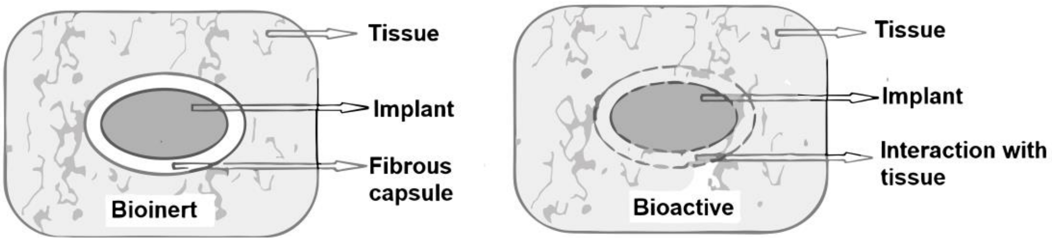

**Figure. 2.2.** Interaction of bioinert and bioactive biomaterials with the surrounding tissue (Anas et al., 2023).

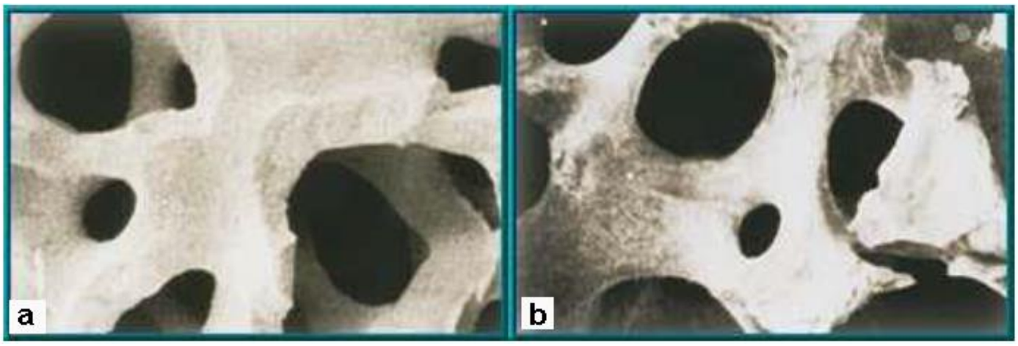

**Figure 2.3.** (a) human bone appearance: (b) hydroxyapatite appearance (Wang et al., 2023)**.**

Bioresorbable biomaterial can be defined as biomaterial that can be degraded and slowly replaced by tissue. Bioresorbable biomaterial should not lead to toxic or allergic effects in the human body after degradation. Thus, this type of biomaterial implanted in the body becomes indistinguishable from tissue over time. At this point, the interface between tissue and bioresorbable biomaterial is a dynamic structure because it is at the highest level compared to other types of biomaterials (Li et al., 2014). Some examples of bioresorbable biomaterials are tricalcium phosphate ($Ca_3(PO_4)_2$), polylactic acid ($(C_3H_4O_2)_n$), calcium phosphate salts and some bioglasses (Adamovic et al., 2018; Agrawal et al., 2023).

### 2.1.2. Biocompatibility

The term ‘biocompatibility’ is used to describe the biological performance of a biomaterial after surgery, but there is still great uncertainty about how the mechanism works. Biocompatibility is not a static phenomenon; it is dynamic. Biocompatibility is strongly dependent upon the corrosion resistance and chemical stability of the biomaterial and other factors not controlled by the surgeon such as the patient's health and age. Before surgery, the biomaterial should be comprehensively analysed in cell cultures (in vitro) or animal models (in vivo) to understand its functionality (see **Table 2.1.**). Biological rejection of the biomaterial implanted into the body may cause an inflammatory response at the implantation site, and it may then need to be removed from the body. In this regard, most research has been conducted on developing the biocompatibility mechanism (Hernandez and Woodrow; 2022).

**Table 2.1.** Different types of tests used to evaluate biocompatibility (Moharamzadeh et al., 2009).

| | |
|---|---|
| In vitro | Membrane permeability test<br>Dentin barrier tests<br>Cytotoxicity test<br>Agar overlay method |
| In vivo | Mucous membrane irritation test<br>Implantation tests<br>Skin sensitisation |

Researchers often use a combination of in vitro and in vivo experiments to gain a comprehensive understanding of biological processes. In vitro studies are valuable for preliminary investigations and for understanding specific cellular or molecular mechanisms, while in vivo studies are essential for assessing the impact of treatments, interventions, or conditions on living organisms. Together, these approaches contribute to our knowledge of biology, medicine, and various scientific fields (Hernandez and Woodrow; 2022).

#### 2.1.2.1. Biocompatibility In Vivo

In vivo biocompatibility refers to testing the biomaterial in a living body (animal model). Various test animals such as rats, hamsters and rabbits can be used for this test. The biomaterial implanted into the living body is removed after a certain period so the biocompatibility of the biomaterial with the surrounding tissues can be analysed experimentally. Histological and biological examinations of the tissue samples taken from the implantation site of the living body can give information about the biocompatibility of the biomaterial (Jensen and Figure, 2009).

#### 2.1.2.2. Biocompatibility In Vitro

Biocompatibility in vitro is to simulate biological reactions of the biomaterial; thus, it offers cheaper ways to evaluate biocompatibility. The biomaterial can be analysed in a medium where cell cultures containing living body cells, viruses or bacteria are artificially grown. This type of test can be performed without any barrier between the biomaterial and the cells, or it can be applied indirectly with a small barrier. In the cell culture, some tissues such as bone, kidney, lung, tumour, or amniotic membranes of various living creatures such as humans, rats and rabbits initially disintegrate into cells. These cells are suspended in nutritious liquids containing various salts, amino acids, and vitamins in a sterilised tube. As this cell suspension is kept at 36 ºC, cells adhere to the wall of the container or tube and cellular division occurs. This structure, which is formed as a result of cell reproduction, is called a cell culture (Franca et al., 2022). At this point, the biocompatibility in vitro is analysed by the cell growth rate, cell survival rate, cellular metabolic functions, or other cellular functions.

This type of test is relatively simple to perform and involves fewer complications compared to in vivo animal models. Therefore, it can be widely used to determine the biocompatibility of the biomaterial (Wu et al., 2022).

### 2.1.3. Biomechanical Concepts

Force: Pushing or pulling upon a body is known as force. Force is a vectorial magnitude; thus, it has direction. The unit of the force is newton (N) in the SI.

There are two main types of forces: contact and non-contact. Some examples of contact forces are muscular and frictional forces, while examples of non-contact forces are magnetic, gravitational, and electrostatic forces (Sakaguchi and Powers, 2012).

Stress: Stress is defined as force per unit area. The magnitude of the stress is associated with the quantity of the force applied and the area. When the force is applied to deform the body, the same magnitude of internal stress is generated within the body, but in the opposite direction. The stress unit is the pascal (Pa = $N/m^2$). 1 MPa = $10^6$ Pa. Stress is formulated in Eq. (2.1.) (Sakaguchi and Powers, 2012).

$$\sigma = F/A \quad \textbf{(2.1.)}$$

σ: Stress ($N/m^2$)
F: Force (N)
A: Area ($m^2$)

Stresses are divided into three major categories: compressive stress, tensile stress, and shear stress. Tensile stress and/or compressive stress can occur when force is applied but in the opposite direction. Shear stress can be caused by the force applied but parallel to the cross-section of the body. The schematic view of the internal stresses is shown in **Fig. 2.4.** (Sakaguchi and Powers, 2012).

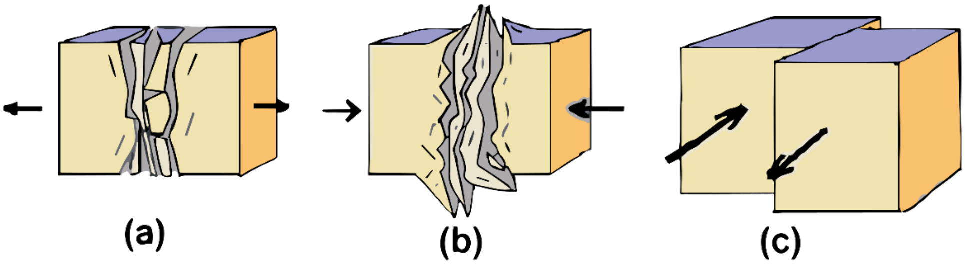

**Figure 2.4.** (a) tensile stress; (b) compressive stress; (c) shear stress (Sakaguchi and Powers, 2012).

Some studies on biomedical applications show that the most damaging types of stress to human bone are shear stress and tensile stress. In contrast, human bone is more resistant to compressive stress. In this regard, the compressive strength of human bone is 30% higher than its tensile strength since bone contains a lot of pores. These pores adversely affect the tensile strength properties as they do not bear the load. In addition, compressive stress has a positive influence on bone-biomaterial interface formation.

Strain: Strain is a dimensional alteration in the body when force is applied (see **Fig. 2.5.**). Strain and stress are different magnitudes. As mentioned previously, stress is a force with vectorial magnitude and direction and its unit is the pascal (Pa), but strain has no units (Tüfekci et al., 2023). Strain is formulated in Eq. (2.2.).

$\varepsilon = \Delta L/L_0$ **(2.2.)**

ε: Strain

ΔL: Changes in dimension (mm)

$L_0$: Original dimension (mm)

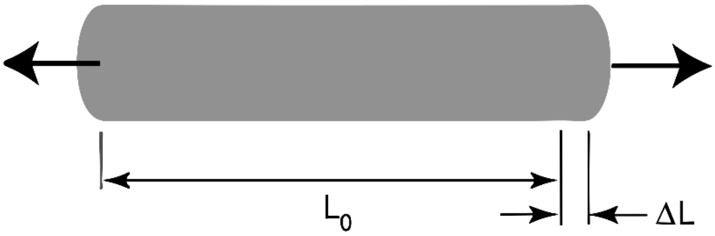

**Figure 2.5.** Strain (Sweeney, 2006).

According to the direction of the load applied to the body, the three major types of strain are longitudinal/tensile strain, volume strain and shearing strain. If the force deforming the body alone produces an alteration in length, the strain is called longitudinal strain or tensile strain. If the force deforming the body alone produces an alteration in volume, the strain is called volume strain. If the force deforming the body alone produces an alteration in the angle tilt, the strain is called shearing strain.

Elasticity: In a solid body, molecules and atoms can fully regain their original dimension thanks to intermolecular forces after the removal of the force, which is called elasticity. Elasticity is a reversible mechanism, as illustrated in **Fig. 2.6**.

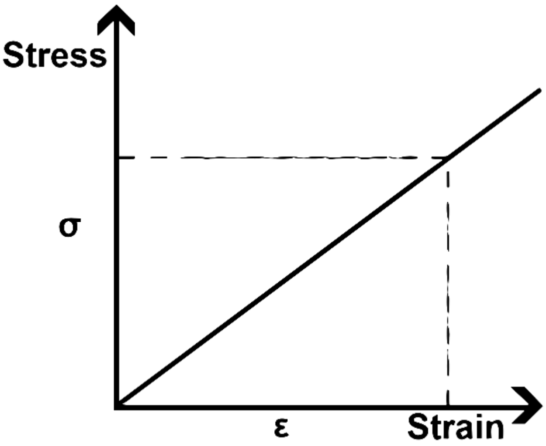

**Figure 2.6**. Elasticity (Sweeney, 2006).

Plasticity: In a solid body, molecules and atoms do not fully regain their original dimension after the removal of the force. In other words, a permanent alteration in the shape or size of the body occurs. If the stress applied exceeds the resultant force per unit area, energy or gravitational force can reach a point where atoms are completely separated. A rupture happens at this point.

Stress-strain curve*:* This gives the mechanical values used to define material performances such as yield strength, elastic limit, ultimate tensile strength, fracture strength, elasticity modulus and elongation (see **Fig. 2.7.**).

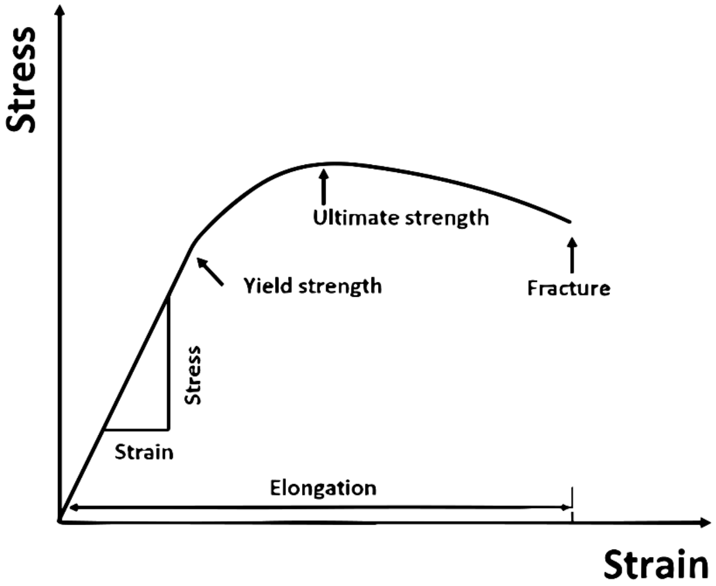

**Figure 2.7.** Stress-strain curve (Sweeney, 2006).

Young's modulus (elastic modulus): This is a mechanical property that indicates the rigidity or stiffness of a solid material, which explains the correlation between stress (force per unit area) and strain (dimensional change). When the elastic modulus of solid material increases, the stiffness of the material also increases (Sakaguchi and Powers, 2012). Young's modulus unit is the same as the unit of stress, called the pascal.

Hooke's law: The elongations occurring in the material are related to the stress within the elastic limits when the force is applied to the material (see **Fig. 2.8.**). In 1678, Hooke introduced the simple linear relationship between force and elongation. Based on Hooke's law, the total elongation of the material is formulated in Eq. (2.3.).

$\Delta L = {}^{F.Lo}/_{A.E}$ **(2.3.)**

F: force (N)

A: Area ($mm^2$)

$\Delta L$: Change in dimension (mm)

$L_0$: Original length (mm)

E: Elastic modulus or Young's modulus (Pa)

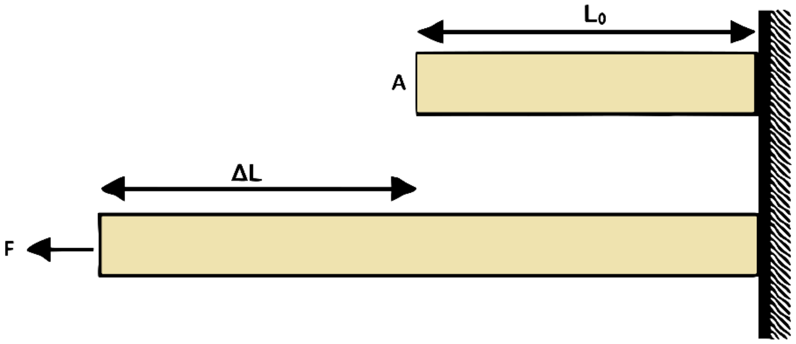

**Figure 2.8.** Hooke's law (Sweeney, 2006).

Poisson's ratio: When a solid material is stretched out in one direction, it will be thinner in the lateral direction; if it is compressed, it tends to get thicker (see **Fig. 2.9.**). For most materials, the Poisson's ratio is in the range between 0 and 0.5 (Sakaguchi and Powers, 2012). Poisson's ratio is formulated in Eq. (2.4.).

$V = -\, {}^{\varepsilon_{lateral}}/_{\varepsilon_{axial}}$ **(2.4.)**

V: Poisson's ratio

$\varepsilon_{lateral}$: Transverse strain

$\varepsilon_{axial}$: Longitudinal or axial strain

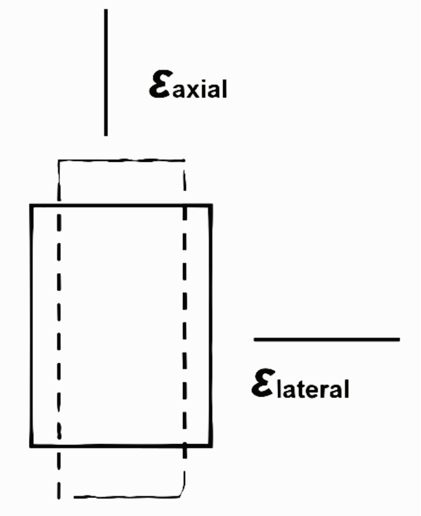

**Figure 2.9.** Poisson's ratio (Sweeney, 2006).

Isotropy and anisotropy: Material with the same mechanical, physical, thermal, and electrical properties in three principal axes (x, y, z) is called isotropic material. In other words, the mechanical properties or other properties do not change depending on the lattice directions. In contrast, material with different mechanical, physical, thermal, and electrical properties in three principal axes (x, y, z) is called anisotropic material. Some researchers have stated that human bone tissue has anisotropic features. Understanding the anisotropic nature of human bone tissue is crucial for designing implants that can mimic the mechanical properties of natural bone. Anisotropic materials have different properties (such as strength and stiffness) in different directions. Implants need to be designed with these variations in mind to ensure they can bear loads and function effectively (Zhu et al., 2022).

### 2.1.4. Classification of Biomaterials

Biomaterials can be classified into four major groups by the type of material used: metal, ceramic, polymer, and composite. Orthopaedic (hard tissue) biomaterials are generally made from metal or ceramic materials while surgical tools are manufactured from metal or polymer. In addition, metal-ceramic or polymer-metal composite biomaterials are employed in various biomedical applications (Dikici, 2016).

Ceramic biomaterials: Ceramic materials are oxides, nitrides, sulphides, and carbides of metals (e.g., $Al_2O_3$, $ZrO_2$) (Subedi, 2013). They can contain ionic, covalent, or partially metallic bonds (Kljajević et al., 2011). In general, ceramic materials have high melting points, outstanding corrosion resistance, high compressive strength, low thermal/electrical conductivity, and low tensile/shearing stress (Kükürtcü, 2008). Thanks to these characteristics, they are a potential biomaterial candidate.

Bio-ceramic or ceramic biomaterials are designed to bond with tissue/bone and have emerged as an alternative to metallic biomaterials (Pina et al., 2018). However, ceramic biomaterials exhibit a much more fragile and harder structure than human bone (Kaur and Singh, 2019). They also have lower fracture toughness compared to human bone (Jazayeri et al., 2018). Ceramic biomaterials should have superior biocompatibility, good chemical stability, non-oxidation property and poor degradability and they should not lead to allergic (i.e., toxic, teratogenic, or carcinogenic) reactions in the body when implanted. They are widely employed in dental and bone-related applications (Anusavice et al., 2012). Today, some synthetic ceramic biomaterials such as zirconia, alumina and titania can be used in different biomedical fields such as calcified tissues, coatings, medical sensors, dentistry, and orthopaedics (Danewalia and Singh, 2021). The use of ceramic biomaterials also opens a new horizon for soft tissue repair and regeneration (Kargozar et al., 2020). Ceramic biomaterials can display some benefits over metallic biomaterials such as lower density and relatively low cost. However, they have some drawbacks such as poor sinterability, machinability and ductility, which may limit their use in biomedical applications.

Polymeric biomaterials: Polymers have large molecules composed of long and repeated subunits (chains), called monomers, made from carbon, oxygen, and hydrogen atoms. Therefore, the mechanical and chemical properties of polymers can be determined by monomers.

Polymeric biomaterials (biopolymers) are materials specially designed for use in biomedical applications. Polymeric biomaterials can be produced to have different chemical and physical properties allowing them to be used in different specific applications such as cosmetic cosmetology and food. The unique flexibility and low density of polymeric biomaterials have great benefits in tissue engineering and biomaterial applications, which make them superior to other types of biomaterials (Ijaola et al., 2022). Additionally, polymeric biomaterials can be easily manufactured in different forms such as film, sheet, and fibre. However, the use of polymeric biomaterials is partly restricted in orthopaedic applications since they exhibit much lower mechanical properties compared to ceramic and metallic biomaterials (Li et al., 2014). Some examples of polymeric biomaterials are polyethylene, ultra-high-molecular-weight polyethylene and polymethyl methacrylate (see **Fig. 2.10.**). Polymethyl methacrylate can be used in the production of contact lenses due to its light transmittance.

Polymeric biomaterials are divided into two major groups by their origins: natural and synthetic (Xia et al., 2022). Examples of natural biopolymers are cellulose, natural rubber, and DNA (genetic material) while examples of synthetic biopolymers are polyethylene, polyurethane, polytetraoroethylene, polyacetal, polymethyl methacrylate, polyethylenetraftalate, polysulfide, polylactic acid, ultra-high-molecular-weight polyethylene and polyglycolic acid (Yetim, 2009).

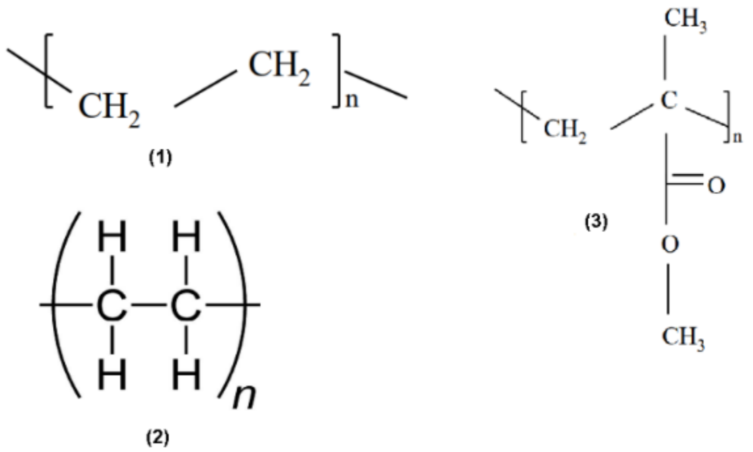

**Figure 2.10.** Chemical structures of polymeric biomaterials: 1) polyethylene, 2) ultra-high-molecular-weight polyethylene, 3) polymethyl methacrylate (Seal et al., 2001).

Composite biomaterials: In general, a composite is a ‘material with multiphase’. On a microscopic or macroscopic size scale, it is composed of two or more distinct constituent materials with different chemical properties. The purpose of using this material is to obtain materials with superior properties (Babu et al., 2022). One of the components of composite material is called the matrix; the other is known as reinforcement, which mechanically supports the matrix (Tiwary et al., 2022). The matrix and reinforcement components can be separated from each other by an interface. Since composite material may contain different chemical structures, the structure of composite material is more complicated compared to that of metal, polymer, or ceramic materials.

Composite biomaterials have superior properties compared to other types of biomaterial groups. The properties of composite biomaterials can be modified. It is possible to produce hard, lightweight materials and flexible composite biomaterials. All constituents of the composite materials used in biomaterial applications must be biocompatible and the interface between the matrix and reinforcement should not be degraded into the body when implanted. Dental filling composites and bone cement are examples of composite biomaterials (see **Fig. 2.11.**) (Bronzino and Peterson, 2014).

**Figure 2.11.** A dental implant made from composite biomaterial (Myer, 2003).

Metallic biomaterials: Metal is the most significant material class used in engineering designs (Dos Santos, 2015). Metal is quite strong and deformable, which explains its widespread use in engineering applications. Metal is known as ‘pure metal’ while metal mixtures made from two or more metals are called alloys. Alloys are not considered composite materials. The common characteristic properties of metals are high density and high conductivity. Today, there are various metal groups, and each metal type has its own characteristics. For example, aluminium and its alloys have ductile properties, while cast iron exhibits hard and fragile structures. Metals and their alloys can be classified into two major groups: ferrous and nonferrous. The former is based on iron and its alloys such as stainless steel and cast iron. The latter consists of other metallic elements and their alloys such as titanium and its alloy and cobalt-chrome alloys. Metals are generally not found pure in the crust except for noble metals. Further, the use of pure metal is not preferred in engineering design and biomedical applications owing to low corrosion resistance and insufficient mechanic properties. For this reason, most metals can be alloyed by other alloyant elements to improve corrosion resistance, mechanical properties, and other properties (Callister and Rethwisch, 2011).

Like other types of biomaterials such as polymer, ceramic and composite biomaterial, a metallic biomaterial (bio-metal) should be biocompatible. The biocompatibility of the metallic biomaterial is related to its corrosion properties in vivo (Niinomi, 2002). Metallic biomaterials are especially employed in hard tissue applications such as hip joint and knee joint prostheses and dental implants due to their good machinability and their acceptable mechanical performance. Vanadium steel is the first bio-metal developed as a biomaterial. However, today, the most widely used metallic biomaterials are titanium and its alloys, stainless steel, cobalt-chromium alloys, and miscellaneous others such as tantalum or gold (Bronzino, 2000).

Steel is an alloy of iron with a carbon content that may range from 0.03% to 2% of its composition. It may also contain chromium, nickel, aluminium, cobalt, manganese, molybdenum, silicon and other alloyant elements, depending on its grade. If the quantity of total alloyant elements is less than 1%, it is called plain carbon steel. If it is more than 1%, it is called alloy steel (Callister and Rethwisch, 2011).

Stainless steel can be used in many industrial applications such as surgical instruments, automotive and construction products, refrigerators and washing machines, cargo ships, and biomedical applications (Seetharaman, 2005). Stainless steel generally contains 10.5% chromium and 8% nickel content, including carbon and other elements. Two stainless steel groups are used in biomedical fields: 316 and 316L stainless steels. The only difference between them is carbon concentration. The 316 is a numerical definition indicating that the alloy is in the austenitic stainless-steel class, while L is a sign that it has a low carbon content (C <0.003) (Niinomi, 2002). These groups of stainless steel are not appropriate to heat treatment, but they can be hardened by cold working. Also, they are not magnetic and have outstanding corrosion resistance. However, 316 and 316L stainless steel may corrode when exposed to tissue and the body. Additionally, previous studies have shown that these stainless steel groups may cause allergic reactions in the body when implanted due to the nickel content in their chemical compositions. To eliminate the allergic effect of nickel, the new research trend is to develop nickel-free stainless steel for use in biomedical applications (Chen and Thouas, 2015). Some biomaterials made from stainless steel are shown in **Fig. 2.12** (Elden, 2016).

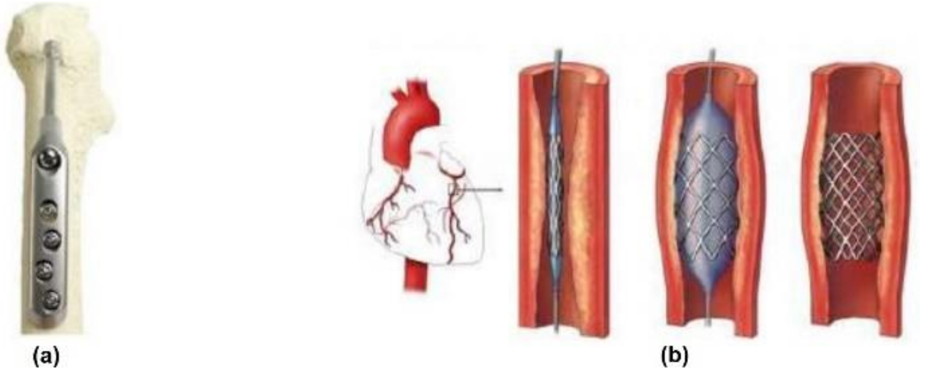

**Figure 2.12.** Implant materials made from stainless steel (a: bone fracture plate; b: cardiac stent) (Elden, 2016).

Cobalt-chrome alloys are divided into two categories: CoCrMo and CoNiCrMo alloys. Castable CoCrMo alloys can be used in dental applications while wrought CoNiCrMo alloys are designed for manufacturing the stems of prostheses. Molybdenum is added to obtain finer grains, thus providing higher strength properties. In addition, when CoNiCrMo alloys can be heat treated, the strengths of these alloys can be enhanced.

Cobalt-chromium alloys exhibit good toughness, high specific strength properties and good biocompatibility. Further, they have superior mechanical performance since they contain precipitation of carbides and multiphase structure. Such conditions can enhance the stiffness of cobalt-chrome alloys significantly. The hardness values of cobalt-chrome alloys are in the range of 550 HV and 800 HV, and their tensile strength values vary between 145 MPa and 270 MPa. Cobalt-chromium alloys exhibit better wear resistance than stainless steel and titanium and its alloys (Park and Kim, 2014). Some biomaterials made from cobalt-chromium alloys are illustrated in **Fig. 2.13**. (Sahoo et al., 2019).

**Figure 2.13.** Femoral component made from cobalt-chromium alloys (Brandt et al., 2013).

Titanium and its alloys can be widely used in implantable devices due to good corrosion resistance, acceptable mechanical performance, and excellent biocompatibility (Banerjee and Williams, 2013). The most common titanium-based alloy used as a biomaterial is Ti-6Al-4V. This type of alloy has about the same fatigue strength (550MPa) as the cobalt-chromium alloys. Titanium has an allotropic transformation; it exhibits a hexagonal close-packed structure (hcp, α-Ti) up to 882$^{o}$C, while above that temperature, it has a body-centred cubic structure (bcc, β-Tı). The phase constituent of the titanium-based alloys can be significantly altered by the addition of alloyant elements, which may play a crucial role in the mechanical properties of titanium-based alloys because the mechanical properties of the α-Ti and β-Ti type phases are different from each other (Pushp et al., 2022). β-Ti type alloys are more ductile than α-Ti type alloys since β-Ti type titanium alloys with body-centred cubic crystal structures have more slip planes than α-type titanium alloys, which have hexagonal close-packed crystal structures. β-Ti type alloys, therefore, are generally preferred in implant applications (Liu et al., 2013). In conclusion, alloying titanium with other alloyant elements is strategically important to enhance mechanical performance and other properties (Liu et al., 2017; Darvell, 2018). Titanium and its alloys are discussed extensively in Chapter 2.2.

### 2.1.5. Problems with Commercial Orthopaedic Biomaterials

Orthopaedic biomaterials, one of the largest markets in the world, have many drawbacks such as limited lifetime, high price, and insufficient mechanical performance. Limited lifetime: orthopaedic biomaterials have a finite lifespan within the body. They may wear off or degrade over time due to factors such as mechanical stresses, corrosion, and inflammatory responses. High price: orthopaedic biomaterials, particularly advanced and biocompatible materials, can be expensive to manufacture and utilize. The development and production of high-quality biomaterials often require specialized processes and materials, which can contribute to their high cost. Insufficient mechanical performance: orthopaedic biomaterials must meet mechanical and structural requirements to withstand the forces and stresses within the human body when implanted. Some biomaterials may not possess the necessary mechanical properties, leading to issues such as implant failure, loosening, or fractures. These drawbacks can necessitate further surgeries. It's important to note that despite these drawbacks, orthopaedic biomaterials have significantly improved the quality of life for many individuals. Advances in materials science and biomedical engineering are continually addressing these issues, striving to develop biomaterials with longer lifespans, better mechanical performance, and more cost-effective solutions. Additionally, latest research aims to enhance the integration of these materials with the human body, minimize adverse reactions, and reduce the need for further revisions.

The 10-year clinical success rate of titanium implants is reported to be up to 99%. Additionally, 91% of all implants remain after 15 years, demonstrating their long-term durability (Nicholson, 2020). This may be less, depending on the patient's age and other conditions. In general, hip and knee problems start from the age of 40. The average age in Europe is 76.4 for men and 82.5 for women, which indicates that the service life of the total joint replacement is much shorter than the human lifespan (Willett et al., 2017). Only one revision surgery helps to provide the desired limb functionality. In contrast, further revision surgeries may significantly limit the patient's functionality due to the removal of some bone fragments (see **Fig. 2.14.**). Therefore, the service life of the orthopaedic biomaterial is of great importance to increase the life of the orthopaedic biomaterial.

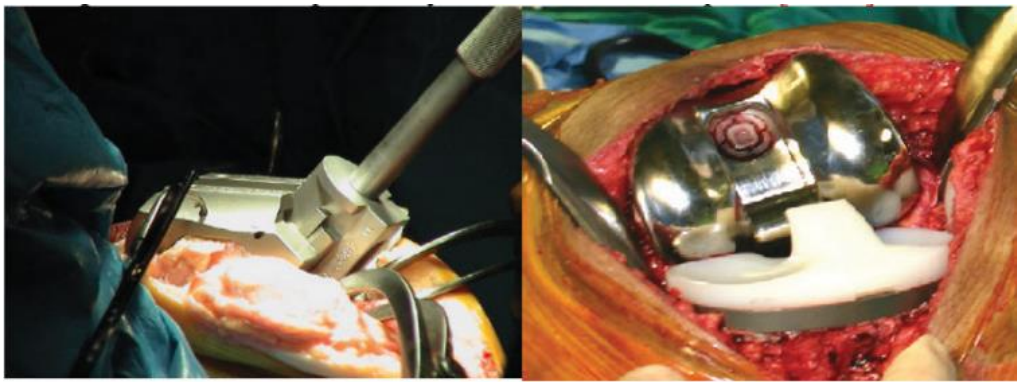

**Figure 2.14.** A revision surgery (Adamczyk and Opiela 2004).

Another problem is the biocompatibility features of orthopaedic biomaterial, as many cases of allergies and infections have been reported in the last few years. When orthopaedic biomaterial is implanted, a variety of biological and chemical reactions may occur between the orthopaedic biomaterial and the tissue. Further, poor biocompatibility levels may lead to the formation of thrombosis and fibrous tissue at the implantation site (see **Fig. 2.15.**) (Williams, 2008).

**Figure 2.15.** Tissue necrosis and osteolysis (Williams, 2008).

As stated before, titanium and its alloys can generally be used as orthopaedic biomaterials due to their superior corrosion resistance, outstanding biocompatibility, and acceptable mechanical performance. Orthopaedic biomaterials made from titanium and its alloys are exclusive and expensive materials that cost up to €3,000 in Europe and €11,000 in the USA (Nytimes, 2010). This amount covers the cost of titanium, alloy production, and risk factor. In more detail, the fabrication of titanium is expensive as titanium is melted several times to ensure high purity (Madehow, 2022). Therefore, the market price of titanium is €82 per kg, while that of titanium sponge is currently €4.6 per kg (Metal pages, 2022). After forging or casting at high temperatures, the cost of titanium products can reach between €800 and €1,000 per kg (Orthopaedic Network News, 2020). Moreover, secondary processes may be required to obtain the desired shape after production. In conclusion, the failure risk of the orthopaedic biomaterials used today is high (see **Table 2.2.**).

**Table 2.2.** Advantages and drawbacks of current biomaterials.

| **Type of raw material** | **Advantages** | **Drawbacks** | **Elastic modulus (Ga)** | **Density (g/cm$^3$)** |
|---|---|---|---|---|
| Stainless steel | ❖ Good strength properties<br>❖ Ease of fabrication<br>❖ Ease of workability | ❖ High elastic modulus | 200 | 8 |
| Cobalt-chromium | ❖ Good strength properties<br>❖ High corrosion resistance<br>❖ Relative wear resistance | ❖ Unknown long-term effects of Co and Cr<br>❖ High elastic modulus | 230 | 8.5 |
| Titanium-based alloys | ❖ Good strength properties<br>❖ Acceptable mechanical properties<br>❖ Corrosion resistance | ❖ Low wear resistance | 106 | 4.4 |
| Bone | - | - | 7-30 | 2 |

Today, there are some regulatory requirements for for implantable materials to show their safety and effectiveness before surgery. Implant material manufacturers must comply with many international standards. These are Premarket Approval (PMA), Investigational Device Exemption (IDE) and Quality System (QS). Only medical devices that meet these standards find a place in the implant market (Morrison, et al., 2015).

#### 2.1.5.1. Stress-Shielding Issue

Biomechanical compatibility, i.e., the matching of mechanical performance such as hardness, ultimate compressive strength, and elastic modulus, between the orthopaedic biomaterial and the surrounding bone tissue is a fundamental requirement for implantology (Wojnar et al., 2001; Adamczyk and Opiela, 2004; Málek et al., 2012; Kunčická et al., 2017). The majority of the metallic biomaterials such as cobalt-chrome alloys, titanium and its alloys and stainless steel used as load-bearing implants have much greater elastic modulus than natural bone. This may result in a reduction in bone mineral density at the implantation site, which is known as the stress-shielding effect. It can also be seen radiographically (see **Fig. 2.16.**) (Sumitomo et al., 2008; Kusano et al., 2018). In other words, bone resorption (osteopenia) may occur over time due to the removal of typical stress from the bone by an implant (Quan et al., 2009; Raffa et al., 2021). The reduction in bone density may cause a periprosthetic osteolysis and aseptic loosening. This may increase healing time and even result in implant failure. Therefore, use of orthopaedic biomaterials, which have mechanical properties close to natural bone tissue, can reduce stress shielding and bone resorption. Therefore, the mechanical performance of the orthopaedic biomaterial should be analysed comprehensively before surgery (Li et al., 2014). In conclusion, the stress-shielding effect may have clinical consequences (Engh Jr et al., 2003).

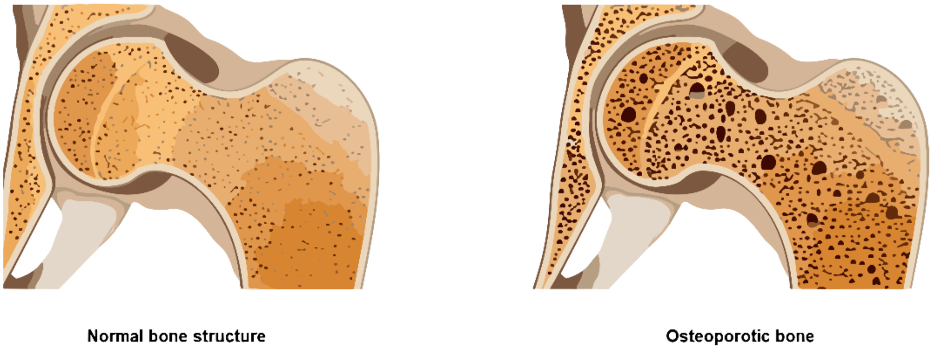
Normal bone structure

Osteoporotic bone

**Figure. 2.16**. Schematic image of healthy vs osteoporotic bone (Kusano et al., 2018).

Based on the literature, there is a relationship between porosity and stress shielding effect. Accordingly, porous orthopaedic biomaterials can reduce the stress shielding effect phenomenon, and the reduction in bone density. Optimal pore size and structure can provide better stress shielding relief by lowering mechanical properties of the orthopaedic biomaterial, which reduce the bio-mechanical mismatch between bone and orthopaedic biomaterial as the lower stiffness can reduce the non-uniform stress distribution.

Osseointegration phenomena are generated by stress that a bone is exposed to through the bone-implant interface. Non-uniform load distribution between the orthopaedic biomaterial and the bone may also cause osseointegration phenomena. The bone structure is aligned along the principal local loading direction, which means that the stress applied is considered a local regulator (Couto et al., 2023). The level of osseointegration phenomena is determined by the roughness of the implant surface (see **Fig. 2.17**.). Further, many biomechanical factors affect the distribution of stress between the orthopaedic biomaterial and the bone (interfacial stress);

these are implant geometry, density, mechanical performance, and bone-tissue interaction (Orr et al., 2006). All these interrelated properties have vital importance for the development of implant stability (Götz et al., 2004). After surgery, there are two types of orthopaedic biomaterial stability: primary and long-term stability. The former is the bone or tissue newly formed around the implantation site (bone-implant interface) (Abrahamsson et al., 2004; Berglundh et al., 2007). The latter is also known as secondary stability and refers to stability after healing over time (Albrektsson and Johansson, 2001).

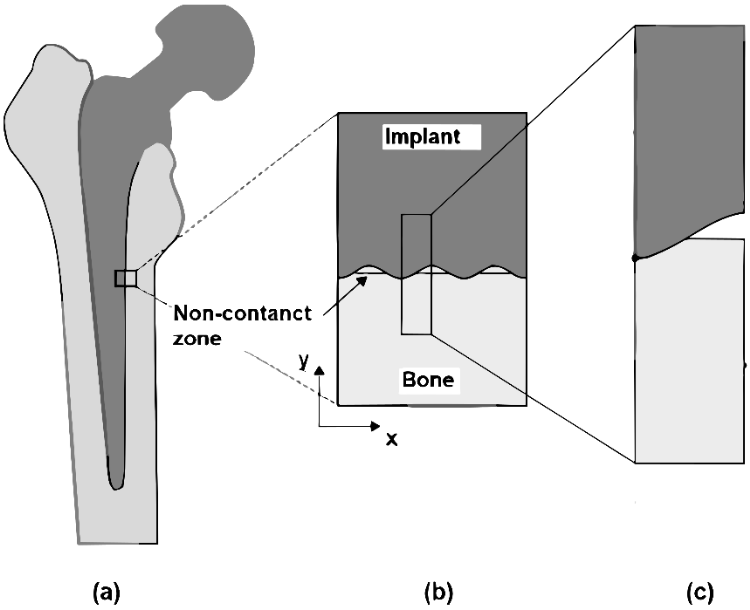

**Figure 2.17.** The geometrical configuration of the bone-implant interface (a: macroscopic appearance b: mesoscopic appearance c: microscopic appearance) (Orr et al., 2006).

On the other hand, the selection of orthopaedic biomaterial is related to clinical requirements, material performance and fabrication cost. Recently, orthopaedic biomaterials with a porous structure, which is beneficial to bone ingrowth and other life activities, have been clinically employed, but clinic failure of short-term or long-term implants still is difficult to predict. The porous structure of the implant material can also help in adjusting mechanical properties like elastic modulus, hardness, and ultimate compressive strength according to the human bone that is under stress, allowing the remodelling and osseointegration of the bone at the implantation site. Thus, mechanical compatibility, which is an inevitable requirement for the load-bearing implant material, can be ensured. There is a delicate balance between the porosity within the implant and the mechanical performances of the implant material. Regarding this, the most significant aspects are pore characteristics such as distribution, morphology and control of porosity (Wen et al., 2002). Consequently, the risk of the stress-shielding effect phenomena can be minimised by adjusting optimal porosity within implant material (Thouas, 2015). Also, design of the orthopaedic biomaterial plays a crucial role on the risk of stress shielding effect. The surface roughness, bone-implant contact ratio, properties of material used should be optimized. These strategies can reduce the risk of stress shielding effect and promote bone ingrowth around the implant.

#### 2.1.5.2. Wear Debris Effect

Another problem relevant to the orthopaedic biomaterial is the release of metal ions (shavings). However, the release of metal shavings from the orthopaedic biomaterials into the tissue can be minimised if orthopaedic biomaterials with good wear resistance are employed in the moving part of the implant where the friction is higher. The metal surfaces of the moving implant parts in contact with the bone create high friction. Therefore, the wear resistance of the orthopaedic biomaterial is essential for long-term implant success. If its wear resistance is too low, wear debris released from the orthopaedic biomaterial may form at the implantation site and then migrate to surrounding tissue. Such a case may cause toxic or allergic reactions in the body (see **Fig. 2.18.**) (Hallab et al., 2005; Sargeant and Goswami, 2006). Therefore, wear debris is a significant determinant of the biocompatibility of the orthopaedic biomaterial. Today, various coating techniques can be employed to enhance the surface quality of the orthopaedic biomaterial.

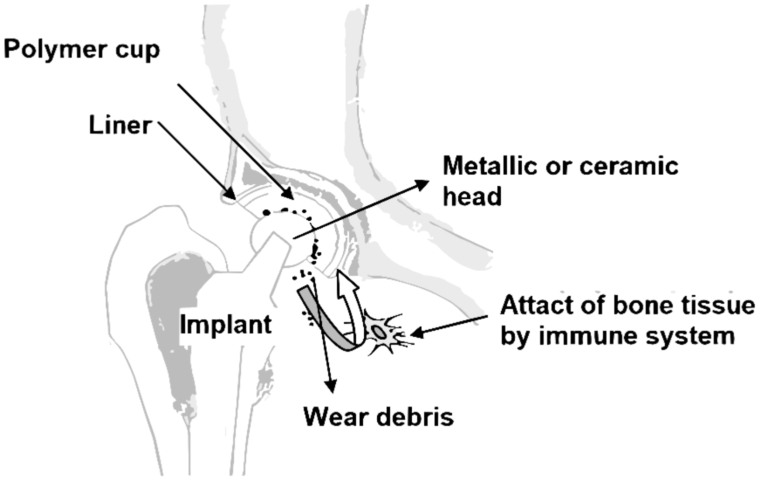

**Figure 2.18.** Wear debris effect (Geetha et al., 2009).

Wear debris characteristics like size, volume fraction and composition are related to the biological reactivity of the orthopaedic biomaterial (Yang et al., 2002). Phagocytised particles ranging from 0.1 µm to 10 µm are the most biologically reactive. Compared to large particles, particles with an average size of <1 µm may lead to more severe inflammatory at the interface between the implant and bone/tissue (Vermes et al., 2000). Such inflammatory reactions forming on the implantation site may cause aseptic loosening. Many studies have revealed that 75% of implant failures are mainly due to loosening from aseptic osteolysis. Some studies have examined the effect of wear debris released from orthopaedic biomaterials such as cobalt, titanium, chromium and stainless steel, alumina ($Al_2O_3$) and zirconia ($ZrO_2$) by using SEM. The size and shape of particle debris have quite a high risk of causing inflammation for osteoblasts (Stratton-Powell et al., 2016; Gibon et al., 2017; Klinder et al., 2018; Connors et al., 2022). Typically, some wear products can be short-chain alkaline and some metal ions, which may generate an additional toxic or allergic effect at the implantation site (Bazhin et al., 2010; Magone et al., 2015; Jonitz-Heincke et al., 2017). For instance, Ti-6Al-4V is the most popular titanium alloy used as an orthopaedic biomaterial; it is called Grade V titanium-based alloy. $V_2O_5$ oxide film forming on the surface of Ti-6Al-4V alloy may generate a toxic effect in the human body when implanted (Gao et al., 2011). Also, aluminium ions released from Ti-6Al-4V alloy may lead to some health problems such as Alzheimer's disease, neuropathy and osteomalacia (Nag et al., 2005; Ou et al., 2017).

Some cell types like dendritic cells, synovial fibroblasts, osteoblasts, and osteoclasts play a role in the formation of osteolysis at the implantation site although chronic inflammatory reactions resulting from the wear debris of the implant are mediated by macrophages (Limmer and Wirtz, 2017; Li et al., 2018). During wear debris, proinflammatory mediators are released by macrophages. In this regard, particle debris interacts with the osteoblast through phagocytic and non-phagocytic mechanisms. Such cases may induce the differentiation, multiplication, and recruitment of osteoclast precursors, ultimately resulting in bone resorption. Further, wear debris inhibits osteoblast functions, which may have adverse effects on cell proliferation. Thus, understanding the biological response of osteoblasts to wear debris is critical for bone resorption.

### 2.1.6. The Human Bone

Natural bone can be divided into two main groups according to its structure: compact (cortical) and cancellous (trabecular or spongy). The typical structure of the bone is shown in **Fig. 2.19**.

Compact (cortical) bone: This is the external layer of the bone structure, which has a dense, strong, durable structure. It helps to strengthen the bone and preserves cancellous tissue underneath.

Cancellous (trabecular or spongy) bone: This is found in the inner layer of the bone structure. It exhibits a less dense and lighter structure compared to cortical bone tissue because its structure possesses more porosity. Its main function is to give flexibility to the bone. It also serves as a shock absorber in case of trauma. It also plays an important role in reducing the weight of the skeletal system due to its lighter structure (Biologydictionary, 2021).

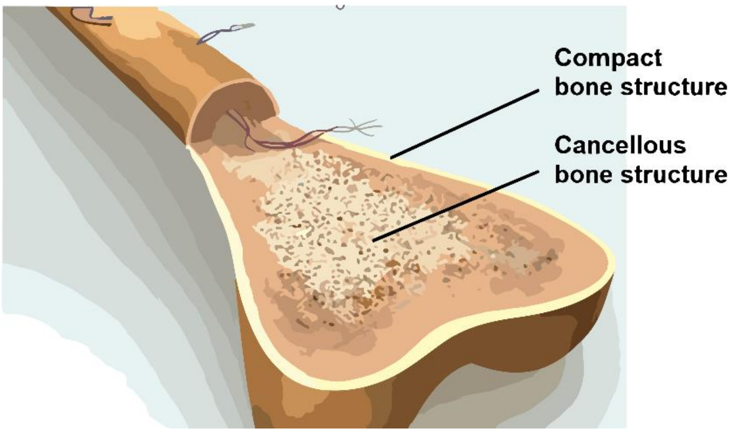

**Figure 2.19.** The typical structure of the natural bone (Biologydictionary, 2021).

The bone tissue should be analysed comprehensively before the surgery. Human bone is a solid living tissue whose structure consists of 70% inorganic substances and 30% organic substances. The inorganic substances contain calcium and phosphate salts, while the organic substances comprise collagen, hydroxyapatite, and fibres. There are four types of cells in bone tissue: osteoblasts, osteocytes, osteoprogenitor cells, and osteoclasts (see **Fig.2.20.**).

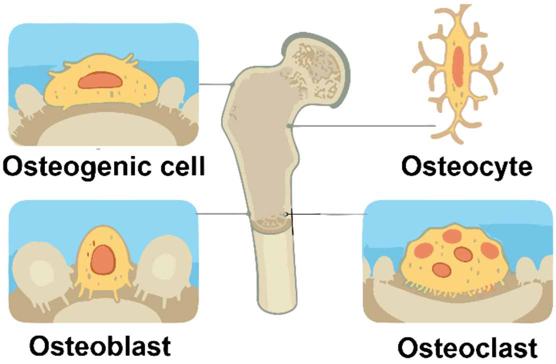

**Figure 2.20.** Cell types of bone tissue (Biology dictionary, 2021).

Human bones have multifunctional structures providing support, protection, and mobility to body. They also play crucial roles in blood cell production, mineral storage, and various other cellular activities. Implant materials can be manufactured to mimic bone properties and provide support or replacement when natural bone is damaged or loss its functionality (Demirel, 2012).

Advantages of natural bone in implantology (Shamsoddin et al., 2019):

- Natural bone can grow and integrate with the implant over time, which results in a fully integration at implantation area.
- Natural bone can remodel itself according to load exposure.
- Implant materials can tightly make a bond with natural bone.

Disadvantages of natural bone in implantology (Shamsoddin et al., 2019):

- Natural bone may not desired quantity or quality for surgery, which depends on the patient's health status, gender, or age. In this case, bone grafting may be needed.
- During surgery, infection and other complications may occur.

### 2.1.6.1. Mechanical Properties of Bone

The mechanical performance of the cortical bone is much greater than that of cancellous (trabecular) bone. For instance, the elastic modulus of the cortical bone is in the range between 3 GPa and 30 GPa, while that of the trabecular bone is between 0.02 GPa and 3 GPa (see **Fig. 2.21.**). Mechanical properties of the bone are dependent upon the chemical (organic or inorganic content) structure, density, porosity fraction, distribution of porosity and shape of the bone.

Cortical bone is about ten times more flexible and three times lighter than stainless steel. A comparison of some mechanical properties such as elastic modulus and tensile strength of orthopaedic biomaterials with human bone is given in **Fig. 2.22.** Human bones do not have a fully compact; they contain pores of different sizes. The porosity of human bone varies between 5% and 95% according to the bone type. As stated before, spongy bone tissue exhibits a more porous structure than cortical bone tissue (Yalçın, 2012).

Disruption of the integrity and continuation of the bone is called ‘breaking’. The cause of breakage may be external stresses or internal stresses. The healing of a bone fracture can take time, depending on the bone type and other factors not controlled by the surgeon such as the patient's health and age (Yalçın, 2012).

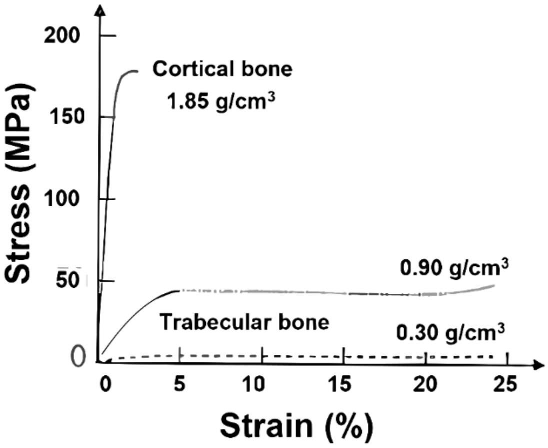

**Figure 2.21.** Stress-strain graph of cortical and trabecular bones (Yalçın, 2012).

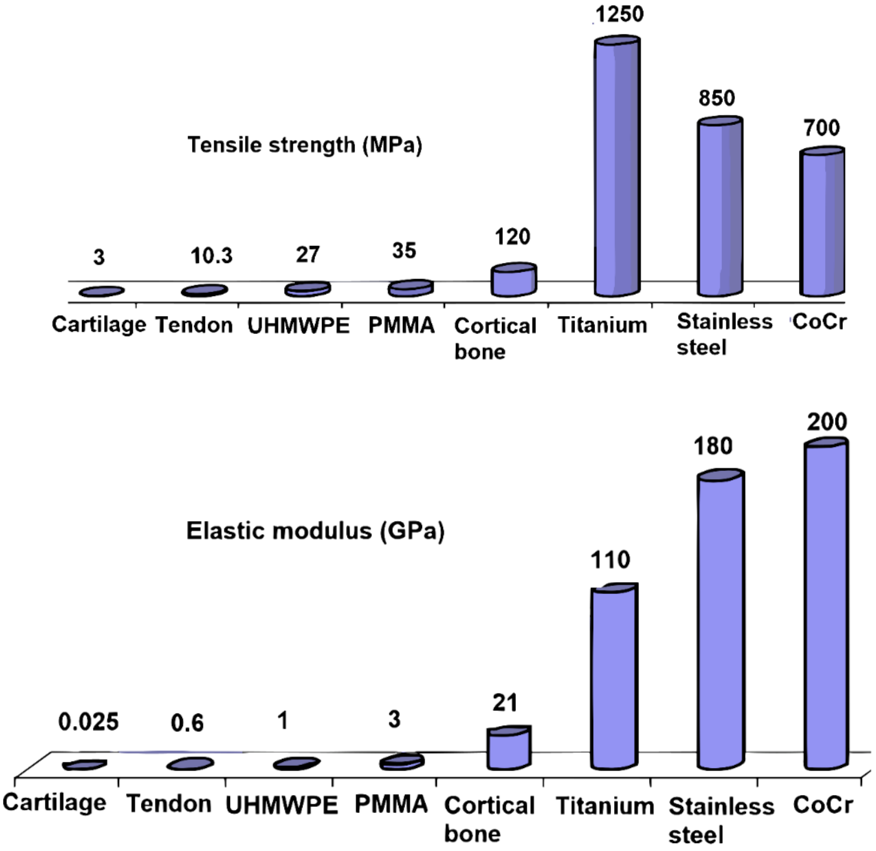

**Figure 2.22.** Tensile strength and elastic modulus values of cortical bone, some tissues, and orthopaedic biomaterials (Yalçın, 2012).

## 2.2. Titanium

### 2.2.1. Titanium Production

Titanium is the third most widely used metal in the industries after aluminium and iron. Titanium ore is the sixth most abundant element in the earth's crust, at 0.6% (Krebs, 2006). Titanium was discovered by Gregor, a mineralogist, in 1791 and was named by Klaproth in 1795 (Donachie, 2000). Nilson and Petterson were first able to manufacture impure titanium in 1887, but in 1919, Hunter produced pure titanium (purity grade: 99%) by extracting it from the ores (Bordbar et al., 2017). Based on this process, the extraction of titanium can be begun by mixing titanium-dioxide with chlorine and coke, a fuel with a high carbon content, and heat treatment is then applied to the titanium-dioxide (rutile; $TiO_2$). The output of this process is titanium-tetrachloride ($TiCl_4$) (see **Fig. 2.23.**).

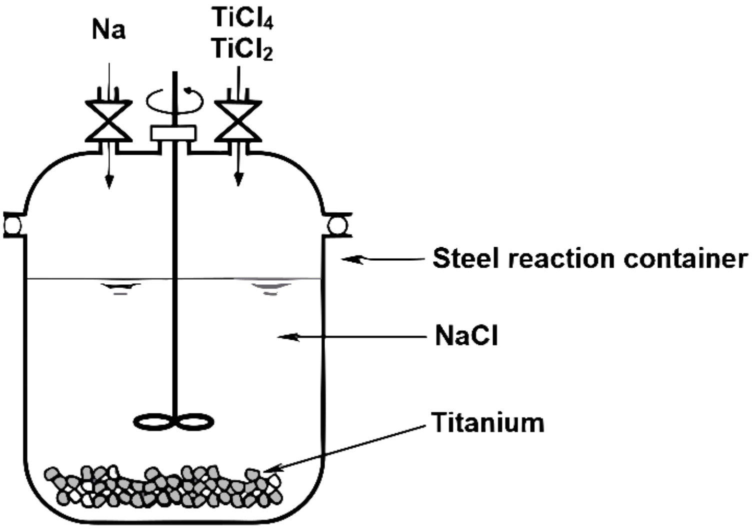

**Figure 2.23.** Schematic image of Hunter's process for titanium extraction (Takeda et al., 2014).

In 1938, William Kroll, a metallurgist, also worked on the reduction of titanium, which is called the modern Kroll's process. This methodology is similar to a process developed by Hunter (see **Fig. 2.24.**).

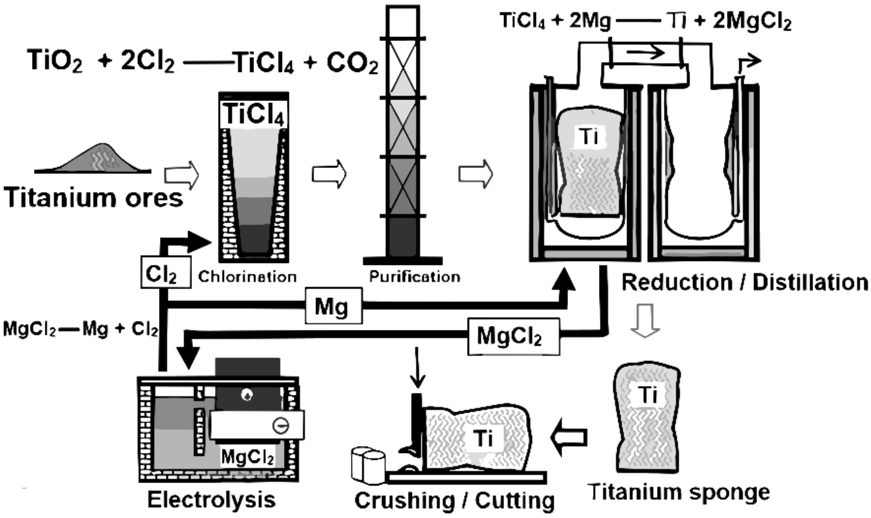

**Figure 2.24.** Schematic of Kroll's process for titanium extraction (Elfghi, 2020).

In 1948, several projects on the production of titanium were supported by the US government. Titanium became the focus of researchers so that it could be efficiently used in many industries. Today, the production of titanium has reached a few million kilograms per year (Pushp et al., 2022). The primary mineral sources of titanium are ilmenite ($FeTiO_3$) and rutile ($TiO_2$) (see **Fig. 2.25.**) (Dikici, 2016). Other ores include perovskite, anatase, brookite and titanite.

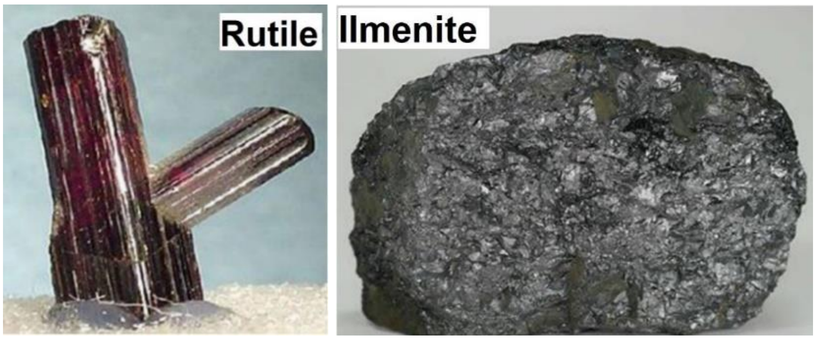

**Figure 2.25.** Primary ores of titanium: rutile and Ilmenite (King, 2015).

The use of titanium metal was exclusive to military applications until its commercialisation. Its initial major use field was the aerospace industry, which accounted for about 75% of the total amount of titanium manufactured in the USA. However, after 1960, titanium metal started to be used in biomedical industries, particularly in implantology. Titanium was also employed in other industries, such as paint, automotive, space, cosmetics, and food production (Leyens and Peters, 2003). China, Russia and Kazakhstan have important shares in the titanium production market (see **Fig. 2.26.**). The knowledge of the top countries in the production of titanium metal used in medical devices is essential for implantology in terms of its availability, quality, cost, and compliance.

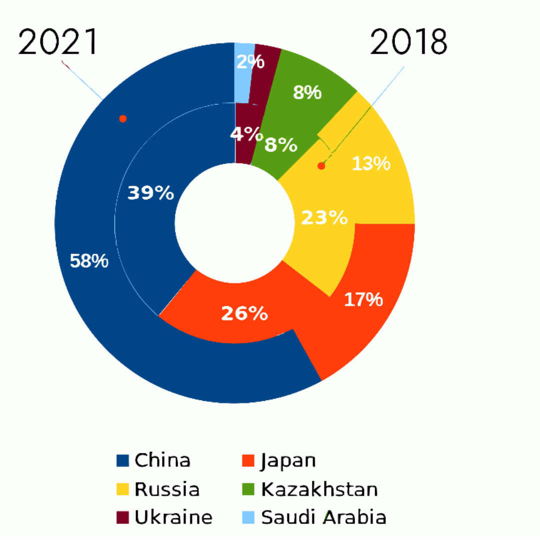

**Figure 2.26.** Top countries in the production of titanium metal (USGS, 2022).

### 2.2.2. Physical and Chemical Properties of Titanium

Titanium is found in the fourth period and is one of the transition metals of the periodic table (see **Fig. 2.27**.). The chemical, physical, and mechanical properties of titanium are shown in **Table 2.3.** (Leyens and Peters, 2003). This metal is solid at ambient temperature. Compared to other metals such as cobalt, aluminium and iron, titanium can exhibit superior strength properties. For instance, titanium is as strong as stainless steel but 45% lighter than stainless steel, and titanium is 60% heavier than aluminium but twice as strong. Therefore, its lightweight characteristic position makes it a competitive metal in engineering and design applications. At this point, it can be considered the best option for biomedical applications.

Moreover, titanium can be manufactured in various product forms such as ingots, rods, sheets, and powders by using differing production methodologies (Balazic et al., 2007; Bersuker, 2010).

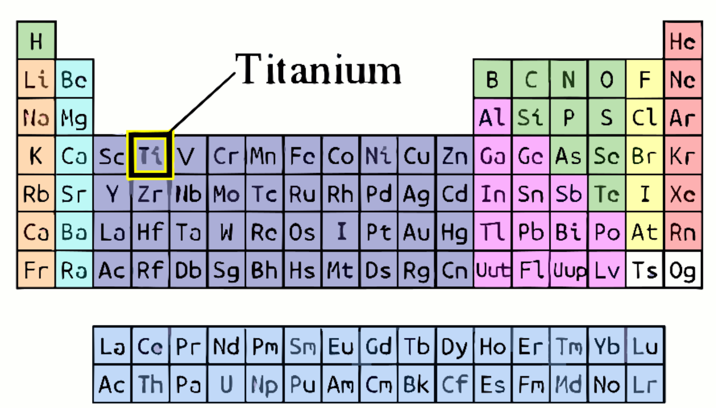

**Figure 2.27.** Periodic table (USGS, 2022).

**Table 2.3.** Chemical, physical, and mechanical properties of titanium (Leyens and Peters, 2003).

| **Chemical Properties** | | **Physical and Mechanical Properties** | |
|---|---|---|---|
| **Symbol** | Ti | **Density (g/cm$^3$)** | 4.51 |
| **Period and group** | 4/4B | **Melting point (ºC)** | 1668 |
| **Atomic number** | 22 | **Boiling point (ºC)** | 3287 |
| **Atomic mass (g/mol)** | 47.87 | **Heat of vaporisation (kj/mol)** | 421 |
| **Atomic diameter (ºA)** | 2 | **Heat capacity (j/g.K)** | 0.52 |
| **Crystal structure under 882 ºC** | Hexagonal close-packed (HCP) | **Electrical conductivity (ohm.cm)** | 0.0234x10$^{-6}$ |
| **Crystal structure above 882 ºC** | Body-centred cubic (BCC) | **Thermal conductivity (W/cm.K)** | 0.219 |
| **Electron distribution** | 1S$^2$, 2S$^2$, 2P$^6$, 3S$^2$, 3P$^6$, 4S$^2$, 3d$^2$ | **Specific heat (J/g.K)** | 0.520 |
| **Crystal structure at high pressure** | Hexagonal close-packed (HCP) | **Tensile strength (MPa)** | 540-740 |
| **Magnetism** | Antimagnetic | **Elastic modulus (GPa)** | 105-110 |

Titanium-dioxide ($TiO_2$) is the most well-known impure form of titanium. **Fig. 2.28** shows the crystal structure of titanium-dioxide. Commercially pure titanium generally contains traces of oxygen, iron, carbon, nitrogen, and hydrogen concentrations as titanium tends to react with these elements even at room temperature (Brunette, 2001). There are five different isotopes of titanium in the earth's crust: 46-Ti, 47-Ti, 48-Ti, 49-Ti and 50-Ti, and the most abundant isotope is 48-Ti (Gerdemann, 2001).

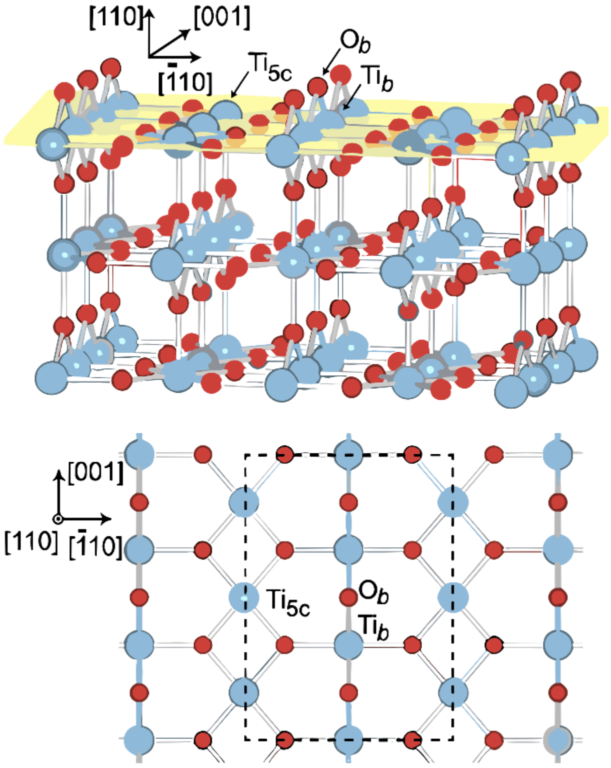

**Figure 2.28.** Titanium-dioxide crystal structure (Moses, 2016).

### 2.2.3. Titanium and Its Alloys

Various types of materials such as titanium and its alloys, stainless steel, and cobalt-chrome alloys used by scientists have biomedical applications. Titanium and its alloys have superior properties to the above-mentioned material groups; titanium and its alloys can be widely employed in biomedical applications due to their low densities, their acceptable mechanical properties, and their outstanding biocompatibilities. Moreover, they are biologically inert and can establish a good bond with osteoblasts in the implantation site when implanted. The first aim of the present thesis is to produce newly developed titanium-based alloys to evaluate their morphologies and microstructures. In this regard, titanium and its alloys achieved in this study are investigated extensively.

Titanium and its alloys can have a wide variety of microstructures according to the chemical composition and thermal treatments applied (Geetha, at al., 2009). Thus, titanium and its alloys are generally categorised according to phase constituents found in the titanium matrix; these are alpha (α-Ti), alpha + beta (α-Ti + β-Ti) and beta (β-Ti) type alloys. Further, the microstructure of commercially pure titanium has a hexagonal closed package (hcp) structure known as the α-Ti phase, while above 882°C it has a body-centred cubic (bcc) structure called the β-Ti phase, as pure titanium can exhibit an allotropic transformation. The α-Ti phase with hcp and the β-Ti phase with bcc structures are shown in **Fig. 2.29.** (Leyens and Peters, 2003).

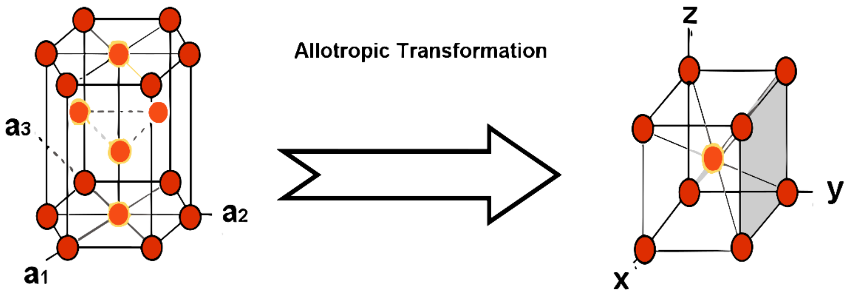

**α-Ti**
**Hexagonal close packed (HCP)**

**β-Ti**
**Body centred close packed (BCC)**

**Figure 2.29.** Crystal structures of titanium (Leyens and Peters, 2003).

Alloyant elements such as oxygen, niobium and tin generally have determinant effects on controlling the microstructures of titanium and its alloys by changing the α-Ti → β-Ti phase transformation temperature of titanium (see **Fig. 2.30.**). According to this concept, some elements affecting the phase structure of titanium-based alloy are given in **Table 2.4.** (Li et al., 2014). Aluminium, nitrogen, oxygen, or carbon stabilises the α-Ti phase, while vanadium, molybdenum, niobium, or tantalum makes the β-Ti phase stable in the microstructure (Eisenbarth et al., 2004). Some neutral elements do not alter the phase constituent of titanium and its alloys. Both phases (α-Ti and β-Ti phases) can be found together in the microstructure of titanium-based alloys according to their chemical composition and the thermal treatment applied.

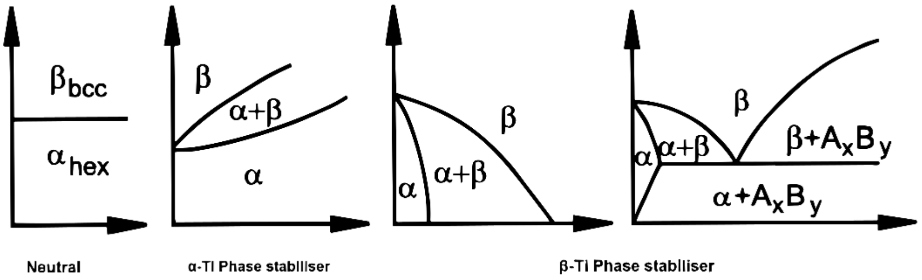

**Figure 2.30.** The α-Ti and the β-Ti solvus line changes (Leyens and Peters, 2003).

**Table 2.4.** The α-Ti and β-Ti stabilisers (Leyens and Peters, 2003).

| Phase structure | Elements |
|---|---|
| α-Ti stabilisers | aluminium, oxygen, nitrogen, boron, gallium, germanium |
| β-Ti stabilisers | niobium, tantalum, molybdenum, vanadium, magnesium, wolfram, iron, chrome, cobalt, nickel, manganese, copper |
| Neutral elements | zirconium, tin, silicon |

### 2.2.3.1. Alpha (α-Ti) Type Alloys

The α-Ti phase stabiliser elements in the titanium matrix generally cause an increase in the α-Ti/β-Ti transition temperature, which inhibits the formation of the β-Ti phase in the microstructure (Leyens and Peters, 2003). Based on the literature, two α-Ti type alloys are available: super α-Ti type and near α-Ti type alloys. In the microstructures of the super α-Ti type titanium alloys, only α-Ti stabiliser elements can be found; thus, their microstructures have only the α-Ti phase. In contrast, the near α-Ti type alloys contain a large amount of the α-Ti stabiliser elements with a small amount of the β-Ti stabiliser elements (<2% wt), and their microstructures can exhibit a large volume fraction of the α-Ti phase with a small volume fraction of retained or transformed the β-Ti phase distributed between α-Ti grains.

The α-Ti phase stabilisers such as aluminium and carbon, nitrogen and oxygen elements are generally found in IIIA and IVA group metals of the periodic table. The strength mechanism for the α-type alloys is based on solid-solution hardening, grain size refinement, and work hardening. Here, the tensile strengths of the α-Ti type alloys can be increased from 350 MPa to 500 MPa with the help of work hardening done by extrusion. The tensile strength of the α-Ti type alloys can be improved from 35 MPa to 70 MPa with the help of solid-solution hardening. For solid-solution mechanisms, only aluminium can be used commercially as an α-Ti phase stabiliser to improve the tensile strength; thus, it is the major alloyant element to obtain the α-Ti phase in the microstructure. Additionally, the light weight or density of aluminium is especially beneficial for biomedical applications. However, when the aluminium content exceeds 8%wt in the titanium matrix, stress corrosion cracking may occur. Therefore, the alloying of aluminium to titanium matrix is limited to avoid this problem. Influences of aluminium concentration on the strength changes and elongation behaviours of the α-type alloys are given in **Fig. 2.31.** (Majumdar and Manna, 2015).

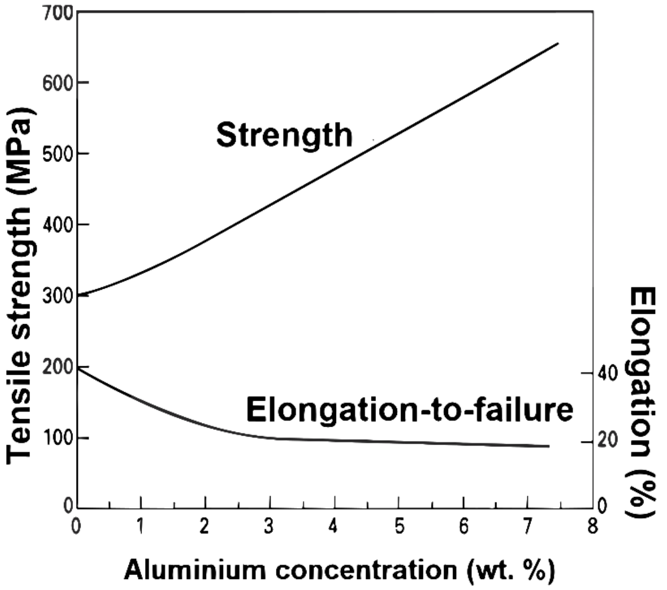

**Figure 2.31.** The effect of aluminium concentration on the strength changes and elongation behaviours of the α-Ti type alloys (Majumdar and Manna, 2015).

The α-type alloys are non-heat treatable but exhibit good weldability. In addition, they have good creep strength and oxidation resistance at elevated temperatures (between 588 K and 811 K); thus, they can be widely used in high-temperature applications such as rocket propulsion systems and gas turbine engines. Moreover, the α-type alloys with hcp structure exhibit higher elastic modulus, lower ductility, and better fracture toughness compared to the β-type titanium alloys with bcc structure (Balazic et al., 2007). Due to these properties, the α-type alloys can also be employed in dental implants. The most well-known α-type alloy is Ti-5Al-2.5Sn.

#### 2.2.3.2. Beta (β-Ti) Type Alloys

The β-Ti type alloys contain the β-Ti phase stabilisers in their microstructures (Sing, 2022). In general, the β-Ti phase stabilisers such as vanadium, tantalum, niobium, copper, and iron are found in the transition groups of the periodic table. Alloying these elements to the titanium matrix generally reduces the α-Ti/β-Ti transition temperature of titanium (Lütjering and Williams, 2007). The β-Ti transus temperature is a transformation temperature from the α-Ti or α-Ti + β-Ti phase field to the β-Ti phase field. This represents the temperature at which the β-Ti phase is stable. Therefore, the β-Ti transus temperature is of vital importance in terms of strength properties and other properties of titanium-based alloys. The β-Ti phase stabilisers do not generate intermetallic compounds in the microstructure when added to the titanium matrix. Such elements can partly dissolve in the β-Ti phase. If the concentration of β-Ti phase stabilisers is sufficient to reduce the martensitic start (Ms) temperature below the room temperature, the α-Ti phase formation can be inhibited in the microstructure; thus, the formation of the β-Ti phase can occur even at room temperature, as can be seen in **Fig. 2.32**. Unlike the α-Ti type alloys, the β-Ti type alloys are suitable for heat treatments (Karasevskaya et al., 2003). Additionally, the β-Ti type alloys are not preferred in high-temperature applications as they exhibit low creep resistance (Balazic et al., 2003; Majumdar and Manna, 2015).

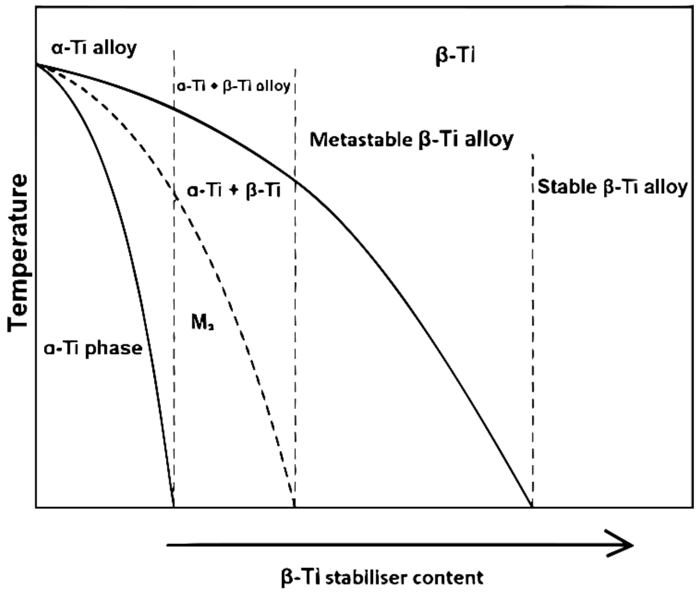

**Figure 2.32.** Schematic illustration of Ti-6Al-4V alloy showing the effect of β stabilizer content (Majumdar and Manna, 2015).

On the other hand, the β-Ti type alloys have more superior biocompatible properties compared to the α-Ti and the α-Ti + β-Ti type alloys. In addition, the mechanical properties of the β-Ti type alloys are more compatible with the bone, which can reduce the stress-shielding effect when implanted. In recent years, β-Ti type alloys have become the focus of orthopaedic implant applications due to the unique combination of better mechanical properties. The production of β-Ti type alloys with superior properties is of vital importance for biomedical applications. The formation of the β-Ti phase in the microstructure considerably reduces the strength properties (Niinomi, 2002; Ikehata et al., 2004; Abdel-Hady et al., 2006). Also, the implant material made from β-Ti type alloys has extraordinary biocorrosion resistance in body fluids. Therefore, these types of alloys can be widely employed in implantology owing to their mechanical performance and better biocompatibility. Further, such alloys are biologically inert and can establish a good bond with osteoblasts when implanted. Moreover, these alloys have excellent specific strength, good machinability, and outstanding fatigue strength.

Here, the formation of the β-Ti phase is essential for developing new titanium-based alloys used in implantology since the β-Ti type alloys can reduce the elastic modulus and provide biological passivity (Yang and Zhang, 2005). Therefore, the β-Ti type titanium alloys have been studied to obtain new β-Ti type alloys with low rigidity. This has a vital effect on enhancing bone healing and bone remodelling in addition to reducing the stress-shielding effect. The rigidity of the α-Ti type alloys is higher compared to that of β-Ti type alloys. However, the rigidity of β-Ti type alloys is still much higher than that of natural bone. Developing β-Ti type alloys with low rigidity is the latest trend in research. The chemical composition and mechanical properties of the new-generation β-type alloys used in implantology are presented in **Table 2.5**. The great unexplored potential of these types of titanium alloys is the driving force behind this work. The second aim of this study is to comprehensively examine the microstructure of new β-Ti type alloys achieved by adding niobium with non-toxic properties.

**Table 2.5.** Chemical composition and mechanical properties of the β-Ti type alloys (E: elasticity modulus, $\sigma_{0.2}$: yield strength, $\sigma_{uts}$: tensile strength (Donachie, 2000)).

| **Alloys** | **Chemical formula (wt.%)** | | | | | | | **Mechanical properties (GPa)** | | |
|---|---|---|---|---|---|---|---|---|---|---|
| | **Fe** | **O** | **Al** | **Sn** | **Zr** | **Mo** | **Others** | **E** | **$\sigma_{0.2}$** | **$\sigma_{uts}$** |
| **Ti-3Al-8V-6Cr-4Mo-4Zr** | 0.3 | 0.1 | 8 | - | 4 | 4 | V:8<br>Cr:6 | 86 | 800 | 900 |
| **Ti-13Nb-13Zr** | - | - | - | - | 13 | - | Nb:13 | 80 | 850 | 100 |
| **Ti-10V-2Fe-3Al** | 2 | 0.1 | 3 | - | - | - | V:10 | 110 | 1000 | 1000 |
| **Ti-8Mo-8V-2Fe-3Al** | 2 | 0.2 | 3 | - | - | 8 | V:8 | 120 | 960 | 1030 |
| **Ti-11.5Mo-6Zr-4.5Sn** | 0.3 | 0.2 | - | 4.5 | 6 | 11 | - | 83 | 800 | 900 |
| **Ti-13V-11Cr-3Al** | 0.3 | 0.2 | 3 | - | - | - | V:13<br>Cr:11 | 110 | 1140 | 1210 |
| **Ti-15V-3Cr-3Al-3Sn** | 0.2 | 0.1 | 3 | 3 | - | - | V:15<br>Cr:3 | 80 | 800 | 800 |
| **Ti-29Nb-13Ta-4.6Zr** | - | - | - | - | 4.6 | - | Nb:29<br>Ta:13 | 80 | 850 | 900 |

Ease of fabrication and low costs combined with superior mechanical performance have given metals a key role in implantology. In this regard, various metallic biomaterials such as titanium-based alloys, cobalt-chromium alloys, and stainless steel have been developed by scientists. However, biomechanical mismatches between the host bone and the metallic biomaterial are a core issue in implantology. The majority of metallic biomaterials may exhibit much higher mechanical properties than natural bone when implanted. Such a condition may lead to a reduction of bone mineral density or bone resorption over time, which is a known stress-shielding issue. This may increase healing time and even result in implant failure (Niinomi, 2002). As shown in **Fig. 2.33**, the elastic modulus of stainless steel, commercially pure tantalum, and cobalt-chrome alloys is much higher than that of titanium and its alloys, which indicates that the possibility of the stress-shielding effect is higher when using biomaterials made from stainless steel or cobalt-chromium alloys compared to titanium and its alloys. The elastic modulus of titanium and its alloys ranges from 200 GPa to 48 GPa. However, the elastic modulus of natural bone is still much lower than that of these values (Rathor and Uddanwadiker, 2022). Researchers have focused on developing new β-Ti types of alloys with low elastic modulus and non-toxic or non-allergic properties. According to the literature, the lowest elastic modulus obtained in the β-Ti type alloys was determined as 40 GPa in Ti-35Nb-4Sn and Ti-24Nb-4Zr-7.9Sn (Matsumoto et al., 2006; Hao et al., 2007). In this context, several non-toxic β-Ti type alloys are used as biomaterials that are close to the elastic modulus of the bone (Niinomi et al., 2006).

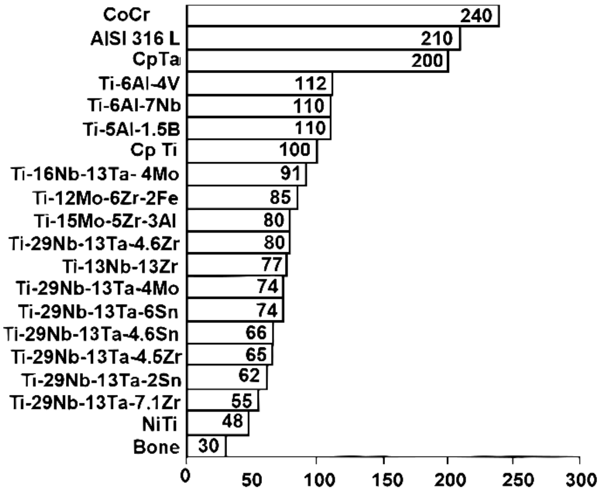

**Figure 2.33.** Comparison of the mechanical properties of some orthopaedic biomaterial materials with natural bone (Geetha et al., 2009).

### 2.2.3.3. Alpha + Beta (α-Ti + β-Ti) Type Alloys

The microstructures of the α-Ti + β-Ti type alloys consist of a combination of the α-Ti and β-Ti phases. Such alloys can contain both the α-Ti stabilisers like aluminium and the β-Ti stabilisers such as vanadium, niobium, and molybdenum to expand the α + β field up to room temperature (Donachie, 2000; Leyens and Peters, 2003; Lütjering and Williams, 2007).

These types of alloys can exhibit high fracture toughness, good creep strength and high fatigue strength. As a result of the thermal treatment applied, the β-Ti phase can be precipitated in the microstructure. Thus, the desired microstructure modifications can be obtained by the presence of the α-Ti + β-Ti phases. Such a microstructure with superior properties is achieved (Brunette et al., 2001).

The Ti-6Al-4V alloy is a typical example of the α-Ti + β-Ti type alloys used in biomedical applications. However, the Ti-6Al-4V alloy was developed for aerospace engineering rather than for biomedical applications. Some properties of this alloy such as excellent specific strength, good workability, and superior fatigue strength provide significant benefits in orthopaedic implant applications. However, the alloyant elements in this alloy have their own adverse influences in the biomedical environment. Based on the literature, vanadium ions released from Ti-6A-4V alloy may lead to a change in the kinetics of the enzyme activity related to inflammatory response cells (Demirci et al., 2022; Nasiłowska et al., 2023). The existence of aluminium, however, may cause Alzheimer's disease through long-term implantation (Ikeda et al., 2002). Therefore, these features of Ti-6A-4V alloy for artificial joints put considerable limitations on their performance. For this reason, vanadium-free and aluminium-free titanium-based alloys are studied in this work. The chemical composition and mechanical properties of some of the α-Ti + the β-Ti type alloys used as biomaterial are given in **Table 2.6**.

**Table 2.6.** Composition and mechanical properties of the α-Ti + the β-Ti type titanium alloys (E: elasticity modulus, $\sigma_{0.2}$: yield strength, $\sigma_{uts}$: ultimate tensile strength) (Donachie, 2000).

| | **Chemical composition (wt.%)** | | | | | | | **Mechanical properties (GPa)** | | |
|---|---|---|---|---|---|---|---|---|---|---|
| **Alloys** | **Fe** | **O** | **Al** | **Sn** | **Zr** | **Mo** | **Others** | **E** | **$\sigma_{0.2}$** | **$\sigma_{uts}$** |
| **Ti-6Al-4V** | 0.3 | 0.2 | 6 | - | - | - | V: 4 | 110 | 800 | 900 |
| **Ti-6Al-6V-2Sn** | 1 | 0.2 | 6 | 2 | - | - | V: 6 | 110 | 950 | 1000 |
| **Ti-6Al-2Sn-2Zr-2Mo-2Cr-0.25Si** | 0.25 | 0.1 | 6 | 2 | 2 | 2 | Cr: 2<br>Si: 0.25 | 110 | 1000 | 1100 |
| **Ti-6Al-2Sn-4Zr-6Mo** | 0.1 | 0.1 | 6 | 2 | 4 | 6 | - | 114 | 1000 | 1100 |
| **Ti-5Al-2Sn-2Zr-4Mo-4Cr** | 0.3 | 0.1 | 5 | 2 | 2 | 4 | Cr: 4 | 112 | 1050 | 1100 |
| **Ti-6Al-7Nb** | 0.2 | 0.2 | 6 | - | - | - | Nb: 7 | 114 | 880 | 900 |
| **Ti-4Al-4Mo-2Sn-0.5Si** | 0.1 | 0.2 | 4 | 2 | - | 4 | Si: 0.5 | 114 | 960 | 1100 |
| **Ti-4.5Al-3V-2Mo-2Fe** | 2 | 0.2 | 4.5 | - | - | 2 | V: 3 | 110 | 900 | 960 |

On the other hand, microstructures of titanium and its alloys may also consist of metastable phases such as $\alpha'$-Ti, $\alpha''$-Ti, and ω-Ti phases according to cooling conditions or the type of alloyant element used. If the β-Ti phase stabilisers in the titanium-based alloys are limited, only the α-Ti and β-Ti phases may form the microstructure of titanium-based alloys. However, for thermodynamically un-equilibrium, metastable phases may also occur at room temperature. Based on the literature, some β-Ti phase stabilisers such as molybdenum, tantalum and vanadium may generate martensitic structures such as $\alpha'$-Ti (hexagonal close-packed) and $\alpha''$-Ti (orthorhombic) phases. Additionally, for limited β-Ti phase stabilisers in titanium matrix, rapid cooling from the β-Ti phase field may cause the formation of martensitic $\alpha'$-Ti phase in the microstructure. For high content of the β-Ti phase stabiliser in the titanium matrix, the martensitic $\alpha'$-Ti phase may lose symmetry and transform into the martensitic $\alpha''$-Ti phase. If titanium-based alloys with the β-Ti stabiliser are exposed to rapid cooling from high temperatures (β-Ti field in titanium phase diagram), the β-Ti phase may transform either into martensitic structures $\alpha'$-Ti (hexagonal close-packed), $\alpha''$-Ti (orthorhombic) phases or the omega (ω-Ti) phase (hexagonal close-packed) (Slokar et al., 2012). The microstructures of Ti-25Nb (wt.%) alloy exposed to different cooling conditions are given in **Fig. 2.34.** Accordingly, the martensitic $\alpha''$-Ti phase was observed in the water-cooled Ti-25Nb (wt.%) while the metastable ω-Ti phase was detected in the same air-cooled alloy (Majumdar and Manna, 2015).

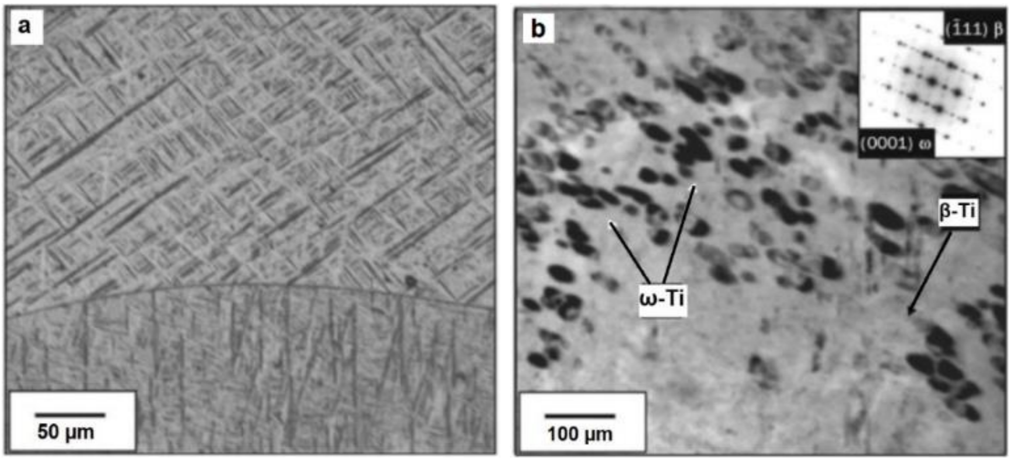

**Figure 2.34.** (a) water-cooled Ti-25Nb (wt.%) alloy revealing martensitic $\alpha''$-Ti phase and (b) air-cooled Ti-25Nb (wt.%) alloy indicating metastable ω-Ti phase dispersed in the β-Ti matrix (Majumdar and Manna, 2015).

Based on the chemical composition of the β-type alloys, the omega (ω-Ti) phase may take place in the microstructure, which is undesirable for many applications as precipitation of a ω-Ti phase may increase the brittleness of the titanium and its alloy. Also, the omega (ω-Ti) phase can form after the ageing of a rapid quenching from medium temperatures, which promotes the formation of an isothermal ω-Ti phase. This is shown in **Fig. 2.35.** (Majumdar and Manna, 2015**).**

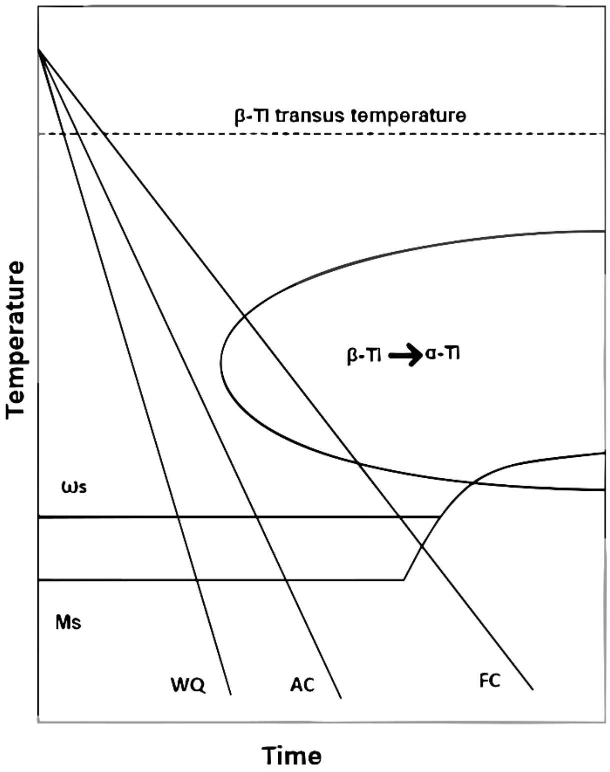

**Figure 2.35.** TTT diagram for β-Ti phase transformation in titanium (Majumdar and Manna, 2015).

When looking at the microstructures of heat-treated titanium and its alloys, it is possible to find the α-Ti phase transforming from the β-Ti phase during slow cooling from the β-Ti field. Subsequently, the α-Ti phase in the microstructure may appear in acicular forms. The resulting microstructure is called the Widmanstatten structure (see **Fig. 2.36.**), and the acicular α-Ti grains grow in the β-Ti matrix throughout the slow cooling (Rajan, 2020).

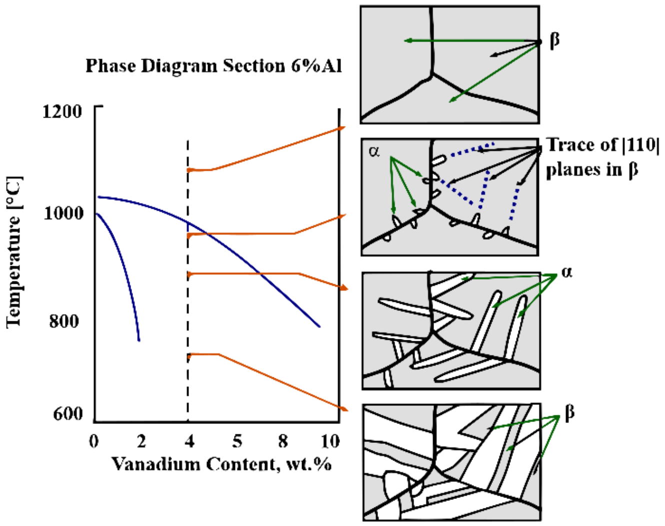

**Figure 2.36.** Formation of Widmanstatten structure (Rajan, 2020).

### 2.2.4. Corrosion Behaviour and Biocompatibility of Titanium and Its Alloys

Electrochemical corrosion tests such as electrochemical impedance spectroscopy (EIS) and potentiodynamic polarisation can be widely employed to understand the corrosion performance of the implant material before surgery (Fojt et al., 2013). Some studies revealed that some passivation behaviours (as in titanium-oxide) may be observed in titanium, which makes it more resistant to corrosion (Fojt et al., 2013; Li et al., 2018). Namely, this passivation can ensure additional corrosion resistance to titanium (Wang et al., 2019). Therefore, pure titanium has good corrosion resistance in many environments such as nitric acid and chromic acid. Also, some titanium-based alloys have extreme corrosion resistance. These are Ti-0.15Pd alloy and Ti-Ni-Pd-Ru-Cr alloy (AKOT) (see **Fig. 2.37.**). However, under high-temperature conditions in highly concentrated solutions such as hydrochloric acid and sulfuric acids, the corrosion resistance of titanium and its alloys may reduce significantly (see **Fig. 2.38.**).

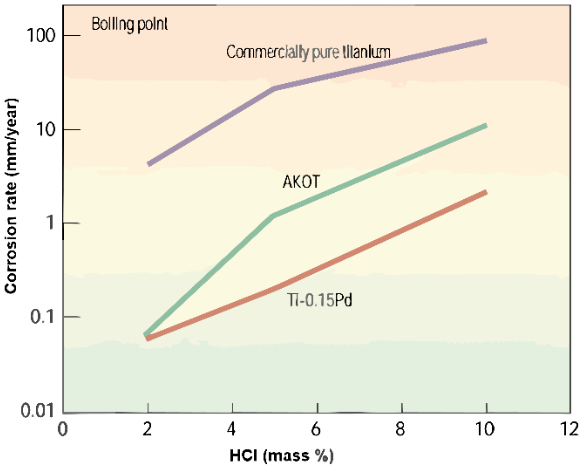

**Figure 2.37.** The corrosion resistance of commercially pure titanium and its alloys in hydrochloric acid solution (Kobelco, 2022).

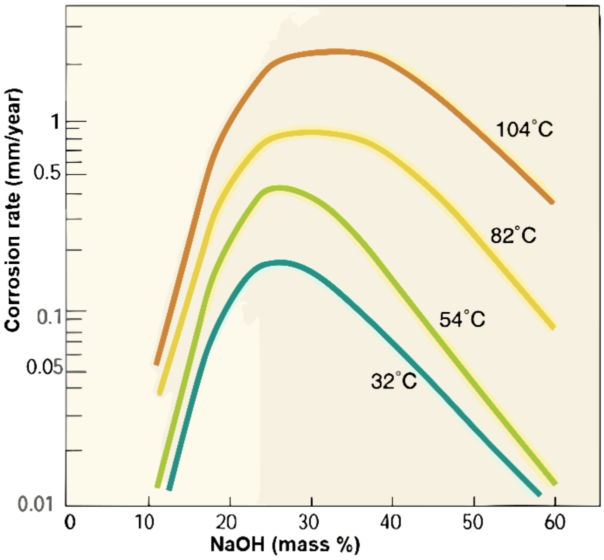

**Figure 2.38.** The corrosion rate of commercially pure titanium in NaOH solution (Kobelco, 2022).

Unlike other metallic materials such as aluminium-brass, stainless steel or copper-nickel alloys, stress corrosion, cracking or pitting corrosion is not observed in commercially pure titanium (see **Table 2.7.**).

**Table 2.7.** The corrosion resistance of titanium and some metal groups (Corrosion resistance rank 1: Excellent, 2: Good, 3: Ordinary, 4: Inferior) (Kobelco, 2022).

| **Type of material** | **Purity of sea water** | **Corrosion resistance rank** | | | | |
|---|---|---|---|---|---|---|
| | | **General corrosion** | **Pitting corrosion** | **Crevice corrosion** | **Stress corrosion cracking** | **Erosion** |
| **Titanium** | **Clean** | 1 | 1 | 1 | 1 | 2 |
| | **Contaminated** | 1 | 1 | 1 | 1 | 2 |
| **Al brass** | **Clean** | 2 | 2 | 2 | 1 | 3 |
| | **Contaminated** | 2 | 4 | 4 | 4 | 3 |
| **70/30 Cu-Ni** | **Clean** | 1 | 2 | 2 | 1 | 3 |
| | **Contaminated** | 2 | 4 | 4 | 4 | 3 |
| **Stainless steel** | **Clean** | 1 | 1 | 2 | 1 | 2 |
| | **Contaminated** | 1 | 2 | 3 | 2 | 2 |

As stated previously, the corrosion performance of titanium and its alloys is generally determined by passivation behaviours. Titanium and its alloys normally have a high chemical affinity for oxygen, hydrogen, and nitrogen gases, which result in a thin oxide film (M: metal; $MO_2$), an extremely protective surface oxide film formed on their surfaces. More importantly, if this passivation is damaged or scratched, it can heal or repair itself when exposed to air or water (Hebatalrahman, 2005). However, this benefit may turn into a disadvantage; especially above 600°C. This is because, above that temperature, oxygen can easily diffuse to the surfaces of titanium and its alloys, making them brittle and fragile, which are undesired features for biomedical applications (Lütjering and Williams, 2007). On the other hand, the passivation behaviour of titanium and its alloys plays a beneficial role in biomedical applications in terms of organic and inorganic interaction between bone and implant (Moffat and Kattner, 1988). The passivation behaviour of titanium and its alloys used in implantology can vary depending on its surface characteristics, chemical compound, and the surrounding biological environment. This oxide layer plays a crucial role on biocompatibility, osseointegration, chemical stability, and corrosion resistance of titanium and its alloys used as implant. These are essential for the long-term success of implants in interacting with bone and other biological tissues. Previous studies have shown that the passivation behaviour formed on surfaces of titanium and its alloys can also enhance cytotoxicity properties. Further, the passivation effect can hinder ion emissions from biomaterial that may occur in the body systems. The reason is that the chemical behaviour of some oxide characters such as $TiO_2$ and $Nb_2O_3$ is similar to that of body liquids. It is claimed these oxides may not be recognised by the muscles, tissues, and body systems (Leyens and Peters, 2003). The corrosion performances of titanium and its alloys used as biomaterial are strongly dependent upon passivation behaviours (Lütjering and Williams, 2007; Pushp et al., 2022). As a result, the passivation behaviours of titanium-based alloys spontaneously formed on their surfaces promote chemical stability. Therefore, titanium and its alloys have excellent corrosion resistance, which is essential for implantology.

The corrosion resistance of the biomaterial is associated with biocompatibility. In other words, biocompatibility is a feature that requires high corrosion resistance. Biomaterials are generally exposed to corrosive mediums when implanted owing to the protein, salt and ions found in the body fluids and blood. Considering this, some corrosion products may form at the implantation site and may lead to unhealthy side-effects in the human body (Bai et al., 2016). Normally, biocompatible behaviour and cytotoxicity of the biomaterial are determined by survival rates of cells, cell adhesion and cell spreading in vivo. The result of a previous study is shown in **Fig. 2.39**. According to the results of this study, titanium was found to have the highest cell survival rate, approximately 90%, while nickel had the lowest cell survival rate. As can be seen here, titanium did not react with the body liquids when implanted. In conclusion, titanium and its alloys are biocompatible with human tissue and/or bone.

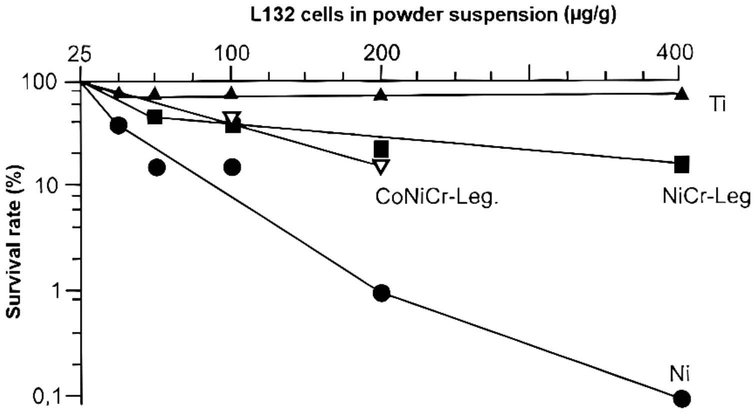

**Figure 2.39.** The survival rate of L132 cells in powder suspension of different implant materials (Leyens and Peters, 2003).

### 2.2.5. Mechanical Properties of Titanium and Its Alloys

The mechanical properties of titanium and its alloys can be determined by the type of alloying element by changing phase microstructures. Some mechanical properties of titanium and its alloys are given in **Table 2.8.** The data for the structural α-Ti, α-Ti + β-Ti and β-Ti type alloys are given in **Fig. 2.40** as a scatter band**.** Here, the yield strengths of titanium and its alloys are distributed in the range of between 100 and 1000 MPa.

**Table 2.8.** Mechanical properties of titanium and its alloys (Krishna 2022).

| **Alloy** | **Tensile strength (MPa)** | **Yield strength (MPa)** | **Elongation (%)** | **Elastic modulus (GPa)** | **Type of alloy** |
|---|---|---|---|---|---|
| Pure titanium (grade 1) | 241 | 171 | 23 | 102.8 | α-Ti |
| Pure titanium (grade 2) | 345 | 273 | 22 | 101.6 | α-Ti |
| Pure titanium (grade 2) | 455 | 375 | 20 | 102.3 | α-Ti |
| Ti–6Al–4V | 894–931 | 824–870 | 5–10 | 111–115 | α-Ti + β-Ti |
| Ti–6Al–7Nb | 905–1060 | 885–955 | 8.1–15 | 114 | α-Ti + β-Ti |
| Ti–5Al–2.5Fe | 1022 | 900 | 14 | 115 | α-Ti + β-Ti |
| Ti–5Al–1.5B | 930–1100 | 825–935 | 15–17.0 | 120 | α-Ti + β-Ti |
| Ti–15Sn–4Nb–2Ta–0.2Pd | 860-1109 | 790 | 21 | 89 | α-Ti + β-Ti |
| Ti–15Zr–4Nb–4Ta–0.2Pd | 715-919 | 693-806 | 18-28 | 94-99 | α-Ti + β-Ti |
| Ti–13Nb–13Zr | 973–1037 | 836–908 | 10–16 | 79–84 | β-Ti |
| TMZF (Ti–12Mo–6Zr–2Fe) | 1060–1100 | 100–1060 | 18–22 | 74–85 | β-Ti |
| Ti–15Mo | 875 | 545 | 20 | 77-80 | β-Ti |
| Ti–15Mo–5Zr–3Al | 850 | 840 | 26 | 80 | β-Ti |
| Ti–35.3Nb–5.1Ta–7.1Zr | 600 | 550 | 20 | 56 | β-Ti |

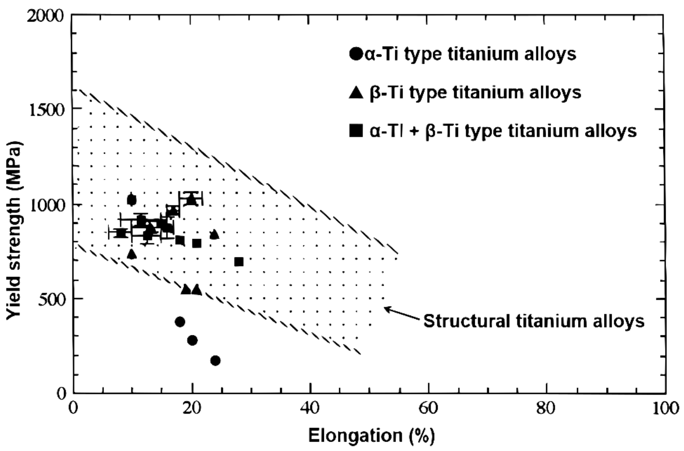

**Figure 2.40.** Relationship between yield strength and elongation for titanium and its alloys (Krishna 2022).

Normally, commercially pure titanium grades have a tensile strength in the range of 200 MPa to 600 MPa. The strengths of titanium grades can be controlled by the presence of interstitial impurity atoms such as carbon, oxygen, and nitrogen contents. In general, these atoms increase the mechanical strength of pure titanium grades but decrease the ductility. For instance, the increase of oxygen content in the titanium matrix from 0.18%wt to 0.4%wt increases the yield strength from 170 MPa to 480 MPa (Luo et al., 2020). To improve tensile strength, commercially pure or unalloyed titanium can be alloyed by alloyant elements such as tin, chrome, iron, vanadium, aluminium, niobium, and zirconium. Thus, titanium and its alloys can exhibit greater tensile strength than commercially pure titanium (Kang and Yang, 2019). A comparison of tensile strength for titanium and its alloys is given in **Fig. 2.41**. As seen in this figure, alloying titanium can increase mechanical properties by altering the phase constituent in the microstructure of titanium (Gogia, 2005).

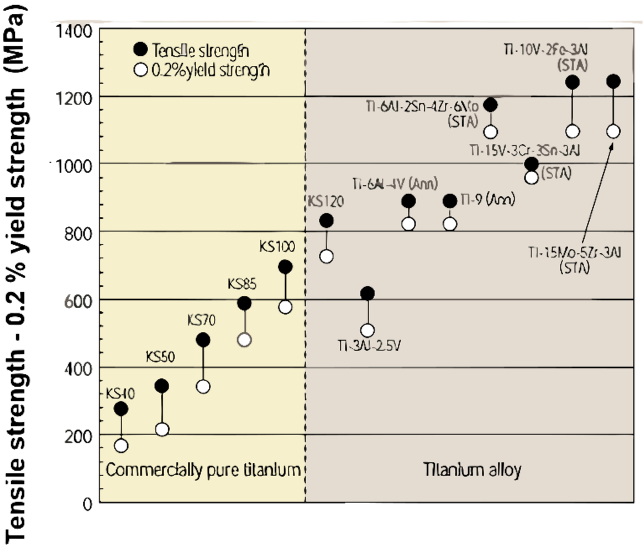

**Figure 2.41.** Comparison of tensile strength for commercially pure titanium grades and its alloys (KS: commercially pure titanium grades) (Kobelco, 2022).

Commercially pure titanium can be also used in engineering designs up to 300°C due to its good specific strength and its high creep strength. When it is alloyed with other metals, this temperature reached can be 500°C. Some mechanical properties of commercially pure titanium and its alloys at high temperatures are given in **Fig. 2.42**. Further, commercially pure titanium and its alloys can be effectively used at low temperatures, even at 4.2 K (-269°C) (see **Fig. 2.43.**).

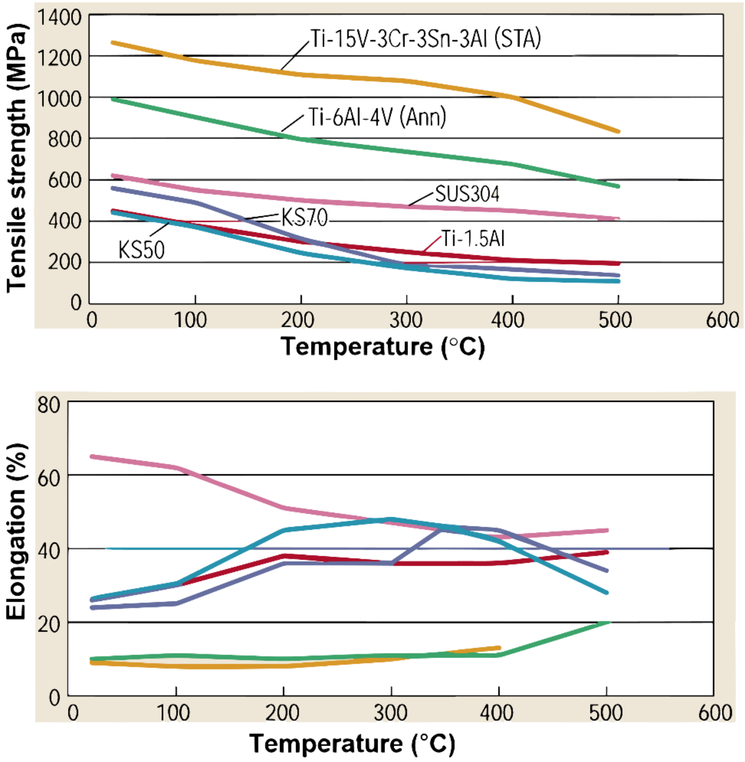

**Figure 2.42.** Some mechanical properties of commercially pure titanium and its alloys at high temperatures (KS: commercially pure titanium grades) (Kobelco, 2022).

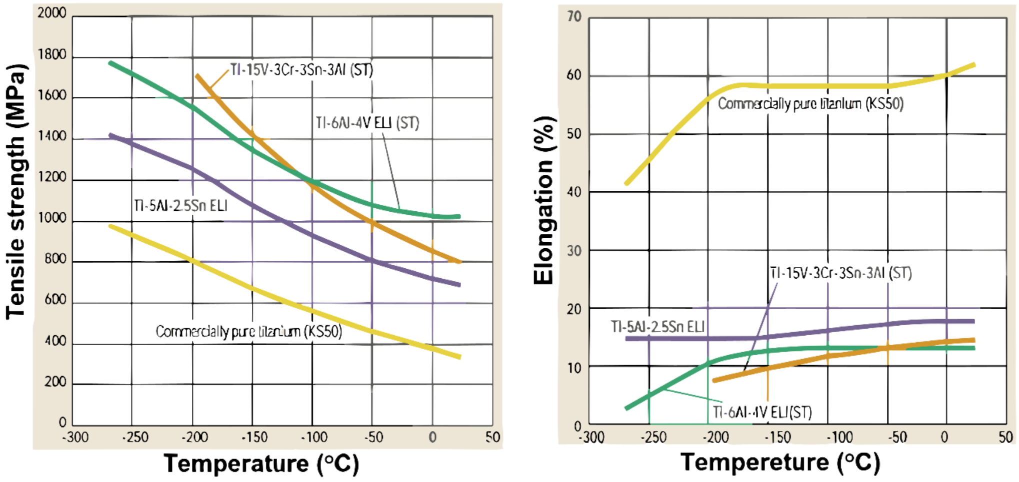

**Figure 2.43.** Some mechanical properties of commercially pure titanium and its alloys at low temperatures (Kobelco, 2022).

As mentioned before, commercially pure titanium and its alloys can maintain their strength values even at high temperatures (Gogia, 2005). Titanium and its alloys can exhibit much better specific strength properties than other metallic materials such as aluminium alloys, magnesium alloys and stainless steel (Ahmed et al., 2014). A comparison of the specific strengths of titanium and its alloys with some metal alloys according to temperature changes is given in **Fig. 2.44.**

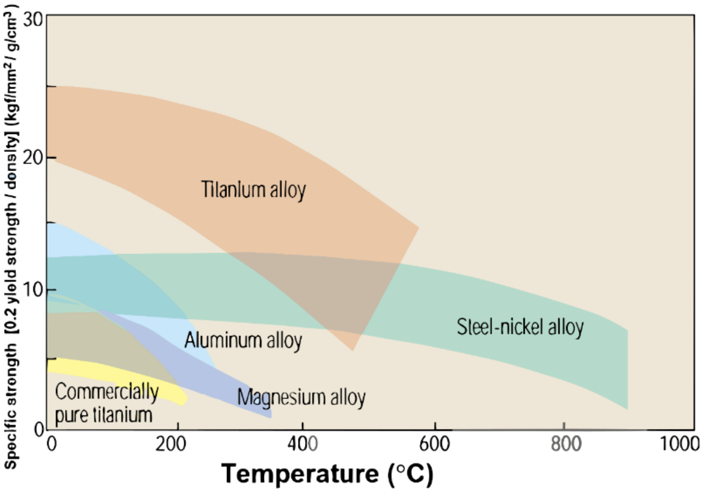

**Figure 2.44**. Comparison of the specific strengths of titanium and its alloys with some metal alloys according to temperature changes (Kobelco, 2022).

Titanium-based alloys and stainless steel have similar hardness properties but exceed aluminium’s hardness. The hardness properties of titanium and its alloys can be altered by the heat treatment applied and the alloyant contents in the titanium matrix (Revankar, 2014).

The Vickers hardness of the titanium and its alloys used as implants do not alter before and after surgery. However, that of 316L used as an implant may be higher after surgery (see **Fig. 2.45.**).

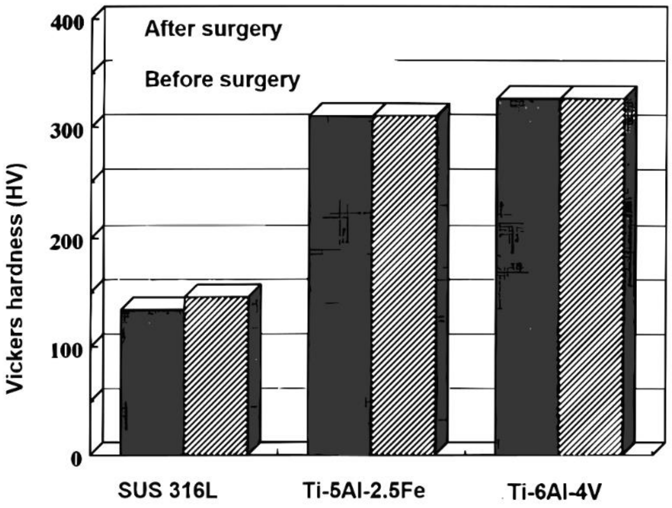

**Figure. 2.45.** The influence of implantation into a vivo on Vickers hardness (Revankar, 2014).

The machinability of commercially pure titanium and its alloys is slightly inferior to stainless steel. This case may vary according to the types of titanium alloys. For instance, the α-Ti type alloys can exhibit superior machinability while the β-Ti type titanium alloys offer the lowest machinability among types of titanium alloys. The α-Ti + β-Ti type alloys have intermediate machinability.

In general, the fatigue strength of commercially pure titanium ($10^7$ cycles) is roughly half of its tensile strength. Further, even in many corrosive environments such as sea water, a reduction in the fatigue strengths of commercially pure titanium and its alloys is not observed (Kobelco, 2022). However, previous studies have declared that the fatigue strength of titanium and its alloys may be adversely affected after surgery. This is because the crack propagation rate of the titanium-based alloys used as a biomaterial in simulated body fluids is higher than in air (see **Fig. 2.46.**).

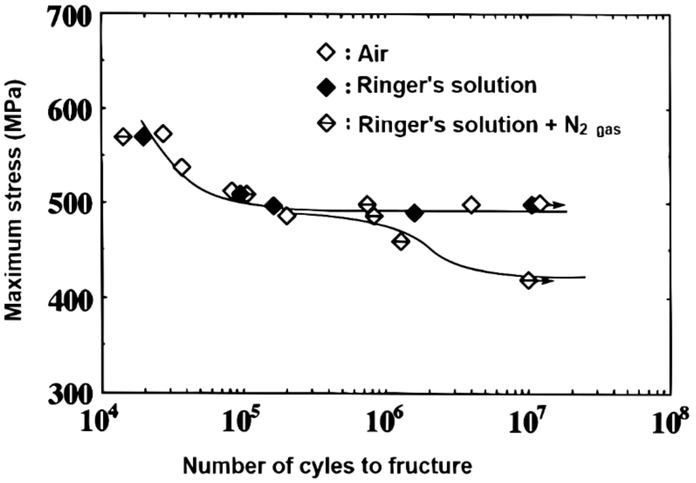

**Figure. 2.46.** S–N curves for Ti-5Al-2.5Fe in air, Ringer's solution and Ringer's solution with $N_2$ gas (Kobelco, 2022).

### 2.2.6. Advantages and Disadvantages of Titanium and Its Alloys Used as Implants

Titanium and its alloys are widely employed in implantology owing to their excellent corrosion resistances, their acceptable mechanical performance, and their outstanding biocompatibility. Moreover, the passivation of titanium-based alloys can absorb some ions released from orthopaedic biomaterial made from titanium and its alloys, which may inhibit necrosis of the tissue surrounding the implantation site. Passivation behaviour is that is a stable oxide film ($TiO_2$) forming on the surface of titanium and its alloys. The passivation behaviour of titanium and its alloys provides significant advantage for biological applications, as they do have an inert structure (Sherif et al., 2022). However, this type of thin film formed on the surface of titanium and its alloys is quite sensitive so it can be damaged easily. Therefore, to protect such film, many treatments such as heating under atmospheric pressure, electrochemical oxidation and anodic oxidation can be conducted, which means extra costs (Wang et al., 2008; Lang et al., 2013).

As stated above, titanium-based alloys have three major phase structures: α-Ti type, β-Ti type, and combinations of these phases (α-Ti + β-Ti). Various alloying elements such as niobium, zirconium, tin, copper, vanadium, aluminium, and hafnium can be employed to alter the phase structure of titanium-based alloys; thus, the chemical and physical properties of titanium-based alloys can be adjusted effectively. The chemical and physical properties of α-Ti type and β-Ti type alloys are different. Here, the mechanical properties of the β-Ti type alloys are closer to those of bone compared to α-Ti type alloys. This reduces the mechanical mismatch between orthopaedic biomaterial and bone. Therefore, β-Ti type alloys with favourable properties can be widely used in biomedical applications.

On the other hand, there are some disadvantages of titanium-based alloys used as load-bearing implant material; these are low deformability (the α-type alloys), low machinability (the β-type alloys), insufficient wear resistance and high affinity to atmospheric gases such as nitrogen and oxygen at elevated temperatures (Li et al., 2014). Further, under some conditions, the presence of titanium ions released from implants made from titanium-based alloys has been proved at the interface between bone and implant (Curtin et al., 2017). In addition, titanium and its alloys may cause an aesthetic problem when implanted due to their grey colour, which can be seen through the thin mucosa. In conclusion, titanium and its alloys should be thoroughly analysed before implantation.

### 2.2.7. Titanium-Based Alloys

#### 2.2.7.1. Binary Titanium-Zirconium Alloys

Zirconium is one of the transition metals in the periodic table. The chemical, physical, and mechanical properties of zirconium are given in **Table 2.9.** Zirconium was found by Martin Heinrich Klapoth, a German chemist, in 1789. The primary mineral sources of zirconium are zirconium silicate ($ZrSO_4$) and baddeleyite ($ZrO_2$). Commercially pure zirconium is generally produced by chlorine, magnesium, and carbon reduction, which is summarised in Eqs. (2.5.) (Kljajević et al., 2011). Commercially pure zirconium can be used in magnet production by alloying with niobium due to its feature of superconductivity at low temperatures.

$$ZrSO_4 + 3C\ (1600\ ^{\circ}C) \rightarrow ZrO_2 + SC + 2CO_{(g)} \qquad \textbf{(2.5a.)}$$

$$ZrO_2 + 2Cl_2 + 2C\ (900\ ^{\circ}C) \rightarrow ZrCl_4 + 2CO \qquad \textbf{(2.5b.)}$$

$$ZrCl_4 + 2Mg\ (1100\ ^{\circ}C) \rightarrow 2MgCl_2 + Zr \qquad \textbf{(2.5c.)}$$

**Table 2.9.** Some properties of zirconium metal (Lenntech, 2022).

| **Chemical properties** | | **Physical and mechanical properties** | |
|---|---|---|---|
| **Symbol** | Zr | **Density (g/cm$^3$)** | 6.51 |
| **Period and group** | 5/4B | **Melting point (ºC)** | 1852 |
| **Atomic number** | 22 | **Boiling point (ºC)** | 2900 |
| **Atomic mass (g/mol)** | 91.224 | **Hardness (HV)** | 903 |
| **Atomic diameter (ºA)** | 2.16 | **Thermal conductivity (W/cm.K)** | 0.226 |
| **Crystal structure** | Hexagonal close-packed (hcp) | **Elastic modulus (GPa)** | 88 |

The titanium-zirconium equilibrium phase diagram is illustrated in **Fig. 2.47**. Accordingly, zirconium in the titanium matrix acts as a neutral or weak β-Ti phase stabiliser as it does not critically shift the α-Ti/β-Ti solvus line of titanium. In addition, zirconium can exhibit a completely solid solution in a titanium matrix (α-Ti phase) even at room temperature; thus, a wide range of titanium-zirconium alloys can be designed. The phase constituent of the titanium-zirconium system consists of only the hcp α-Ti phase, which shows that zirconium concentration in the titanium matrix does not play a crucial role in phase constituents of the titanium. On the other hand, the addition of zirconium to the titanium matrix can slightly enhance mechanical properties such as hardness, yield strength, and tensile strength due to the solid-solution mechanism.

For biomedical applications, zirconium is a favourable candidate for alloying to titanium matrix because it does not exhibit toxic and allergic effects when implanted. This is due to the formation of a thermodynamically stable oxide layer ($ZrO_2$) on the zirconium surface within nanoseconds when reacted with oxygen (Brunette et al., 2001; Chopra et al., 2022; Ardhy et al., 2023).

Titanium-zirconium systems are a new-generation implant material that combines good biocompatibility and high strength. Titanium-zirconium alloys have better mechanical strength and superior osseointegration compared to commercially pure titanium and commercially pure zirconium. They are specifically designed for use in dental implantology ($ZrO_2$) (Gottlow et al., 2012). Binary titanium-zirconium alloys generally contain 13% to 17% zirconium, which provides high strength properties and high wear resistance. This is essential for dental applications. Also, adding zirconium to titanium matrix enhances biocompatibility properties, which reduces the risk of adverse reaction in the body when implanted.

Titanium-zirconium implants are marketed as Roxolid® (Institut Straumann AG, Basel, Switzerland). This type of implant, made from titanium-zirconium alloys, has a tensile strength of 953 MPa and a fatigue strength of 230 MPa, according to the tests applied at ISO 14801 standards (data on file for Straumann). It is, thus, deemed reasonable for the alloying of titanium with zirconium.

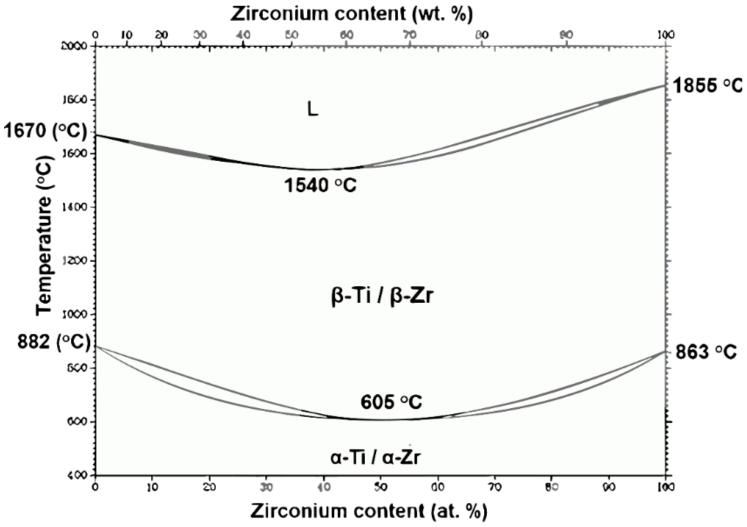

**Figure 2.47.** Titanium-zirconium binary equilibrium phase diagram (Gasik and Yu, 2009).

Wang et al. produced Ti-xZr (x: 5, 15, 25, 35, 45; wt. %) binary alloys by using the powder metallurgy method. They declared that all binary Ti-xZr alloys achieved in this study exhibited a significant continuous increase in mechanical performance due to solid-solid strength mechanisms (Wang et al., 2019).

Vicente et al. studied the effect of oxygen concentration in Ti-xZr alloys (x: 5, 10, 15; wt. %). They showed that an increase in oxygen concentration from 0.02 wt.% to 0.04 wt.% did not affect the biocompatibility features and phase structures of the alloys but significantly increased the mechanical properties of the alloys such as hardness and elastic modulus (Vicente et al., 2014).

Kobayashi et al. examined the mechanical performance of Ti-xZr (x: 0, 20, 25, 30, 35, 40, 45, 50, 55, 60, 65, 70, 75, 80,100; wt.%) alloys. They stated that titanium with up to 50 wt.% zirconium concentration exhibited greater tensile strength and hardness compared to commercially pure titanium and commercially pure zirconium. All alloys achieved in this study had a favourable potential for use as load-bearing implants in terms of their biocompatible features (Kobayashi et al., 1995).

Ti-10Zr (wt.%) was fabricated by a commercial arc-melting vacuum-pressure-type casting system. Microstructure evaluation revealed that the microstructure consisted completely of the α-Ti phase with an hcp crystal structure. Ti-10Zr (wt.%) exhibited higher mechanical properties than commercially pure titanium (Ho et al., 2009).

Calderon Moreno et al. examined the corrosion performance of Ti-20Zr (wt.%) alloys with α-Ti + β-Ti phase microstructure. In this regard, passivation ($Ti_2O_3$, $TiO_2$, and $ZrO_2$) formed on the surfaces of the alloys was determined by XPS analysis. The long-term corrosion performance of the alloys was achieved due to the passivation behaviours of the alloys (Calderon Moreno et al., 2014).

Zhang et al. investigated the wear resistances of the Ti-xZr (x:1, 2, 16; wt.%) alloys produced by an arc-melting furnace under an argon environment. They declared that with increasing zirconium concentration in the titanium matrix, the wear resistance of the alloys achieved increased dramatically (Zhang, 2018).

### 2.2.7.2. Binary Titanium-Niobium Alloys

Niobium is a metal with quite beneficial functions in many alloys; its atomic number is 41. Niobium was discovered by Charles Hatchett, an English mineralogist, in 1801. It is widely used in steel pipe construction as the corrosion resistance of steel is enhanced when niobium is alloyed with steel. The chemical, physical, and mechanical properties of niobium are given in **Table 2.10**. The primary mineral sources of niobium are pyrochlore oxides ($NaCaNb_2O_6F$ and $(Fe, Mn)(Nb, Ta)_2O_6$ ores). These minerals can be fully dissolved with strong sulfuric acid, and $Nb_2O_5$ and FeTaNb compounds can then be obtained. The chemical reactions of pure niobium production are given in Eqs. (2.6.) (Wu et al., 2022).

$$3Nb_2O_5 + 10Al\ (1000\ ^{\circ}C) \rightarrow 6Nb + 5Al_2O_3 \qquad \textbf{(2.6a.)}$$

$$Nb_2O_5 + 7C\ (1950\ ^{\circ}C) \rightarrow 2NbC + 5CO \qquad \textbf{(2.6b.)}$$

$$5NbC + Nb_2O_5\ (1950\ ^{\circ}C) \rightarrow 7Nb + 5CO \qquad \textbf{(2.6c.)}$$

**Table 2.10.** Some properties of niobium metal (Lenntech, 2022).

| **Chemical properties** | | **Physical and mechanical properties** | |
|---|---|---|---|
| **Symbol** | Nb | **Density (g/cm$^3$)** | 8.4 |
| **Period and group** | 5/5B | **Melting point (ºC)** | 2469 |
| **Atomic number** | 41 | **Boiling point (ºC)** | 4744 |
| **Atomic mass (g/mol)** | 92.9 | **Hardness (HV)** | 1320 |
| **Atomic diameter (ºA)** | 2.08 | **Thermal conductivity (W/cm.K)** | 0.537 |
| **Crystal structure** | Body-centred cubic (BCC) | **Elastic modulus (GPa)** | 105 |

Biocompatibility: Binary titanium- niobium alloys have excellent biocompatibility. These alloys are generally used in orthopaedic implants and dental applications since they can integrate well with the human body without causing adverse reactions.

Corrosion resistance: Binary titanium- niobium alloys exhibit high corrosion resistance. That can play vital role on corrosion performances of these alloys employed for implantology.

Low modulus of elasticity: Commercially pure titanium can have more elastic modulus than binary titanium- niobium alloys. This feature is essential for orthopaedic applications since it can lead to stress shielding relief between implant and bone tissue.

Biological stability: Some studies showed that binary titanium- niobium alloys are biologically stable. On the other hand, when implanted, they may not release harmful ions or particles over time.

Super elasticity: Some binary titanium- niobium alloys can have super elastic characteristics. On the other hand, they can maintain their original shape after deformation. This feature provides a great advantage for medical devices such as stents.

As seen from the titanium-niobium equilibrium phase diagram (see **Fig. 2.48.**), there are two stable solid phases: the hcp α-Ti and the bcc β-Ti phases. The melting temperatures of the titanium and niobium metals are Ti β→L=1670°C and Nb β→L=2469°C. The allotropic transformation temperature of titanium begins at 882˚C. The stable phase at room temperature is the α-Ti phase up to 3% (at.) niobium content in the titanium matrix. Niobium acts as a strong β-Ti stabiliser in the microstructure of titanium-niobium mixtures. Thus, the volume fraction of the β-Ti phase generally increases with the increasing niobium concentration. The β-Ti phase becomes stable with 40% (at.) niobium at room temperature. Under normal conditions, the β-Ti phase is stable at high temperatures. Niobium content in the titanium matrix reduces the allotropic transformation temperature (α-Ti/β-Ti solidus line) and stabilises the β-Ti phase in the titanium microstructure (Zhuravleva, 2014). As mentioned before, the bcc β-Ti phase is essential for implantology due to its low elastic modulus and other favourable mechanical properties. Here, titanium-niobium systems exhibit low strength due to the formation of the bcc β-Ti phase in the microstructure. Previous studies have revealed that the niobium concentration in the titanium matrix may also promote the formation of the hcp ω-Ti (omega) phase according to the thermal treatment applied and the cooling rate from the β-Ti phase field. The hcp ω-Ti phase is an undesirable phase structure in biomaterial applications because this type of phase exhibits the highest elastic modulus among titanium-related phases. Based on the literature, some mechanical properties of different titanium-related phases are compared in **Fig. 2.49**.

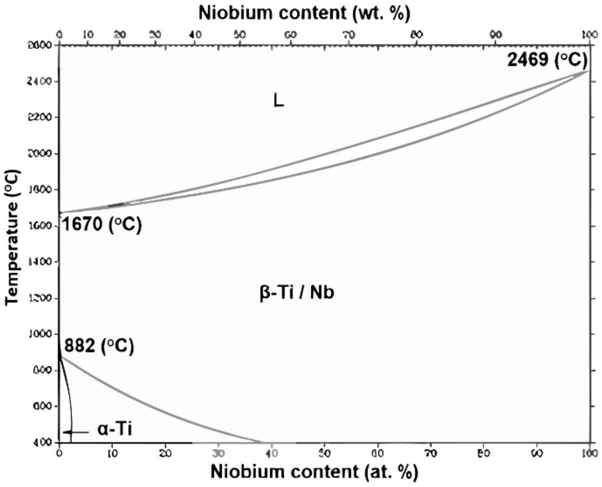

**Figure 2.48.** Titanium-niobium binary equilibrium phase diagram (Gasik and Yu, 2009).

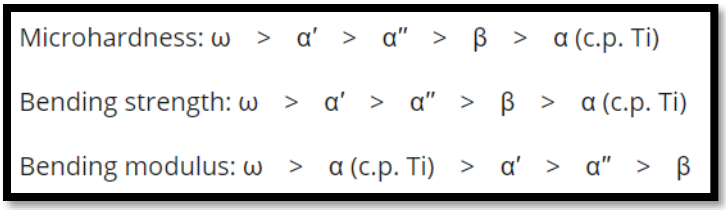

Microhardness: ω > α′ > α″ > β > α (c.p. Ti)

Bending strength: ω > α′ > α″ > β > α (c.p. Ti)

Bending modulus: ω > α (c.p. Ti) > α′ > α″ > β

**Figure 2.49.** Comparison of mechanical properties of different titanium-related phases (Zhuravleva, 2014).

Lee et al. investigated the microstructures of Ti-xNb (x: 5, 10, 15, 17.5, 20, 22.5, 25, 27.5, 30, 35; wt.%) fabricated by arc-melting. They stated that the microstructure and morphology of the alloys obtained in this study were sensitive to niobium concentration and all alloys exhibited superior corrosion resistance due to passivation behaviours (Lee et al., 2002).

Han et al. studied the influence of niobium concentration on the mechanical performance, microstructure, and cytotoxicity of the Ti-xNb (x: 10, 15, 20; wt%) alloys. The results showed that microstructures mainly consisted of a combination of the α-Ti and the β-Ti phases with precipitation of the isothermal ω-Ti phases. With increasing niobium concentration, the volume fraction of the ω-Ti phase increased, which enhanced the mechanical properties of the alloys. The biocompatibility of titanium-niobium mixtures was excellent for use in implantology (Han et al., 2015).

Santos et al. studied Ti-35Nb (wt.%) fabricated by the powder metallurgy method. They declared that the microstructures of the alloy sintered at high temperatures consisted of a combination of the α-Ti and the β-Ti phases, which revealed that phase transformation temperatures of the alloys reduced with increasing niobium concentration in the titanium matrix. This case showed us that niobium concentration in titanium matrix acted as a strong β-Ti stabiliser (Ozturk et al., 2011).

Ruan et al. examined the mechanical properties and biocompatibility of Ti-25Nb (wt.%) alloy produced by the combination of the sponge impregnation method and the sintering process. They declared that porous Ti-25Nb (wt.%) exhibited appropriate mechanical performance and outstanding biocompatibility in the use of surgical applications (Ruan et al., 2016).

#### 2.2.7.3. Ternary Titanium-Niobium-Zirconium Alloys

Ternary titanium-niobium-zirconium alloys have been attracting great interest from researchers though they are new concepts in the science world. As stated previously, titanium-based alloys can be alloyed with highly biocompatible elements such as niobium and zirconium to achieve appropriate microstructure depending on the field of use. Niobium-titanium binary alloys generally have the β-Ti phase structure based on the niobium concentration in the titanium matrix and thermal treatment applied. Therefore, the volume fraction of the β-Ti phase can be adjusted in the microstructure of titanium-niobium alloys (Bottino et al., 2009). Further, these types of alloys exhibit a low modulus of elasticity, acceptable mechanical strength, outstanding biocompatibility, shape memory and super elastic properties (Bozzolo et al., 2007). On the other hand, zirconium is a neutral or weak β-Ti stabiliser element when individually alloyed to a titanium matrix (Abdel-Hady, 2006).

Therefore, both phases (α-Ti and β-Ti) can be found together in the microstructure of titanium-niobium-zirconium alloys (Kim et al., 2005).

The martensite start temperature (Ms) is suppressed by the addition of zirconium to titanium-niobium mixtures (Hao et al., 2005). In this regard, the same can be said for the addition of niobium to titanium-zirconium mixtures (Kim et al., 2005). For every 1 wt.% increase of zirconium content in ternary Ti-22Nb-xZr (x: 2 and 8; wt.%) alloys, the Ms temperature is reduced by 38 K; it is lowered by 40 K for every 1 wt.% increase of niobium content in the same alloy. However, niobium and zirconium contents in the titanium matrix have different effects on the α-Ti/β-Ti solvus line of titanium (see **Fig. 2.50.**). As a result, the equiatomic substitution of niobium element with zirconium element causes an increase in the α-Ti/β-Ti solvus line of titanium but does not alter the Ms temperature of titanium. For instance, the α-Ti/β-Ti solvus line of titanium can be increased by 70 K for Ti–20Nb–6Zr (at.%) when compared to Ti–26Nb(at.%) without changing the Ms temperature (Sun et al., 2011). The change in the volume fraction of the β-Ti phase in the microstructure may increase the super elasticity of the article owing to positive effects on the reversible the β-Ti, or the α″-Ti martensitic transformation.

Previous studies have shown that the Ti-13Nb-13Zr alloy, the most widely used titanium-niobium-zirconium alloy for biomedical applications, exhibits excellent corrosion resistance because the passivation of titanium, niobium, and zirconium can provide a permanent protective layer in simulated body fluids such as Hank's balanced salt solution (HBSS), Ringer's solutions, and phosphate-buffered saline (PBS). Therefore, Ti-13Nb-13Zr alloy has potential in implantology and dental applications (Lee et al., 2015).

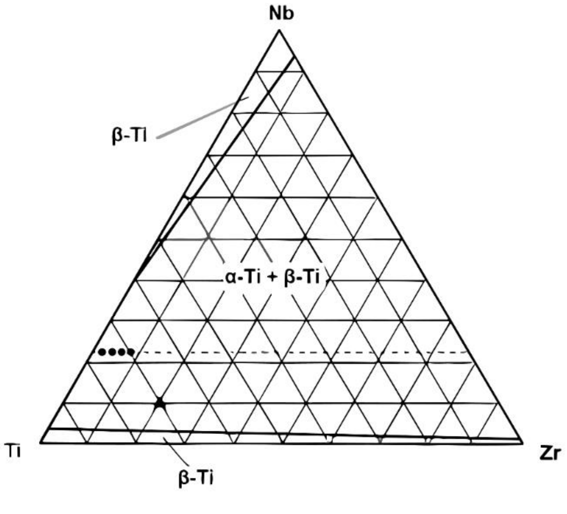

**Figure 2.50.** Titanium-niobium-zirconium ternary phase diagram (Cui et al., 2010).

Kaya et al. studied the biocompatibility and corrosion resistance of the Ti-10Nb-10Zr (at.%) produced by the powder metallurgy method. They stated that the presence of both zirconium and niobium in the titanium matrix significantly improved the corrosion resistance of the alloy due to oxide films formed on the surface. Further, to evaluate the biocompatibility of the Ti-10Nb-10Zr (at.%), in vivo analysis was performed. The results showed that Ti-10Nb-10Zr (at.%) alloy can be used in load-bearing implant applications (Kaya et al., 2019).

Hoppe et al. examined the mechanical performance and biological properties of the Ti-13Nb-13Zr alloy. The results revealed that the alloy had better mechanical properties and superior corrosion resistance compared to pure titanium, pure zirconium, and pure niobium. Further, the cytotoxicity result of the alloy showed that it could meet medical implant requirements (Hoppe et al., 2021).

Kim et al. studied the phase stability of Ti-Nb-Zr alloys with differing zirconium contents. The microstructure of the alloys studied comprised the β-Ti phase and the α'-Ti martensite phase. Moreover, to form the β-Ti phase in the microstructure, niobium content in the titanium matrix suppressed the martensitic transformation (Kim et al., 2020).

You and Song studied the microstructure and mechanical properties of Ti-Nb-Zr alloys designed by employing the electron alloy theory. The results showed that the microstructure of the alloys composed of the β-Ti phase and the mechanical properties of the alloys were determined by the formation of the β-Ti phase in the microstructure (You and Song, 2012).

### 2.2.8. Production of Porous Titanium-Based Alloys via Powder Metallurgy

A range of materials can be used in biomedical applications. Implant material selection depends on clinical requirements, material properties and manufacturing cost. For most biological applications, porous implant materials can enhance the integration (adherence) between the implant and the bone tissue since they facilitate the penetration of bone tissue cells within the porous structure of the implant material for bone ingrowth and physiological transport. Porous implants made from titanium and its alloys have favourable features for surgery implantation due to good chemical stability, excellent biocompatibility, and acceptable mechanical properties (see **Fig. 2.51.**). Moreover, porous titanium and its alloys used as implants can stimulate bone ingrowth and new bone formation at the implantation site (Esen and Bor, 2011). Many production methods such as powder metallurgy are combined with the space holder technique, 3D printing and foaming in the literature to produce the appropriate porosity characteristics such as porosity level, pore size, pore structure and mechanical functionality (Ryan et al., 2006). Conventional powder metallurgy is essential for producing porous structures. However, powder metallurgy combined with the space holder technique, used in this thesis, is the most efficient technique to create extra general porosity in implantology (Rodriguez-Contreras et al., 2021).

Previous studies have revealed that the general porosity ratio is an indicator showing the sum of the formation of macro and micro pores in the microstructure. This is determined by the shrinkage ratio of the particles during the sintering stage. Therefore, there is a strong relationship between sintering conditions and the general porosity ratio (Edosa et al., 2022).

**Figure 2.51.** Titanium implants with differing porosities (Edosa et al., 2022).

Liquid processing for titanium and its alloys is difficult due to the high melting temperature of titanium and its alloys and its extreme affinity to react with atmospheric gases such as nitrogen and oxygen above 400°C. Therefore, high-temperature processing equipment or a high vacuum may be required because liquid titanium and its alloys are extremely reactive. However, the powder metallurgy method combined with the space holder technique has the potential to fabricate porous titanium or its alloy components at much lower temperatures and under conditions of reduced chemical reactivity. With this method, pore characteristics and process variables can be also controlled precisely by changing powder metallurgy production parameters and powder characteristics (An et al., 2005; Lee et al., 2007; Edosa et al., 2022).

## 2.3. Powder Metallurgy

### 2.3.1. Definition of Powder Metallurgy

Powder metallurgy is a mature production method with a 5000-year history (Samal and Newkirk, 2015). It is defined as a process of forming metal by heating pressed metal powders to below the melting temperature. It can be widely employed in many fields such as the automotive industry, heavy equipment, gas turbines, parts of guns, the lamp industry, the aircraft and space industry and biomedical applications.

The schematic diagram of the powder metallurgy method is given in **Fig. 2.52.** Many factors affect the physical, chemical, and mechanical properties of the final product fabricated by powder metallurgy, including the particle characteristics used (i.e., shape, chemical composition, and size), compaction pressure, sintering temperature, and time (James, 2015; Rafandi et al., 2016).

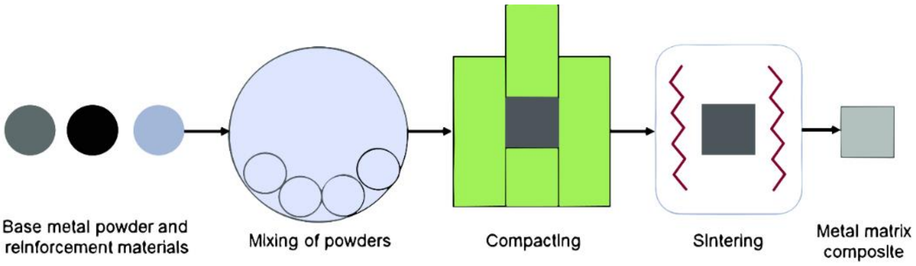

**Figure 2.52.** Schematic diagram of powder metallurgy method (Sankhla et al., 2022).

The powder metallurgy method consists of three basic steps as illustrated below (Angelo et al., 2022):

Blending or mixing

Compacting or pressing

Sintering

Blending/mixing: This is the first stage of powder metallurgy. The terms 'blending' and 'mixing' are different from each other. In this context, the term 'mixing' refers to the mixing of metal powders with different chemical structures, while the term 'blending' refers to the blending of metal powders with the same chemical structure in a specially designated container to obtain a homogeneous powder mixture, which is essential for a good sintering stage. For further homogenisation, chemical agents such as lubricants, binders and deflocculants can be used to enhance the flow characteristic of the powder used. There are several types of mixing/blending mechanisms in the literature, as shown in **Fig. 2.53.** (Groover, 2020).

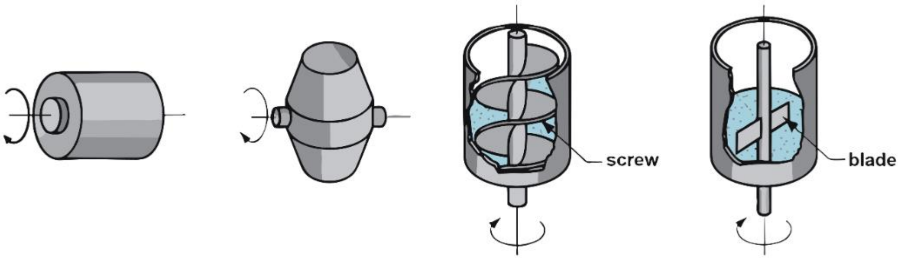

**Figure 2.53.** Several types of mixing/blending mechanisms (Groover, 2020).

In this stage, different types of powders such as pre-alloyed or pure element powders can be used. Powder production methods include atomisation, solid-state reduction, and electrolysis. The most widely used powder production method is atomisation, which accounts for 80% of total powder production. With this method, ferrous metal powders such as stainless steel, titanium-based alloys and nickel-based alloys can be manufactured effectively. The characteristics of the powders used in this stage play a crucial role in the compaction behaviour and the sintering stage.

Some studies have shown that the optimal fill rate of the container used in the mixing or blending stage should be in the range of 20% to 40% (Kondoh, 2012). During the mixing or blending, agglomeration, which is undesirable phenomenon when seeking to obtain a homogeneous structure, may occur depending on the type of blending/mixing mechanism used, powder properties, fill rate, blending time and temperature selected (Soyler, 2007; Kevenlik, 2013).

Compacting / pressing: This is the second stage of powder metallurgy. Powder mixtures are compacted or briquetted by using high pressure to manufacture green bulk (unsintered, compacted powders) samples with sufficient strength for the sintering stage. At this stage, the voids between the powders are eliminated and the density of the article is increased (Al-Qureshi et al., 2005).

Based on the literature, there are different types of compacting mechanisms; die, roll, and extrusion. The most widely used pressing method is die compaction. In the die compacting stage, two punches (lower and upper) made from stainless steel are used to compact the powder mixtures (Kevenlik, 2013). The die design depends on the desired shape. After compacting, the ease of the ejection of green bulk from the die is essential. **Fig. 2.54.** shows the schematic diagram of the die compacting (Paris and Mousavinasab, 2022).

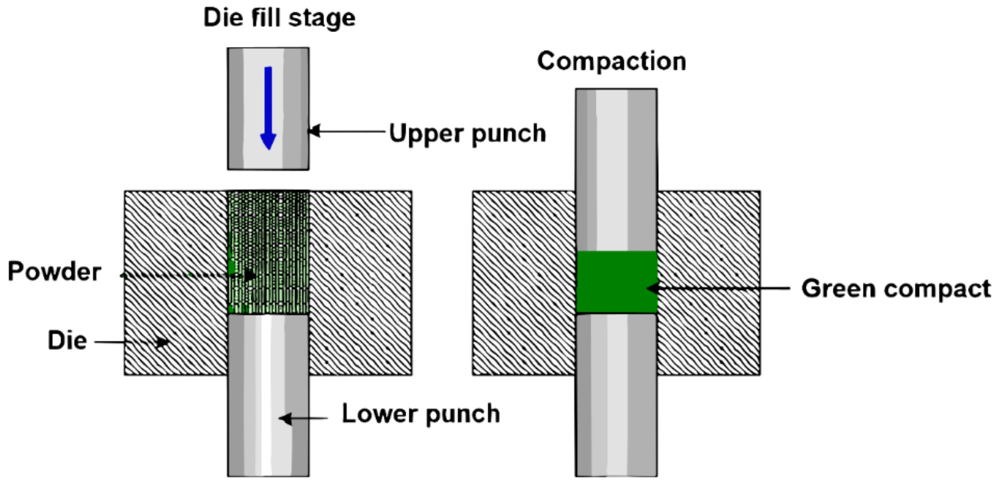

**Figure 2.54.** The schematic image of die compacting (Paris and Mousavinasab, 2022).

Sintering: This is the last stage of powder metallurgy. It is a heat treatment applied to green bulk samples to convert the mechanical bonds formed between powders into chemical (metallurgical) bonds, enhancing the metallurgical bonds (German, 2005). Sintering is the most important stage of powder metallurgy and can determine the strength and other properties of the article. This is because, at this stage, all mass or atom transport in the article can occur by diffusion of atoms as a result of high temperature applied. The temperature is usually below the melting point of the powders used in the article (~70% to 90% of the melting temperature of the metal powder). The driving force for sintering is a reduction in the surface energy of the metallic powders, which results from the formation of the inter-particle bond or the densification of the green bulk samples during sintering. Dimensional changes (shrinkage), phase transformations, and new formation of compounds may happen in this stage, improving the physical and mechanical properties of the final product. The elemental or alloy powders may react with gases in the atmosphere as sintering is performed at high temperatures; thus, protective gas or a vacuum furnace should be employed during this stage (Chang and Zhao, 2013). Sintering time and temperature can be chosen according to the chemical properties of the powders used. As stated previously, densification or neck formation takes place, and general porosity between particles reduces (see **Fig. 2.55.**). Low sintering time or temperature may result in inadequate diffusion and high pore formation in the microstructure of the article, which means that the final product may exhibit low density and low strength properties. Long sintering times and high temperatures are also not preferred as powders with a low melting point in the green compacts may evaporate or full melting may occur. **Fig. 2.56.** shows the development of the metallurgical bonds between the particles and structural changes during sintering (Pan et al., 2023). Sintering techniques mentioned in the literature include microwave sintering, spark sintering and laser sintering.

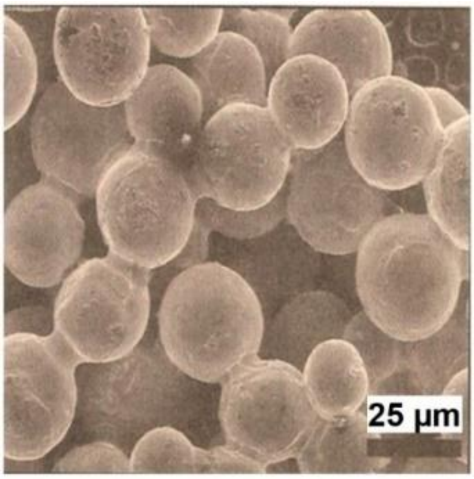

**Figure 2.55.** Neck formation (Pan et al., 2023).

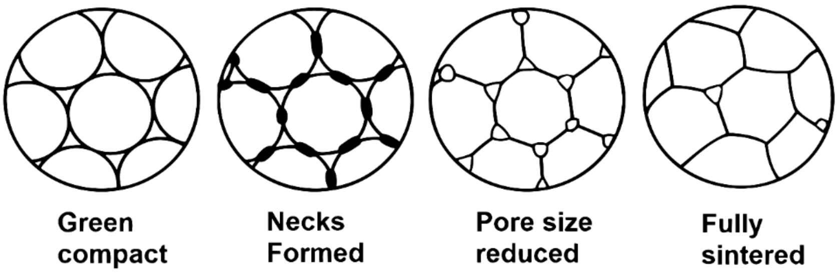

**Figure 2.56.** Sintering mechanism (Pan et al., 2023).

### 2.3.2. Porosity and Pore Characteristics

There are many production methods to achieve materials with porous structure such as 3D printing, laser-based powder bed fusion, metallic foam, powder metallurgy etc. The selection of production methods depends on the type of material used and desired pore characteristics. Powder metallurgy with space holder technique possesses several advantages such as adjustable porosity proportion, appropriate pore distribution and pore size. Therefore, in this thesis, powder metallurgy with space holder technique is selected as production method.

The general porosity produced by powder metallurgy techniques can provide to obtain the desired mechanical performances of the final product. It has also crucial effect on thermal and electrical conductivity, magnetic permeability, acoustic wave velocities, dielectric constant, diffusion coefficient, and biocompatibility features. (Ji et al., 2006). (see **Fig. 2.57.**).

Pores inside the final product can markedly influence the density, strength, and other properties. To control pore characteristics such as distribution, size and structure, various factors or parameters need to be considered in powder metallurgy techniques. The pore characteristics can determine the general porosity level, morphology, size, distribution, and shape of pores.

Powder type: The characteristics of powder material can play a crucial role in the final product manufactured with powder metallurgy techniques. Powder type should be carefully selected based on its size, shape, and composition. Especially, powders having irregular shapes may cause more significant pore formation on the material.

Powder packing: Compacting can make metallurgic bond between particles. This bond provides sufficient strength for sintering stage. Therefore, appropriate compaction is critical. There are several compaction techniques.

Sintering conditions: Sintering temperature and time play vital role in general porosity. Higher temperatures and longer sintering times can result in materials with fewer pores. Noted that it may lead to over-sintering. Therefore, there is a sensitive balance between sintering conditions and pore formation.

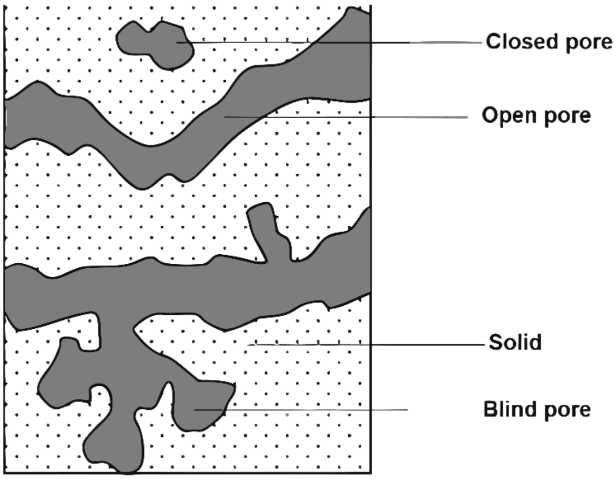

**Figure 2.57.** Schematic pore types (Nuilek, 2020).

The pore model that gives ideal particle packaging is recommended for improved mechanical behaviours for biomaterial applications. Therefore, there is a delicate balance between the porosity and mechanical properties of the biomaterial. The most significant aspects are the distribution, morphology, and control of porosity, which is essential for ingrowth and osteogeneses. In the literature, many production methods offer differing pore types. Fabrication of biomaterial with such porosity can be achieved by conventional powder metallurgy or by combining it with the space holder technique. The porous biomaterial produced by this method is based on numerous parameters influencing the packing of particles, such as compaction pressure, sintering temperature, and time. These parameters may ensure limited porosity for bone ingrowth and adjusting mechanical properties. Recently, the powder metallurgy method with space holder is being used since it has advantages like adjustable porosity proportion, appropriate pore distribution and pore size. Pore characteristics can be controlled by removing the space holder agent. Desirable morphology can be achieved in the microstructure (Esen, 2007).

### 2.3.3. The Space Holder Technique

To achieve complex geometries with a controlled porosity, the space holder technique can be applied with different supporting technologies such as powder compaction (PC), additive manufacturing (AM), and metal injection moulding (MIM) and 3D printing. This can be employed for different applications; these are biomedical implants and aerospace components. The space holder technique has been accepted as one of the reliable methods for the fabrication of metallic biomedical scaffolds.

Various types of biomaterials can be produced with powder metallurgy methods. With the parameters of powder metallurgy methods such as blending/mixing, compacting, sintering temperature and time, general porosity levels and pore sizes achieved in the article are limited. However, alloys with greater porosity levels and large pore sizes can be fabricated by powder metallurgy with the space holder technique. The literature reports several types of space holder agents: polymer particles or hollow polymer spheres, ceramic particles or hollow spheres, salts, and some metals. While using the space holder technique, some binders such as methylcellulose, PEG4000, and carboxymethyl cellulose (CMC) can be also used. These binders are generally removed by evaporation before the sintering stage.

The space holder agents are mixed with the metal powders used in the article to mechanically establish a bond with the metal powders. Later, the powder and space holder mixtures are pressed to give them the required strength for the sintering stage (Gibson, 2000). Lastly, the space holder agent is slowly removed from the compacts (bulk) to generate the required porosity in the microstructure. Processes for removal of the space holder agent from the bulk material include heat treatment, using an aqueous solvent or leaching in water or solution.

Titanium and its alloys are widely used in biomedical applications. In this regard, porosity characteristics such as type of pore, pore size and pore distribution should be adjusted according to the natural bone structure to be mechanically compatible (Kokubo and Yamaguchi, 2009; Mutlu, 2013). Some space holder agents can be added to titanium and its alloys produced by conventional powder metallurgy to achieve desired mechanical properties and porous structure; thus, different porosity levels and pore dimensions can be obtained, which is beneficial in the production of biomedical nanocomponents designed to be compatible with bone tissue. However, to achieve the target properties for titanium and its alloys used in biomedical applications, one of the major criteria is the selection of the appropriate space holder. Here, the space holder agent should not react with the titanium matrix; should not produce any residue or contaminate the titanium matrix and should have sufficient strength properties so that it cannot be deformed during compaction operation.

Titanium and its alloys fabricated by powder metallurgy combined with the space holder technique are not frequently used. Some studies are listed below.

According to Bram et al., titanium-based alloys studied in their work were separately mixed with the addition of 60, 70 and 80 wt.% spherical and angular carbamide particles. The blended carbamide/titanium powders were compacted under 166 MPa and the space holder agent was then removed from the titanium compacts by using a thermal treatment below 200 °C. After removing the space holder, the green titanium compacts were sintered at 1200 °C and 1400 °C for two hours. The general porosities obtained were about 60% for 1400 °C and 80% for 1200 °C. Based on the shape of the space holder agents used, differing porous structures were achieved (see **Fig. 2.58.**) (Bram et al., 2000).

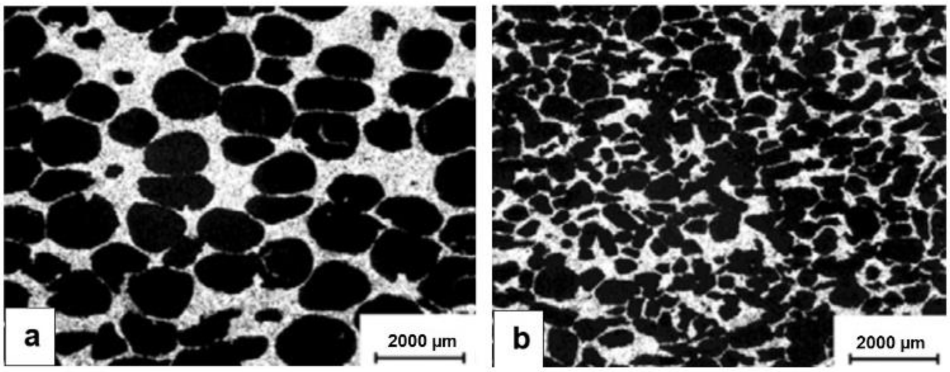

**Figure 2.58.** The morphology of pore structures achieved (a: spherical carbamide, b: angular carbamide) (Bram et al., 2000).

Titanium foam was produced by using ammonium hydrogen carbonate particles as a space holder agent. After the removal space holder agent, titanium foam was sintered at 1200 °C for two hours. The general porosity obtained in titanium foam was 79%. The elastic modulus and compressive strength of titanium foams were determined as 5.3 GPa and 35 MPa, respectively, which showed that these mechanical properties of titanium foam were close to the mechanical properties of bone. On the other hand, no carbonate particle of ammonium hydrogen contamination was found in titanium foams (Willie et al., 2010).

Kennedy manufactured titanium scaffolds by using polymer granules as a space holder. The polymer granules were removed from titanium scaffolds at 130 °C. Titanium scaffold compacts were sintered at 1100 °C and 1250 °C. The tensile strength of titanium scaffolds was 0.3 GPa for 1100 °C and 16 GPa for 1250 °C, while the elastic modulus values for titanium scaffolds sintered at 1100 °C and 1250 °C were 1.5 MPa and 30 MPa, respectively. As foreseen, the general porosities achieved in titanium scaffolds adversely affected the mechanical properties (Kennedy, 2012).

In another study regarding titanium foams produced as a load-bearing implant material, ammonium hydrogen carbonate was used as a space holder agent. Titanium foams produced exhibited open cellular-pore morphology. General porosities for titanium foams were in the range of 35% to 80%; pore sizes were between 200 μm and 500 μm (Wen et al., 2002).

Titanium foams were manufactured by powder metallurgy with the space holder technique (ammonium hydrogen carbonate, and carbamide). The mixtures of space holder agents and titanium powders were compacted under 100 MPa. Then, the space holder agent was removed from the titanium compacts at 200 °C for two hours. As a result, titanium foams with porosities between 78% and 87% were fabricated. The macro pore sizes of titanium foams achieved were between 200 μm and 500 μm. Large pores deteriorated the mechanical properties of titanium foams (Wen et al., 2001).

Imwinkelried used ammonium hydrogen carbonate as a space holder agent to produce open-pore titanium foams. Titanium powder and ammonium hydrogen carbonate powder were mixed in tumbling glass bottles and then compacted. The ammonium hydrogen carbonate powder was removed from the compacts by heat treatment applied at 95 °C for twelve hours. Here, general porosities for titanium foams were in the range of 50% to 80%. Pore sizes were between 100 μm and 500 μm (Imwinkelried, 2007).

Li and Zhu manufactured titanium foams with controlled porosity and pore size. Carbamide powder (urea) as a space holder was removed from titanium foams at 200 °C for two hours. Sintering was done at 1200 °C for four hours under an argon gas environment. As a result, porosity and pore size could be controlled by the presence of urea powders (Li and Zhu, 2006).

In a study conducted by Wen et al., titanium-zirconium alloy foams were produced as load-bearing implant material. Afterwards, titanium initial powder, zirconium initial powder and ammonium hydrogen carbonate powder used as space holder were mixed and then compacted under 200 MPa. Ammonium hydrogen carbonate powder was removed by thermal treatment carried out at 200 °C for five hours. Lastly, the sintering stage was performed at 1300 °C for two hours in a vacuum furnace. The resulting titanium-zirconium foams exhibited interconnected pore structures that can mimic the human bone. Pore sizes for the alloys obtained were between 200 μm and 500 μm (Wen et al., 2006).

In titanium foams, the polymeric space holder agents have limited usage due to their contaminations during the removal step or decomposition from the compacts. Rausch and Banhart used polymer granules as a space holder agent to produce porous titanium samples. The removal step of polymer granules was done by a chemical process at 130°C. Afterwards, porous titanium samples were sintered at 1100°C and 1250°C in a vacuum furnace. In conclusion, porosities obtained were 55% for 1400°C and 80% for 1100°C. The pore sizes were 200 μm for 1400°C and 300 μm for 1100°C (Fujii et al., 2022).

Some space holder agents used in the production of porous titanium and its alloys may cause undesirable residues or some interstitial elements such as oxygen, hydrogen, and nitrogen in the structure, which may deteriorate the mechanical properties of titanium and its alloys by changing its phase constituent in the microstructure. However, metallic space holder agents do not cause any residues in the microstructure. Since magnesium exhibits limited dissolution characteristics in titanium, magnesium could be used as a space holder (see **Fig. 2.59.**). The mixed titanium-magnesium powders were hot compacted below the melting point of magnesium. Afterwards, magnesium powders were removed from the compact titanium and Ti-6Al-4V alloy at 1000°C in a vacuum furnace. The sintering process was performed at 1400°C. The resulting general porosity values for the titanium and Ti-6Al-4V alloy produced were 25% and 82% (Ju et al.,2022).

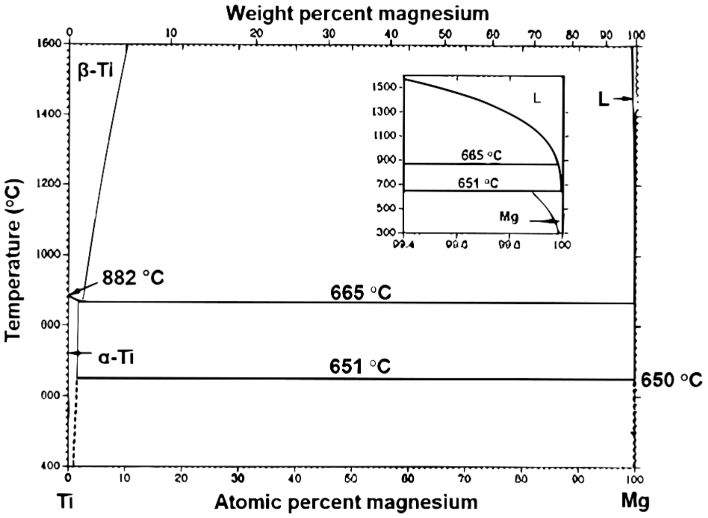

**Figure 2.59.** Equilibrium phase diagram for titanium-magnesium (Ju et al.,2022).

In another study, magnesium was employed as a space holder agent in the manufacturing of porous titanium and its alloys. Titanium powder and magnesium powder with amounts of 5% and 75% were mixed in a specially designed container. Then, polyvinyl alcohol was added to the mixtures as a binder. Afterwards, the paste prepared was applied to surface of titanium and its alloys. The surfaces coated were heated to 650°C and 800°C in a vacuum furnace. In that case, titanium and magnesium adhered to the substrate. Magnesium was then used as a space holder agent and was removed from the substrate surface at 1000°C by immersion in an acid solution (Liu et al., 2023).

### 2.3.4. Porous Structure for Bone Fixation

In implantology, cement or screws are generally employed for the early fixation of metallic implant material (Hong et al., 2008). Bone cement possesses several important functions, primarily in the fixation of implants and the stabilization of bone structures. The most common type of bone cement used in orthopaedics is polymethyl methacrylate (PMMA). (Tuncer, 2011). Unfortunately, this fixation strategy may generate a mismatch in stiffness between the implant and the surrounding bone. Here, additional operations may be required. Therefore, cementless replacements of porous orthopaedic biomaterial allowing bone ingrowth and body fluid transport within the pores have recently become the focus of attention (see **Fig. 2.60.**). Recently, the use of cementless replacements has increased because of reductions in thromboembolic disease, fat embolisms, and healing time.

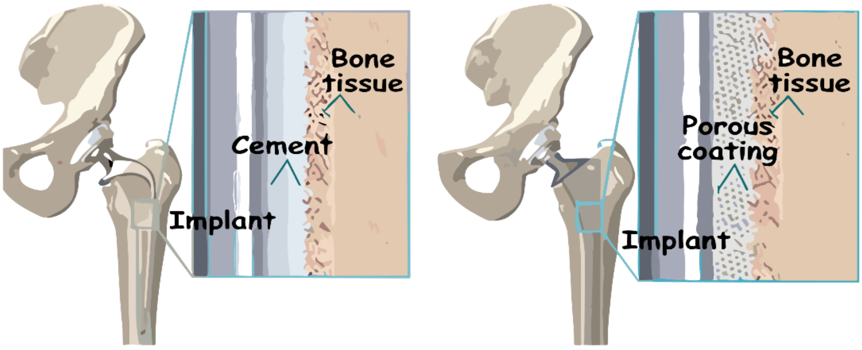

**Figure 2.60.** Cemented and cementless implants (Tuncer, 2011).

Based on the literature, a porous structure may enhance the mechanical and chemical bond between the orthopaedic biomaterial and the bone tissue for bone ingrowth (Baldissera et al., 2011). In general, porous implant materials can be categorised as fully porous implants and solid implants coated with a porous structure. The literature shows many studies on the benefits of porous implants for bone ingrowth (Bhattarai et al., 2008). Previous studies have shown that implants with porous structures can also meet the requirements for bone infiltration. This promotes cell proliferation and nutrient and oxygen transport since porous structures within implants can provide adequate sites (Lee et al., 2008; Li et al., 2009). A general porosity level with macropore sizes in the range of 100 μm to 600 μm can promote bone ingrowth, and a general porosity level with micropore sizes up to 20 μm can allow osteoconductive (Xiang et al., 2012; Asık and Bor, 2015; Arifvianto et al., 2016).

As mentioned previously, general porosity is essential for reducing the mechanical mismatch between the implant and bone tissue (Xiang et al., 2012). With the volume fraction of porosity in implant material, mechanical properties such as elastic modulus, yield strength and compressive strength can be adjusted effectively. Today, porosity adjustments can be made in the range of 50% to 80% by using differing production techniques. Further, the density of the implant material can be adjusted by altering the general porosity, which makes it closer to the density of bone. Thus, abrasion between implant and bone can be minimised by matching densities (Oppenheimer and Dunand, 2010; Lee et al., 2014). The general porosity of the implant material may eliminate the stress-shielding effect. In addition, adjusting general porosity level and pore sizes maintain the implant structure and stability (Esen and Bor, 2011; Monda et al., 2015).

### 2.3.5. Advantages and Disadvantages of Powder Metallurgy

Powder metallurgy has many advantages and limitations compared to other material production methods.

Advantages (Angelo et al., 2022):

- Minimal material loss or efficient use of materials (above 95%)
- Good surface quality
- Enables mass production
- Enables the production of refractory materials
- Close tolerance or near net shape
- Environmentally friendly

Limitations (Ak, 2014):

- High investment cost
- Powder preparation
- Lower ductility and strengths compared to full-dense or stiff material
- Difficulty in manufacturing large and complex-shaped parts
- Non-uniform structure

## 2.4. Summary

Porous titanium-based alloys are primarily composed of titanium with the addition of other elements such as aluminium, nickel and vanadium. However, some studies have shown that some alloyant elements may have detrimental influence for human body when implanted. In this thesis, it was aimed to produce aluminium, nickel, and vanadium- free titanium-based alloys. In this context, niobium and zirconium were used as alloying elements.

The porous structure of orthopaedic implants refers to a deliberate design feature. This porosity can be achieved through various techniques such as powder metallurgy, foaming, or additive manufacturing. The pores create an interconnected network within the implant, which is essential for bone ingrowth and other cellular activities. Also, porosity formation reduces the mechanical mismatch between orthopaedic implant and bone by lowering mechanical properties. In this thesis, titanium-based alloys with different porosity ratios were produced to see the effect of porosity on cellular activities and mechanical properties.

# Chapter 3. Materials and Methodologies

This chapter describes the powder metallurgy method and procedures. To facilitate the metallurgical observation, sample preparation methods and their procedures are illustrated. Characterisation and quantification techniques used in the experiment are also introduced.

In this thesis, experimental investigations were performed to develop new aluminium, nickel, and vanadium-free titanium-based alloys fabricated via powder metallurgy combined with the space holder technique and to better understand the sintering behaviour, microstructural and mechanical properties of the porous alloys. To investigate the effect of niobium and zirconium added to the titanium matrix, porous Ti-xNb (x: 10, 20 and 30; at.%), Ti-20Zr (at.%) and Ti-xNb-10Zr (x: 10 and 20; at.%) alloys were chosen. Each alloy was separately mixed with the addition of a 20 wt.% space holder agent (Ammonium bicarbonate: $NH_4HCO_3$) to generate higher porosities. Thus, the influence of general porosities on microstructural, and mechanical properties was also evaluated experimentally.

On the other hand, in vitro studies such as cell viability and proliferation, adhesion potential, and genotoxicity were examined by performing MTT assay, fibronectin adsorption, and plasmid-DNA interaction assay. The chemical formulas of porous alloys manufactured by powder metallurgy method with space holder technique and process parameters used in this thesis are given in **Table 3.1.** According to this concept, porous alloys with space holder agents are classified as high porous alloys, while porous alloys without space holder agents are categorised as low porous alloys.

**Table 3.1.** Chemical formulas of the alloys and process parameters used in this thesis (SH: space holder agent).

| **Alloy group** | **Chemical formula (at.%)** | **Mixing time (h)** | **Compaction pressure (MPa)** | **Sintering temperature (ºC)** | **Sintering time (h)** |
|---|---|---|---|---|---|
| **Low porous alloys** | **Ti-10Nb** | 10 | 300 | 1200 | 6 |
| | **Ti-20Nb** | 10 | 300 | 1200 | 6 |
| | **Ti-30Nb** | 10 | 300 | 1200 | 6 |
| | **Ti-20Zr** | 10 | 300 | 1200 | 6 |
| | **Ti-10Nb-10Zr** | 10 | 300 | 1200 | 6 |
| | **Ti-20Nb-10Zr** | 10 | 300 | 1200 | 6 |
| **Highly porous alloys** | **Ti-10Nb + 20 (wt.%) SH** | 10 | 300 | 1200 | 6 |
| | **Ti-20Nb + 20 (wt.%) SH** | 10 | 300 | 1200 | 6 |
| | **Ti-30Nb + 20 (wt.%) SH** | 10 | 300 | 1200 | 6 |
| | **Ti-20Zr + 20 (wt.%) SH** | 10 | 300 | 1200 | 6 |
| | **Ti-10Nb-10Zr + 20 (wt.%) SH** | 10 | 300 | 1200 | 6 |
| | **Ti-20Nb-10Zr + 20 (wt.%) SH** | 10 | 300 | 1200 | 6 |

Commercially pure titanium initial powder (purity: 99.5%, particle size: 44 µm, Alfa Aesar), commercially pure zirconium initial powder (purity: 99.7%, particle size: 23 µm, Alfa Aesar), and commercially pure niobium initial powder (purity: 99.8%, particle size: 35 µm, Alfa Aesar) were employed to produce the low and highly porous Ti-xNb, Ti-20Zr and Ti-xNb-10Zr alloys. Ammonium bicarbonate ($NH_4HCO_3$) (purity: 99%, Fisher) was also used as a space holder agent. The elemental analysis of titanium, niobium, and zirconium initial powders is given in **Table 3.2.**

**Table 3.2** The elemental analysis of titanium, niobium, and zirconium initial powders used in the experiment.

| **Initial powders** | **Elements (wt.%)** | | | | | | | | |
|---|---|---|---|---|---|---|---|---|---|
| | **Ti** | **Nb** | **Zr** | **Hf** | **N** | **C** | **H** | **Fe** | **O** |
| **Titanium** | Bal | - | - | - | 0.03 | 0.1 | 0.015 | 0.2 | 0.18 |
| **Niobium** | 0.02 | Bal | 0.02 | 0.02 | 0.01 | 0.01 | 0.0015 | 0.005 | 0.015 |
| **Zirconium** | - | - | Bal | 4.5 | 0.025 | 0.05 | 0.005 | 0.2 | 0.16 |

The experimental procedure of the present study is summarised in the flow chart shown in **Fig. 3.1**.

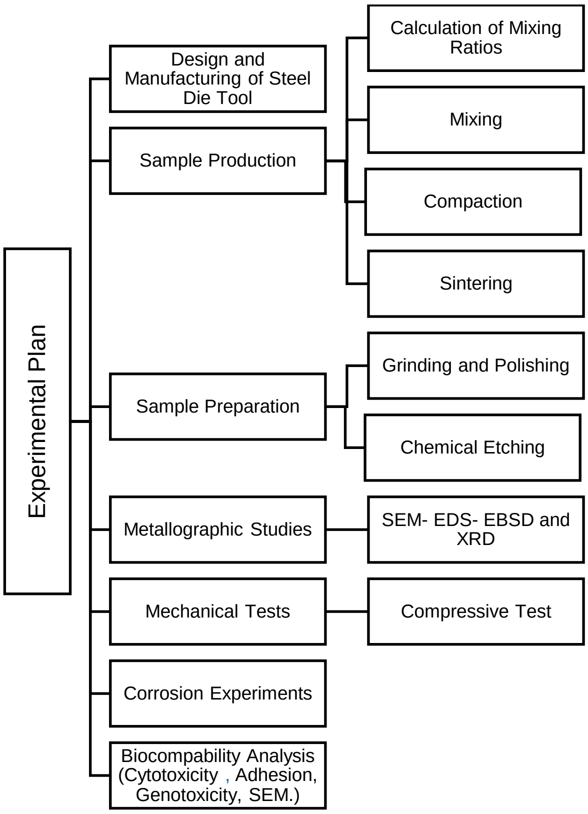

**Figure 3.1.** The flow chart of the experimental procedures used.

### 3.1. Design and Manufacturing of Steel Die Tool

A cylindrical steel die tool was designed for compressive tests and other metallographic examinations according to EN 24506 standards. The constructive shape of the steel die tool used in the experiment are shown in **Fig. 3.2.**

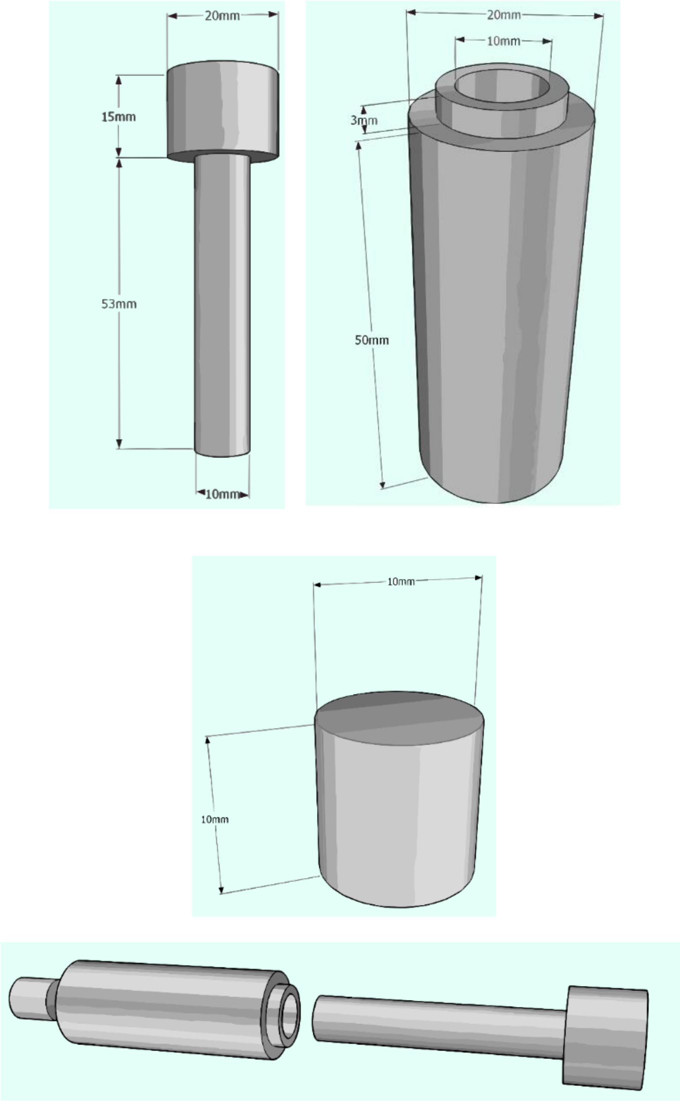

**Figure 3.2.** Constructive shape of the steel die tool used in the experiment.

All parts of the steel die tool were made from AISI 1010 (plain carbon steel). The elemental analysis of the plain carbon steel is shown in **Table 3.3**. The inner die parts and rigid punches were prepared by grinding and polishing to improve their surface qualities for sample production.

**Table 3.3.** The chemical composition of plain carbon steel (Maity, J., & Sharma, 2023).

| Element | C | Si | Mn | Cr | S | Fe |
|---|---|---|---|---|---|---|
| wt.% | 0.12 | 0.09 | 0.43 | 0.06 | 0.01 | Bal. |

## 3.2. Sample Production

### 3.2.1. Calculation of Mixing Ratios

The powder preparation is the first step of sample production in powder metallurgy before blending. Eqs. (3.1) can be used to convert the values given in atomic ratios (at.%) to weight ratios (wt.%). Titanium, niobium, and zirconium initial powders were prepared according to the nominal formulas given in **Table 3.1.**

$$\mathrm{X_{Ti}}\frac{\mathrm{m_{Ti}} * \mathrm{N}}{\mathrm{A_{Ti}}} \qquad \text{and} \qquad \%\,\mathrm{X_{Ti}} = \frac{\mathrm{X_{Ti}}}{\mathrm{X_{Ti}} + \mathrm{Y_{Nb}} + \mathrm{Z_{Zr}}} * 100 \qquad (\mathbf{3.1a.})$$

$$\mathrm{Y_{Nb}}\frac{\mathrm{m_{Nb}} * \mathrm{N}}{\mathrm{A_{Nb}}} \qquad \text{and} \qquad \%\,\mathrm{Y_{Nb}} = \frac{\mathrm{Y_{Nb}}}{\mathrm{X_{Ti}} + \mathrm{Y_{Nb}} + \mathrm{Z_{Zr}}} * 100 \qquad (\mathbf{3.1b.})$$

$$\mathrm{Z_{Zr}}\frac{\mathrm{m_{Zr}} * \mathrm{N}}{\mathrm{A_{Zr}}} \qquad \text{and} \qquad \%\,\mathrm{Z_{Zr}} = \frac{\mathrm{Z_{Zr}}}{\mathrm{X_{Ti}} + \mathrm{Y_{Nb}} + \mathrm{Z_{Zr}}} * 100 \qquad (\mathbf{3.1c.})$$

$X_{Ti}$ = Weight percentage of titanium
$Y_{Nb}$ = Weight percentage of niobium
$Z_{Zr}$ = Weight percentage of zirconium
$m_{Ti}$ = Atomic percentage of titanium
$m_{Nb}$ = Atomic percentage of niobium
$m_{Zr}$ = Atomic percentage of zirconium
N = Avogadro's number
$A_{Ti}$ = Atomic mass of titanium
$A_{Nb}$ = Atomic mass of niobium
$A_{Zr}$ = Atomic mass of zirconium

The chemical compositions in weight percentage (wt.%) are shown in **Tables 3.4, 3.5. and 3.6**.

**Table 3.4**. The chemical composition of binary titanium-niobium alloys in weight percentage (wt.%).

| **Alloy type (at.%)** | **Composition of elements (wt.%)** | | |
|---|---|---|---|
| | **Ti** | **Nb** | **$NH_4HCO_3$** |
| **Ti-10Nb** | 82.28 | 17.72 | - |
| **Ti-20Nb** | 67.32 | 32.68 | - |
| **Ti-30Nb** | 54.61 | 45.39 | - |
| **Ti-10Nb + 20 SH** | 65.82 | 14.18 | 20 |
| **Ti-20Nb + 20 SH** | 53.86 | 26.14 | 20 |
| **Ti-30Nb + 20 SH** | 43.69 | 36.31 | 20 |

**Table 3.5**. The chemical composition of binary titanium-zirconium alloys in weight percentage (wt.%).

| **Alloy type (at.%)** | **Composition of elements (wt.%)** | | |
|---|---|---|---|
| | **Ti** | **Zr** | **$NH_4HCO_3$** |
| **Ti-20Zr** | 67.73 | 32.27 | - |
| **Ti-20Zr + 20 SH** | 54.18 | 25.82 | 20 |

**Table 3.6**. The chemical composition of ternary titanium-niobium-zirconium alloys in weight percentage (wt.%).

| **Alloy type (at.%)** | **Composition of elements (wt.%)** | | | |
|---|---|---|---|---|
| | **Ti** | **Nb** | **Zr** | **$NH_4HCO_3$** |
| **Ti-10Nb-10Zr** | 67.58 | 16.37 | 16.05 | - |
| **Ti-20Nb-10Zr** | 54.75 | 30.35 | 14.90 | - |
| **Ti-10Nb-10Zr + 20 SH** | 54.06 | 13.1 | 12.84 | 20 |
| **Ti-20Nb-10Zr + 20 SH** | 43.8 | 24.28 | 11.92 | 20 |

### 3.2.2. Mixing

In this thesis, titanium, niobium, and zirconium initial powders with the nominal compositions given in **Tables 3.4, 3.5 and 3.6** were weighed by a precision scale with a sensitivity of 0.1 mg (shown in **Fig. 3.3**). Afterwards, they were mixed using a powder blending apparatus at a rotation rate of 24 rpm for ten hours in a specially designed container to ensure compositional homogeneity (see **Fig. 3.4**). In addition, ammonium bicarbonate powder used as a space holder agent was added to each porous alloy to generate extra porosity. A small piece of sieve made from stainless steel was placed inside the specially designed container to prevent agglomeration during the mixing procedure.

**Figure 3.3.** The precision scale.

© Artisan Technology Group

**Figure 3.4.** The powder mixing apparatus.

### 3.2.3. Compacting

After the mixing stage, the powder mixtures were charged into the cylindrical steel die tool with a size of Φ10 mm. The cylindrical steel die tool was then placed in the chamber of the universal tension-compressive test machine and positioned as shown in **Fig. 3.5**. The powder mixtures in the cylindrical steel die tool were compacted under a pressure of 300 MPa by using a 100 kN capacity universal tension-compressive test machine (Zwick/Roell Z600) at a compaction rate 0.1 mm/min, following EN 24506 standards. All compacting procedures were performed with three samples at room temperature. As a result of this procedure, cylinder-shaped green (unsintered) compacts with a size of Φ10mm x 15mm were manufactured.

**Figure 3.5.** The universal tension-compressive test machine.

### 3.2.4. Sintering

The digitally controlled furnace used for sintering is shown in **Fig. 3.6**. Two sintering stages were applied in this thesis. In the first stage, low porous test (green) alloys briquetted or compacted were only heated to 1200°C at 5°C / min and kept for six hours. This sintering temperature was determined from other studies on porous titanium-based alloys used as orthopaedic implant. Throughout the sintering, the furnace worked under gas sintering conditions by using argon gas so that green alloys did not react with gases in the air at high temperatures. The graph of the sintering regime for low porous alloys is given in **Fig. 3.7**.

**Figure 3.6.** The digitally controlled furnace.

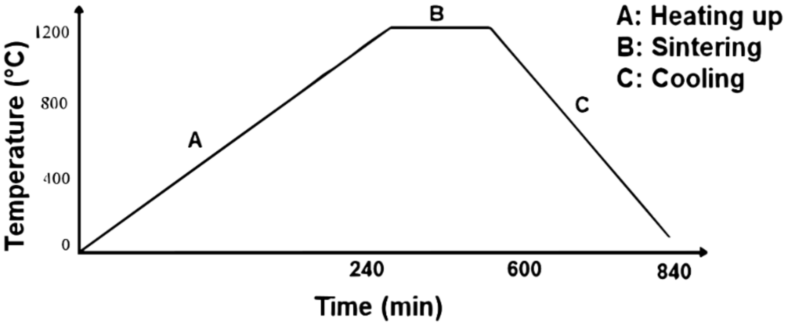

**Figure 3.7.** The graph of the sintering regime for low porous alloys.

In the second stage, highly porous alloys were sintered in two steps. In the first step, they were held at 180°C for two hours to remove the ammonium bicarbonate ($NH_4HCO_3$) from the green compacts. Afterwards, like the sintering regime of the low porous alloys, highly porous alloys were heated to 1200°C at 5°C/min and kept for six hours in an argon atmosphere. The graph of the sintering regime for the highly porous alloys is given in **Fig. 3.8**.

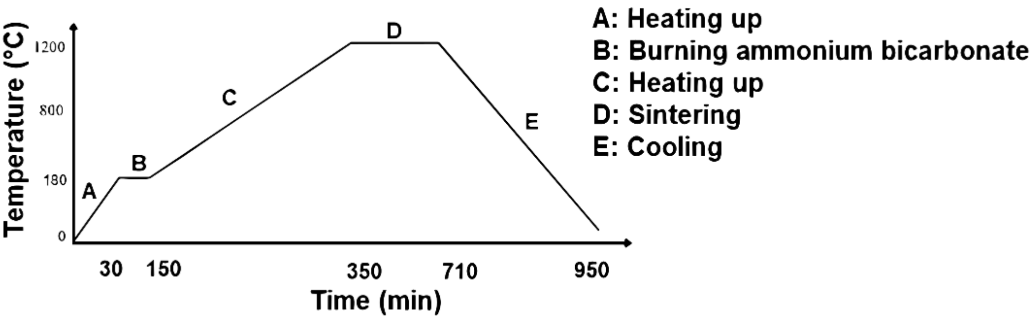

**Figure 3.8.** The graph of the sintering regime for highly porous alloys.

After the sintering of the low and highly porous alloys, they were cooled to 200°C at 5°C/min. Thus, low, and highly porous alloys with different chemical compositions and porosities were achieved. Macro images of the low and highly porous alloys produced by the conventional sintering technique with the space holder technique for the compressive test, other metallographic analysis, and biocompatibility test in vitro are shown in **Fig. 3.9**.

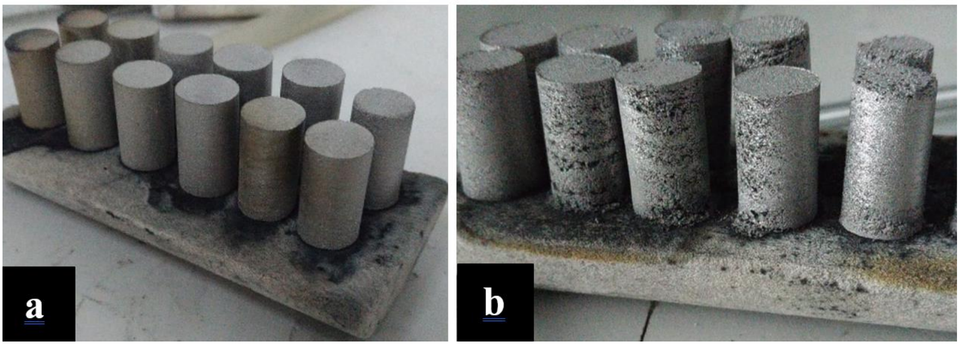

**Figure 3.9.** Macro images of the low and highly porous alloys sintered at 1200°C for six hours ((a) low porous alloys: (b) highly porous alloys).

## 3.3. Metallographic Preparation

### 3.3.1. Grinding and Polishing

For metallographic examination, the low and highly porous alloys sintered at 1200°C for six hours were cut from various areas, depending on the observation needs. The all-porous alloys were then mounted using a Simpli-Met 3000 mounting machine (Buehler, UK). The metallographic preparation route is shown in **Table 3.7**. The surface preparation of the porous alloys was performed by wet grinding with a series of silicon carbide (SiC) abrasive papers to 4000 grits. To achieve the desired surface quality, the polishing process was done by using a piece of fabric and 0.04 µm $SiO_2$ OP-S (water-based $SiO_2$ suspension). The polished alloys were cleaned ultrasonically in ethanol to eliminate impurities and dried by air blowing.

**Table 3.7.** The metallographic sample preparation route used in the experiment.

| **Abrasive** | **Force (N)** | **Time (min:sec)** | **Rotation speed (rpm)** | | **Rotation direction (base/head)** |
|---|---|---|---|---|---|
| | | | Base | Head | |
| **P320 SiC** | 25 | Until flat | 300 | 50 | >> |
| **P800 SiC** | 20 | 5:00 | 150 | 50 | >> |
| **P1200 SiC** | 20 | 5:00 | 150 | 50 | >> |
| **P4000 SiC** | 20 | 5:00 | 150 | 50 | >> |
| **0.04μm SiO2 OP-S** | 15 | 12:00 | 150 | 50 | > < |
| All consumables were provided by Brunel University London Labs. | | | | | |

### 3.3.2. Chemical Etching

All-porous alloys presenting morphology faceted are remarkably anisotropic along different crystal orientations. This may make it difficult to characterise their morphologies through 2-D observation. For this reason, the 3-D morphologies of the alloys sintered at 1200°C for six hours were characterised by a chemical etching process. The station of chemical etching was set up as given in **Fig 3.10**. The porous alloy surfaces were subjected to water-based Keller's solution (190 ml $H_2O$, 5 ml $HNO_3$, 3 ml HCl and 2 ml HF) for about six to ten seconds at room temperature to reveal their microstructures (Qu et al., 2016). Afterwards, the porous alloys were taken from the Keller's solution and cleaned well with ethanol ($C_2H_5OH$) before drying in a hot air stream.

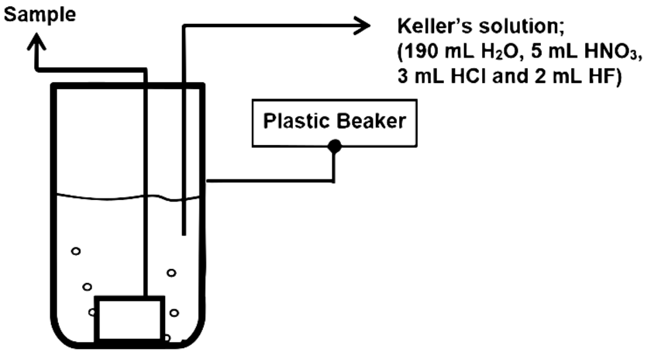

**Figure 3.10.** A schematic illustration of the chemical etching station.

### 3.4. Calculation of General Porosity Ratio

To determine the porosity ratio (open and closed pores) (ε) of the low and highly porous alloys sintered at 1200°C for six hours, the theoretical and the sintered (bulk) densities were employed. Normally, the theoretical density of an element is calculated by using the number of atoms in the unit cell, atomic mass, and lattice parameters, but it is hard to say the same for an alloy. This is because the alloy can contain various phases and compounds in its microstructure. These phases and compounds may cause distortions in the lattice parameters. Therefore, the theoretical density ($\rho o$) of the alloy can be calculated from the atomic mass and specific density of individual elements making up the alloy, as indicated in Eq. (3.2). The sintered (bulk) density of the alloy or element is determined from its mass-to-volume ratio (see Eq. (3.3)). To calculate the volume of the porous alloys, the cylinder volume formula ($V = \pi * r^2 \times h$) was used since the final products achieved in this thesis have a cylindrical shape. The π, r and h are pi (3.14), radius (cm) and height (cm), respectively. To see the mass value, each porous alloy was weighed by a precision balance with a sensitivity of 0.1 mg (shown in **Fig. 3.3**) and the sintered (bulk) density values were calculated directly from the mass-to-volume ratio. Lastly, the porosity ratio (ε) of the low and highly porous alloys sintered at 1200°C for six hours were separately calculated for each alloy by using theoretical density and sintered density values (see Eq. (3.4)) (Li et al., 2000; Çakmak et al., 2022). The porosity ratio results are the arithmetic average of three measurements of the same low and highly porous alloys sintered at 1200°C for six hours.

$$\mathrm{\rho_o} = \frac{\mathrm{m_{Ti}} + \mathrm{m_{Nb}} + \mathrm{m_{Zr}}}{\mathrm{V_{Ti}} + \mathrm{V_{Nb}} + \mathrm{V_{Zr}}} \qquad (\mathbf{3.2.})$$

$$\mathrm{\rho_o} = \frac{\mathrm{m}}{\mathrm{V}} \qquad (\mathbf{3.3.})$$

$$\varepsilon = \left(1 - \frac{\rho}{\rho_o}\right) * 100 \qquad (\mathbf{3.4.})$$

$\rho_o$ = Theoretical density (g/cm$^3$)

$m_{Ti}$ : Mass of titanium used in the alloy (g)

$V_{Ti}$ : Volume of titanium used in the alloy (cm$^3$)

$m_{Nb}$ : Mass of niobium used in the alloy (g)

$V_{Nb}$ : Volume of niobium used in the alloy (cm$^3$)

$m_{Zr}$ : Mass of zirconium used in the alloy (g)

$V_{Zr}$ : Volume of zirconium used in the alloy (cm$^3$)

ρ = Sintered (bulk) density (g/cm$^3$)

m = Mass of the alloy (g)

v = Volume of the alloy (cm$^3$)

ε = General porosity (%)

## 3.5. Metallographic Examinations

### 3.5.1 Optical Microscopy

Metallographic sections for OM and SEM were done by using the metallographic procedures mentioned in Section 3.3. The optical images of the porous alloys sintered at 1200°C for six hours were taken using a Zeiss Optical Axio Microscope A1 (Zeiss Group, Oberkochen, Germany) equipped with a Zeiss Axiocam ICc3 digital camera (Zeiss Inc., 2017) (seen in **Fig. 3.11**). The optical microscope is connected to a camera and a computer. Thus, the Axiocam software installed gave wide observation possibilities.

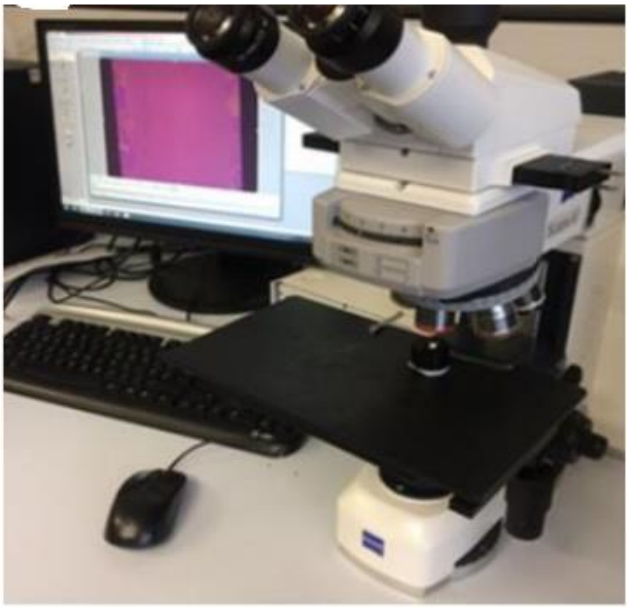

**Figure 3.11.** The Zeiss Optical Axio Microscope A1.

### 3.5.2 Scanning Electron Microscopy and Energy Dispersive Spectrometry

SEM examinations were performed using a Zeiss Supra 35 microscope (Zeiss Group, Oberkochen, Germany) equipped with an EDAX EDS (see **Fig. 3.12.**). Various signals on this device can be produced owing to the interaction between the beam and the sample. This provides detailed information about the grain size, grain boundaries, elemental analysis, and elemental distribution (Goodhew et al., 2000). SEM employed in this experiment has different operational modes like back scattered electron (BSE) and secondary electron imaging (SE).

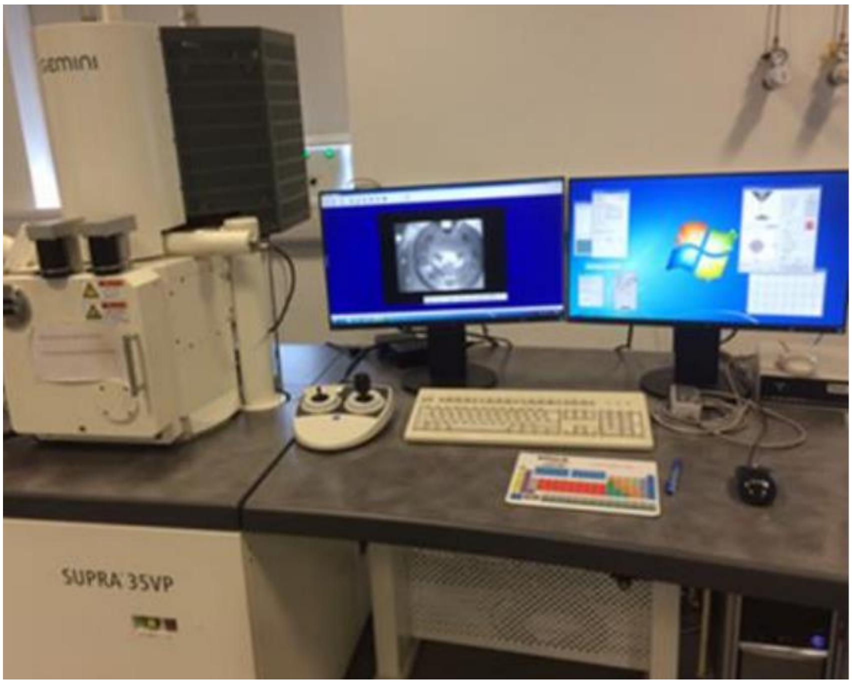

**Figure 3.12.** The Zeiss Supra 35 microscope.

### 3.5.3. Electron Backscattered Diffraction

The low and highly porous alloys sintered at 1200°C for six hours were prepared using the metallographic procedures mentioned above. EBSD analysis was done by the Zeiss Supra 35VP fitted with a high-sensitivity Digi View camera (EDAX Inc., NJ, U.S.), as shown in **Fig. 3.12**, with EDAX TEAM 4.3 system (EDAX, 2017). During EBSD analysis, the working distance, accelerating voltage and condenser aperture employed were 12 mm, 20 kV and 120µm, respectively, in high current mode. The step size selected was a range of 0.2 µm to 1 µm according to the area size and grain size.

### 3.5.4. X-ray Diffraction

Crystallographic characterisations of the low and highly porous alloys sintered at 1200°C for six hours were performed by a Bruker D8 Advance Cu-Kα source (see in **Fig. 3.13**). X-ray diffraction (XRD) analysis was done on the surfaces of the polished alloys to get good diffraction peaks. The step size, acquisition time, and 2θ angle range used in this work were 0.02˚, 1 second, and 30˚to 80˚, respectively.

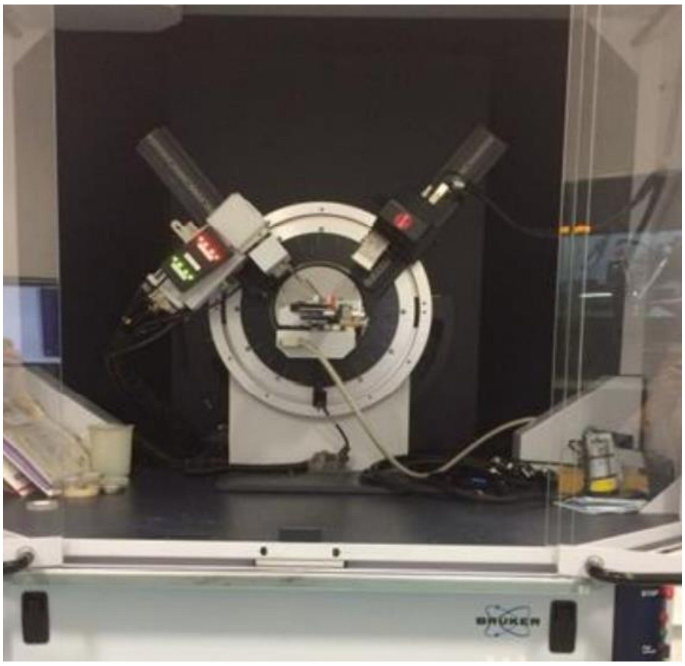

**Figure 3.13.** Bruker D8 Advance XRD.

## 3.6. Mechanical Tests

### 3.6.1. Uniaxial Compressive Test

The low and highly porous alloys sintered at 1200°C for six hours were prepared according to EN 24506 standards with dimensions of Φ10mm x15mm. The surfaces of the alloys were quite rough due to the presence of pores on the surface. Therefore, the surfaces of the alloys were mechanically ground with a series of SiC abrasive papers to 1200 grit before the compressive test. Mechanical testing was performed by uniaxial compression using samples of Φ10 mm × 15 mm. The compression tests were carried out three times for each sample condition on in a universal tensile-compression testing machine (Zwick/Roell Z600) with a capacity of 100 kN, following EN 24506 standard. The elastic modules of the alloys achieved in this thesis were calculated from curves fitted to the linear elastic regions of the stress-strain curves. Also, the 0.2% offset method was used to determine the compression yield strength values of the alloys. Lastly, based on the results of the experiments, comparisons were made with empirical and analytical models used for porosity-stress relations.

**Figure 3.14.** The Zwick/Roell Z600 test machine.

### 3.7. Electrochemical Analysis

For the electrochemical corrosion test, the low and highly porous alloys sintered at 1200°C for six hours were mechanically ground with a series of SiC abrasive papers to 4000 grit and then carefully cleaned in an ultrasonic bath. Afterwards, a potentiodynamic polarisation test equipment was carried out by using a potentiostat (EZstat) with an electrochemical flat cell (seen in **Fig. 3.15**). The alloys were exposed to HBSS (350 mL.cm$^{-2}$, Fisher Scientific) at room temperature (25°C). The alloys were used as the working electrode (exposed area of 1 cm$^{2}$). A standard calomel electrode (SCE) was selected as the reference electrode. Lastly, a plate of platinum was determined as a counter electrode. The Tafel curves of the alloys were scanned at a scan rate of 0.01 V.s$^{-1}$ after open circuit potential measurements for 30 minutes. The scan range was chosen between -0.75 V and 1.25 V. Tafel curves were used to determine the corrosion current density ($i_{corr}$), corrosion potential ($E_{corr}$) and polarisation resistance ($R_p$) of the alloys sintered at 1200°C for six hours (Witte et al., 2006).

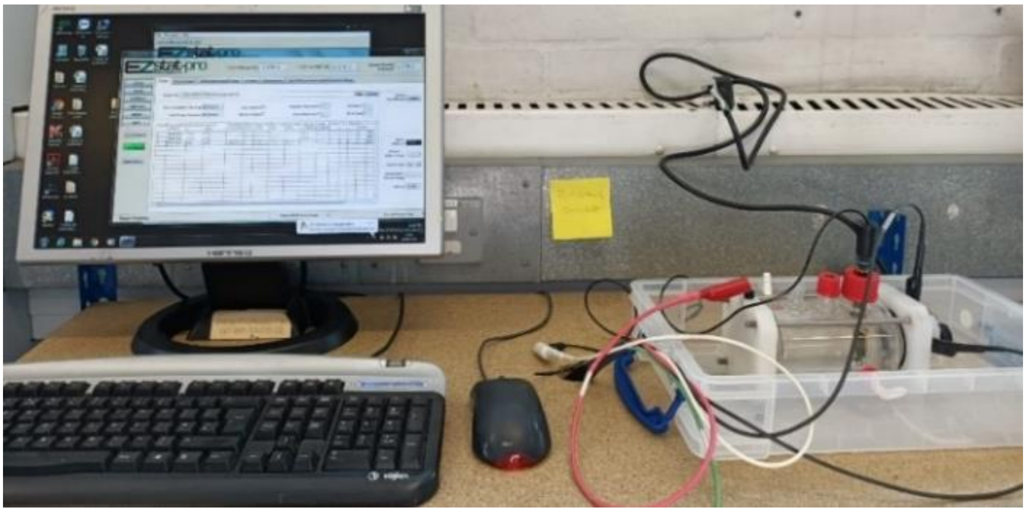

**Figure 3.15.** The potentiodynamic polarisation test equipment.

### 3.8. Biological Evaluations of In Vitro Models

In vitro studies such as cell viability and proliferation, adhesion potential, and genotoxicity were examined by performing MTT assay, fibronectin adsorption, and plasmid-DNA interaction assay following the ISO 10993-5 for the biological assessment of implantable devices.

### 3.8.1. Sterilisation

The low and highly porous alloys sintered at 1200°C for six hours were cut into discs of Φ8mm x 2mm in thickness. The surfaces of the alloy discs were mechanically ground with SiC up to 2500 grits. For sterilisation, all alloy discs under consideration were placed in 70% (v/v) ethanol solution for two hours. Afterwards, the ethanol solutions were renewed and exposed to ethanol sterilisation for two more hours. The ethanol solutions were removed and dried completely. After that, the alloy discs were sterilised at 120˚C by autoclaving for 30 minutes. Finally, they were washed four times with PBS (DPBS; pH: 7.4).

### 3.8.2. Cell Viability MTT Assays

Cell culture conditions: Mouse fibroblast NCTC clone 929 cell line (L929) and human bone osteosarcoma cell line (Saos-2) were purchased from American Tissue Culture Collection (ATCC, VA, USA). The L929 and Saos-2 were grown in DMEM supplemented with 10% fetal bovine serum (heat-inactivated, Gibco, #10500-064), and 1% antibiotic-antimycotic solution (10,000 units/mL of penicillin, 10,000 µg/ml of streptomycin, and 25 µg/ml of Amphotericin B, Gibco, #15240-062) in a 37ºC, 5% $CO_2$ incubator. The medium was replaced with fresh DMEM every two days, and the cells were harvested with Trypsin-EDTA solution, 0.25% (Gibco, #25200-056) when they reached 70% to 80% confluency (Cetin et al., 2020).

In vitro biocompatibility of the low and highly porous alloys sintered at 1200°C for six hours was examined to assess the individual effects of zirconium and niobium concentrations in titanium matrix and the porosity ratio on cell viability compared to reference TiGR4 material by extract and direct contact methods, following ISO 10993-5.

MTT assay extract method: The low and highly porous alloys sintered at 1200°C for six hours were sterilised at 120$^{o}$C by autoclaving for 30 minutes and extracted at a ratio of 0.2 g/ml in DMEM at 37$^{o}$C and 120 rpm for 72 hours. The L929 and Saos-2 cells were seeded at a cell density of 15 x $10^3$ cells/well for one day of incubation, 6 x $10^3$ cells/well for three days, and 2.5 x $10^3$ cells/well for seven days into a 96-well plate and incubated at 37°C and 5% $CO_2$ for 24 hours. The following day, 100 µl of extract from each sample was added to the cell monolayers and incubated at 37°C and 5% $CO_2$ for one day, three days, and seven days. After each incubation period, the sample and control extracts were aspirated from each well and 100 µl DMEM including 10% of 3-(4,5-Dimethyl-2-thiazolyl)-2,5-diphenyl-2H-tetrazolium bromide, Thiazolyl blue (MTT, 0.5 mg/ml in DPBS), (Sigma-Aldhrich #M5655) was added. The cells were then incubated at 37$^{o}$C and 5% $CO_2$ for four hours. The formazan crystals formed due to the metabolic activity of live cells were then dissolved by adding 100 µl of DMSO to each well and placed in a shaker for two hours at room temperature. The absorbance of formazan production was measured at 570 nm to 630 nm by a Microplate reader (Biotek Instruments, Inc., USA). The images were taken under a microscope with 10X magnification (Leica DMI 6000). The absorbance of the treated cells was normalised to the control cells and cell viability was then calculated as the percentage of the control.

MTT Assay Direct Contact Method: The low and highly porous alloy discs (cut into 8 mm diameter x 2 mm thickness discs) were prewashed with DPBS and placed in the wells of a six-well plate. L929 and Saos-2 cells were seeded at a cell density of 4 x $10^5$ cells/well for one day of incubation, 2 x $10^5$ cells/well for three days, and 1 x $10^5$ cells/well for seven days into the six-well plate and incubated at 37°C and 5% $CO_2$ for 24 hours. Cell densities were determined by counting cells onto the haemocytometer grids under inverted microscope after obtaining the homogenous cell suspension (see **Table 3.8.**). Cell densities were higher in seven days incubation period due to doubling time of the cells. Doubling time of L929 and Saos-2 are 24 hr and 36 hr, respectively, therefore they could be divided 6 and 4 times. Seeding cell densities were determined upon seeding cells with serial dilutions and incubated at the same testing period. Then the seeding cell number was chosen at exponential phase of the cell growth curve. According to the graph, seeding cell number for each cell and each incubation time were determined.

**Table 3.8.** Seeding cell number for each cell and each incubation time.

| Cells | 1-day | 3-day | 7-day |
|---|---|---|---|
| **L929** | $10x10^3$ | $6x10^3$ | $2.5x10^2$ |
| **Saos-2** | $15x10^3$ | $7x10^3$ | $3x10^3$ |

Following each incubation period, fresh DMEM including 10% of MTT reagent (0.5 mg/ml in DPBS) was added. The cells were then incubated at 37°C and 5% $CO_2$ for four hours. To observe the violet formazan crystals formed by viable cells, the images were taken under a fluorescence microscope using 10X magnification. Then the formazan crystals were dissolved by adding 500 µl of DMSO to each well and placed in a shaker for two hours. The cytotoxic effects of the samples directly contacted with the cells were examined by analysing the intensity of formazan crystals formation in each well compared to the reference dental implant and negative control.

### 3.8.3. Live-Dead Viability/Cytotoxicity Assay

The Cell Imaging Kit is a sensitive two-colour fluorescence cell viability assay optimised for FITC and Texas Red™ filters. It allows discrimination between live and dead cells with two probes that measure recognised parameters of cytotoxicity and cell viability-intracellular esterase activity and plasma membrane integrity. The cell viability test kit (Molecular Probes #L3224) is based on measuring cell viability-intracellular esterase activity with intensely green fluorescent calcein (ex/em ~495 nm/~515 nm) retained in the live cells and plasma membrane integrity with ethidium homodimer, EthD-1 (ex/em ~495 nm/~635 nm) bound to the nucleic acids in the membrane-damaged dead cells.

Live-dead viability extract method: Parallel to the MTT cell viability assay, after each incubation period, the cells were washed twice with DPBS to remove serum esterase activity and 100 µl of DPBS including 2 µM calcein AM and 4 µM EthD-1 was added on the cell monolayers and incubated for 30 to 45 minutes at room temperature. The images were taken under a fluorescence microscope (Leica DMI 6000) using 10X magnification.

Live-dead viability direct contact assay: The low and highly porous alloy discs were placed into each well of a six-well plate. Following each incubation period, the cell monolayers were washed twice with DPBS to remove serum esterase activity, and 2 µl of DPBS including 2 µM calcein AM and 4 µM EthD-1 was added to the wells. The plates were incubated for 30 to 45 minutes, and the images were taken under a fluorescence microscope using 10X magnification.

### 3.8.4. Fibronectin Adsorption

Cell adhesion and growth over biomaterials are strongly influenced by the adsorption and conformation of adhesive proteins from blood and extracellular matrix, such as fibronectin (FN). Specific adsorption of fibronectin was evaluated by a modified enzyme-linked immunosorbent assay (ELISA) method, as described in the literature (Kohavi et al., 2013). First, 24-well ELISA plates were coated with 250 µl of 1% Bovine serum albumin (BSA) dissolved in the PBS and incubated at 37°C for hours. An ELISA's requirement is that it must be specific for the target, and the capture antibody provides this specificity. Therefore, selecting validated antibodies that are extremely specific for the analyte is one way to achieve specificity. Fibronectin adsorption assay was performed to evaluated adherence potential of the disc. Then the BSA solution was aspirated from each well and the plate was incubated at +4°C overnight. The following day, FN solution (2.5 µg/ml in PBS, Sigma) in 550 µl was added to the alloy disks and the TiGR4 reference disks in the 24-well plate and incubated for two hours at 37°C in a 5% $CO_2$ atmosphere. After washing with PBS, the samples were blocked with 1% (w/v) BSA solution incubated for two hours at 37°C and then washed with PBS. Later, 550 µl primer monoclonal anti-fibronectin antibody (dilution 1:10000, Sigma) was added to each well overnight at 4°C for one hour, followed by washing three times with PBS. Then, 550 µl of secondary antibody (goat anti-mouse immunoglobulin G conjugated with horse radish peroxidase, dilution 1:30000, Sigma) was added and incubated at 4°C and 37°C for 30 minutes. Following the washing with PBS three times, 550 µl of stop solution, 3,3′,5,5′-Tetramethylbenzidine in 200 µg/ml (TMB for ELISA, Sigma) was added to the wells and the formation of blue colour was observed. Then 275 µl 2M $H_2SO_4$ was added to the wells. Colourimetric detection was performed by reading the absorbance of the colour intensity measured spectrophotometrically at 450 nm. The experiments were repeated in triplicate.

### 3.8.5. Plasmid-DNA Interactions (Genotoxicity)

The pBOS-$H_2$B-GFP plasmid (5.8 kb, BD Pharmingen William Saunders) was employed for the assay (grown in E-coli and purified using Machery Nagel DNA isolation kit). Each low and highly porous alloy extract was incubated with 200 ng of plasmid DNA in ddH$_2$O for 16 hours at ambient temperature (25°C) in a total reaction volume of 20 ml. The alloys and controls were electrophoresed on 1% agarose gels at 100 V for one hour using a TAE buffer. The gel was stained by using ethidium bromide. The photos of the bands were taken by the ChemiDoc imaging system (BioRad).

When uncut plasmid DNA is isolated and run on an agarose gel, plasmid DNA can exist in three conformations. These are supercoiled DNA, open-circular DNA, and linear DNA (see **Fig. 3.16**.). These bands can represent different conformations of plasmid DNA. Normally, nicked circle and supercoiled are naturally occurring. However, other DNA forms can be non-genotoxic and biosafe. How these forms will appear on the agarose gel (in terms of relative migration rates) is shown in the diagram below. In supercoiled DNA, migration of the plasmid is fastest on the agarose gel, followed by linear and nicked molecules.

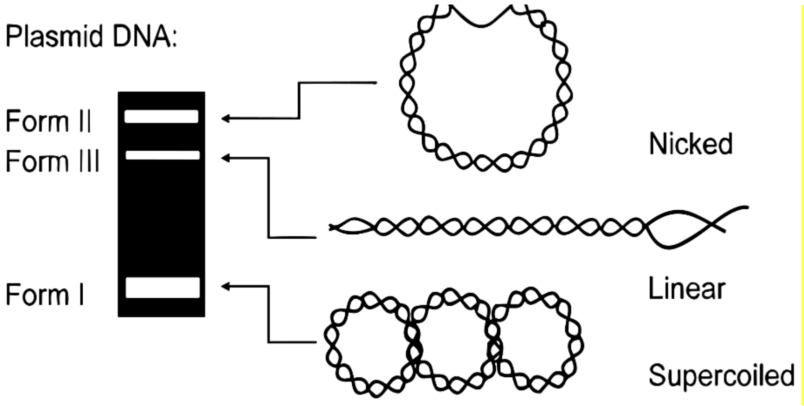

**Figure 3.16.** Different plasmid conformations (Te Riele, et al., 1986).

### 3.8.6. Morphology Observation of Cells: SEM

The morphologies of the L929 and Saos-2 cells were seeded on low and highly porous discs at a cell density of 4 x $10^5$ cells/well for one day of incubation, 2 x $10^5$ cells/well for three days, and 1 x $10^5$ cells/well for seven days into a six-well plate and incubated at 37°C and 5% $CO_2$. After each incubation period, the cells were fixed in buffered 4% formaldehyde/2.5% glutaraldehyde solution overnight for 16 hours. Alcohol of various concentrations was then added to dehydrate the sample for 10 to 15 minutes. The cell morphologies of all discs were observed by SEM (Zeiss EVO MA10).

### 3.8.7. Statistical Analysis

Statistical analysis was performed using GraphPad Prism 8.0.2 and the statistical differences were calculated using one-way ANOVA and two-way ANOVA Turkey's multiple comparisons tests. The significance of each data point (n = 3) was determined when $P < 0.05$ was considered statistically significant.

# Chapter 4. Material Characterisations

## 4.1. Results

In this chapter, the material characterisations of the Ti-xNb (x: 10, 20, and 30; at.%), Ti-20Zr (at.%) and Ti-xNb-10Zr (x: 10 and 20; at.%) alloys achieved by the powder metallurgy method combined with the space holder technique were analysed by general porosity calculations, optical microscope (OM), X-ray diffraction analysis (XRD), Energy Dispersive Spectroscopy (EDS), Scanning Electron Microscopy (SEM), and Electron Backscatter Diffraction (EBSD).

### 4.1.1. Raw Metal Powders

The low and highly porous Ti-xNb, Ti-20Zr, and Ti-xNb-10Zr alloys were fabricated from commercially pure titanium, commercially pure zirconium, and commercially pure niobium initial powders (Alfa Aesar, Germany). The purity of the titanium, niobium, and zirconium initial powders was 99%, 99.5%, and 99.5%, respectively. Ammonium bicarbonate ($NH_4HCO_3$) (Fisher, purity: 99%) was used as a space holder agent. The morphological structure and atomic compositions of the initial metal powders used in this thesis were analysed with SEM and EDS before the mixing stage; the SEM and EDS measurements are shown in **Fig. 4.1**. EDS evaluation revealed that peak of titanium, niobium, and zirconium elements were detected. This confirmed that the initial metal powders used in the experiments possessed high purity. According to SEM micrographs, average particle sizes for titanium, niobium, and zirconium initial powders specified from SEM micrographs were determined as 44 µm, 35 µm and 23 µm, respectively. Zirconium initial powder was more agglomerated than titanium and niobium initial powders due to its smaller particle size. As seen in SEM micrographs, particle shapes for titanium, niobium, and zirconium initial powders were irregular with sharp corners.

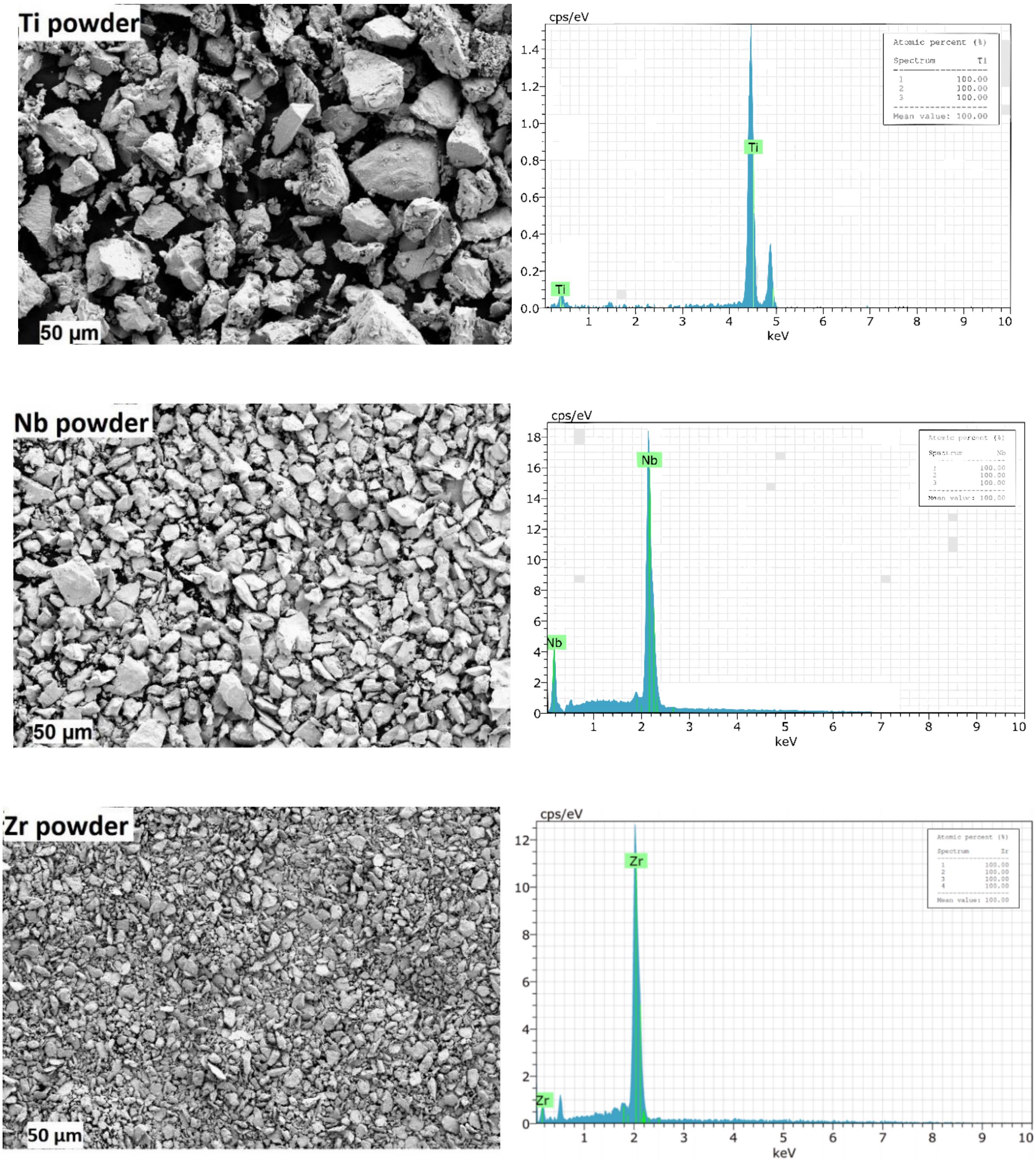

**Figure. 4.1.** SEM and EDS analysis of titanium, niobium, and zirconium initial powders.

### 4.1.2. General Porosity

The general porosity levels for Ti-xNb, Ti-20Zr and Ti-xNb-10Zr alloys were separately calculated for each alloy by using the theoretical and bulk density values. This was done three times for each alloy, and the arithmetic average of the results was recorded. Here, the porous alloys achieved had two general porosity ranges: low and highly porous categories, with porosities ranging from 20% to 29% and from 43% to 58%, respectively. The results showed some differences in general porosity of the porous alloys achieved since the sintering temperature selected in this thesis was far below the melting point of the titanium (1668°C), zirconium (1852°C) and niobium (2469°C) elements (Medvedev et al., 2016).

### 4.1.2.1. General Porosity of Binary Titanium-Niobium Alloys

Theoretical density values of the low and highly porous binary Ti-xNb alloys were calculated from the chemical composition of each alloy (see Eq. (3.2.)). The theoretical density values for binary Ti-xNb alloys with nominal niobium contents (x: 10, 20 and 30; at.%) were 4.91 g.cm$^{-3}$, 5.32 g.cm$^{-3}$, and 5.74 g.cm$^{-3}$, respectively. The bulk density values of the low and highly porous binary Ti-xNb alloys were determined from the mass-to-volume ratio (see Eq. 3.3.). The resulting bulk density values of the low porous binary Ti-xNb alloys were about 3.92 g.cm$^{-3}$ for Ti-10Nb, 3.98 g.cm$^{-3}$ for Ti-20Nb and 4.11 g.cm$^{-3}$ for Ti-30Nb, while those of the highly porous binary Ti-xNb alloys were approximately 2.21 g.cm$^{-3}$ for Ti-10Nb, 2.30 g.cm$^{-3}$ for Ti-20Nb and 2.42 g.cm$^{-3}$ for Ti-30Nb. The results are shown in **Fig. 4.2.** as a function of niobium concentration in the titanium matrix and the presence of the space holder agent.

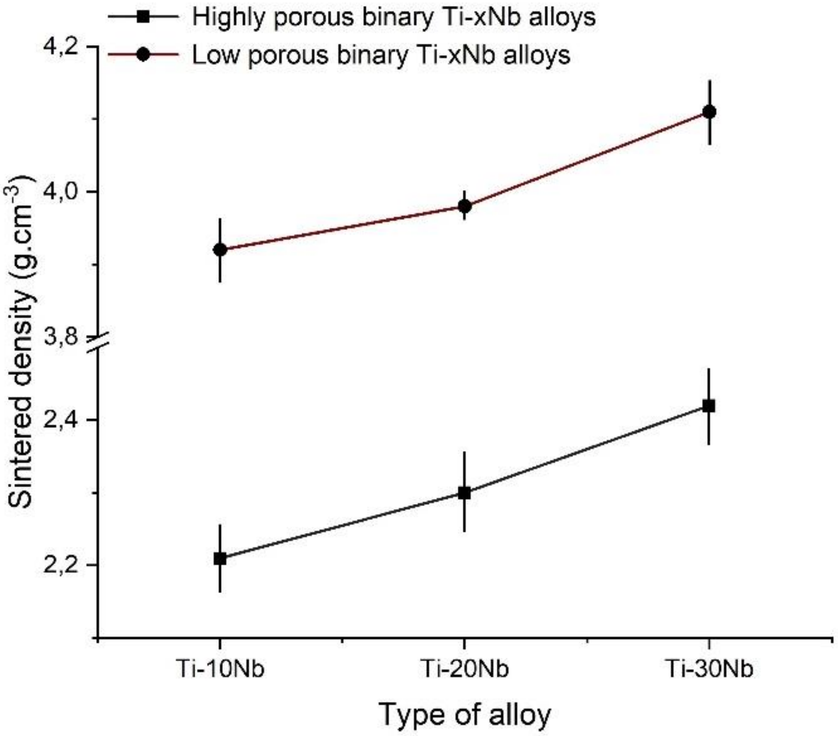

**Figure 4.2.** Sintered densities of the low and highly porous binary Ti-xNb (x: 10, 20, and 30; at.%) alloys (The error bars represent standard deviation).

The general porosity results for the low and highly porous binary Ti-xNb alloys of nominal niobium contents (x: 10, 20 and 30; at.%), separately calculated for each alloy by using the theoretical and bulk density values, are given in **Fig. 4.3**. The all-porous binary Ti-xNb alloys exhibited different general porosities depending on the niobium concentration in the titanium matrix and the presence of the space holder agent. As seen in **Fig. 4.3**, the general porosity values for the highly porous binary Ti-xNb alloys were much higher than those for the low porous binary Ti-xNb alloys. This is mainly because the space holder agent ($NH_4HCO_3$) degraded to ammonia ($NH_{3(g)}$) and carbon dioxide ($CO_{2(g)}$) when heated to 180°C and was replaced by pores in the microstructure.

On the other hand, the general porosity values slightly increased with increasing niobium content from 10 to 30 in low porous binary Ti-xNb alloys. Here, when the niobium concentration in the titanium matrix increased, the general porosity increased from 20% to 29%. The same tendency was observed in the highly porous binary Ti-xNb alloys. Accordingly, the general porosity values of highly porous binary Ti-xNb alloys were about 55% for Ti-10Nb, 56% for Ti-20Nb, and 58% for Ti-30Nb. These findings were consistent with other studies (Bidaux et al., 2013; Nagaram and Ebel, 2016; Yilmaz et al., 2018). Zhao et al. reported that the general porosity values of Ti-10Nb, Ti-16Nb, and Ti-22Nb (wt.%) alloys sintered at 1500°C were below 5% and the general porosity values of the alloys increased with increased niobium concentrations in the titanium matrix (Zhao et al., 2013).

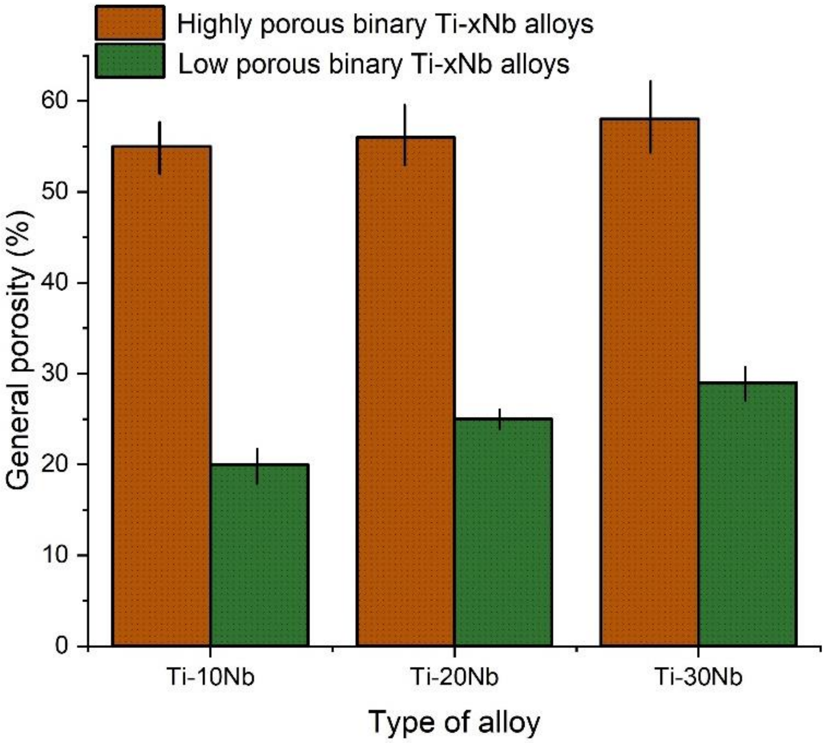

**Figure 4.3.** General porosities for the low and highly porous binary Ti-xNb (x: 10, 20 and 30; at.%) alloys (The error bars represent standard deviation).

### 4.1.2.2. General Porosity of Binary Titanium-Zirconium Alloys

For the low and highly porous binary Ti-20Zr alloys, the theoretical density and bulk density values were determined by using Eq.(3.2.) and Eq. (3.3.). Accordingly, sintered density values are shown in **Fig. 4.4**. In this regard, the theoretical densities of the low and highly porous binary Ti-20Zr alloy were identical each other due to same chemical composition, which was 4.99 g.cm$^{-3}$. The resulting bulk (sintered) density value for the low porous binary Ti-20Zr alloy was 3.87 g.cm$^{-3}$, while that of the highly porous binary Ti-20Zr alloy was 2.32 g.cm$^{-3}$.

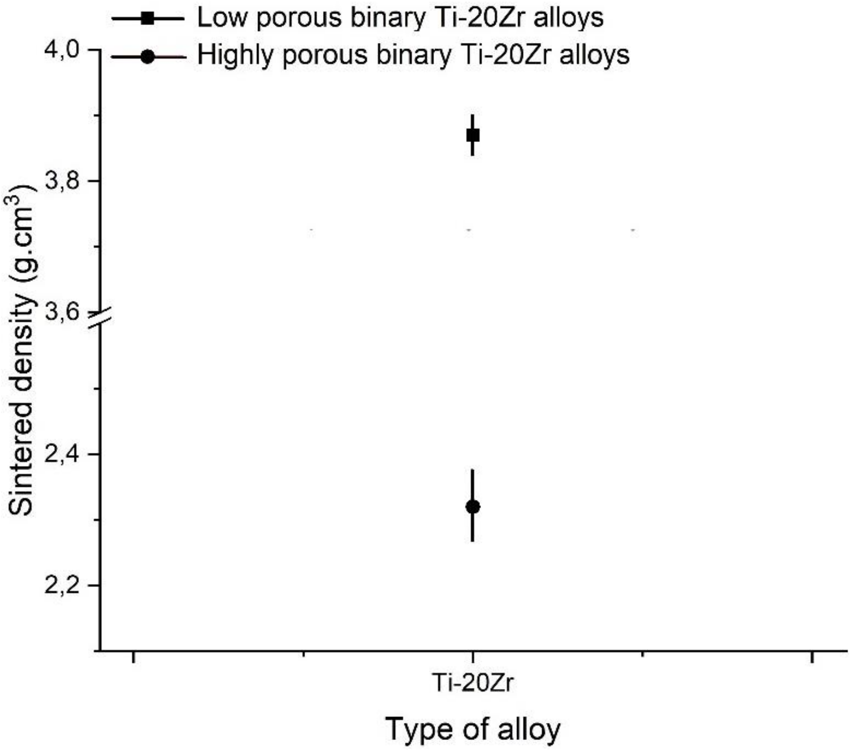

**Figure 4.4.** Sintered densities of the low and highly porous binary Ti-20Zr (at.%) alloys (The error bars represent standard deviation).

For the low and highly porous binary Ti-20Zr alloys, the results of the general porosity calculated from Eq. (3.4.) are depicted in **Fig. 4.5** as a function of the presence of the space holder agent. The highly porous binary Ti-20Zr alloy manufactured by conventional sintering procedure exhibited a general porosity ratio of 43%, while the low porous binary Ti-20Zr alloy under the same conditions showed a general porosity ratio of 22%. That is, the general porosity ratio of the highly porous binary Ti-20Zr alloy was almost two times that of the low porous binary Ti-20Zr alloy.

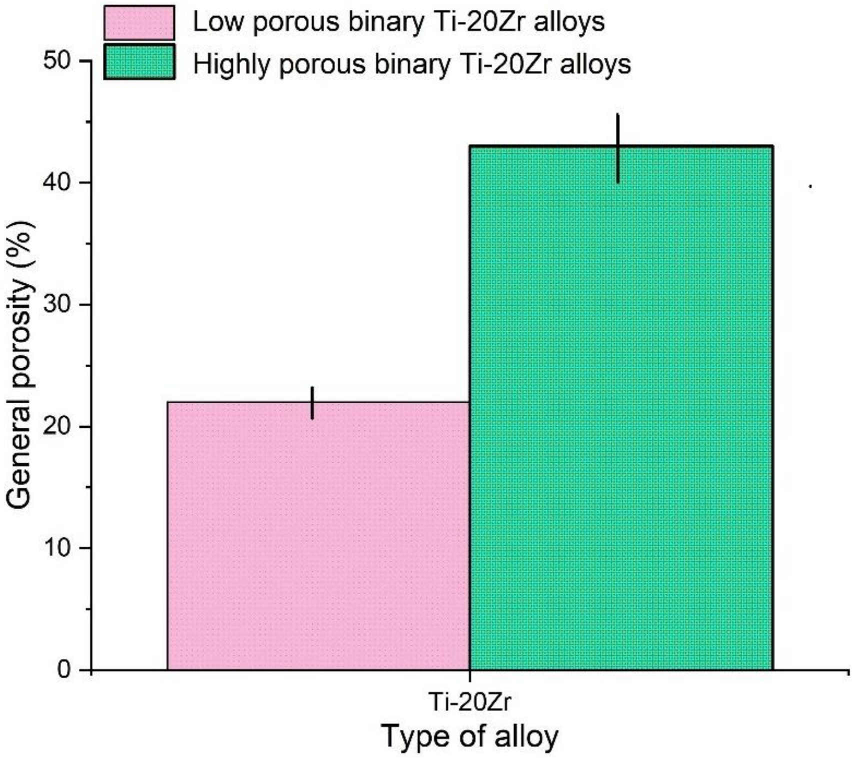

**Figure 4.5.** General porosities of the highly and low porous binary Ti-20Zr (at.%) alloys (The error bars represent standard deviation).

### 4.1.2.3. General Porosity of Ternary Titanium-Niobium-Zirconium Alloys

For the low and highly porous ternary Ti-xNb-10Zr alloys, theoretical density and bulk density values were determined by using Eq. (3.2.) and Eq. (3.3.) Accordingly, sintered density values are shown in **Fig. 4.6**. The theoretical density values of the porous ternary Ti-xNb-10Zr alloys were calculated as 5.15 g.cm$^{-3}$ for Ti-10Nb-10Zr and 5.55 g.cm$^{-3}$ for Ti-20Nb-10Zr. Moreover, the sintered density values for the low porous ternary Ti-xNb-10Zr (x:10 and 20; at.%) alloys were calculated as 4.07 g.cm$^{-3}$ and 4.17 g.cm$^{-3}$, while those for the highly porous ternary alloys were 2.5 g.cm$^{-3}$ and 2.56 g.cm$^{-3}$, respectively. The sintered density values for highly porous ternary Ti-xNb-10Zr alloys were much lower than those for low porous ternary Ti-xNb-10Zr alloys, which were consistent with general porosity ratio changes of the alloys. The bulk density and general porosity were inversely proportional to each other. When the general porosity decreased, the bulk density increased, and vice versa.

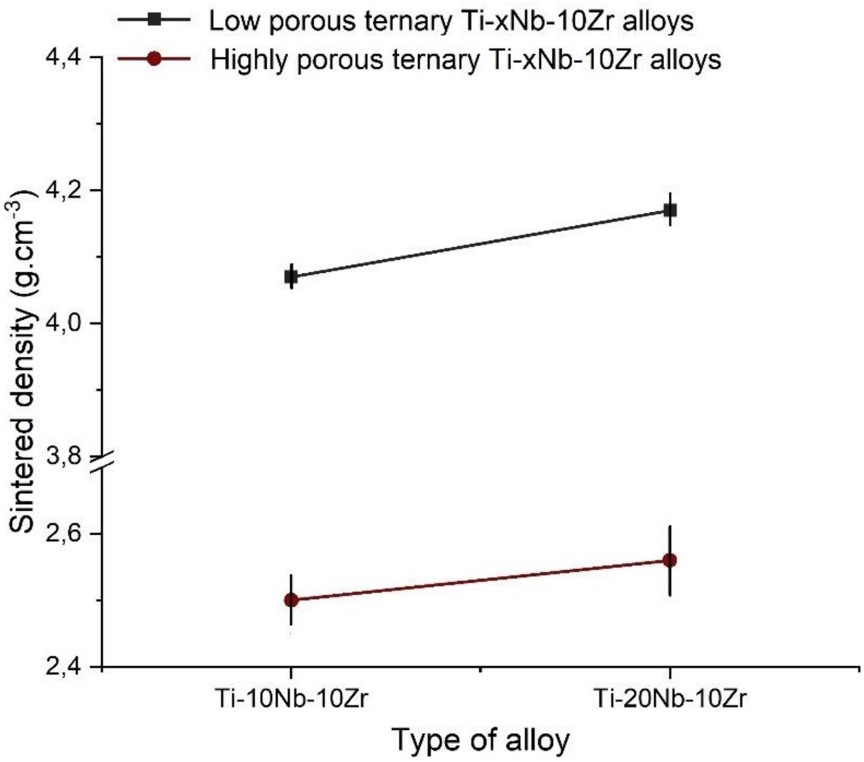

**Figure 4.6.** Sintered densities of the highly and low porous ternary Ti-xNb-10Zr (x: 10 and 20; at.%) alloys (The error bars represent standard deviation).

General porosity ratios for the low and highly porous ternary Ti-xNb-10Zr alloys are given in **Fig. 4.7.** All-porous ternary Ti-xNb-10Zr alloys exhibited differing general porosities depending on niobium concentration in the titanium matrix and presence of space holder. Accordingly, general porosity ratios for the highly porous ternary Ti-xNb-10Zr (x:10 and 20: at.%) alloys were in the range of 50% to 56%, while those for the low porous ternary alloys were 21% and 25%, respectively.

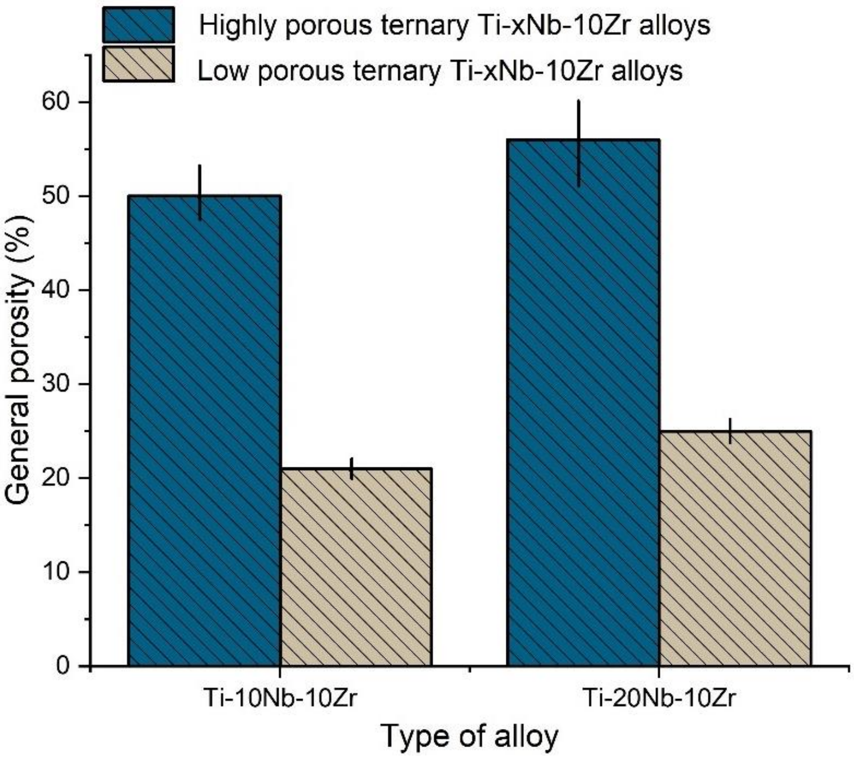

**Figure 4.7.** General porosities of the low and highly porous ternary Ti-xNb-10Zr (x: 10, and 20; at.%) alloys (The error bars represent standard deviation).

### 4.1.3. Optical Microscopy Analysis

The optical images of the low and highly porous Ti-xNb, Ti-20Zr, and Ti-xNb-10Zr alloys produced following a standard powder metallurgy route combined with the space holder technique are shown in **Figs. 4.8** to **4.12**. The black areas in optical micrographs were residual porosities and connectives, which were formed as a result of the sintering stage. Closed-pore structures were determined in the low porous alloys, while open-pore (interconnected) structures were found in the highly porous alloys. Further, pore sizes and distributions for the highly porous alloys were much higher than those for the low porous alloys, which revealed that the characteristics of pores achieved were consistent with the porosity level of the alloys. Two types of pores were observed in the alloys achieved: macro and micro pores. Connectivity between pores in the low porous alloys was achieved with micropores, while in the highly porous alloys, it was achieved with macropores. Macro pores were formed by the evaporation of the space holder agent ($NH_4HCO_3$) during the sintering stage, which remarkably increased the general porosity values. Therefore, the added space holder agent provided a marked increase in pore diameter and connectivity. On the other hand, micropores could be due to insufficient sintering procedures. The sintering temperature selected in this thesis (1200˚C) did not eliminate the micro pore formations since the distance of the diffusivity between particles was too high (Slokar et al., 2019).

The microstructural evaluation revealed that small and irregular pores located on the walls were observed in all-low porous alloys, while large and interconnected open pores were found in all-highly porous alloys. This is essential to expand the cell adhesion for bone ingrowth, resulting in a stronger bond between bone and implant.

#### 4.1.3.1. Optical Images of Binary Titanium-Niobium Alloys

The morphological characteristics of the low and highly porous binary Ti-xNb alloys sintered at 1200°C for six hours were analysed with the optical microscope. Their microstructures are presented in **Fig. 4.8** and **Fig. 4.9**. Median pore diameter values for the low porous binary Ti-xNb (x:10, 20 and 30; at.%) alloys sintered at 1200 ˚C specified on their optical micrographs were about 64 µm, 75 µm, and 83 µm, while those for the highly porous binary alloys sintered under the same conditions were about 116 µm, 124 µm, and 132 µm, respectively. The pore diameters of the low porous binary Ti-xNb alloys were thus much lower than those of the highly porous binary Ti-xNb alloys. On the other hand, not only highly porous binary Ti-xNb alloys but also the low porous binary Ti-xNb alloys were favourable for bone ingrowth and body fluid transport. The low and highly porous binary Ti-xNb alloys studied in this thesis were suitable for use as orthopaedic biomaterials in terms of pore size for allowing bone ingrowth and blood transportation.

In addition, primary niobium phases (bright white areas) were observed on the low and highly porous binary Ti-xNb alloys. Depending on niobium concentration in titanium matrix, higher niobium concentration slightly led to thinner grain α-Ti phase (white areas). Additionally, volume fraction of β-Ti phase increased according to increased niobium concentration in titanium matrix.

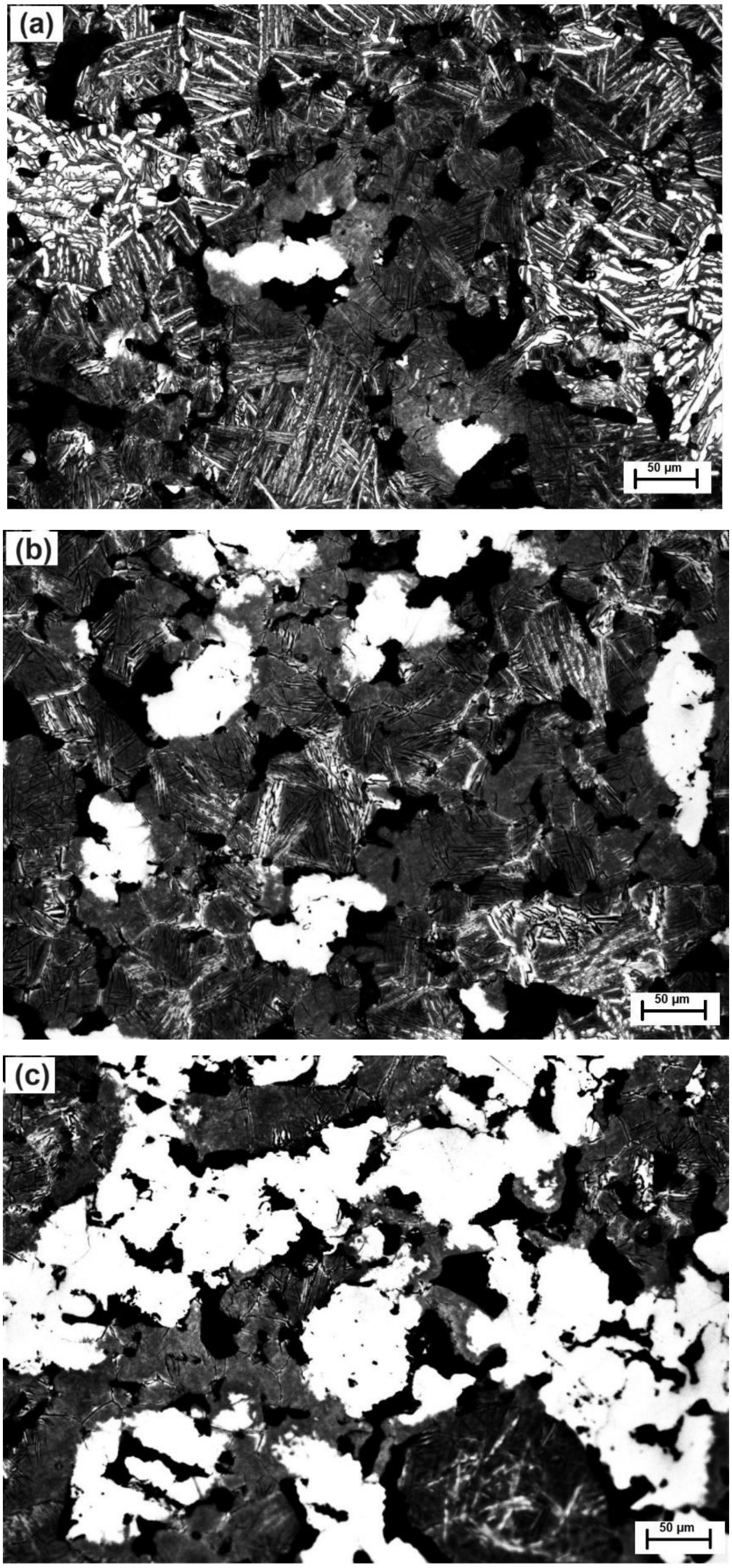

**Figure 4.8.** Optical micrographs of the low porous binary Ti-xNb alloys (a: Ti-10Nb, b: Ti-20Nb, c: Ti-30Nb).

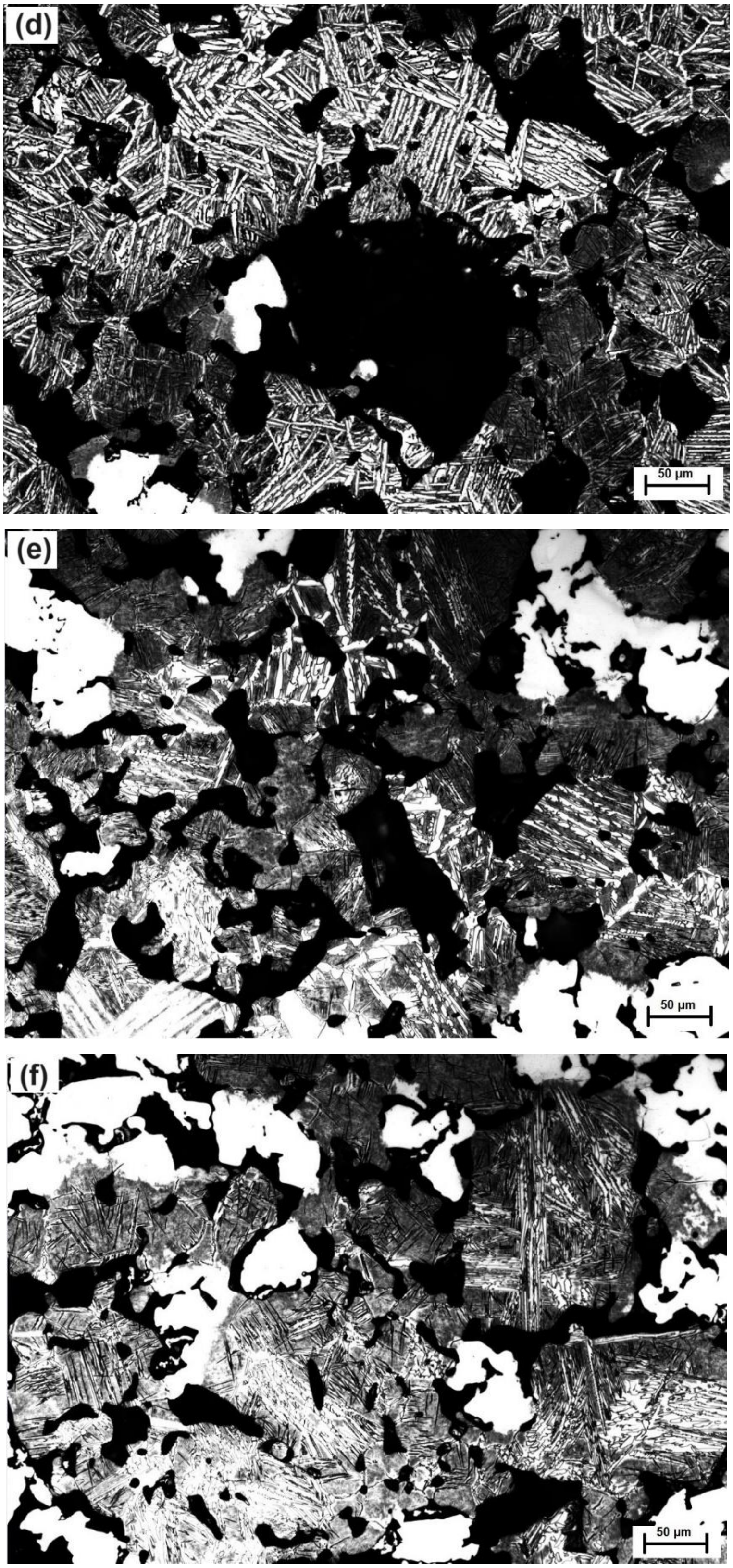

**Figure 4.9.** Optical micrographs of the highly porous binary Ti-xNb alloys (d: Ti-10Nb + 20SH, e: Ti-20Nb + 20SH, f: Ti-30Nb + 20SH).

### 4.1.3.2. Optical Images of Binary Titanium-Zirconium Alloys

The optical images of the low and highly porous binary Ti-20Zr alloys sintered at 1200°C for six hours are given in **Fig. 4.10**. The mean pore sizes for the low and highly porous binary Ti-20Zr alloys were about 78 µm, 121 µm, respectively. As foreseen and as shown in the optical images, a considerable increase in pore size and its connectivity in highly porous binary Ti-20Zr alloys occurred with the addition of a space holder, which was a desirable feature for cell proliferation. Pore size values for the low and highly porous Ti-20Zr alloys produced in this thesis had adequate pore sizes for bone ingrowth when implanted. On the other hand, adding space holder did not affect the phase structure and grain size of the low and highly binary porous Ti-20Zr alloys.

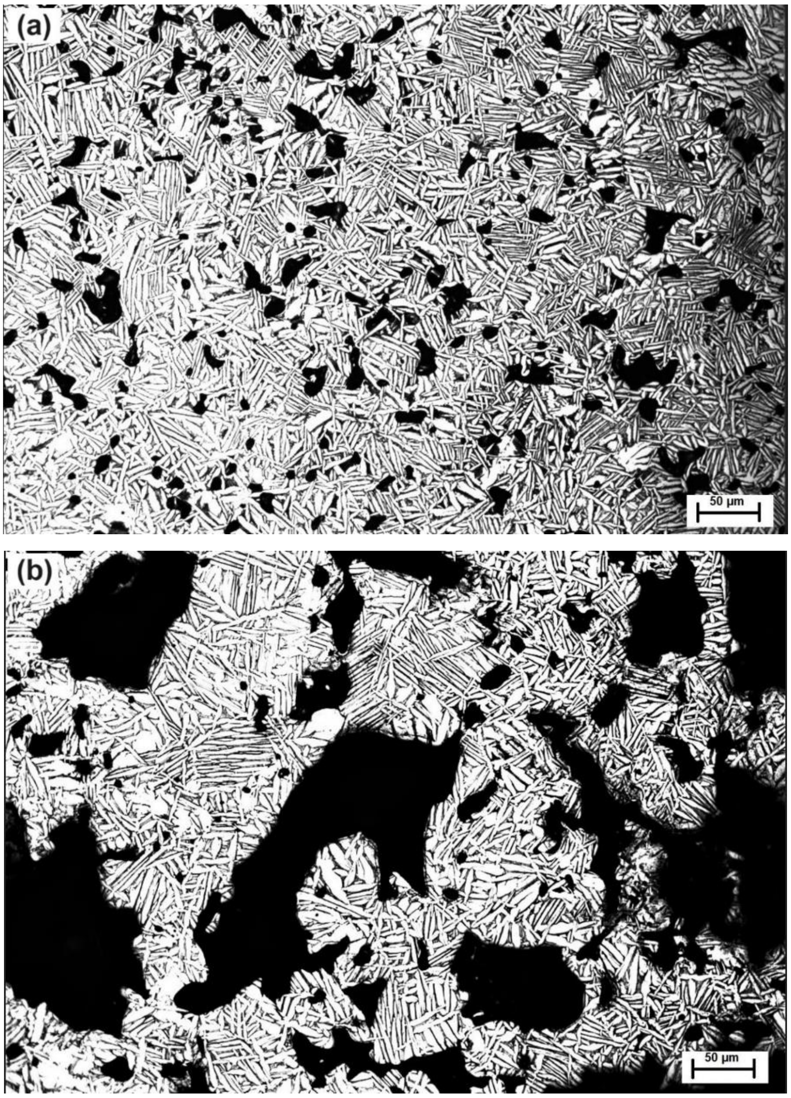

**Figure 4.10.** Optical micrographs of the low and highly porous binary Ti-20Zr (at.%) alloys (a: Ti-20Zr, b: Ti-20Zr + 20SH).

#### 4.1.3.3. Optical Images of Ternary Titanium-Zirconium-Niobium Alloys

The microstructures of the low and highly porous ternary Ti-xNb-10Zr alloys sintered at 1200°C for six hours are shown in **Figs. 4.11** and **4.12**. Optical images of the alloys showing the pore morphology and distribution were evaluated to estimate the average pore size. In this regard, average pore sizes of the low and highly porous ternary Ti-xNb-10Zr (x:10, and 20; at.%) alloys increased from 67 μm to 117 μm and 82 μm to 143 μm, respectively, as a consequence of the solid-state sintering. The results revealed that adding a space holder increased the maximum pore size and distribution in the microstructures. Rao et al. confirmed this finding. They stated that in Ti-20Nb-15Zr and Ti-35Nb-15Zr (wt.%) alloys produced by a two-step foaming powder metallurgy method, there was a substantial increase in the average pore size from 8.4 μm to 57.2 μm, 71.5 μm, and 88.9 μm with the addition of a 20%, 35%, and 50 wt. % space holder agents, respectively (Rao et al., 2014). Lastly, the pore sizes for the low and highly porous ternary Ti-xNb-10Zr alloys were compatible with the pore sizes for implantable devices to accelerate osteoblast aggregation for bone ingrowth. On the other hand, the microstructure of low and highly porous ternary Ti-xNb-10Zr alloys primarily consists of a combination of α-Ti, β-Ti, and primary niobium phases. The specific phase composition was sensitive to niobium concentration.

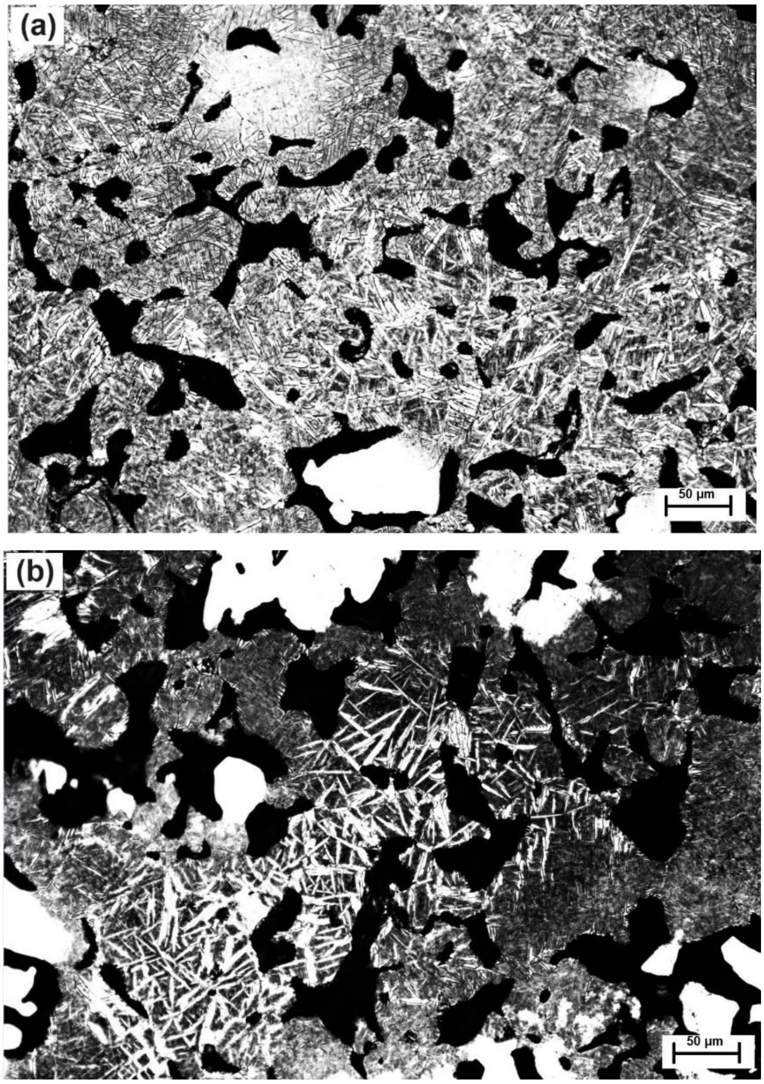

**Figure 4.11.** Optical micrographs of the low porous ternary Ti-xNb-10Zr alloys (a: Ti-10Nb-10Zr, b: Ti-20Nb-10Zr).

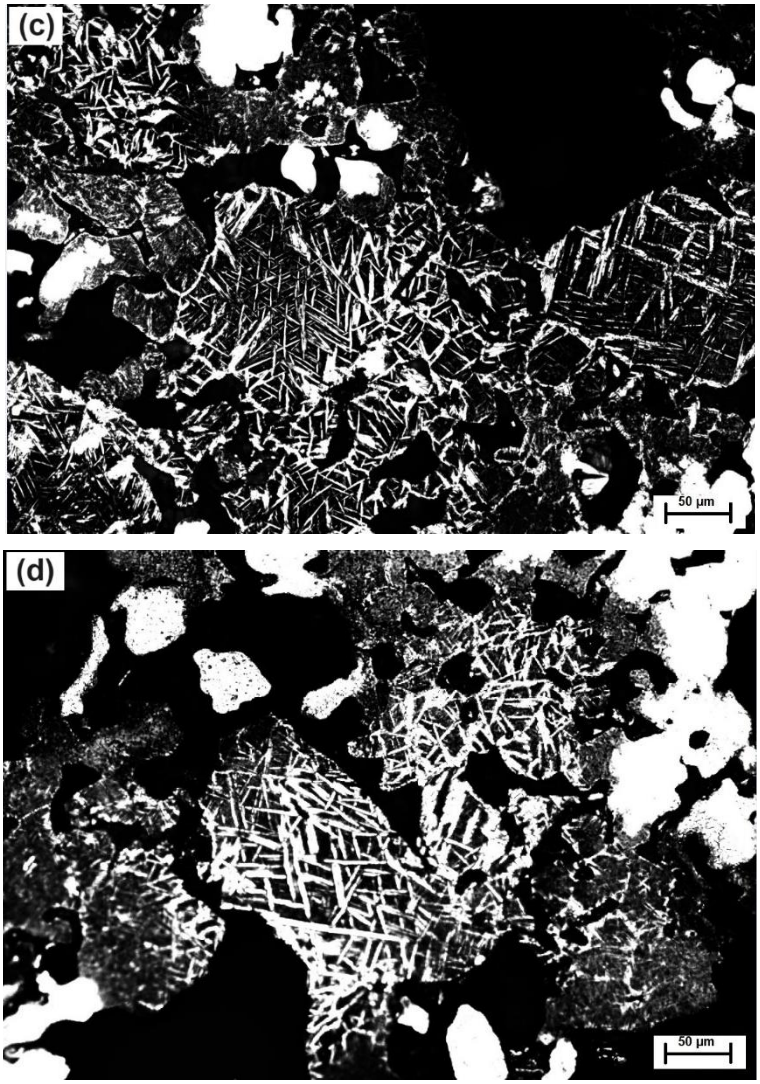

**Figure 4.12.** Optical micrographs of the highly porous ternary Ti-xNb-10Zr alloys (c: Ti-10Nb-10Zr + 20SH, d: Ti-20Nb-10Zr + 20SH).

#### 4.1.4. X-Ray Diffraction Analysis

The XRD spectra of the low and highly porous Ti-xNb (x:10, and 30; at.%), Ti-20Zr (at.%) and Ti-xNb-10Zr (x:10 and 20; at.%) alloys produced following standard powder metallurgy combined with space holder technique appear in **Figs. 4.13** to **4.15**.

##### 4.1.4.1. X-Ray Diffraction of Binary Titanium-Niobium Alloys

The XRD spectra of the low and highly porous binary Ti-10Nb and Ti-30Nb alloys sintered at 1200°C for six hours are presented in **Fig. 4.13**. The results revealed the coexistence of the hcp α-Ti (ICDD PDF No. 00-044-1294) and bcc β-Ti (ICDD PDF No. 00-044-1288) related to the titanium phases and the niobium primary phase. No other obvious impurity peak, such as oxide, hydride, or intermetallic compounds, was detected. The major phase for the low porous binary Ti-10Nb alloy was the hcp α-Ti phase. After adding 30% niobium, the major phase became the bcc β-Ti phase in the microstructure. An increase in niobium concentration in the low porous binary Ti-30Nb alloy depressed hcp α-Ti phase formation, resulting in the α-Ti phase peak gradually diminishing (Ho et al., 2008). Such behaviour was related to the dissolution of niobium in the titanium matrix. Higher niobium dissolution in the titanium matrix stimulates the transformations from the α-Ti to the β-Ti. The same was observed in the highly porous binary Ti-30Nb alloy.

The phase structure of the highly porous binary Ti-10Nb and Ti-30Nb alloys was almost identical to that of the low porous alloys. However, the intensities of solute diffraction peaks of highly porous binary Ti-10Nb and Ti-30Nb alloys decreased with increasing general porosity. The sintering phenomenon is physically based on diffusion, and adding a space holder agent to titanium-niobium mixtures may hinder the transformation of the β-Ti phase in the microstructure since a space holder agent surrounding niobium and titanium particles increased in the diffusion pathways between particles, which caused a reduction in the diffraction peak intensity of the β-Ti and α-Ti phases in the highly porous binary Ti-10Nb and Ti-30Nb alloys (Prakash et al., 2020).

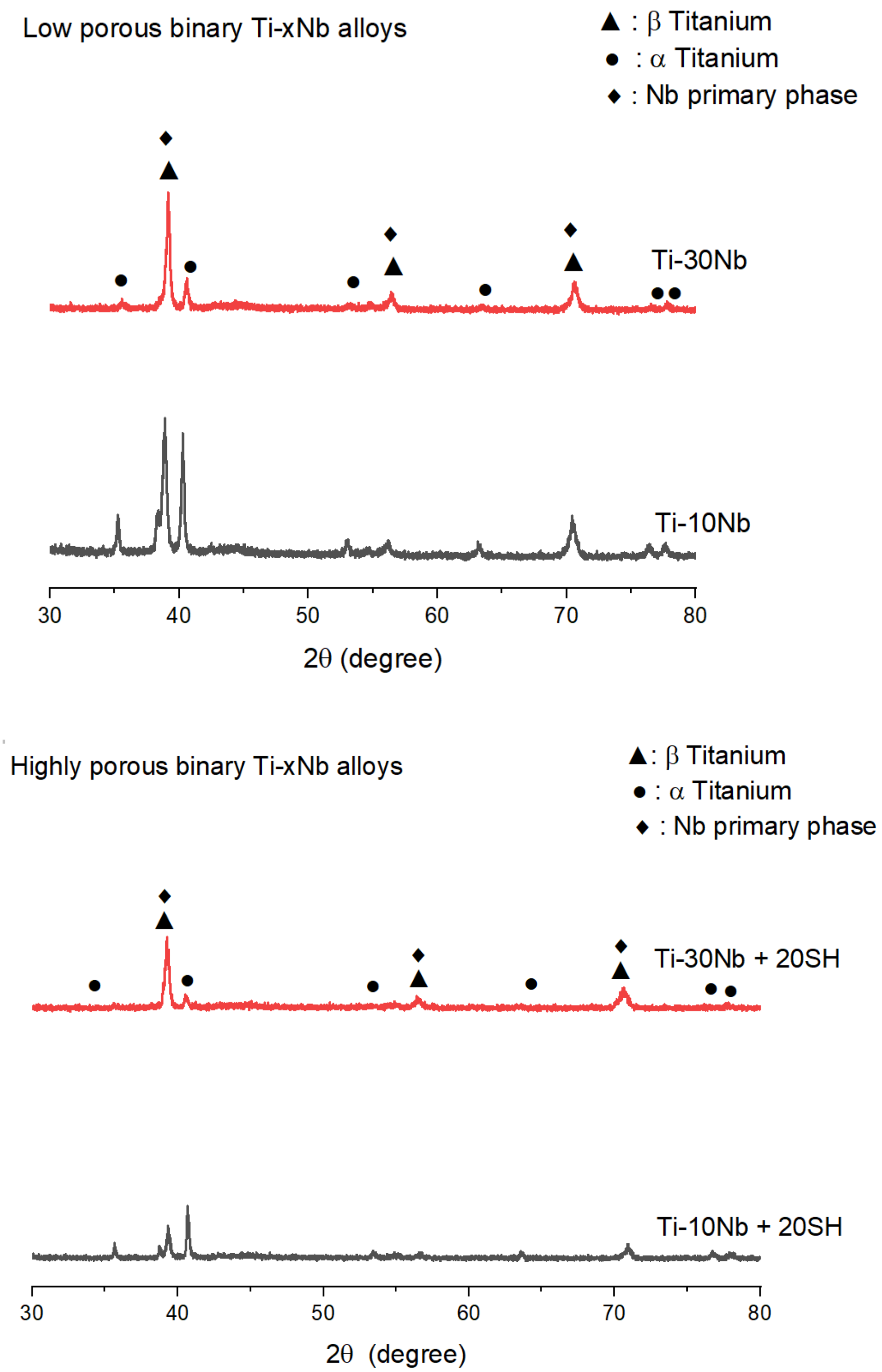

**Figure 4.13.** XRD spectra for the low and highly porous binary Ti-10Nb and Ti-30Nb (at.%) alloys.

### 4.1.4.2. X-Ray Diffraction of Binary Titanium-Zirconium Alloys

The XRD spectra of the low and highly porous binary Ti-20Zr alloys sintered at 1200°C for six hours are shown in **Fig. 4.14**. All the diffraction peaks were properly matched with the predominant hcp α-Ti (ICDD PDF No. 00-044-1294) phase and some distorted hcp α'-Ti (ICDD PDF 00–044-1294) phases. No bcc β-Ti, hcp ω-Ti or other intermetallic compound related to titanium phases or pure zirconium was found in any of the recorded XRD patterns of the low and highly porous binary Ti-20Zr alloys. The titanium-zirconium equilibrium phase diagram demonstrated that zirconium exhibited a completely solid solution in the titanium matrix (α-Ti phase) (Cacciamani et al., 2011). This explains why the α-Ti and the α'-Ti phases were detected in microstructures of the low and highly porous binary Ti-20Zr alloys (Rao et al., 2014). According to this concept, the distorted α'-Ti phase was detected as completely dissolved zirconium in the titanium matrix. This caused stress in the lattice structure of the hcp α-Ti phase because the difference in atomic radius between the titanium (1.47 Å) and zirconium (1.6 Å) atoms generated stress in the lattice parameters of the hcp α-Ti phases (Ho et al., 2008). Thus, the individual presence of zirconium in the titanium matrix did not dramatically alter the crystalline structure (formation of β-Ti phase) (Wang et al., 2009).

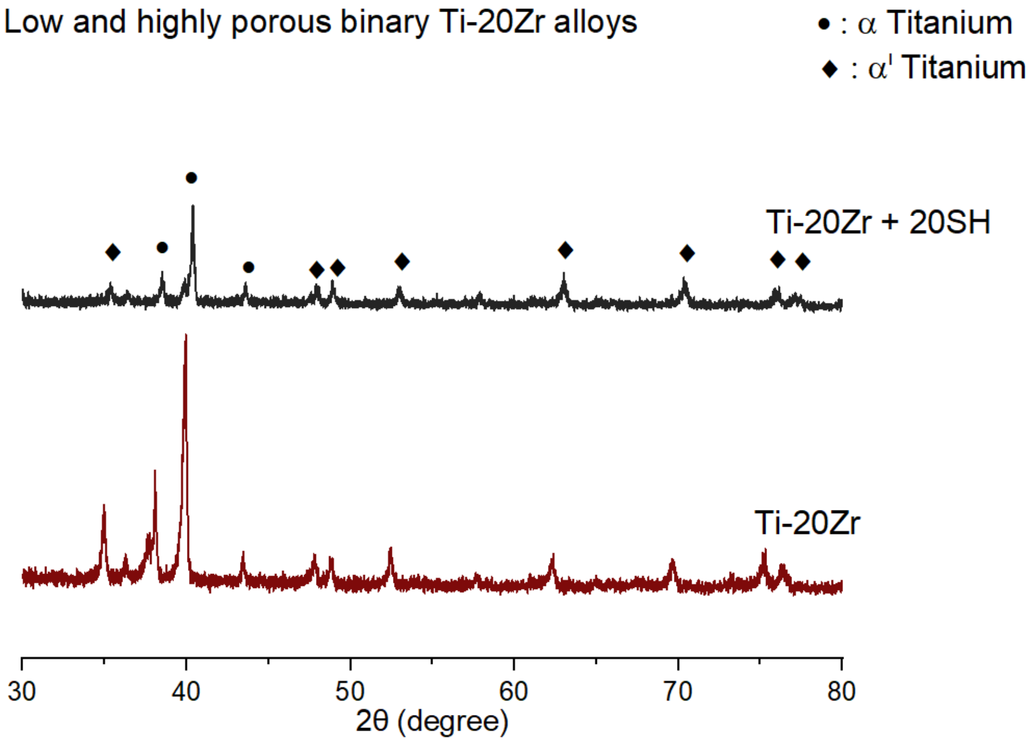

**Figure 4.14.** XRD spectra of the low and highly porous binary Ti-20Zr (at.%) alloys.

### 4.1.4.3. X-Ray Diffraction of Ternary Titanium-Niobium-Zirconium Alloys

The XRD spectra of the low and highly porous ternary Ti-10Nb-10Zr and Ti-20Nb-10Zr alloys sintered at 1200°C for six hours are presented in **Fig. 4.15**. Detailed examination of the XRD results to understand the phase structure showed that predominantly the bcc β-Ti (ICDD PDF No. 00-044-1288) phases with some hcp α-Ti (ICDD PDF No. 00-044-1294) phases and the niobium primary phase were detected in the low and highly porous ternary Ti-10Nb-10Zr and Ti-20Nb-10Zr alloys achieved. The XRD results showed that alloying with both niobium (a strong β-Ti stabiliser) and zirconium (a weak β-Ti stabiliser or neutral element) reduced the proportion of the α-Ti phase in the microstructure. Therefore, the formation of the β-Ti phase generally increased with increases in the niobium and zirconium concentrations in the low and highly porous ternary Ti-10Nb-10Zr and Ti-20Nb-10Zr alloys (Geetha et al., 2004).

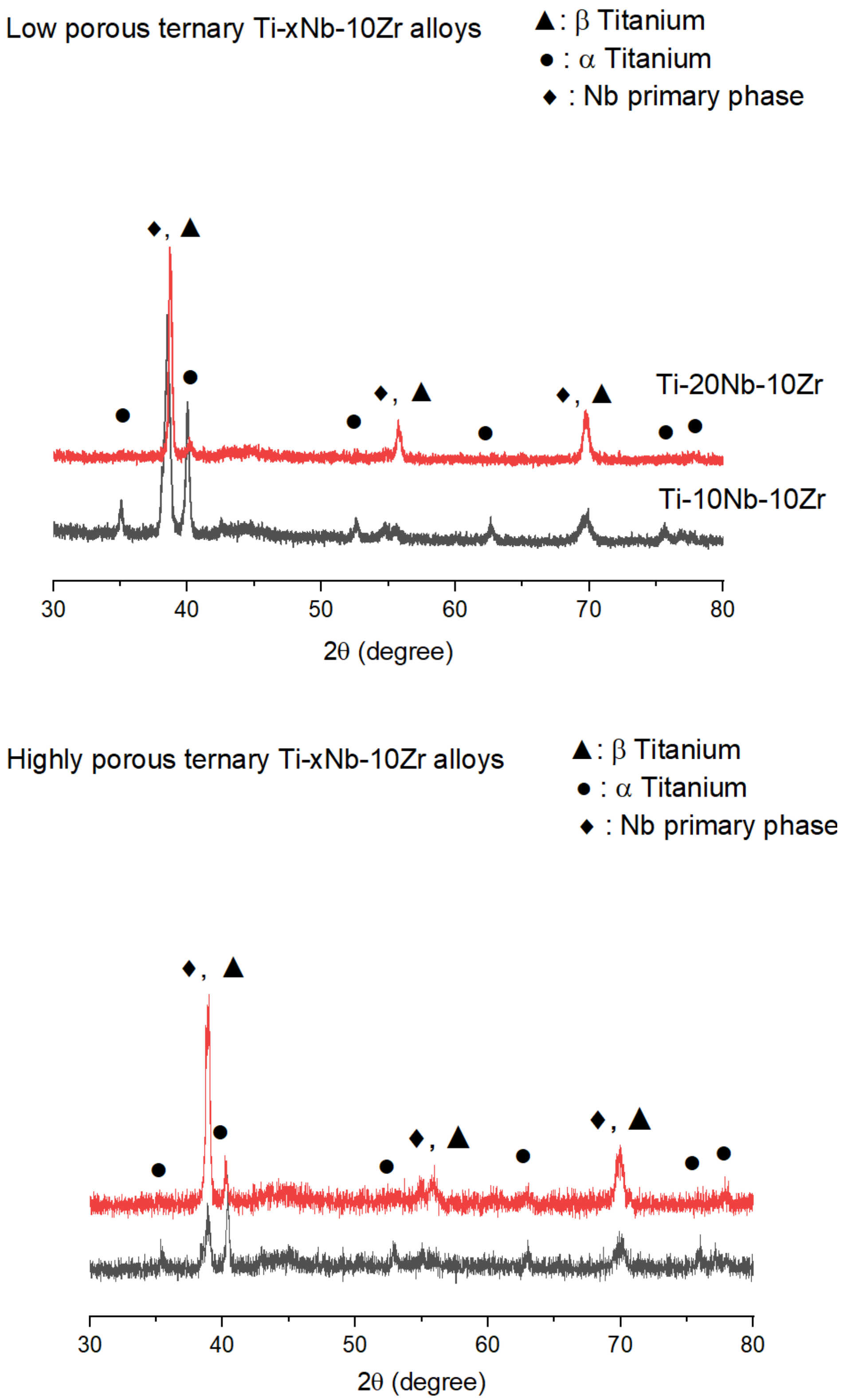

**Figure 4.15.** XRD spectra of the low and highly porous ternary Ti-10Nb-10Zr and Ti-20Nb-10Zr (at.%) alloys.

### 4.1.5. Energy Dispersive Spectroscopy Analysis

EDS analysis showing SEM micrograph and individual EDS points for the low and highly porous Ti-xNb (x:10, 20 and 30; at.%), Ti-20Zr (at.%) and Ti-xNb-10Zr (x: 10 and 20; at.%) alloys produced following a standard powder metallurgy route combined with the space holder technique are given in **Figs. 4.16** to **4.18**. The EDS results showed that significant alterations were observed in terms of titanium, zirconium, and niobium concentrations during the sintering stage as the sintering process led to phase transformations within the alloys. Peaks for the low and highly porous alloys were comprised of Ti-Kβ, Ti-Kα and Nb-L. No other peak belonging to an undesirable element was found. Further, no oxidation was observed in the all-porous alloys studied.

#### 4.1.5.1. EDS Analysis of Titanium-Niobium Binary Alloys

The atomic compositions of the low and highly porous binary Ti-xNb alloys were detected. EDS summary of the low and highly porous binary Ti-xNb alloys (x: 10, 20, and 30; at. %) is shown in **Table 4.1**. EDS analysis showing SEM micrograph and individual EDS points is shown in **Fig. 4.16**. The atomic compositions of areas selected (1 to 3) for the low porous binary Ti-10Nb alloy sintered at 1200°C for six hours were Ti-87Nb (at. %), Ti-6.71Nb (at.%) and Ti-1.64Nb (at.%), while the atomic compositions of the areas selected (1 to 3) for the highly porous binary Ti-10Nb alloy were Ti-86.28Nb (at.%), Ti-5.86Nb (at.%) and Ti-1.74Nb (at.%), respectively. The low and highly porous binary Ti-10Nb alloy had partly bright-white areas corresponding to almost primary niobium, as seen in the EDS results. The atomic compositions of the areas selected (1 to 3) for the low porous binary Ti-20Nb alloy were 100Nb (at.%), Ti-12.67Nb (at.%) and Ti-20.88Nb (at.%), while those for the highly porous binary Ti-20Nb alloy were Ti-99.96Nb (at.%), Ti-16.18Nb (at.%) and Ti-2.97Nb (at.%), respectively. The atomic compositions of the areas selected (1 to 3) for the low porous binary Ti-30Nb alloy were Ti-99.80Nb (at.%), Ti-19.76Nb (at.%) and Ti-3.52Nb (at.%), while those for the highly porous binary Ti-30Nb alloy were Ti-98.89Nb (at.%), Ti-18.98Nb (at.%) and Ti-2.6Nb (at.%), respectively. As seen in the SEM micrographs of the low and highly porous binary Ti-xNb alloys showing EDS points, the α-Ti and the β-Ti phases were irregularly dispersed in the microstructure, caused by the inhomogeneity of powder metallurgy production method.

The EDS results revealed that the α-Ti phase corresponding to the dark-grey areas exhibited extremely limited dissolution of niobium, whereas the β-Ti phase corresponding to the light-grey areas had a good dissolution of niobium in the titanium matrix (Romero-Resendiz et al., 2023). Han et al. (2015). confirmed this result. With the increase of niobium (a strong β-Ti stabiliser) content in titanium-niobium mixtures, the volume fraction of the light-grey (β-Ti phase) areas also increased in the microstructures, which was seen in the XRD results of this thesis (Nazari et al., 2015; Yılmaz et al., 2017).

**Table 4.1.** EDS summary of the low and highly porous binary Ti-xNb alloys (x: 10, 20, and 30; at. %).

| | **Area 1 (at. %)** | | **Area 2 (at. %)** | | **Area 3 (at. %)** | |
|---|---|---|---|---|---|---|
| **Alloys** | **Ti** | **Nb** | **Ti** | **Nb** | **Ti** | **Nb** |
| **Ti-10Nb** | 13 | 87 | 93.29 | 6.71 | 98.36 | 1.64 |
| **Ti-20Nb** | - | 100 | 87.33 | 12.67 | 79.12 | 20.88 |
| **Ti-30Nb** | 0.2 | 99.80 | 80.24 | 19.76 | 96.48 | 3.52 |
| **Ti-10Nb + 20SH** | 13.72 | 86.28 | 94.14 | 5.86 | 98.26 | 1.74 |
| **Ti-20Nb + 20SH** | 0.04 | 99.96 | 83.82 | 16.18 | 97.03 | 2.97 |
| **Ti-30Nb + 20SH** | 1.11 | 98.89 | 81.02 | 18.98 | 97.4 | 2.6 |

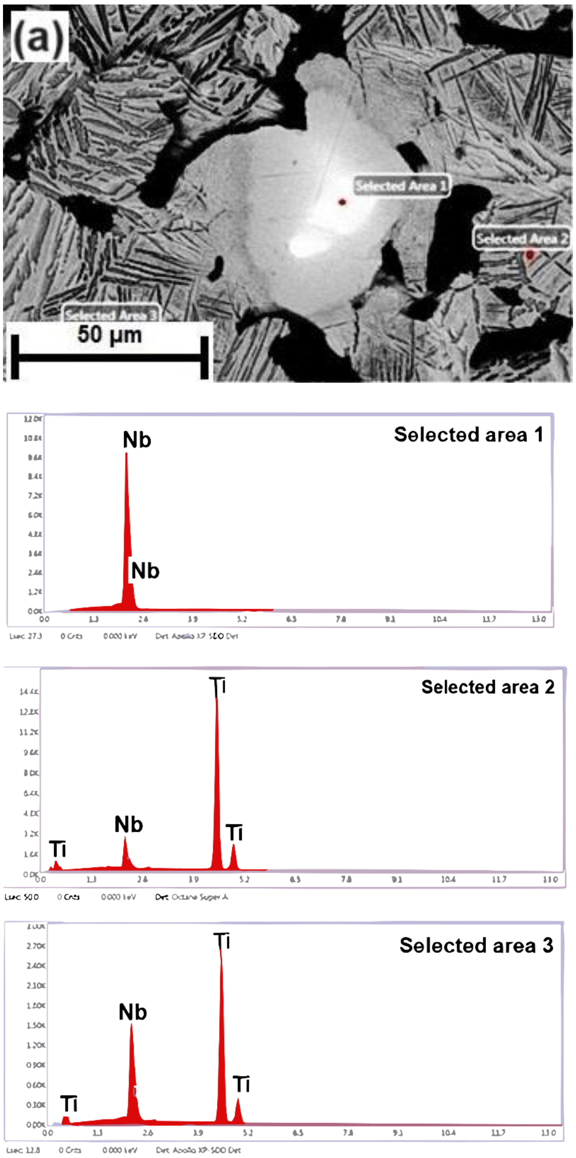
(a)
Selected Area 1
Selected Area 2
Selected Area 3
50 µm
Nb
Nb
Selected area 1
Ti
Nb
Ti
Ti
Selected area 2
Ti
Nb
Ti
Ti
Selected area 3
0.0
1.3
2.6
3.9
5.2
6.5
7.8
9.1
10.4
11.7
13.0

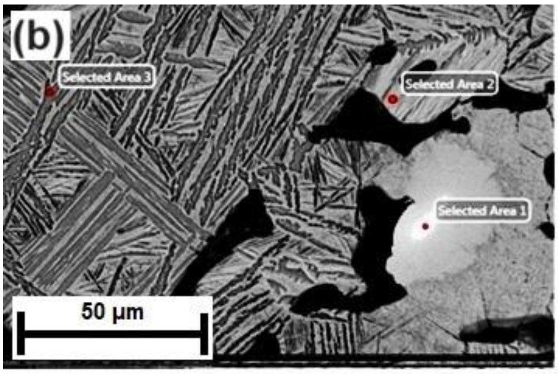
(b)
Selected Area 3
Selected Area 2
Selected Area 1
50 µm

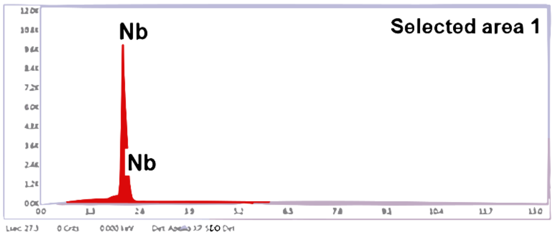
Selected area 1
Nb
Nb
12.0K
10.8K
9.6K
8.4K
7.2K
6.0K
4.8K
3.6K
2.4K
1.2K
0.0K
0.0
1.3
2.6
3.9
5.2
6.5
7.8
9.1
10.4
11.7
13.0
Lsec: 27.3
0 Cnts
0.000 keV
Det: Apollo XP SDD Det

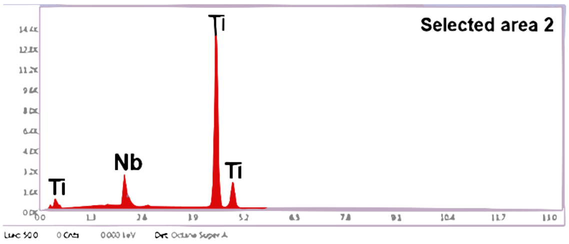
Selected area 2
Ti
Nb
Ti
Ti
14.4K
12.8K
11.2K
9.6K
8.0K
6.4K
4.8K
3.2K
1.6K
0.0K
0.0
1.3
2.6
3.9
5.2
6.5
7.8
9.1
10.4
11.7
13.0
Lsec: 50.0
0 Cnts
0.000 keV
Det: Octane Super A

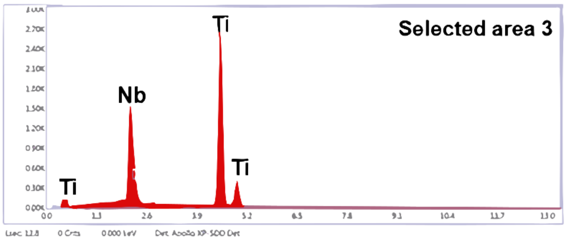
Selected area 3
Ti
Nb
Ti
Ti
2.70K
2.40K
2.10K
1.80K
1.50K
1.20K
0.90K
0.60K
0.30K
0.00K
0.0
1.3
2.6
3.9
5.2
6.5
7.8
9.1
10.4
11.7
13.0
Lsec: 12.8
0 Cnts
0.000 keV
Det: Apollo XP-SDD Det

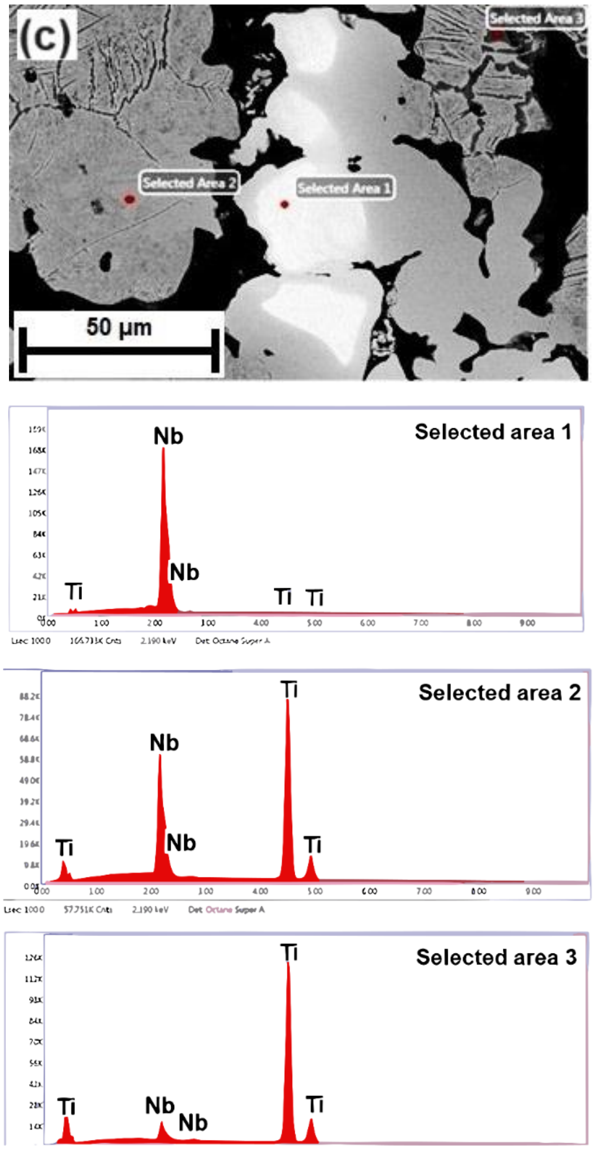
(c)
Selected Area 3
Selected Area 2
Selected Area 1
50 µm
Nb
Selected area 1
Nb
Ti
Ti
Ti
0.00
1.00
2.00
3.00
4.00
5.00
6.00
7.00
8.00
9.00
Lsec: 100.0
106.731K Cnts
2.190 keV
Det: Octane Super A
Ti
Selected area 2
Nb
Ti
Nb
Ti
0.00
1.00
2.00
3.00
4.00
5.00
6.00
7.00
8.00
9.00
Lsec: 100.0
57.751K Cnts
2.190 keV
Det: Octane Super A
Ti
Selected area 3
Ti
Nb
Nb
Ti

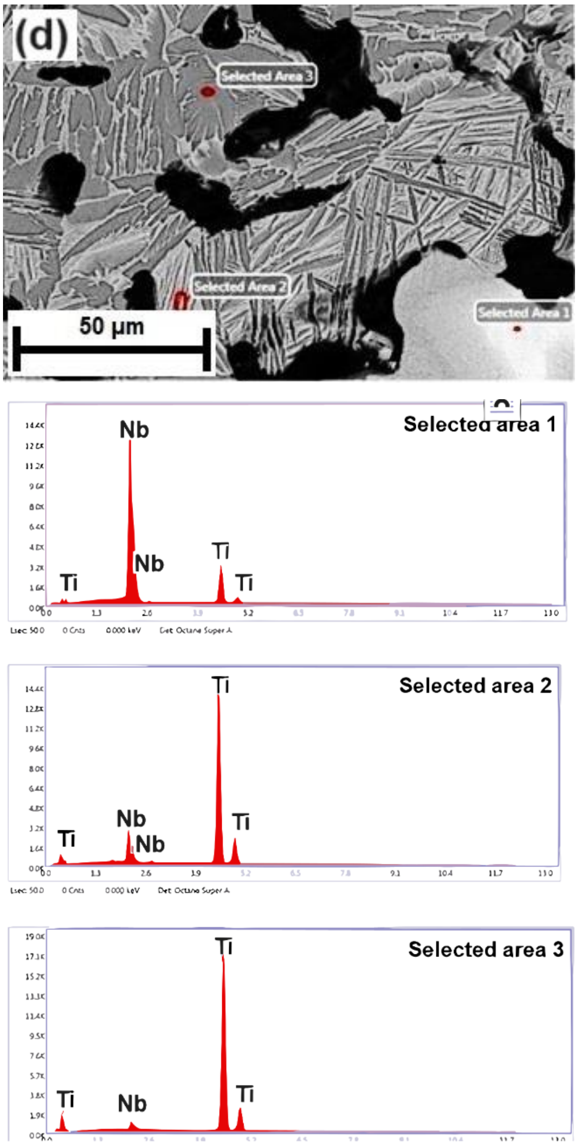
(d)
Selected Area 3
Selected Area 2
Selected Area 1
50 µm
Selected area 1
Nb
Nb
Ti
Ti
Ti
14.4K
12.8K
11.2K
9.6K
8.0K
6.4K
4.8K
3.2K
1.6K
0.0
0.0
1.3
2.6
3.9
5.2
6.5
7.8
9.1
10.4
11.7
13.0
Lsec: 50.0
0 Cnts
0.000 keV
Det: Octane Super A
Selected area 2
Ti
Nb
Nb
Ti
Ti
Selected area 3
Ti
Ti
Nb
Ti
19.0K
17.1K
15.2K
13.3K
11.4K
9.5K
7.6K
5.7K
3.8K
1.9K
0.0

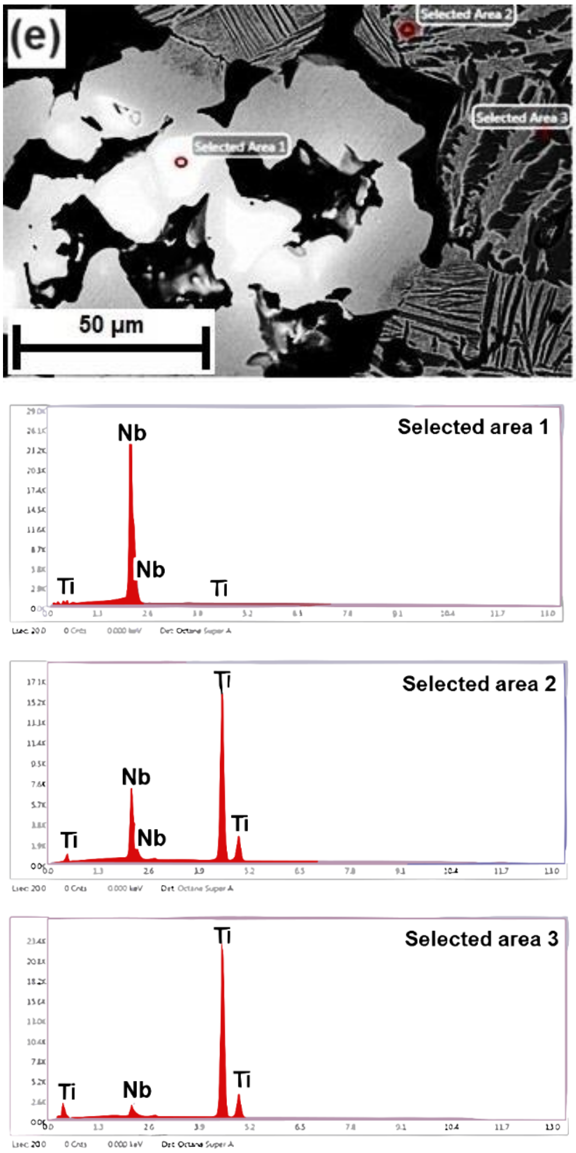
(e)
Selected Area 1
Selected Area 2
Selected Area 3
50 µm
Selected area 1
Nb
Nb
Ti
Ti
Selected area 2
Ti
Nb
Ti
Nb
Ti
Selected area 3
Ti
Ti
Nb
Ti

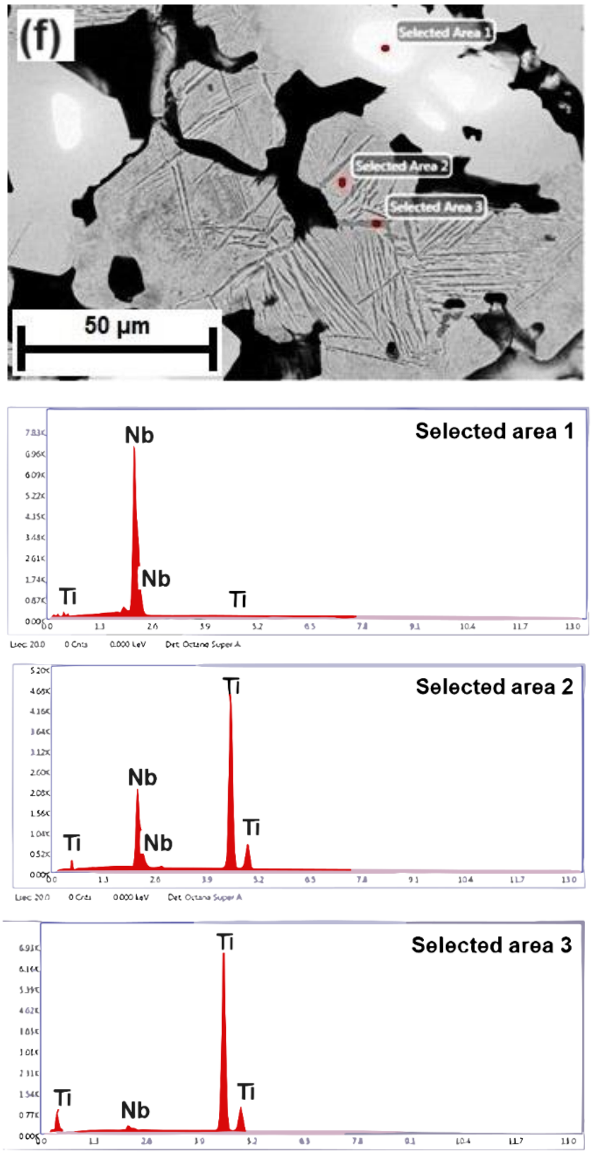

**Figure 4.16.** EDS analysis showing SEM micrograph and individual EDS points for low and highly porous binary Ti-xNb alloys (a: Ti-10Nb, b: Ti-20Nb, c: Ti-30Nb, d: Ti-10Nb + 20SH, e: Ti-20Nb + 20SH, f: Ti-30Nb + 20SH).

### 4.1.5.2. EDS Analysis of Binary Titanium-Zirconium Alloys

The EDS analysis showing SEM micrograph and individual EDS points for the low and highly porous binary Ti-20Zr alloys sintered at 1200°C for six hours is given in **Fig. 4.17**. EDS summary of the low and highly porous binary Ti-20Zr alloys is given in **Table 4.2.** EDS peaks of titanium and zirconium elements were detected in the nominal composition of all-porous binary Ti-20Zr alloys. The atomic compositions of the areas selected (1 to 2) for the low porous binary Ti-20Zr alloy were Ti-22.78Zr (at.%) and Ti-10.18Zr (at.%), while those for the highly porous binary Ti-20Zr alloy were Ti-27.32Zr (at.%) and Ti-11.79Zr (at.%), respectively.

According to the EDS results of the low and highly porous binary Ti-20Zr alloys, the light-coloured area classified as a distorted hcp α'-Ti phase was rich in zirconium concentration, while the remaining grey area identified as hcp α-Ti was rich in titanium concentration. This finding concluded that zirconium concentration was non-homogenously distributed in the microstructures because the porous structure of the alloys caused by insufficient sintering temperature far below the melting points of zirconium (1855°C) and titanium (1668°C) resulted in insufficient diffusion phenomenon. Therefore, both low and highly porous binary Ti-20Zr alloys had no uniform structure across the entire areas analysed.

**Table 4.2.** EDS summary of the low and highly porous binary Ti-20Zr alloys.

| | **Area 1 (at. %)** | | **Area 2 (at. %)** | |
|---|---|---|---|---|
| **Alloys** | **Ti** | **Zr** | **Ti** | **Zr** |
| **Ti-20Zr** | 77.22 | 22.78 | 89.82 | 10.18 |
| **Ti-20Zr + 20SH** | 72.68 | 27.32 | 88.21 | 11.79 |

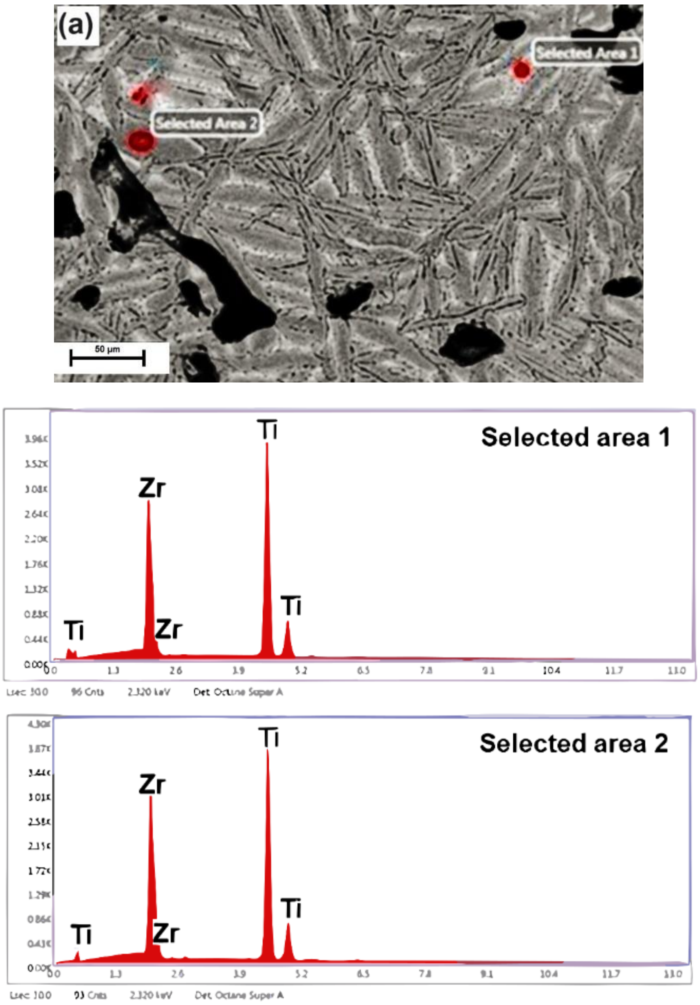
(a)
Selected Area 1
Selected Area 2
50 µm
Selected area 1
Ti
Zr
Ti
Ti
Zr
3.96K
3.52K
3.08K
2.64K
2.20K
1.76K
1.32K
0.88K
0.44K
0.00K
0.0
1.3
2.6
3.9
5.2
6.5
7.8
9.1
10.4
11.7
13.0
Lsec: 30.0
96 Cnts
2.320 keV
Det: Octane Super A
Selected area 2
Ti
Zr
Ti
Ti
Zr
4.30K
3.87K
3.44K
3.01K
2.58K
2.15K
1.72K
1.29K
0.86K
0.43K
0.00K
0.0
1.3
2.6
3.9
5.2
6.5
7.8
9.1
10.4
11.7
13.0
Lsec: 30.0
93 Cnts
2.320 keV
Det: Octane Super A

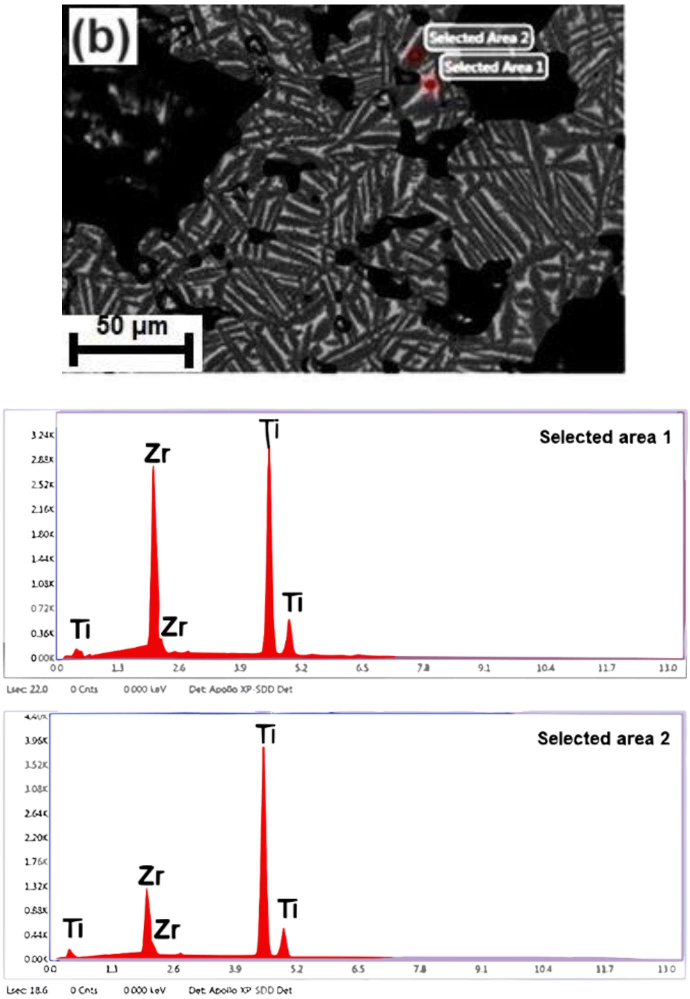

**Figure 4.17.** EDS analysis showing SEM micrograph and individual EDS points for the low and highly porous binary Ti-20Zr (at.%) alloys (a: Ti-20Zr, b: Ti-20Zr + 20SH).

### 4.1.5.3. EDS Analysis of Ternary Titanium-Niobium-Zirconium Alloys

The EDS analysis showing SEM micrograph and individual EDS points for the low and highly porous ternary Ti-xNb-10Zr alloys sintered at 1200°C for six hours is depicted in **Fig. 4.18**. EDS summary of the low and highly porous ternary Ti-xNb-10Zr alloys is illustrated in **Table 4.3**. The atomic compositions of the areas selected (1 to 3) for the low porous ternary Ti-10Nb-10Zr alloys were Ti-30.83Nb-7.46Zr (at.%), Ti-11.37Nb-8.45Zr (at.%) and Ti-12.17Nb-8.53Zr (at.%), respectively. The atomic compositions of the areas selected (1 to 3) for the low porous ternary Ti-20Nb-10Zr alloys were Ti-97.40Nb-2.29Zr (at.%), Ti-18.85Nb-7.41Zr (at.%) and Ti-11.67Nb-7.31Zr (at.%), respectively. On the other hand, the atomic compositions of the areas selected (1 to 3) for the highly porous ternary Ti-10Nb-10Zr alloys were Ti-87.56Nb (at.%), Ti-16.82Nb-7.87Zr (at.%) and Ti-13Nb-7.87Zr (at.%), while those for the highly porous ternary Ti-20Nb-10Zr alloys were Ti-52.08Nb (at.%), Ti-5.83Nb (at.%) and Ti-12.06Nb-10.04Zr (at.%), respectively. Based on the EDS results obtained, niobium concentration was poor in some areas compared to the nominal composition; these areas were classified as the hcp α-Ti phase (dark-grey areas). Some areas with high niobium concentrations corresponded to the bcc β-Ti phase (light-grey areas) due to the preferential dissolution of niobium.

Like the low and highly porous binary Ti-20Zr alloys, no undissolved zirconium was found in either low or highly porous ternary Ti-xNb-10Zr alloys. This was expected as zirconium is fully dissolvable in the titanium matrix, but niobium has limited solubility in the α-Ti phase. The relatively low dissolution of niobium in titanium-zirconium mixtures has a crucial effect on the formation of an inhomogeneous structure.

**Table 4.3.** EDS summary of the low and highly porous ternary Ti-xNb-10Zr alloys.

| | **Area 1 (at. %)** | | | **Area 2 (at. %)** | | | **Area 3 (at. %)** | | |
|---|---|---|---|---|---|---|---|---|---|
| **Alloys** | **Ti** | **Nb** | **Zr** | **Ti** | **Nb** | **Zr** | **Ti** | **Nb** | **Zr** |
| Ti-10Nb-10Zr | 61.71 | 30.83 | 7.46 | 80.18 | 11.37 | 8.45 | 79.3 | 12.17 | 8.53 |
| Ti-20Nb-10Zr | 0.31 | 97.40 | 2.29 | 73.74 | 18.85 | 7.41 | 81.02 | 11.67 | 7.31 |
| Ti-10Nb-10Zr + 20SH | 12.44 | 87.56 | - | 75.31 | 16.82 | 7.87 | 79.13 | 13 | 7.87 |
| Ti-20Nb-10Zr + 20SH | 47.92 | 52.08 | - | 94.17 | 5.83 | - | 77.9 | 12.06 | 10.04 |

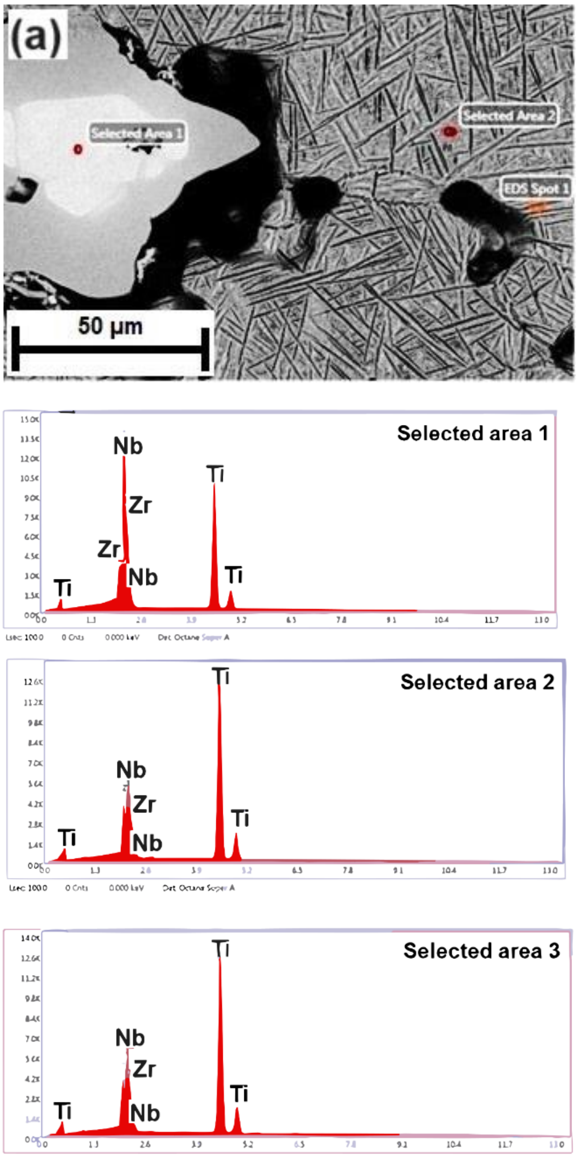
(a)
50 µm
Selected Area 1
Selected Area 2
EDS Spot 1
Selected area 1
Nb
Zr
Zr
Nb
Ti
Ti
Ti
Selected area 2
Ti
Nb
Zr
Ti
Ti
Nb
Selected area 3
Ti
Nb
Zr
Ti
Ti
Nb

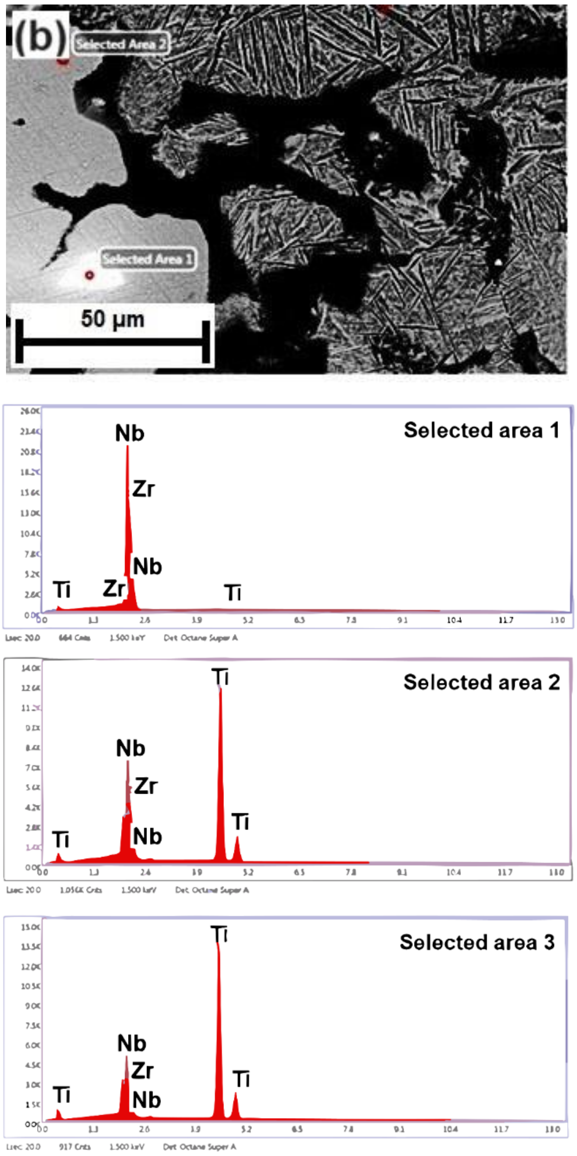
(b)
Selected Area 2
Selected Area 1
50 µm
26.0K
23.4K
20.8K
18.2K
15.6K
13.0K
10.4K
7.8K
5.2K
2.6K
0.0K
Nb
Zr
Nb
Ti
Zr
Ti
Selected area 1
0.0
1.3
2.6
3.9
5.2
6.5
7.8
9.1
10.4
11.7
13.0
Lsec: 20.0 664 Cnts 1.500 keV Det: Octane Super A
14.0K
12.6K
11.2K
9.8K
8.4K
7.0K
5.6K
4.2K
2.8K
1.4K
0.0K
Ti
Nb
Zr
Nb
Ti
Ti
Selected area 2
Lsec: 20.0 1.056K Cnts 1.500 keV Det: Octane Super A
15.0K
13.5K
12.0K
10.5K
9.0K
7.5K
6.0K
4.5K
3.0K
1.5K
0.0K
Ti
Nb
Zr
Nb
Ti
Ti
Selected area 3
Lsec: 20.0 917 Cnts 1.500 keV Det: Octane Super A

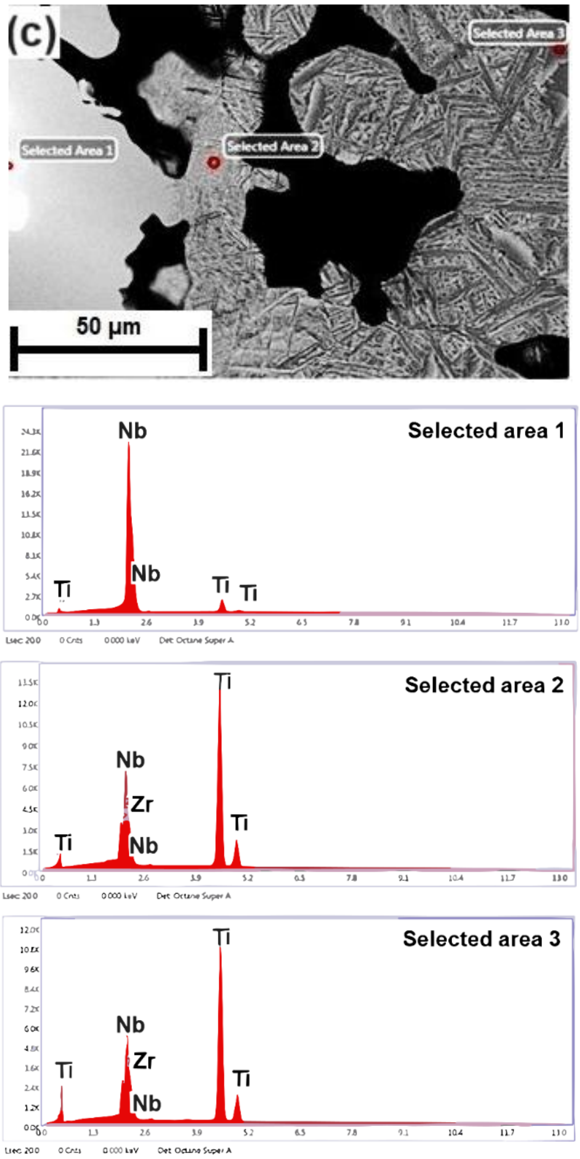
(c)
Selected Area 1
Selected Area 2
Selected Area 3
50 µm
Selected area 1
Nb
Nb
Ti
Ti
Ti
Selected area 2
Ti
Nb
Zr
Nb
Ti
Ti
Selected area 3
Ti
Nb
Zr
Nb
Ti
Ti
0.0
1.3
2.6
3.9
5.2
6.5
7.8
9.1
10.4
11.7
13.0
Lsec: 20.0
0 Cnts
0.000 keV
Det: Octane Super A

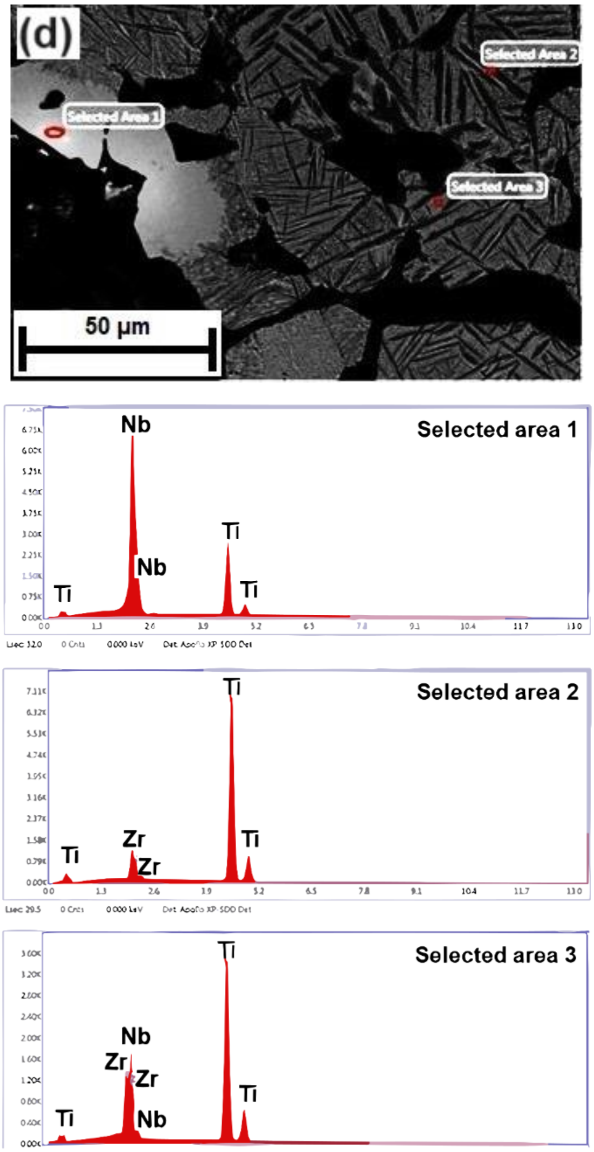

**Figure 4.18**. EDS analysis showing SEM micrograph and individual EDS points for low and highly porous ternary Ti-xNb-10Zr alloys (a: Ti-10Nb-10Zr, b: Ti-20Nb-10Zr, c: Ti-10Nb-10Zr + 20SH, d: Ti-20Nb-10Zr + 20SH).

### 4.1.6. Scanning Electron Microscopy Analysis

SEM micrographs showed irregularly shaped pores with sharp corners in the microstructures. Backscattered Electron (BSE) mode was employed to see whether the primary niobium phase was present in the microstructures because it was quite difficult to distinguish in Secondary electron (SE). Closed-pore structures were determined in the low porous alloys, while open-pore (interconnected) structures were found in the highly porous alloys, allowing for cell ingrowth. As mentioned previously, pore sizes and distributions for the highly porous alloys were much higher than for the low porous alloys, which revealed that the characteristics of pores achieved were consistent with the general porosity level of the alloys.

### 4.1.6.1. SEM Analysis of Binary Titanium-Niobium Alloys

SEM micrographs of the low and highly porous binary Ti-xNb alloys sintered at 1200°C for six hours are given in **Figs. 4.19.** and **4.20.** EDS results showed that the dark-grey area rich in titanium concentration was classified as α-Ti phase, while the remaining grey area rich in niobium concentration was identified as β-Ti phase. The bright-white area was detected as a primary niobium phase. Microstructural results revealed that the hcp α-Ti and bcc β-Ti phase formations were observed in the low and highly porous binary Ti-xNb alloys. This finding was consistent with the XRD results in this thesis. The microstructures of the low and highly porous binary Ti-10Nb alloys exhibited typical lath-type morphologies. Those of the low and highly porous binary Ti-20Nb and Ti-30Nb had a similar structure to the typical lamellar morphologies, growing with the dissolution of niobium in the titanium matrix. In addition, based on the microstructural evaluation. The primary niobium phase was observed in microstructures of the low and highly porous binary Ti-10Nb, Ti-20Nb and T-30Nb alloys produced under the same conditions. In particular, as can be seen in the SEM micrographs of the highly porous binary Ti-30Nb alloy, the proportion of the white area (primary niobium phase) was the highest among the all-porous binary Ti-xNb alloys due to increased diffusion pathways between particles and niobium concentration.

As the niobium concentration in the low and highly porous Ti-xNb alloys increased, the volume fraction of the bcc β-Ti phase also increased gradually because niobium in the titanium matrix acted as a strong β-Ti stabiliser. Also, the distribution of the hcp α-Ti and the bcc β-Ti phases in the microstructure was not uniform due to the insufficient sintering temperature selected in this thesis (1200°C).

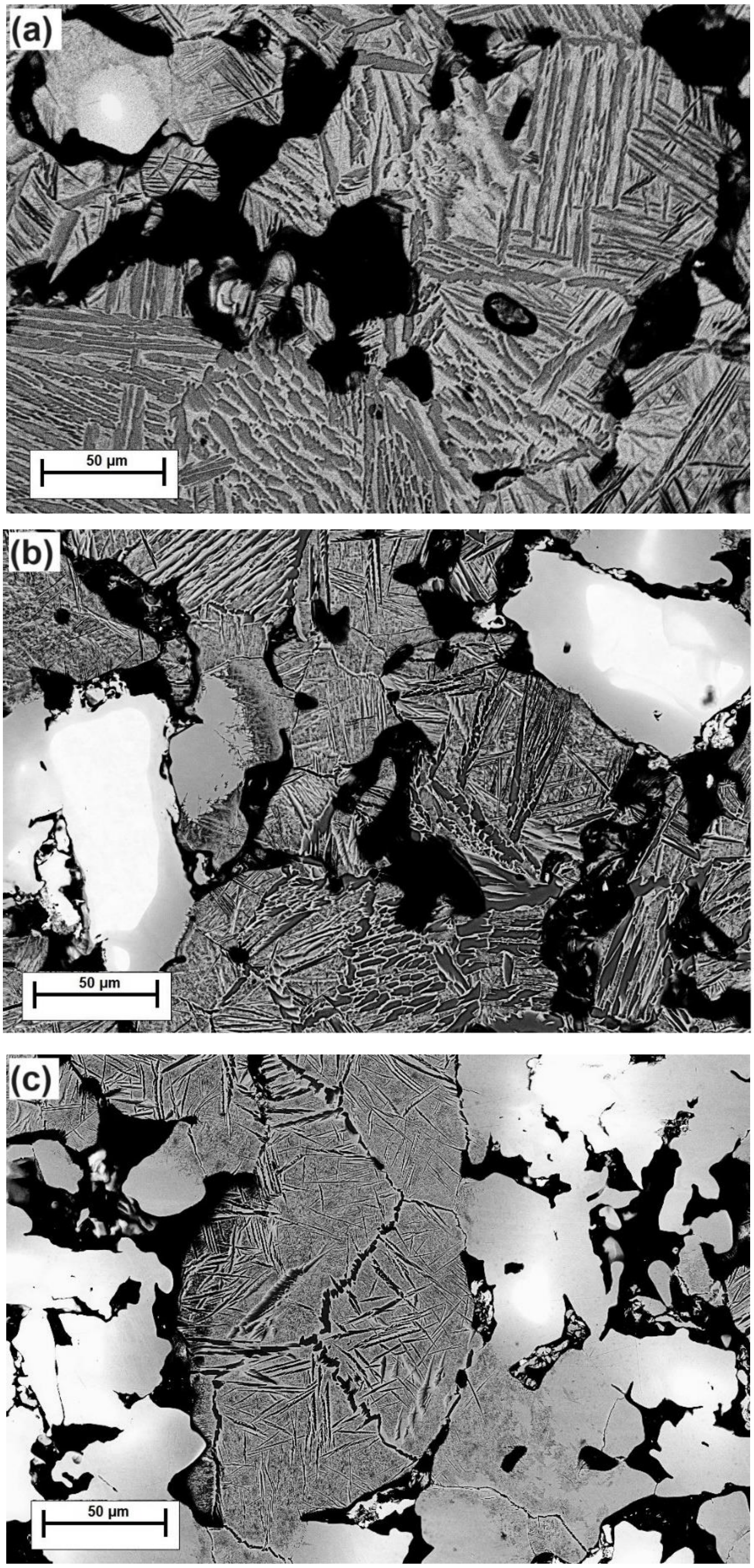

**Figure 4.19.** SEM micrographs of the low porous binary Ti-xNb alloys (a: Ti-10Nb, b: Ti-20Nb, c: Ti-30Nb).

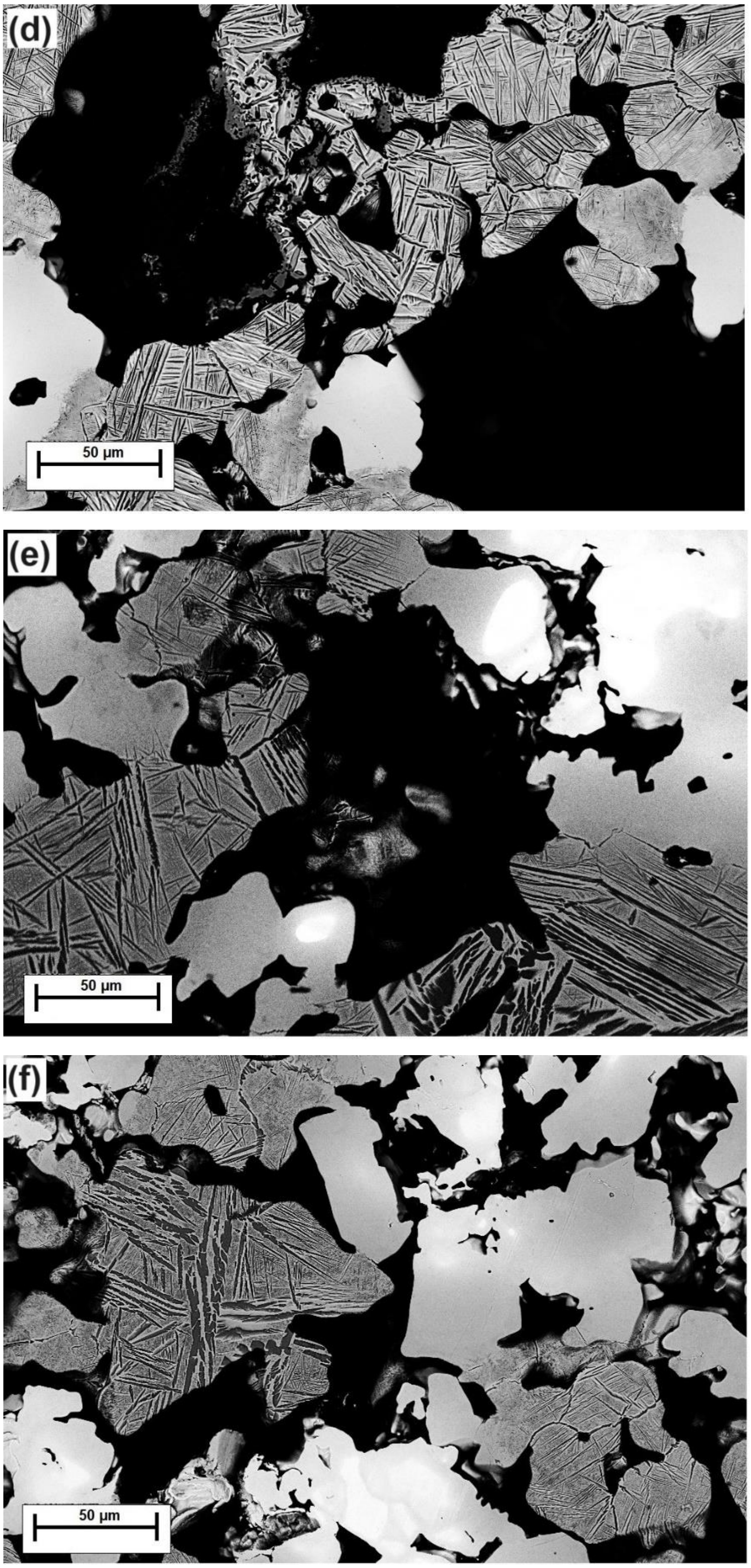

**Figure 4.20.** SEM micrographs of the highly porous binary Ti-xNb alloys (d: Ti-10Nb + 20SH, e: Ti-20Nb + 20SH, f: Ti-30Nb + 20SH).

.

### 4.1.6.2. SEM Analysis of Binary Titanium-Zirconium Alloys

SEM micrographs of the low and highly porous binary Ti-20Zr alloys sintered at 1200°C for six hours are illustrated in **Fig. 4.21**. Lamellar-shaped microstructures were observed in the low and highly porous binary Ti-20Zr alloys; these were the martensitic α′-Ti phase with a distorted hcp structure and α-Ti phase with hcp (Gottlow et al., 2012). In this regard, the grey area rich in titanium concentration corresponded to the hcp α-Ti phase, while the light-grey area rich in zirconium concentration was classified as a distorted hcp α'-Ti phase. In addition, microstructures of the low and highly porous binary Ti-20Zr alloys showed a completely solid solution, which was confirmed by other studies (Zhao et al., 2023).

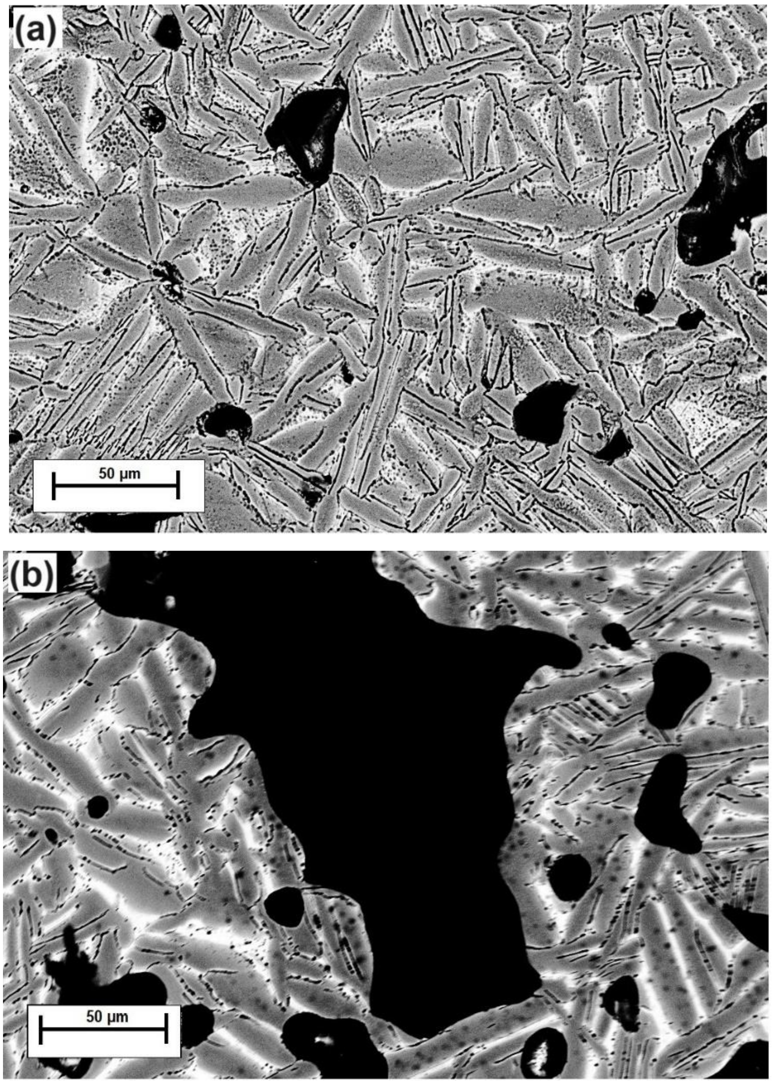

**Figure 4.21.** SEM micrographs of the low and highly porous binary Ti-20Zr (at.%) alloys (a: Ti-20Zr, b: Ti-20Zr + 20SH).

### 4.1.6.3. SEM Analysis of Ternary Titanium-Niobium-Zirconium Alloys

SEM micrographs for the low and highly porous ternary Ti-xNb-10Zr alloys sintered at 1200°C for six hours are given in **Figs. 4.22** and **4.23**. Following microstructural examination, the all-porous ternary Ti-xNb-10Zr alloys were found to have a dual-phase microstructure composed of finely dispersed acicular hcp α-Ti needles in the bcc β-Ti matrix. No formation of the ω-Ti phase was determined in their microstructures. A fine acicular α-Ti phase transformation occurred in the low porous ternary Ti-10Nb-10Zr alloy, while an extremely fine acicular α-Ti phase was observed in the low porous ternary Ti-20Nb-10Zr alloy, depending on increasing niobium concentrations in the titanium-zirconium mixtures. Like all-porous binary Ti-xNb alloys, the dark-grey area rich in titanium and zirconium contents corresponded to the α-Ti phase, the light-grey area rich in niobium content corresponded to the β-Ti phase, and the bright-white area was identified as the primary niobium phase. Further, some areas with the primary niobium phase surrounded by the β-Ti phase were found in the low and highly porous ternary Ti-10Nb-10Zr and Ti-20Nb-10Zr alloys (Henriques et al., 2010).

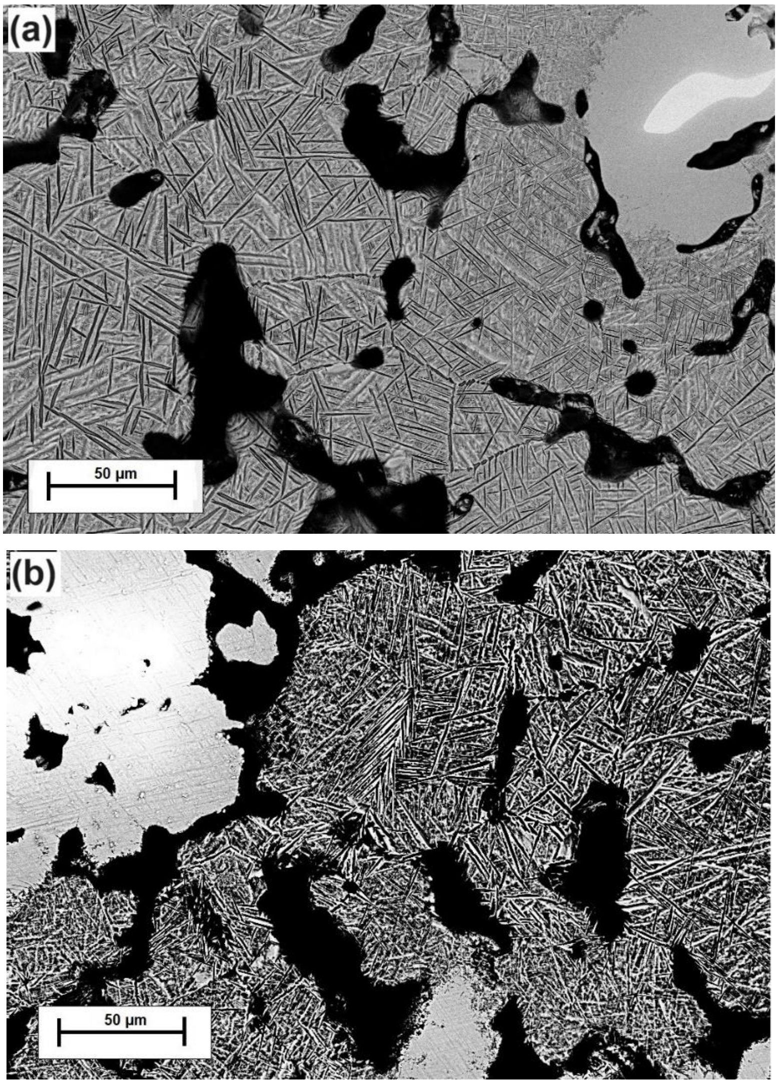

**Figure 4.22.** SEM micrographs of the low porous ternary Ti-xNb-10Zr alloys (a: Ti-10Nb-10Zr, b: Ti-20Nb-10Zr).

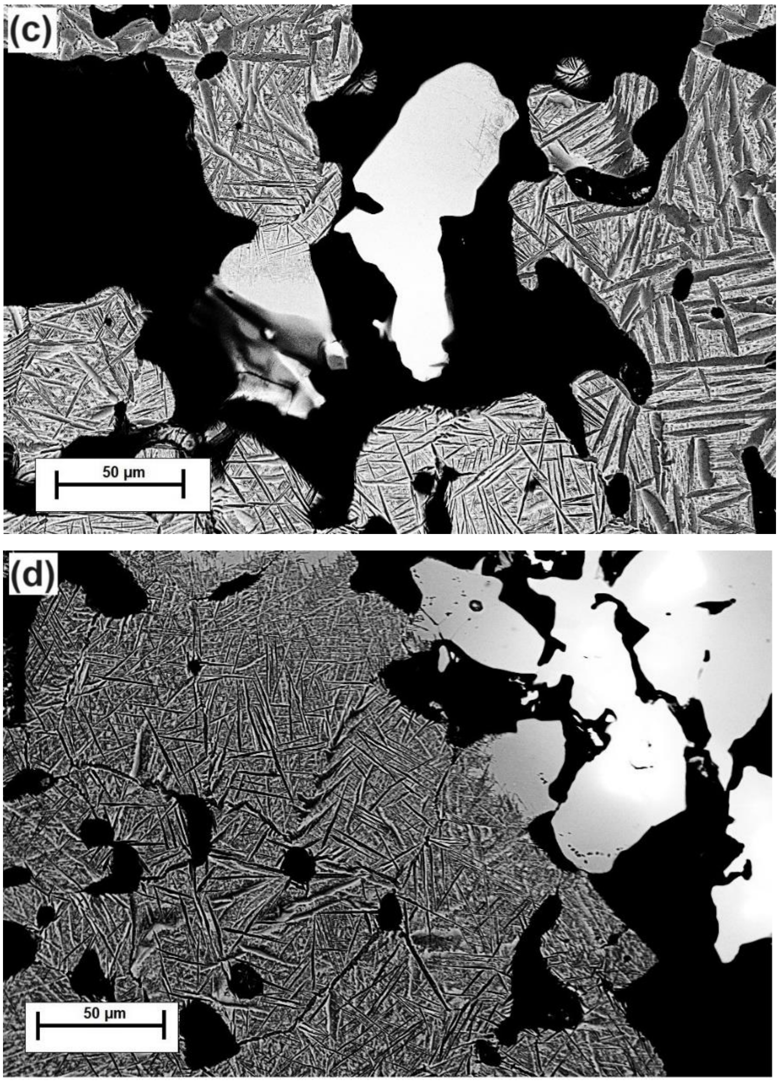

**Figure 4.23.** SEM micrographs of the highly porous ternary Ti-xNb-10Zr alloys (c: Ti-10Nb-10Zr + 20SH, d: Ti-20Nb-10Zr + 20SH).

### 4.1.7. Electron Backscatter Diffraction

#### 4.1.7.1. EBSD Analysis of Titanium-Niobium Binary Alloys

EBSD results illustrating the orientation colour maps and grain size distribution of the low porous binary Ti-xNb alloys sintered at 1200°C for six hours are shown in **Fig. 4.24** as a function of niobium concentration in the titanium matrix. The white regions on the EBSD-IPF images corresponded to unindexed regions due to remaining porosity after the sintering stage. The results showed a typical columnar-shape microstructure with random orientation comprised of the bcc β-Ti phase and the hcp α-Ti phase. This was induced by the inhomogeneity of the powder metallurgy method. As seen in **Fig. 4.24.**, the fractions of the β-Ti phase determined in the low porous binary Ti-xNb (x:10, 20 and 30: at.%) alloys were 3%, 11% and 40%, respectively. This finding showed that, depending on the increasing niobium concentration in the titanium-niobium mixtures, the α-Ti grains transformed into β-Ti grains in the microstructures, which supported the idea that niobium acted as a strong β-Ti stabiliser in the titanium matrix. Previous studies also reported that the stability of the β-Ti phase was directly proportional to the fraction of niobium dissolved in the titanium matrix (Ehtemam-Haghighi et al., 2016). However, insufficient sintering temperature and remaining general porosity caused by the powder metallurgy method adversely affected the dissolution of niobium in the titanium-niobium mixtures. Based on the EBSD mapping results, the primary niobium phase detected in the low porous binary Ti-xNb (x:10, 20 and 30: at.%) alloys were 4%, 11% and 41%, respectively. This also played a key role in the formation of the β-Ti phase in the titanium matrix. Further, the mean grain sizes determined from the EBSD-IPF images for the low porous binary Ti-xNb alloys were calculated separately for each alloy. Those for the hcp α-Ti phase were 17.57 µm for Ti-10Nb, 14,6 µm for Ti-20Nb and 10.54 µm for Ti-30Nb. The average grain sizes for the hcp α-Ti phase decreased with increasing niobium concentration in the titanium matrix. However, the average grain sizes for low porous binary Ti-xNb alloys were generally greater than 10 µm, which showed that relatively course-grained α-Ti phases could be produced via the powder metallurgy method used in this thesis. In conclusion, after sintering, elongated α-Ti grains were observed in the low porous binary T-xNb alloys. Also, α-Ti grains slightly decreased in size and became thinner with increasing niobium concentrations in the titanium matrix.

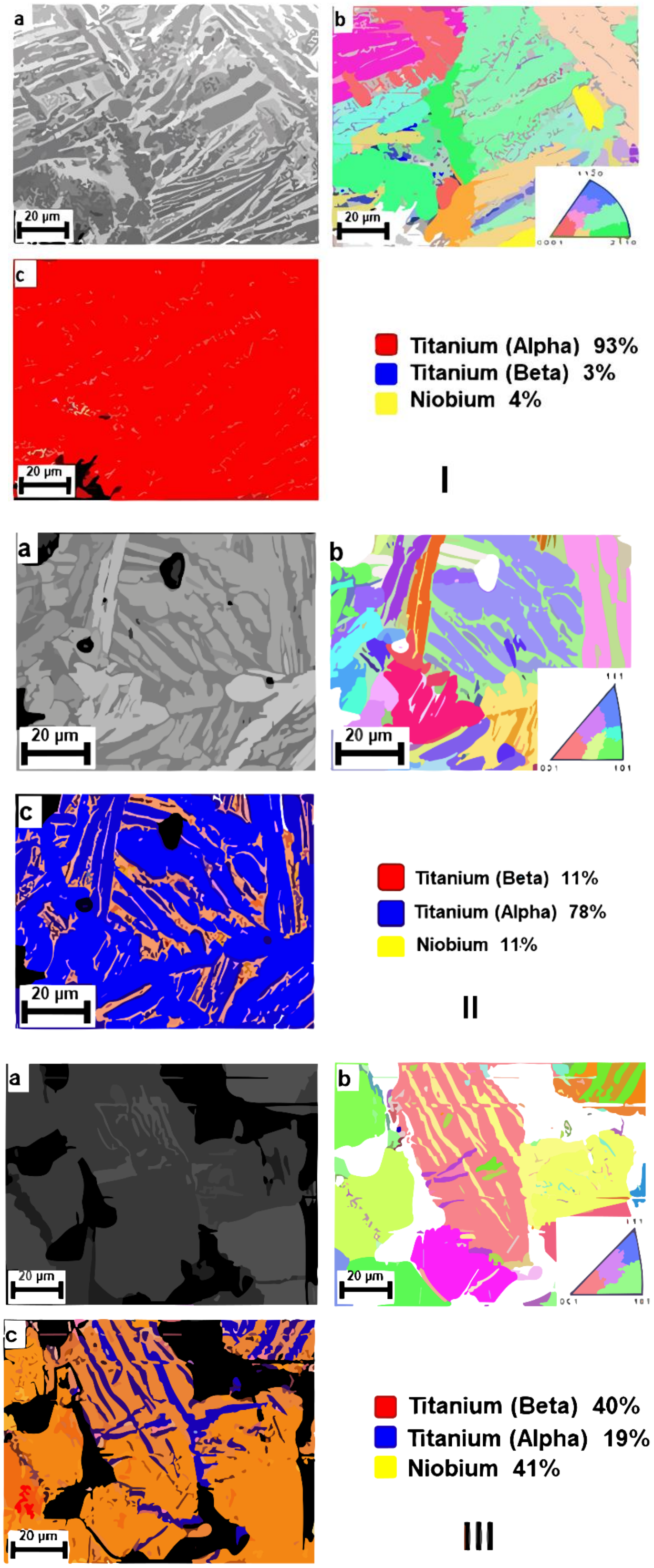

**Figure 4.24.** EBSD data showing the microstructure, grain morphology and phase constituents and distribution for the low porous binary Ti-xNb (at.%) alloys (I: Ti-10Nb, II: Ti-20Nb, III: Ti-30Nb); a) IQ map, b) IPF map and c) phase map.

#### 4.1.7.2. EBSD Analysis of Binary Titanium-Zirconium Alloys

The grain boundaries map and phase map are shown in **Fig. 4.25**. The EBSD analysis was performed for the low porous binary Ti-20Zr alloy. The EBSD-IPF map did not exhibit any trace of the amorphous phase related to titanium or zirconium. Therefore, there were no black regions or dots because the amorphous structure could not create Kikuchi lines due to the absence of lattice planes (Li et al., 2021). According to the image quality and IPF map examined with EBSD, the microstructure morphology for the low porous binary Ti-20Zr alloy consisted of lath grains accompanied by pores as a result of the sintering stage. No alignment was observed in the hcp α-Ti grains but randomly elongated hcp α-Ti grains were found in the low porous binary Ti-20Zr alloy. The blue colours in the phase map represented the percentage of the hcp α-Ti phase inside the low porous binary Ti-20Zr alloy. It was thus evident that the fraction of the hcp α-Ti phase was much higher than that of the bcc β-Ti phase in titanium-zirconium mixtures. At this point, the volume fractions of the hcp α-Ti and the bcc β-Ti phases were 96% and 4%, respectively. This result revealed that the phase structure of the low porous binary Ti-20Zr alloy was not remarkably affected by adding zirconium to the titanium matrix. Here, the zirconium element acted as a weak β-Ti stabiliser in the titanium matrix. The average grain size determined from the EBSD-IPF map for the hcp α-Ti phase was calculated as about 19.89 µm. On the other hand, a small quantity of β-Ti grains was detected between the α-Ti grains. The β-Ti phase was preferably observed where zirconium concentrations were abundant, according to the EDS result of the low porous binary Ti-20Zr alloy. The β-Ti grains were well fragmented and scattered in the microstructure, giving a lower fraction. It was concluded that the EBSD analysis revealed the coexistence of high amounts of hcp α-Ti and small amounts of bcc β-Ti in low porous Ti-20Zr binary alloys.

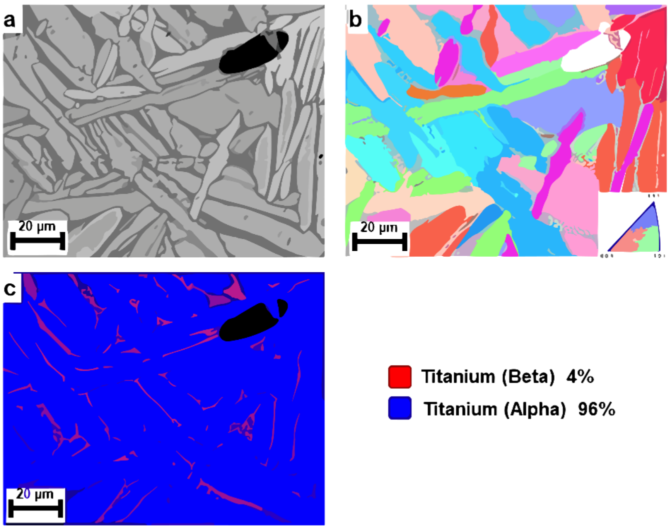

**Figure 4.25.** EBSD data showing the microstructure, grain morphology and phase constituents and distribution for the low porous binary Ti-20Zr (at.%) alloy; a) IQ map, b) IPF map and c) phase map.

#### 4.1.7.3. EBSD Analysis of Ternary Titanium-Niobium-Zirconium Alloys

The grain boundaries map and phase map are shown in **Fig. 4.26** as functions of niobium concentration in titanium-zirconium mixtures. As mentioned previously, white regions corresponding to the remaining pores were unindexed. A dual-phase microstructure consisting of bcc β-Ti grains and thin hcp α-Ti needles was observed. Niobium and zirconium concentrations in the titanium matrix reduced the martensite transition temperature (Ms) of the alloy, separately. Therefore, the hcp α-Ti grains could not grow any further. On the other hand, the volume fraction of the hcp α-Ti phase in the low porous ternary Ti–10Nb–10Zr (78%) alloy was greater than that in the low porous ternary Ti-20Nb-10Zr alloy (53%). Based on the EBSD results, the evidence demonstrated that a finely dispersed acicular hcp α-Ti phase in the bcc β-Ti matrix was observed after the sintering stage. The hcp α-Ti grain boundaries were also obvious. The mean grain sizes obtained from the EBSD-IPF image for the hcp α-Ti phase in the low porous ternary Ti-xNb-10Zr (x:10 and 20: at.%) alloys were calculated as 9.89 µm and 9.13 µm, respectively. This revealed that grain size for the α-Ti phase decreased with increasing niobium concentrations. Moreover, the volume fraction of the bcc β-Ti phase in the low porous ternary Ti-xNb-10Zr (x:10 and 20: at.%) alloys were detected as 11% and 23%, respectively. Like low porous binary Ti-xNb alloys, the primary niobium phase was observed in the microstructure of the low porous ternary Ti-xNb-10Zr (x:10 and 20: at.%) alloys, which were 12% and 25%, respectively.

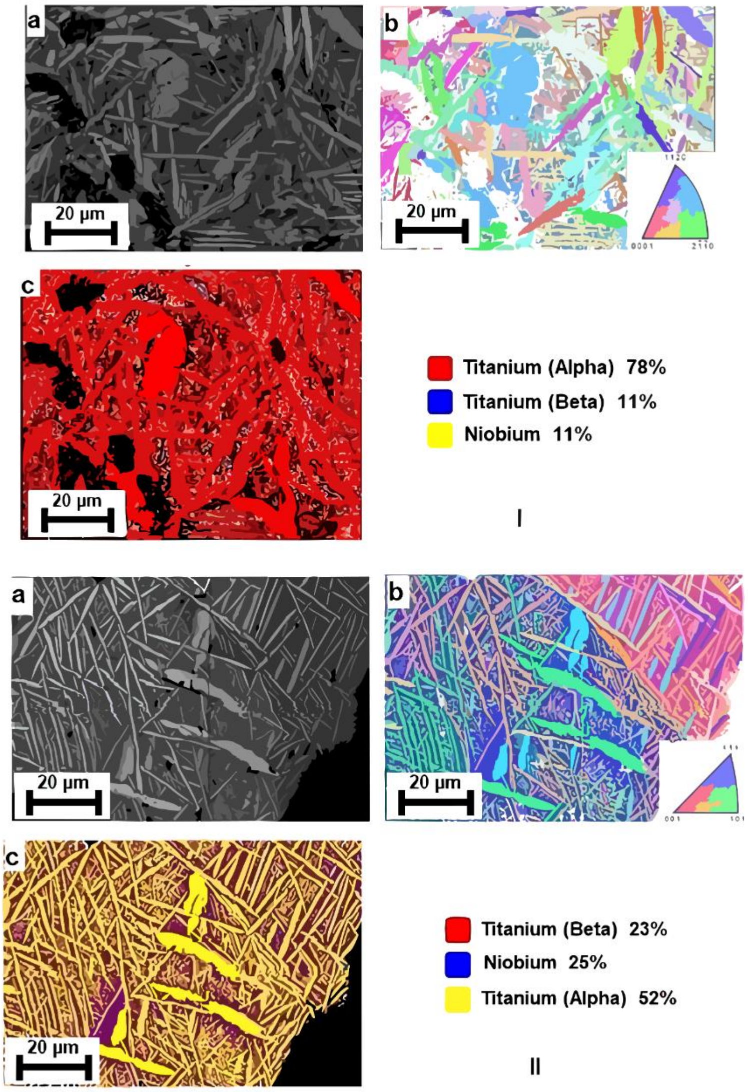

**Figure 4.26.** EBSD data showing the microstructure, grain morphology and phase constituents and distribution for the low porous ternary Ti-xNb-10Zr (at.%) alloys (I: Ti-10Nb-10Zr, II: Ti-20Nb-10Zr); a) IQ map, b) IPF map and c) phase map.

## 4.2. Discussion

This result was expected and suggested that the use of $NH_4HCO_3$ as a space holder agent was dramatically effective in generating high porosities. No residues of $NH_4HCO_3$ were found in the alloys studied after the sintering stage, which indicated that the space holder agent was completely degraded to ammonia ($NH_3$(g)) and carbon dioxide ($CO_{2(g)}$), leaving pores in the material. The variations of general porosity within both low and high categories were limited, suggesting that the processing parameters for mixing, compaction and sintering were well-controlled and consistent. After examining the effects of niobium addition on the general porosity measured, it seemed that niobium concentration contributed, partially, to the variations of the porosity as the upper bound of porosities for both low and high porosity categories are associated with high niobium concentrations. It is reasonable to believe that a full range of porosities required for clinical applications can be achieved by adjusting space holder agent additions and sintering conditions. Adding a space holder agent was a major factor in obtaining desirable general porosity in the alloys compared to addition of niobium.

The porous structures of the alloys achieved in this thesis are essential for bone ingrowth, nutrient transport, and healing time (Chang et al., 2017). Previous studies have shown that cell growth and other cellular activities only take place with the help of the pores existing inside the implant material. Therefore, natural bone can contain a porous structure ranging from 10% to 85%, depending on the type and age of the bone (Zhou et al., 2023). At this point, the results obtained from the general porosity ratios showed that the Ti-xNb, Ti-20Zr and Ti-xNb-10Zr alloys manufactured in this thesis remained within these limits, so the alloys can be considered promising candidates for orthopaedic applications. The general porosity level of load-bearing implant materials may vary according to where they are used in the body. Therefore, it is quite difficult to say which alloy achieved in this thesis has the optimal general porosity level. All general porosity levels achieved in this study were appropriate for mimicking the bone structure. Such behaviour also positively affected the biocompatibility properties of the alloys. It was concluded that the all-porous alloys achieved in this thesis had an adequate general porosity ratio for bone ingrowth and other cellular activities.

In implantology, the most critical point regarding a porous implant material is the size and distribution of the macro and micropores in the microstructure. We can see conflicting research on the optimal pore size for implantology in the literature. However, most studies have shown that the optimal pore size should be in the range of 100 µm to 600 µm (Aydoğmus, 2010; Sebastián et al., 2023). The pores in implant material should be larger than the minimum pore size allowing the blood and nutrient flow for bone ingrowth. The results from the general porosity evaluations showed that the alloys could be divided into low and highly porous categories, with pore sizes from 64 µm to 83 µm and 116 µm to 143 µm, respectively. The highest pore size of 143 µm was measured in the highly porous ternary Ti-20Nb-10Zr alloy; the lowest pore size of 64 µm was observed in the low porous binary Ti-10Nb alloy. Further, pore size and distribution found in all-porous alloys fabricated in this thesis were congruent with the pore size and distribution aimed for when the process began. As mentioned before, adding a space holder was a key factor in adjusting pore size and distribution. Some studies investigating the effect of cellular activity on pore size have demonstrated that cell adherence increased when pore characteristics such as pore size and distribution increased (Murphy et al., 2010). The pore size measurements of this study revealed that specific surfaces affected initial cell adherence, which is in good agreement with previous studies. Here, cell adherences of the highly porous Ti-xNb, Ti-20Zr, and Ti-xNb-10Zr alloys were greater than low porous alloys. This trend continued with even pore size from 64 µm to 143 µm. In vitro studies showed that low and highly porous alloys allowed for enhanced cell attachment. This revealed existing evidence that low and highly porous alloys met sufficient pore size requirements for cellular activities. Along with more remaining porosities, rougher surfaces were observed in the highly porous Ti-xNb, Ti-20Zr, and Ti-xNb-10Zr alloys compared to low porous alloys, which is a desirable feature for bone tissue engineering because the rough surface of the implant material can enhance contact with bone tissue when implanted (Li et al., 2009).

The XRD results revealed that adding a space holder agent did not alter the phase constituents of the alloys. As mentioned previously, the porosity characteristics could be effectively adjusted by adding a space holder agent. However, the addition of niobium was a crucial factor for the formation of the β-Ti phase, as it increases the lattice parameter of titanium and encourages the new crystal structure formation in the microstructure. Research has shown that niobium dissolution in titanium is dependent on many parameters, including niobium concentration, temperature, and cooling rate (Gou et al., 2020). The formation of a β-Ti phase can be effectively controlled by these parameters. Thus, desirable microstructures with superior mechanical properties can be obtained. The β-Ti phase is of vital importance for biomedical applications due to its unique mechanical properties (Hoppe et al., 2020). In this thesis, increasing the niobium concentration from 10% to 30% increased the formation of the β-Ti phase despite insufficient sintering conditions. This finding is consistent with research conducted in the past. The phase constituents of the alloys studied in this thesis could be modified to achieve appropriate microstructures. On the other hand, as zirconium is neutral element for titanium-based alloys, the low and highly porous Ti-20Zr alloys did not exhibit any trace of the β-Ti phase on the X-ray patterns. Additionally, we could not see the peak that belongs to pure zirconium since zirconium can be fully dissolve in titanium both phase (α-Ti phases).

Research on powder metallurgy has shown that several factors can cause a non-homogeneous structure in materials produced by the powder metallurgy method. A common cause is the incomplete mixing of powders, which can lead to areas with different chemical structures and properties within the article (Rodriguez-Contreras et al., 2021). Inadequate sintering temperature or time is another factor that can result in incomplete densification or porosity between particles (Angelo et al., 2022). EDS analysis was employed to detect the elemental composition of the low and highly porous Ti-xNb, Ti-20Zr, and Ti-xNb-10Zr alloys**.** The results showed that fully homogeneous structures could not be obtained in the alloys studied. Different phases were formed in the microstructures of the alloys. The presence of pure niobium cores in the microstructure of the low and highly porous Ti-xNb and Ti-xNb-10Zr alloys was an indication of insufficient sintering temperature selected in this thesis (Ruan et al., 2016; Zheng et al., 2023). On the other hand, no primary zirconium phase was detected in the microstructure of the alloys fabricated. Zirconium exhibited better dissolution in the titanium matrix than niobium (Wang et al., 2018; Mishchenko et al., 2020; Hon et al., 2023).

Increased pore size and distribution in the highly porous Ti-xNb, Ti-20Zr and Ti-xNb-10Zr alloys led to inhomogeneity as general porosity increased the diffusion path between particles, which led to more undissolved niobium particles in the highly porous Ti-xNb and Ti-xNb-10Zr alloys. Elemental concentrations of the low porous alloys were typically more uniform than those of the highly porous alloys. A strong relationship between general porosity and the dissolution of niobium (formation of the bcc β-Ti) in the titanium matrix was concluded. This finding was consistent with research conducted in the past (Medvedev et al., 2016; Rodriguez-Contreras et al., 2021). Adding a space holder played a key role in the inhomogeneous structure of alloys by changing the general porosities, while it did not seriously influence the phase constituents of the alloys. In contrast, adding niobium to the titanium matrix and titanium-zirconium mixtures altered the phase constituents of the alloys, although it did not dramatically alter the general porosity. Thus, in this thesis, desirable general porosity and desirable phase structure can be achieved by adding appropriate niobium and a space holder. On the other hand, as mentioned before, sintering is based on a physical diffusion process. The volume fraction of the α-Ti or the β-Ti and the dissolution of the pure niobium core in the titanium matrix are closely related to sintering temperature and time. Rao et al. stated that higher sintering temperatures affected the dissolution of niobium particles in the titanium matrix, suppressing the Widmanstatten morphology and increasing the volume fraction of the β-Ti phase in the microstructure (Rao et al., 2014). However, histological examinations showed that the inhomogeneous structure did not adversely affect the cell viability or cell proliferation of the alloys, since both niobium and zirconium are biocompatible. The alloys studied in this thesis were biosafe.

# Chapter 5. Compressive Performance

In this chapter, the compressive performances of the Ti-xNb (x: 10, 20, and 30; at.%), Ti-20Zr (at.%) and Ti-xNb-10Zr (x: 10, and 20; at.%) alloys processed by the powder metallurgy method combined with the space holder technique were assessed by uniaxial compressive tests. To determine the elastic modulus, the slope for the linear part (elastic region) of the curves was measured. In addition, yielding is the point at which a material begins to deform plastically (permanent deformation) under load. There are several methods to determine the yield strength from a stress-strain curve, but 0.2% offset yield method was employed to specify the yield strength of the alloys achieved in this thesis. The average yield strengths and ultimate compressive strengths were determined from stress-strain curves.

## 5.1. Results

### 5.1.1. Compressive Performance of Binary Titanium-Niobium Alloys

The stress-strain curves obtained from the uniaxial compressive test for low and highly porous binary Ti-xNb alloys sintered at 1200°C for six hours are given in **Fig. 5.1** as a function of the presence of a space holder and niobium concentrations in the titanium matrix. The mechanical properties of the low and highly porous binary Ti-xNb alloys are summarised in **Table 5.1.** The ultimate compressive strength values, known as maximum stress, in the stress-strain curves for low porous binary Ti-10Nb with general porosity of 20%, Ti-20Nb with general porosity of 25% and Ti-30Nb with general porosity of 29% alloys were 1295 MPa, 802 MPa and 618 MPa, while those for highly porous binary Ti-10Nb with general porosity of 55%, Ti-20Nb with general porosity of 56% and Ti-30Nb with general porosity of 58% alloys were 331 MPa, 127 MPa and 48 MPa, respectively (see **Fig. 5.2.**). The yield strength values for low porous binary Ti-xNb (x: 10, 20, and 30; at.%) alloys with general porosities of 20%, 25%, and 29%, respectively, were recorded as 687 MPa, 136 MPa and 112 MPa; those for highly porous binary Ti-xNb (x: 10, 20, and 30; at.%) alloys with general porosities of 55%, 56%, and 58% were measured as 64 MPa, 46 MPa and 22 MPa, respectively. As foreseen, with increasing general porosity, the ultimate compressive strength and yield strength values of the highly porous binary Ti-xNb alloys were reduced significantly (see **Fig. 5.2.**). This could be due to the porosity properties of the highly porous binary Ti-xNb alloys since adding a space holder agent to titanium-niobium mixtures caused a marked increase in pore size and distribution. In addition, Gibson and Ashby theoretically showed a strong correlation between mechanical properties and general porosity (Gibson et al., 2010). The results demonstrated that the ultimate compressive and yield strengths of low and highly porous binary Ti-xNb alloys could be adjusted by the general porosity of the alloys.

However, the mechanical properties of all alloys achieved might be linked not only with general porosity levels but also with phase constituents (β-Ti and α-Ti phases) with the solid-solid phase transformations. Accordingly, increasing niobium concentrations from 10% to 30% decreased the mechanical performance, as niobium acted as a β-phase stabiliser in the microstructure. Based on the literature, the α-Ti phase with hcp structure exhibits a higher elastic modulus, lower ductility, and better fracture toughness than the β-Ti phase with bcc structure (Balazic et al., 2007; Liu et al., 2013; Chang et al., 2017). The addition of a substitutional niobium alloyant element to the titanium matrix contributed to the formation of the β-Ti phase in the microstructure by lowering the α-Ti → β-Ti phase solvus line in all-porous binary Ti-xNb alloys. Research conducted in the past have shown that the phase transformation from the α-Ti to the β-Ti phase for commercially pure titanium normally starts at approximately 882°C, but the α-Ti → the β-Ti phase solidus transformation for the Ti-15Nb (wt.%) alloy occurs at about 777°C and that for the Ti-20Nb (wt.%) alloy occurs at about 734°C. It was concluded that with the increase of niobium concentrations in the titanium matrix, a reduction in the solvus line promoted the β-Ti phase formation, which resulted in lower ultimate compressive strength and yield strengths values in the all-porous binary Ti-xNb alloys achieved in this thesis (Nazari et al., 2015).

The elastic modulus of the low and highly porous binary Ti-xNb alloys decreased with the presence of a space holder from 41 GPa to 12 GPa for Ti-10Nb, 32 GPa to 6.7 for Ti-20Nb, and 28 GPa to 4.5 GPa for Ti-30Nb, which revealed that general porosity had a great influence on the elastic modulus of the highly porous binary Ti-xNb alloys. The results demonstrated that the highest elastic modulus of 41 GPa was obtained from the low porous binary Ti-10Nb alloy with general porosity of 20%; the lowest, of only 4.5 GPa, was achieved from the highly porous binary Ti-30Nb alloy with general porosity of 58%. The elastic modulus of the low porous binary Ti-10Nb alloy was about 12 times higher than that of the highly porous binary Ti-30Nb alloy. Consequently, the general porosity reduced the elastic modulus of the alloys achieved in this thesis.

**Table 5.1.** Compressive performance of the low and highly porous binary Ti-xNb (x: 10, 20, and 30; at.%) alloys.

| **Mechanical properties** | **Ti-10Nb** | **Ti-20Nb** | **Ti-30Nb** | **Ti-10Nb+ 20SH** | **Ti-20Nb+ 20SH** | **Ti-30Nb+ 20SH** |
|---|---|---|---|---|---|---|
| Ultimate compressive strength (MPa) | 1295 | 802 | 618 | 331 | 127 | 48 |
| Yield strength (MPa) | 687 | 136 | 112 | 64 | 46 | 22 |
| Elastic modulus (GPa) | 41 | 32 | 28 | 12 | 6.7 | 4.5 |

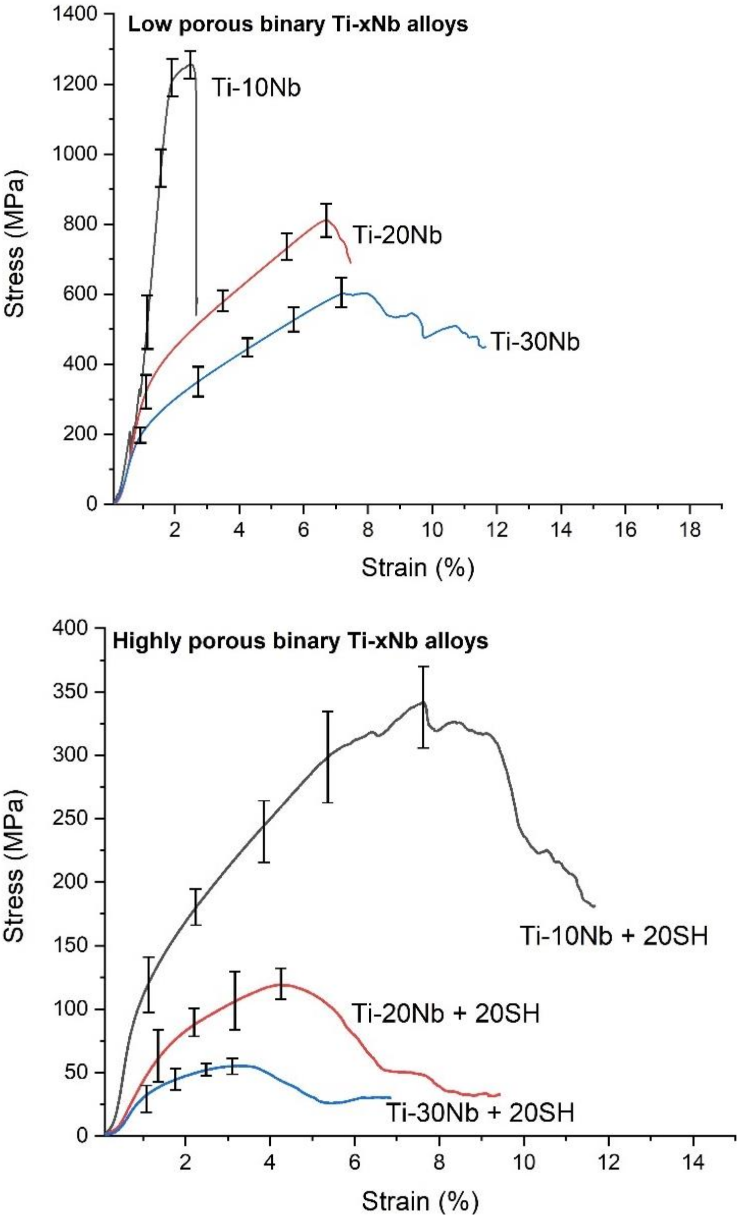

**Figure 5.1.** Stress-strain curves of the low and highly porous binary Ti-xNb (x: 10 20, and 30; at.%) alloys (The error bars represent standard deviation).

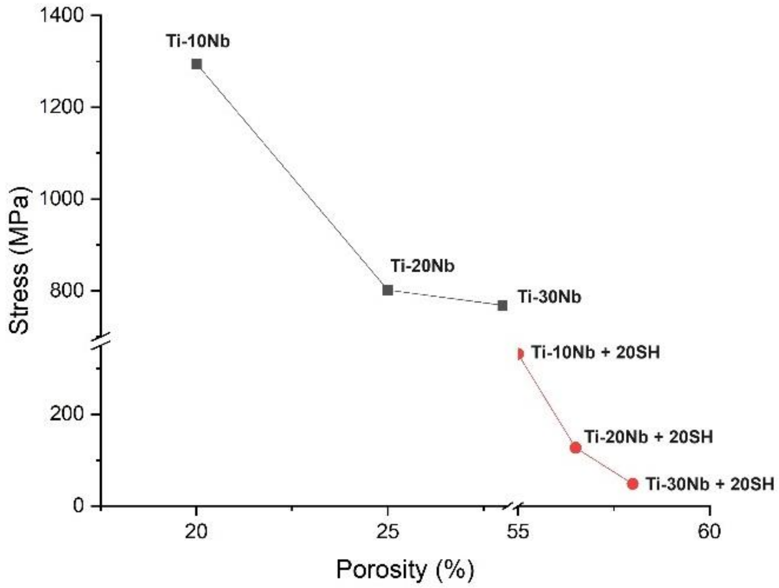

**Figure 5.2.** Stress-general porosity relationship of the low and highly porous binary Ti-xNb (x: 10 20, and 30; at.%) alloys.

### 5.1.2. Compressive performance of Binary Titanium-Zirconium Alloys

The stress-strain curve of the low and highly porous binary Ti-20Zr alloys sintered at 1200°C for six hours is presented in **Fig. 5.3.** The mechanical properties of the alloys are summarised in **Table 5.2**. The ultimate compressive strength value of the low porous binary Ti-20Zr with general porosity of 22% alloy was 1376 MPa, while that of the highly porous binary Ti-20Zr with general porosity of 44% alloy was 356 MPa (see **Fig. 5.4.**). This finding demonstrated that ultimate compressive strength values of the alloys were highly dependent on the fixed amount of the space holder agent. The same tendency was observed in yield strengths. Regarding this, the yield strengths of the low and highly porous binary Ti-20Zr alloys with general porosities of 22% and 43% were about 644 MPa and 103 MPa, respectively.

On the other hand, the elastic modulus values decreased from 49 GPa to 14 GPa by adding a space holder agent, which was consistent with the research conducted in the past (Torres-Sanchez et al., 2017). The elastic modulus of the low porous binary Ti-20Zr alloy with general porosity of 22% was about three times higher than that of the highly porous binary Ti-20Zr alloy with general porosity of 21%.

However, in this thesis, general porosity was not the only criterion to evaluate the mechanical performance of the low and highly porous binary Ti-20Zr alloys. The other key parameter affecting mechanical performance was microstructure. According to the equilibrium phase diagram of the titanium-zirconium binary systems, no intermetallic compound formed. Therefore, the mechanical performance of the titanium-zirconium systems, including ultimate compressive strength and yield strength, is also intrinsically linked to solid-solution strengthening by distorting the crystalline lattices (Ho et al., 2008). The microstructural examination results of the low and highly porous Ti-20Zr binary alloys showed Widmanstatten patterns composed of the hcp α-Ti phase and some distorted hcp α'-Ti phases, as seen in the SEM micrographs.

**Table 5.2.** Compressive performance of the low and highly porous binary Ti-20Zr (at.%) alloys.

| **Mechanical properties** | **Ti-20Zr** | **Ti-20Zr + 20SH** |
|---|---|---|
| Ultimate compressive strength (MPa) | 1376 | 356 |
| Yield strength (MPa) | 644 | 103 |
| Elastic modulus (GPa) | 49 | 14 |

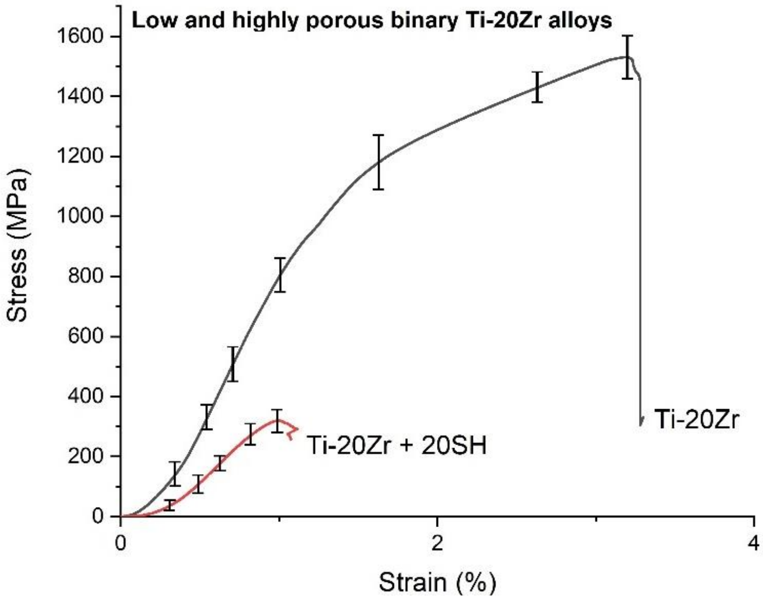

**Figure 5.3.** Stress-strain curves of the low and highly porous binary Ti-20Zr (at.%) alloys (The error bars represent standard deviation).

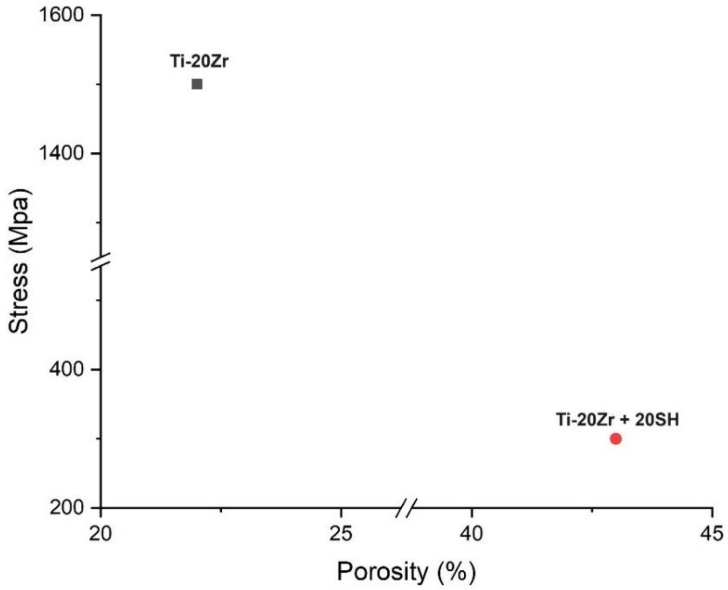

**Figure 5.4.** Stress-general porosity relationship for the low and highly porous binary Ti-20Zr (at.%) alloys.

### 5.1.3. Compressive performance of Ternary Titanium-Niobium-Zirconium Alloys

The experimental stress-strain curve obtained by a compressive test of the low and highly porous ternary Ti-xNb-10Zr alloys sintered at 1200°C for six hours is presented in **Fig. 5.5**, as a function of the presence of a space holder agent and niobium concentrations in titanium-zirconium mixtures. The mechanical properties of the low and highly porous ternary Ti-xNb-10Zr alloys achieved in this thesis are summarised in **Table 5.3**. The different results were found in the mechanical performance of the alloys. Accordingly, the ultimate compressive strength values for low porous ternary Ti-10Nb-10Zr with general porosity of 21% and Ti-20Nb-10Zr with general porosity of 25% were found as 1019 MPa and 767 MPa, while those for highly porous ternary Ti-10Nb-10Zr with general porosity of 50% and Ti-20Nb-10Zr with general porosity of 56% alloys were determined as 173 MPa and 78 MPa, respectively (see **Fig.5.6.**). The yield strength values for the low porous ternary alloys were about 523 MPa for Ti-10Nb-10Zr with general porosity of 21% and 394 MPa for Ti-20Nb-10Zr with general porosity of 25%, while those for the highly porous ternary alloys were 155 MPa for Ti-10Nb-10Zr with general porosity of 50% and 63 MPa for Ti-20Nb-10Zr with general porosity of 56%. With increasing general porosity, the ultimate compressive strengths and yield strengths of the highly porous ternary Ti-xNb-10Zr decreased remarkably. Research conducted in the past revealed that porosity properties such as porosity level, pore size, and pore distribution influenced crack initiation during compressive tests (Zheng et al., 2023). This is because cracks preferentially occurred in the pores expanded with increasing compressive strength, which resulted in a serious reduction in the ultimate compressive strengths and yield strengths in highly porous ternary Ti-xNb-10Zr alloys. The pore characteristics of the highly porous ternary Ti-xNb-10Zr (x: 10 and 20; at.%) alloys with general porosities of 50% and 55% were visible from their SEM micrographs, consistent with the general porosity ratios of the alloys.

**Table 5.3.** Mechanical properties of the low and highly porous ternary Ti –xNb-10Zr (x: 10 and 20; at.%) alloys.

| **Mechanical properties** | **Ti-10Nb-10Zr** | **Ti-20Nb-10Zr** | **Ti-10Nb-10Zr + 20SH** | **Ti-20Nb-10Zr + 20SH** |
|---|---|---|---|---|
| Ultimate compressive strength (MPa) | 1019 | 767 | 173 | 78 |
| Yield strength (MPa) | 523 | 394 | 155 | 63 |
| Elastic modulus (GPa) | 32 | 25 | 6.6 | 3.9 |

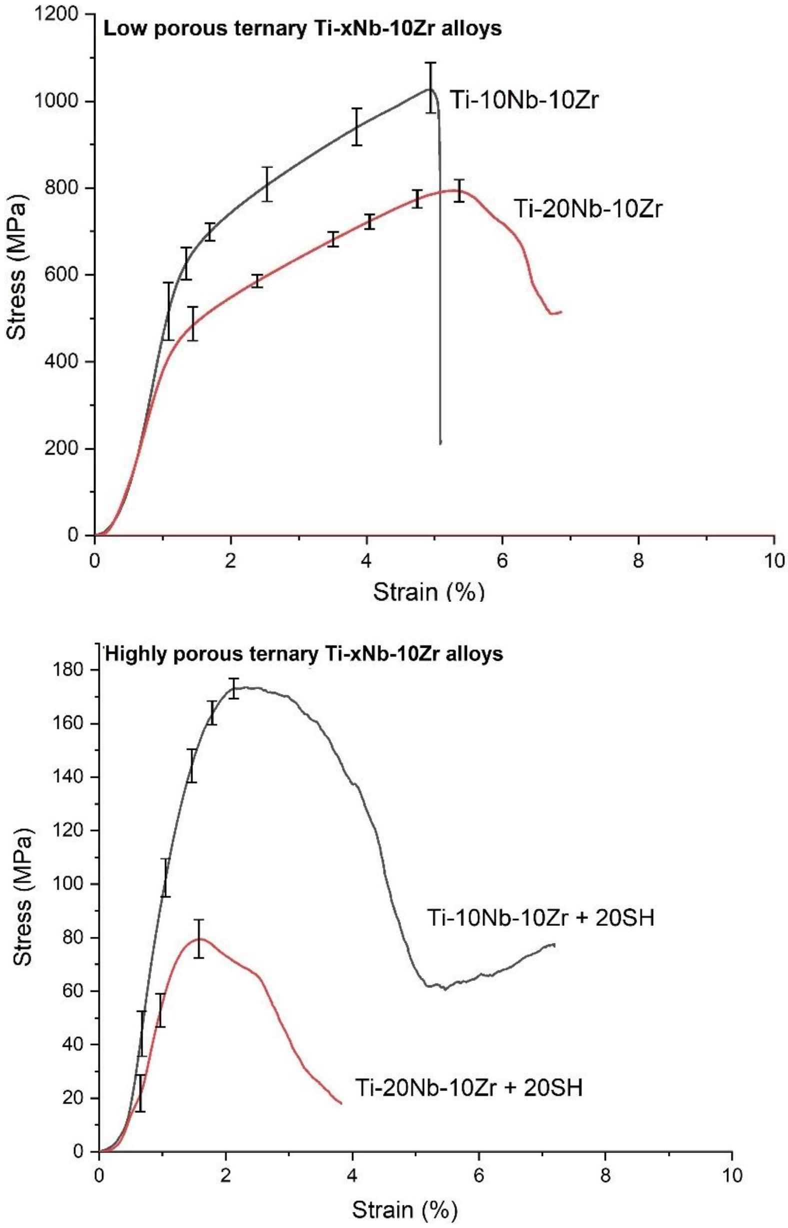

**Figure 5.5.** The stress-strain curves of the low and highly porous ternary Ti –xNb-10Zr (x: 10 and 20; at.%) alloys (The error bars represent standard deviation).

As seen in **Table 5.3**, elastic modulus values for low porous ternary Ti-xNb-10Zr (x: 10 and 20; at.%) alloys were 32 GPa and 25 GPa, while those for the highly porous ternary Ti-xNb-10Zr alloys were 6.6 GPa and 3.9 GPa. The maximum modulus of elasticity was 32 GPa for low porous ternary Ti-10Nb-10Zr alloy with general porosity of 21%. Also, the resulting elastic modulus was only 3.9 GPa, as the general porosity of the highly porous ternary Ti-20Nb-10Zr alloy increased to 57%. The elastic modulus of the low porous ternary Ti-10Nb-10Zr alloy was about eight times higher than that of the highly porous ternary Ti-20Nb-10Zr alloy.

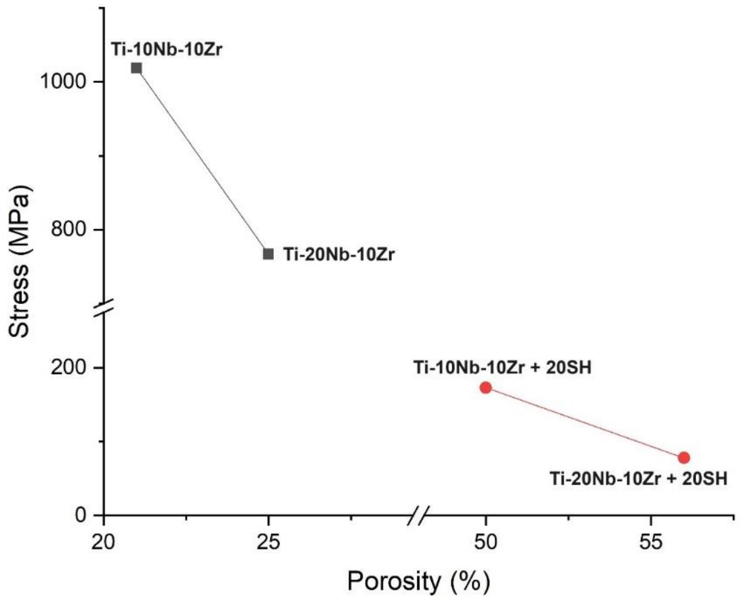

**Figure 5.6.** Stress-general porosity relationship of the low and highly porous ternary Ti-xNb-10Zr (x: 10 and 20; at.%) alloys.

## 5.2. Discussion

Based on the literature review, the mechanical properties of the final alloy fabricated by powder metallurgy can be optimised by modifying the processing parameters, such as adding a space holder, composition of the initial powders used, compacting, sintering temperature, and time. The alloys achieved in this thesis were fabricated by powder metallurgy with two categories of porosities, 20% to 29% and 43% to 56%. The space holder technique was employed to generate the high porosities. Human bone possesses a porous structure. These general porosities are essential for bone ingrowth and other cellular activities. Additionally, some studies revealed these general porosities were appropriate for reducing the risk of the stress-shielding effect (Savio and Bagno, 2020). In this thesis, to mimic this feature of natural bone, the alloys achieved were produced to have a porous structure. Accordingly, the highly porous alloys with general porosities in the range of 43% to 56% exhibited mechanical performance closer to the mechanical behaviour of human bone than the low porous alloys with general porosities between 20% and 29%. Such conditions showed that powder metallurgy with the space holder technique was a crucial factor for adjusting the mechanical properties of the alloys studied in this thesis by generating extra porosity inside the microstructure. According to this concept, the highly porous binary Ti-30Nb alloy with the highest general porosity of 56% had the lowest stress of 48 MPa, while maximum stress was obtained in the low porous binary Ti-10Nb alloy the with lowest general porosity of 22% as 1376 MPa. As seen from here, there was an inverse proportion between ultimate compressive strength and general porosity. In tissue engineering, general porosity is essential for cell viability and other cellular activities because it encourages the migration of cells and the growth of tissue by facilitating the exchange of nutrients and oxygen (Prakoso et al., 2023). However, it adversely affects the strength and stiffness of the implant material, so implant failure may occur at loads that are much lower than the loads that the implant can withstand. In addition, some studies suggest that larger pores may lead to shorter fatigue lives as fatigue cracks tend to initiate at the pore surface (Tammas-Williams et al., 2017). Therefore, there is a delicate balance between mechanical properties and the general porosity of the material. The mechanical performance of the alloys achieved in this study was lower than that of the alloys with stiff structures due to their porosity values. Some studies have shown that when the general porosity of the material increases, the elastic modulus exponentially reduces (Wang et al, 2013). On the other hand, randomly distributed pores can agglomerate and become a defect. Therefore, size, morphology, and distribution of the pores have crucial effect on mechanical testing of the alloys. The mechanical performances of the alloys were strongly related to porosity characteristics. It was concluded that general porosity of the alloys achieved in this thesis should be carefully checked to obtain the desired mechanical properties.

However, general porosity was not the only criterion to determine the mechanical performance of the low and highly porous alloys studied in this thesis. The other key parameter affecting mechanical testing was the microstructure or chemical composition of the alloys. Many studies demonstrated that the strength properties of titanium-based alloys can be controlled by altering phase structure (Ma et al., 2022). Different niobium contents were therefore alloyed to titanium and titanium-zirconium mixtures to see the individual effects of the chemical composition. Accordingly, increasing niobium concentrations from 10% to 30% slightly decreased the strength properties of the low and highly porous binary Ti-xNb alloys by increasing the formation of the β-Ti phase in the titanium-niobium mixtures, which was confirmed by other studies. Compared to the α-Ti phase, the β-Ti phase tends to have less stiffness and greater ductility, which makes it a suitable candidate for biomedical applications (Alabort et al., 2022). Altering the phase constituents of the alloys obtained in this thesis played a minimal role in the mechanical behaviours compared to adding a space holder agent. On the other hand, zirconium is a neutral element for titanium-based alloys. Therefore, adding zirconium did not change the microstructure of the low and highly porous Ti-20Zr alloys. However, alloying niobium concentration had a crucial impact on their microstructure and mechanical testing. In summary, our findings on the mechanical performance of fabricated all-porous Ti-xNb, Ti-20Zr, and Ti-xNb-10Zr alloys were supported by research conducted in the past. Kaya mentioned that adding niobium into titanium matrix diminished the elastic modulus of the alloys, which provided better mechanical match between the alloy used as implant material and bone structure (Kaya et al., 2019).

# Chapter 6. Corrosion Performance

This chapter discusses the corrosion resistance performance of the low and highly porous Ti-xNb (x: 10, 20, and 30; at.%), Ti-20Zr (at.%) and Ti-xNb-10Zr (x: 10, and 20; at.%) alloys, which was analysed by potentiodynamic polarisation experiment on an E-Zastat potentiostat workstation, using an electrochemical flat cell that contains Hanks' Balanced Salt Solution (HBSS) (350 mL.cm$^{-2}$, Fisher Scientific). The alloy sample, an SCE, and a plate of platinum were employed as working electrodes (exposed area of 1 cm$^2$), reference electrode and counter electrode, respectively. Potentiodynamic polarisation curves were measured from -0.75 V (vs. open circuit potential) to 1.25 V with a scan rate of 0.01 V.s$^{-1}$. Here, the corrosion potential ($E_{corr}$) and the corrosion current density ($i_{corr}$) of the alloys were determined by fitting the data to the Tafel curves. Based on the electrochemistry concept, a high value of $E_{corr}$ and a low value of $i_{corr}$ are reliable indicators showing a material's good corrosion resistance (Qin et al., 2018; Abdelrhman et al., 2019). The polarisation resistance ($R_p$) was acquired using the Stern-Geary equation (see Eq. 6.1.) (Stern and Geary, 1957).

$$R_p = \frac{\beta_a \times \beta_c}{2{,}303 \times I_{corr}(\beta_a + \beta_c)} \quad \textbf{(6.1.)}$$

$R_p$ : Polarisation resistance (Ω/cm$^2$)

$\beta_a$ : The anodic Tafel slope (V dec$^{-1}$)

$\beta_c$ : The cathodic Tafel slope (V dec$^{-1}$)

$i_{corr}$ : Corrosion density (μA cm$^{-2}$)

## 6.1. Results

The corrosion performance of the low and highly porous Ti-xNb, Ti-20Zr and Ti-xNb-10Zr alloys sintered at 1200°C for six hours was determined by using a potentiostat (EZstat) to ascertain the effect of chemical formula on the Tafel plots. The detailed chemical compositions of the HBSS used in the electro-corrosion experiment are given in **Table 6.1**.

**Table 6.1.** The chemical compositions of HBSS used in the experiment (Zhang et al., 2018).

| **Components** | **Concentration (g/l)** |
|---|---|
| NaCl | 8.0 |
| $CaCl_2$ | 0.14 |
| KCl | 0.37 |
| $NaHCO_3$ | 0.30 |
| $C_6H_{12}O_6$ | 1.0 |
| $MgCl_2•6H_2O$ | 0.10 |
| $Na_2HPO_4•12H_2O$ | 0.03 |
| $KH_2PO_4$ •$12H_2O$ | 0.03 |
| $MgSO_4•7H_2O$ | 0.03 |

### 6.1.1. Corrosion Performance of Binary Titanium-Niobium Alloys

The corrosion behaviours of the low and highly porous binary Ti-xNb alloys sintered at 1200°C for six hours were examined by the Tafel extrapolation method in HBSS. The graphic data resulting from Tafel slopes are given in **Fig. 6.1**. Also, the corrosion kinetics parameters are listed in **Table 6.2**. $E_{corr}$ values for the low porous binary Ti-xNb alloys with different niobium concentrations (10, 20 and 30; at.%) were -0.64 mV, -0.26 mV, -0.21 mV; $i_{corr}$ values for these alloys were 0.65 µA.cm$^{-2}$, 1.63 µA.cm$^{-2}$, and 1,77 µA.cm$^{-2}$ respectively. According to this concept, the minimum corrosion rate was observed on the low porous binary Ti-30Nb alloy (porosity: 25%) with an $E_{corr}$ of -0.21 mV, and $i_{corr}$ of 1.77 µA.cm$^{-2}$, while the maximum was achieved from the low porous binary Ti-10Nb (porosity: 21%) alloy with an $E_{corr}$ of -0.64 mV and $i_{corr}$ of 0.65 µA.cm$^{-2}$. On the other hand, $E_{corr}$ values for the highly porous binary Ti-xNb alloys with different niobium concentrations (10, 20 and 30; at.%) were -0.51 mV, -0.27 mV, -0.22 mV; $i_{corr}$ values for these alloys were 0.84 µA.cm$^{-2}$, 1.45 µA.cm$^{-2}$ and 0.49 µA.cm$^{-2}$, respectively. According to this concept, the low and highly porous binary Ti-xNb alloys exhibited superior corrosion resistance and good passivity. In addition, as seen in the polarisation curves, a slight shift in the $E_{corr}$ values in the positive direction was observed depending upon increasing niobium concentration, which showed that a slight enhancement in the corrosion rate occurred (Li et al., 2018; Choubey et al., 2018; Pandey et al., 2022; Tanji et al., 2022). However, adding a space holder agent to the titanium matrix did not seriously change the corrosion rate of the highly porous binary Ti-xNb alloys. It was concluded that low and highly porous binary Ti-xNb alloys were good candidates for orthopaedic biomaterial application in terms of corrosion rate.

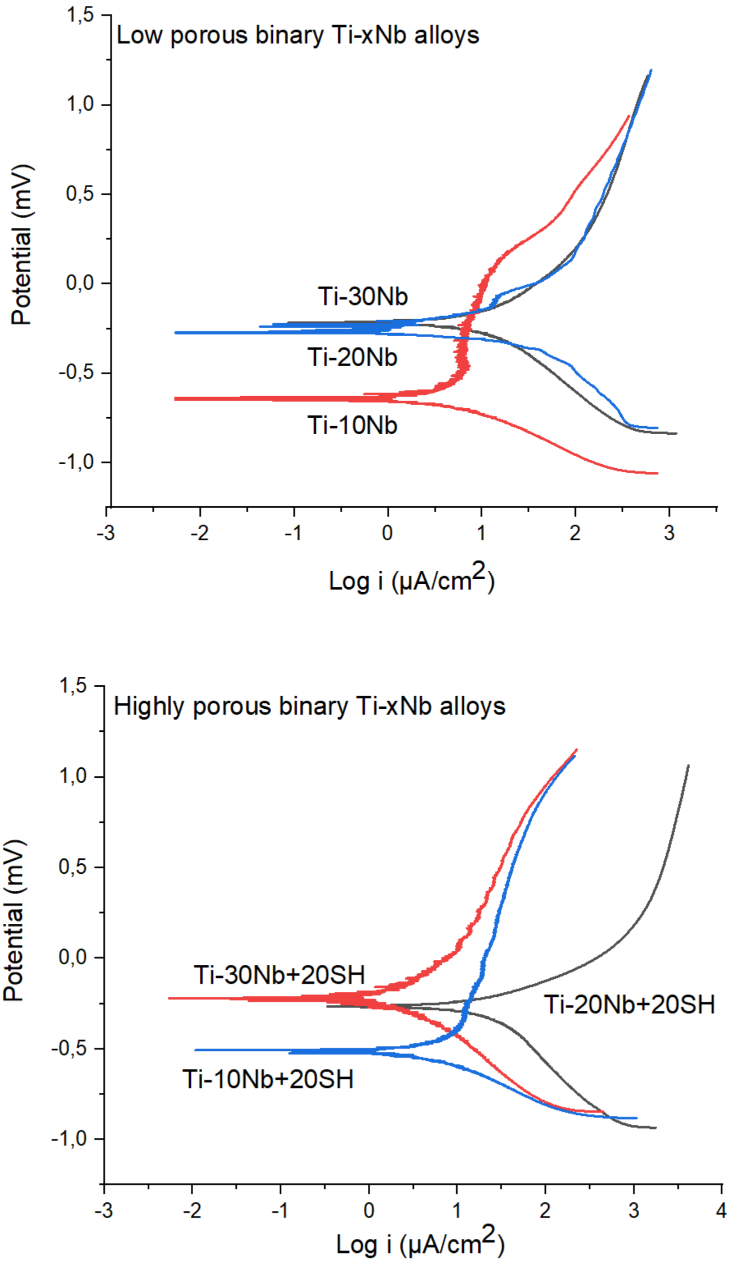

**Figure 6.1.** Representative polarisation curves for the low and highly porous binary Ti-xNb (x:10, 20 and 30; at.%) alloys.

**Table 6.2.** The corrosion kinetics parameters for low and highly porous binary Ti-xNb (x:10, 20 and 30; at.%) alloys in HBSS.

| | **$E_{corr}$ (mV.SCE)** | **$\beta_a$ (V dec$^{-1}$)** | **$\beta_c$ (V dec$^{-1}$)** | **$i_{corr}$ (µA/cm$^2$)** | **$R_p$ (Ω/cm$^2$)** |
|---|---|---|---|---|---|
| **Ti-10Nb** | -0.64 | 0.73 | 0.17 | 0.65 | 0.09 |
| **Ti-20Nb** | -0.26 | 1.24 | 0.47 | 1.63 | 0.08 |
| **Ti-30Nb** | -0.21 | 0.53 | 0.42 | 1.77 | 0.05 |
| **Ti-10Nb+20SH** | -0.51 | 0.65 | 0.22 | 0.84 | 0.085 |
| **Ti-20Nb+20SH** | -0.27 | 0.25 | 0.40 | 1.45 | 0,046 |
| **Ti-30Nb+20SH** | -0.22 | 0.54 | 0.17 | 0.49 | 0.11 |

### 6.1.2. Corrosion Performance of Binary Titanium-Zirconium Alloys

The polarisation curve of the low and highly porous binary Ti-20Zr alloys in HBSS is presented in **Fig. 6.2**. As stated before, the current density ($i_{corr}$) and potential ($E_{corr}$) values were calculated by using the extrapolation method. Tafel curves of anodic and cathodic branches (βa and βc) and other parameters are given in **Table 6.3**. Regarding this, the $E_{corr}$ values for low and highly porous binary Ti-20Zr alloys were −0.35 mV, −0.44 mV, while $i_{corr}$ values for these alloys were determined as 0.33 µA.cm$^{-2}$ and 0.67 µA.cm$^{-2}$, respectively. The polarisation resistances were calculated from the Stern-Geary equation given previously as 0.15 Ω/cm$^2$ for low porous binary Ti-20 alloy (porosity: 22%) and 0.14 Ω/cm$^2$ for highly porous binary Ti-20Zr alloy (porosity: 43%). As seen in **Fig. 6.2**, the anodic currents of the low and highly porous binary Ti-20Zr alloys increased by the potential applied. This behaviour showed that $Ti_xO$ or $Zr_yO$ (i.e., $Ti_2O_3$, $TiO_2$, and $ZrO_2$) films were formed on their surfaces. This is because titanium or zirconium reacts with oxygen, which can self-passivate the material and protect the alloys from corrosion (Cvijović-Alagić et al., 2011). As a result, low and highly porous binary Ti-20Zr alloys studied in this thesis were potential candidates for biomedical applications.

Relatively higher $E_{corr}$ and lower $i_{corr}$ values showed us that the low porous binary Ti-20Zr alloy exhibited slightly better corrosion resistance compared to other alloys. This slight difference in corrosion resistance could be because the exposed surface areas for the highly porous binary Ti-20Zr alloy were much higher than those for the low porous binary Ti-20Zr alloy during the polarisation test. According to this, adding a space holder to titanium-zirconium mixtures did not enhance the polarisation features.

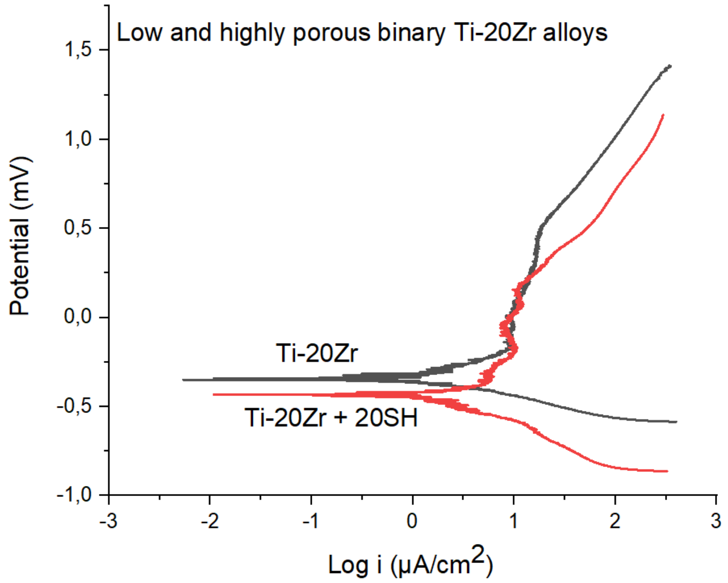

**Figure 6.2.** Representative polarisation curves for low and highly porous binary Ti-20Zr (at.%) alloys.

**Table 6.3.** The corrosion kinetics parameters for low and highly porous binary Ti-20Zr (at.%) alloys in HBSS.

| | **$E_{corr}$ (mV.SCE)** | **$\beta_a$ (V dec$^{-1}$)** | **$\beta_c$ (V dec$^{-1}$)** | **$i_{corr}$ (μA/cm$^2$)** | **$R_p$ (Ω/cm$^2$)** |
|---|---|---|---|---|---|
| **Ti-20Zr** | -0.35 | 0.74 | 0.14 | 0.33 | 0.15 |
| **Ti-20Zr + 20SH** | -0.44 | 0.80 | 0.30 | 0.67 | 0.14 |

### 6.1.3. Corrosion Performance of Ternary Titanium-Niobium-Zirconium Alloys

The typical cyclic potentiodynamic polarisation curve for the low and highly porous ternary Ti-xNb-10Zr alloys is given in **Fig. 6.3.** The summary of the results is also given in **Table 6.4.** $E_{corr}$ for low porous ternary Ti-xNb-10Zr (x: 10 and 20; at.%) alloys were found in a range from -0.07 mV to -0.077 mV in HBSS. The Tafel curve of low porous ternary Ti-20Nb-10Zr alloy (porosity: 28%) was slightly closer to the positive side of the corrosion potential, which revealed that this type of alloy had a lower current density ($i_{corr}$: 2.26 μA.cm$^{-2}$) than low porous ternary Ti-10Nb-10Zr alloys (porosity: 20%) ($i_{corr}$: 2.40 μA.cm$^{-2}$). Further, $R_p$ values for low porous ternary alloys were about 0.09 Ω/cm$^2$ for Ti-10Nb-10Zr and 0.06 Ω/cm$^2$ for Ti-20Nb-10Zr. This finding indicated that the corrosion rate for low porous ternary Ti-20Nb-10Zr alloys was slightly lower than that for low porous ternary Ti-10Nb-10Zr alloys due to increased niobium concentrations in titanium-zirconium mixtures. On the other hand, $E_{corr}$ for the highly porous ternary Ti-xNb-10Zr (x: 10 and 20; at.%) alloys were -0.55 mV and -0.48 mV, while $i_{corr}$

for these alloys was about 0.67 µA.cm$^{-2}$ and 0.39 µA.cm$^{-2}$, respectively. Further, $R_p$ values calculated from these results ($E_{corr}$ and $i_{corr}$) were 0.12 Ω/cm$^2$ and 0.16 Ω/cm$^2$, respectively. As understood from the $R_p$ values, the low and highly porous ternary Ti-xNb-10Zr alloys fabricated in this study exhibited enhanced corrosion resistances, as adding niobium and zirconium contributed to the formation of the oxide film. In conclusion, low and highly porous ternary Ti-xNb-10Zr alloys had superior corrosion behaviours and were suitable for use as orthopaedic biomaterials.

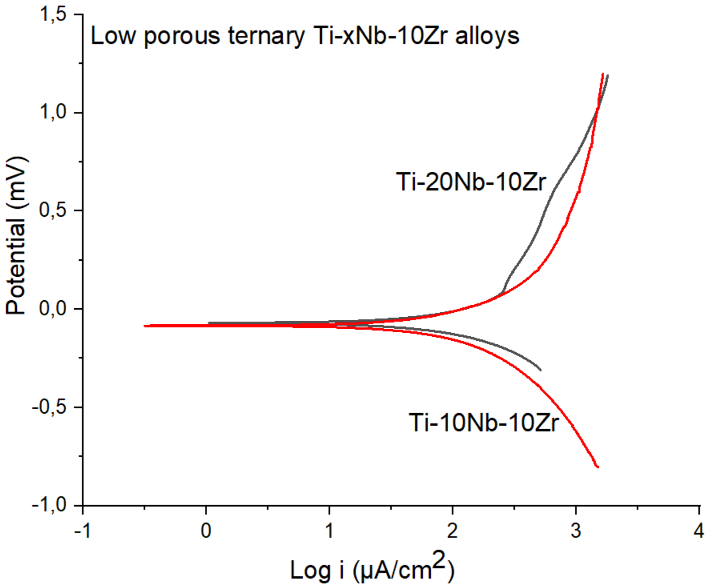

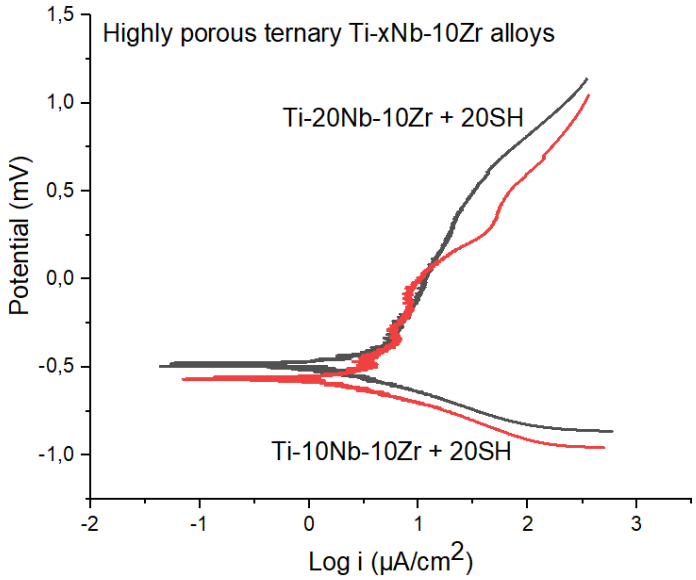

**Figure 6.3.** Representative polarisation curves for low and highly porous ternary Ti-xNb-10Zr (x: 10 and 20; at.%) alloys.

**Table 6.4.** The corrosion kinetics parameters for low and highly porous ternary Ti-xNb-10Zr (x: 10 and 20; at.%) alloys in HBSS.

| | **$E_{corr}$ (mV.SCE)** | **$\beta_a$ (V $dec^{-1}$)** | **$\beta_c$ (V $dec^{-1}$)** | **$i_{corr}$ (µA/$cm^2$)** | **$R_p$ (Ω/$cm^2$)** |
|---|---|---|---|---|---|
| **Ti-10Nb-10Zr** | -0.07 | 1.75 | 0.75 | 2.40 | 0.09 |
| **Ti-20Nb+10Zr** | -0.077 | 1.52 | 0.4 | 2.26 | 0.06 |
| **Ti-10Nb-10Zr + 20SH** | -0.55 | 0.86 | 0.24 | 0.67 | 0.12 |
| **Ti-20Nb+10Zr + 20SH** | -0.48 | 0.92 | 0.18 | 0.39 | 0.16 |

## 6.2. Discussion

The unique combination of acceptable strength properties, good corrosion resistance, and superior biocompatible features makes titanium-based alloys highly attractive for biomedical, aerospace, and chemical industries (Makurat-Kasprolewicz and Ossowska, 2023). In particular, corrosion performance is a key factor in determining the reliability and durability of titanium-based alloys for biomedical applications (Seo et al., 2023). Potentiodynamic polarisation results showed that the low porous Ti-xNb, Ti-20Zr and Ti-xNb-10Zr alloys met the corrosion performance criteria required for orthopaedic biomaterial use although these alloys had inhomogeneous structures caused by powder metallurgy. This is mainly due to the fact that the individual elements that make up the alloys are resistant to corrosion (Majumdar et al., 2023; Chen et al., 2023). The same tendency was observed in the highly porous alloys. This situation showed that general porosity did not play a vital role in corrosion resistance of the alloys achieved in this thesis. This result was consistent with other studies. Accordingly, influence of general porosity on the corrosion performance is not straightforward. However, it can be said that increased general porosity of the material may be slightly caused reduced corrosion resistance (Guerra et al., 2020). General porosity created by space holders can generate areas where corrosion is more likely to initiate and propagate. Therefore, highly porous alloys exhibited slightly lower corrosion resistance compared to low porous alloys. Nevertheless, the low and highly porous Ti-xNb, Ti-20Zr, and Ti-xNb-10Zr alloys had superior corrosion behaviours and were suitable for use as orthopaedic biomaterials. This finding had a positive effect on the biocompatibility features of the alloys. It was concluded that general porosity should be carefully controlled to obtain the desired corrosion resistance.

However, adding niobium had a crucial effect on the corrosion rate of the alloys achieved in this thesis. Niobium can promote the formation of a stable and protective oxide layer on the surface of the alloy, which enhances the alloy's corrosion resistance. However, optimal niobium concentration is related to different parameters and should be controlled according to the specific application. Our findings on corrosion resistances of fabricated all-porous Ti-xNb, Ti-20Zr and Ti-xNb-10Zr alloys were supported by other studies. Increased niobium concentration improved the corrosion resistances of the low and highly porous Ti-xNb, Ti-xNb-10Zr alloys.

Corrosion performances of Ti-xNb and Ti-xNb-10Zr alloys were determined to be more sensitive to niobium concentration in titanium matrix than general porosity level, while mechanical behaviour of the alloys achieved in this thesis were dramatically affected by general porosity. All elements (titanium, zirconium, and niobium) used in this thesis exhibited biocompatible features. In this context, the main criterion that will determine the success of the alloys produced in this thesis is the mechanical properties of the alloys. Obtaining mechanical properties close to bone tissue is essential in this study. It is a fact that; The mechanical properties of highly porous Ti-xNb, Ti-20Zr and Ti-xNb-10Zr alloys were closer to the mechanical properties of bone tissue. This also reduced the risk of stress shielding effect.

# Chapter 7. In Vitro Analysis

This chapter discusses fibroblasts of the L929 cell type, which are the most abundant cells in the connective tissues of animals and have many functions. Their main function is to synthesise the protein collagen, which plays a crucial role in wound healing (Cannella et al., 2019). Osteoblasts of the Saos-2 cell type are another type of cell that can mimic the response of human bone. Therefore, in this thesis, these types of cell lines were selected to examine during in vitro studies such as cell viability and proliferation, adhesion potential, and genotoxicity, fibronectin adsorption and plasmid-DNA interaction assay.

## 7.1. Results

### 7.1.1. In Vitro Analysis of Binary Titanium-Niobium Alloys

Cytotoxicity assay extract method: The cell viability percentage of L929 and Saos-2 exposed to the low and highly porous binary Ti-xNb alloys, Dulbecco's modified eagle medium - Cell Culture Ingredients (DMEM), and the TiGR4 (reference sample) extracts for one day, three days and seven days is reported in **Fig. 7.1** ($p < 0.05$)**.** According to the results obtained, the different incubation times (one day, three days and seven days) did not lead to any dramatic influence on the L929 and Saos-2 cell viabilities, which demonstrated that all examined binary Ti-xNb alloys were not cytotoxic or allergic at tested conditions. In this regard, the cell viability upon exposure to the extracts of all-porous binary Ti-xNb alloys studied in this thesis was found to be 87% to 96% for L929 and 73% to 90% for Saos-2 cell lines ($p < 0.05$). The maximum L929 cell viability rate of 99.42% was observed in highly porous binary Ti-30Nb alloy with general porosity of 58% for seven days. This finding was even higher than the cell viability rates of TIGR4. This behaviour showed that highly porous structures within such alloys promoted biological fixation by providing sites for cell growth and proliferation. This is because the presence of highly porous structures has a specific effect: it encourages and supports the attachment and growth of cells. This phenomenon is significant in medical and tissue engineering applications. The minimum L929 cell viability rate of 87.35% was found in low porous binary Ti-10Nb alloys with general porosity of 20%. This finding was almost identical to cell viability rates of TIGR4 for all incubation times. Parallel results were obtained from the Saos-2 cell line viabilities. Here, the highly porous binary Ti-30Nb alloy with general porosity of 58% for seven days exhibited the highest Saos-2 cell viability rate of 89.71%, while the highly porous binary Ti-10Nb alloy with general porosity of 55% for one day had the lowest rate at 70%. Even though all-porous binary Ti-xNb alloys were found to be biocompatible, they had significant differences in cell viability. However, these results showed that all pore characteristics achieved in this thesis provided an adequate site for cell ingrowth and proliferation. According to this concept, low and highly porous binary Ti-xNb alloys had excellent L929 and Saos-2 cell viability for all incubation times. Alloying niobium with titanium and adding a space holder improved the L929 and Saos-2 cell viability of titanium-niobium mixtures. In conclusion, the results revealed that the low and highly porous binary Ti-xNb alloys studied in this thesis provided the criteria of biocompatibility required for the use of orthopaedic biomaterial, which was at least 70% according to ISO 10993-5.

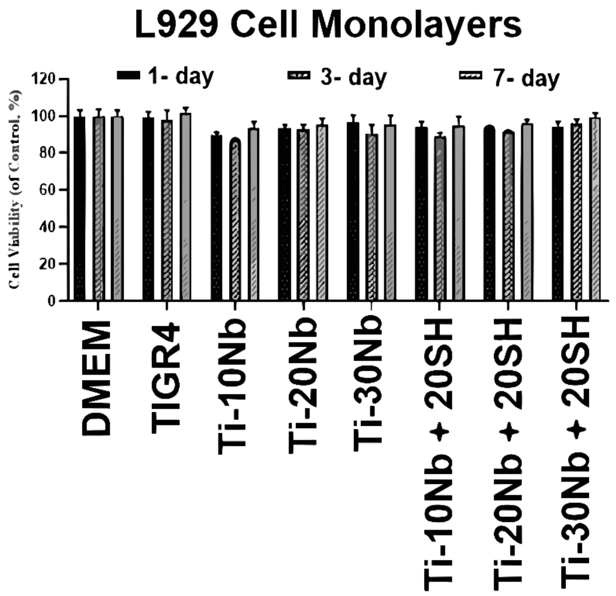
L929 Cell Monolayers

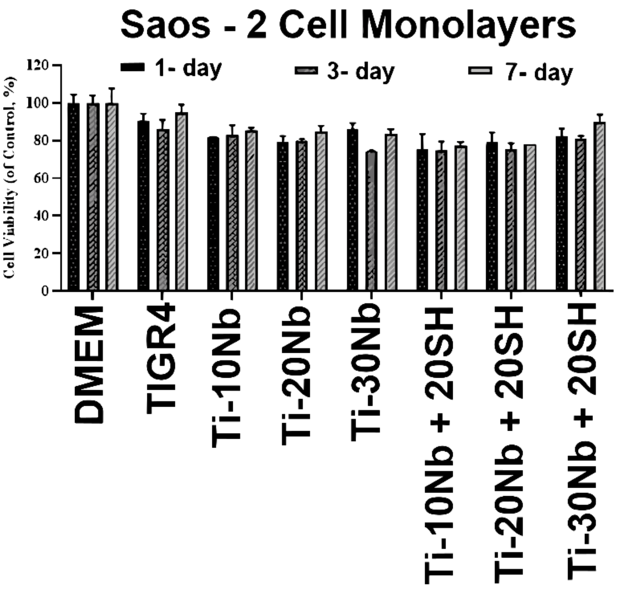
Saos - 2 Cell Monolayers

**Figure 7.1.** The cell viability of L929 and Saos-2 exposed to the extracts of the reference TiGR4 and all-porous binary Ti-xNb (x:10, 20 and 30; at.%) alloys for one day, three days and seven days and measured by MTT assay (data represent mean ± SD, n = 3. for $p < 0.05$).

The violet formazan crystals are a product of the MTT assay. It is a reliable indicator for showing proliferation and cell viability in vitro. At his point, the MTT assay can be widely employed for analysing the cell viability and proliferation. The intensity of the formazan colour gives us number of viable cells. The images of the violet formazan crystals occurring due to the activity of viable L929 and Saos-2 cells upon exposure to the extracts of DMEM and the reference TiGR4, low and highly porous binary Ti-xNb alloys for one day, three days and seven days were taken under an optical microscope (see **Fig. 7.2.**). The results of MTT assay obtained from quantitative OD values were statistically analysed. **Fig. 7.2** showed that intensity of L929 cell line was better than that of Saos 2 cell line. This was dependent on many factors such as cell type used, substrate, temperature, or other cell conditions. According to the results obtained from **Fig. 7.3.**, dark areas on the optical images showed the number of viable cells distribution in the alloy. Proportion of the dark areas increased according to increasing incubation times (1day, 3-day, and 7-day). It was concluded that L929 and Saos-2 cell monolayers exhibited good cellular morphology and good interaction between L929 and Saos-2 cells and substrates for all incubation times.

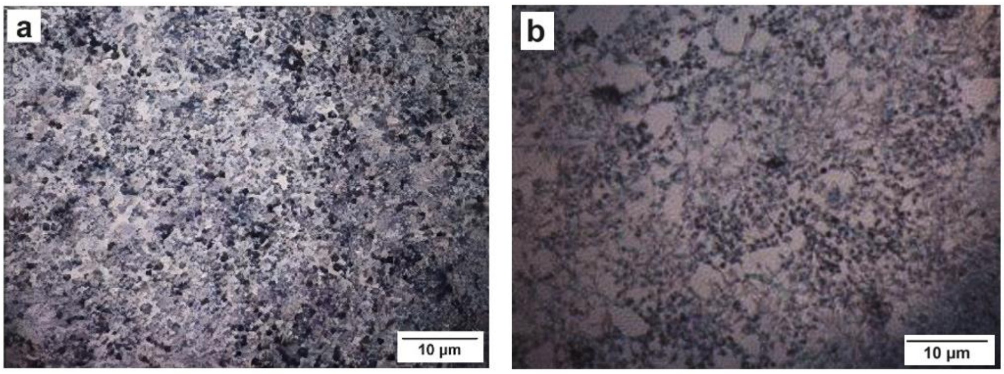

**Figure 7.2.** The observed cell morphology of (a) L929 and (b) Saos 2 cells on DMEM after being treated for 24 h.

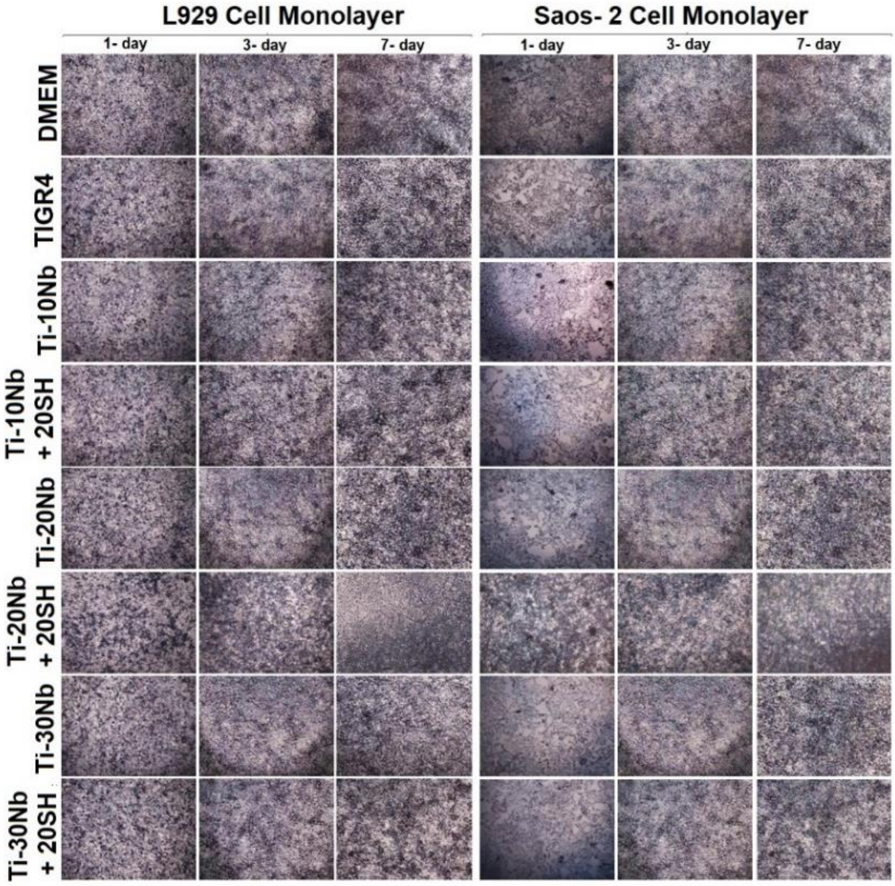

**Figure 7.3.** Images of violet formazan crystals occurring due to the activity of viable L929 cells and Saos-2 cells upon exposure to the extracts of DMEM, TiGR4 and all-porous binary Ti-xNb (x:10, 20 and 30; at.%) alloys for one day, three days and seven days with 10X magnification.

Live-dead viability extract method: The Live/Dead viability extract method is a method employed to see live and dead cells in an implant material. L929 and Saos-2 cells were exposed to DMEM and the reference TiGR4, the low and highly porous binary Ti-xNb alloy extracts for one day, three days and seven days. The fluorescent agents were then added to observe the live and dead cells (see **Fig.7.4.**). In addition to the calorimetric MTT assay, the cell viability of L929 and Saos-2 were qualitatively observed after 24 hours of treatment with the all-porous binary Ti-xNb alloys, DMEM, and TIGR4. As illustrated in **Fig.7.4**, the high green fluorescence intensity was seen in both cell monolayers. The red fluorescence intensity was not clearly visible from the optical images of the alloys achieved in this thesis. The optical images with 10x magnification qualitatively confirmed the increased cell viability and proliferation of all-porous binary Ti-xNb alloys with increased green fluorescence.

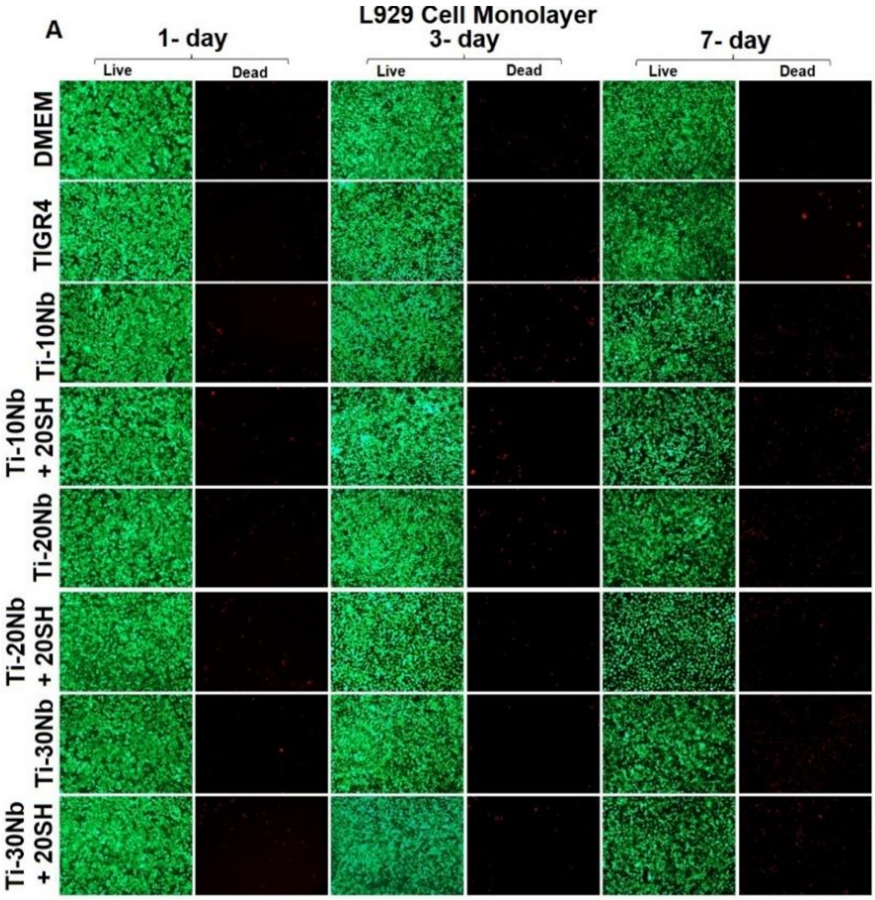
A
L929 Cell Monolayer
1- day
3- day
7- day
Live
Dead
Live
Dead
Live
Dead
DMEM
TIGR4
Ti-10Nb
Ti-10Nb + 20SH
Ti-20Nb
Ti-20Nb + 20SH
Ti-30Nb
Ti-30Nb + 20SH

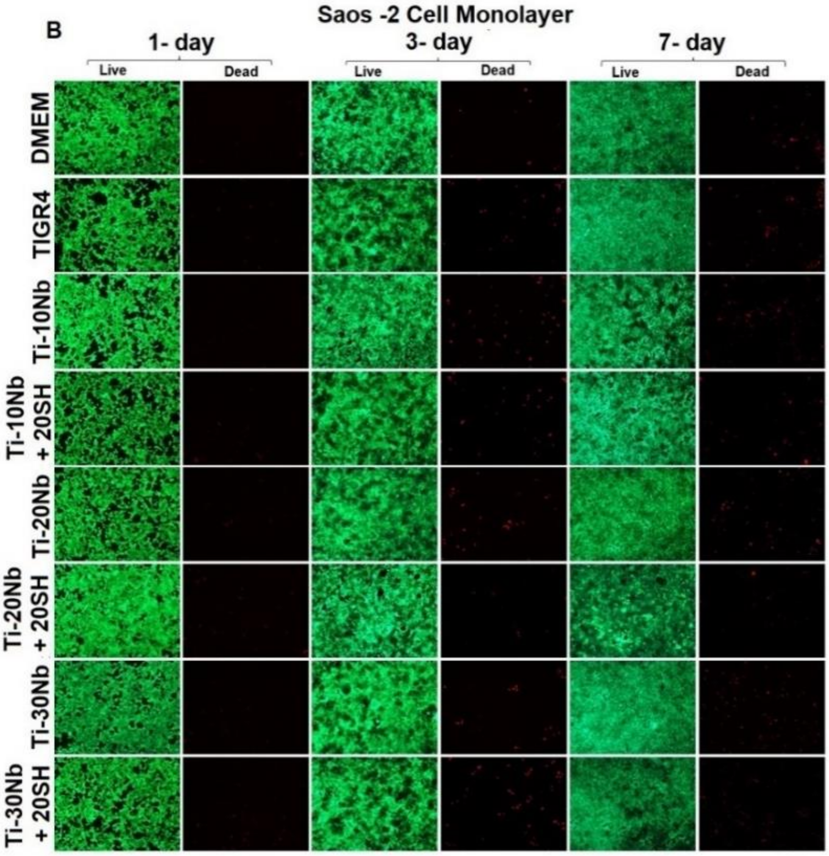

**Figure 7.4.** The images of L929 cells and Saos-2 cells upon exposure to the extracts of the TiGR4, DMEM, and all-porous binary Ti-xNb (x:10, 20 and 30; at.%) alloys for one day, three days and seven days were taken by fluorescence microscope with 10X magnification. Green fluorescent calcein (ex/em ~495 nm/~515 nm) was retained in the live cells and red fluorescent Ethidium homodimer, EthD-1 (ex/em ~495 nm/~635 nm) bound to the nucleic acids in the membrane-damaged dead cells.

Fibronectin adsorption: Fibronectin adsorption have a crucial role in migration, cell adhesion, proliferation, and cell viability in vitro. It was determined after two hours of incubation at 37°C in a 5% $CO_2$ atmosphere by the ELISA method (data represent mean ± SD, n = 3. for $p < 0.05$) (see **Fig. 7.5.**). Increasing the niobium concentration from 10% to 30% in titanium-niobium mixtures did not significantly affect the fibronectin adsorption capacity of the all-porous binary Ti-xNb alloys. However, higher porosity dramatically increased the fibronectin adsorption capacity of the highly porous binary Ti-xNb alloys ($p < 0.05$). Moreover, the fibronectin adsorption capacity of the examined low and highly porous binary Ti-xNb alloys was correlated with the results of the cell viability and morphological images.

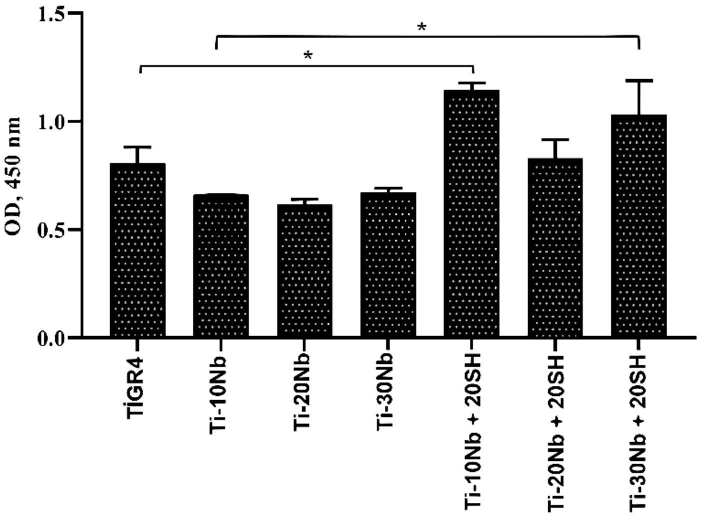

**Figure 7.5.** Fibronectin adsorption on the TIGR4, all-porous binary Ti-xNb (x:10, 20 and 30; at.%) alloy disks after two hours of incubation at 37°C in a 5% $CO_2$ atmosphere (data represent mean ± SD, n = 3 for $p<0.05$).

Plasmid-DNA interactions: To extensively examine the biocompatibility in vitro, the DNA damage was also evaluated by genotoxicity. The migration pattern of plasmid DNA incubated with extracts of the developed low and highly porous binary Ti-xNb alloys, negative control group and TiRG4 reference materials is shown in **Fig. 7.6.** The bands achieved in this thesis were labelled as NC: Nicked circular, SC: supercoiled, $ddH_2O$ was served as negative control. According to this, highly porous Ti-10Nb alloy exhibited Nicked circular DNA plasmid form, while the other alloys displayed supercoiled DNA form, including TiGRA 4 and negative control group. These results achieved showed that neither low porous nor highly porous binary Ti-xNb alloys induced DNA damage into L929 and Saos-2 cell lines. In other words, the low and highly porous binary Ti-xNb alloys studied in this thesis did not interact with the DNA plasmid.

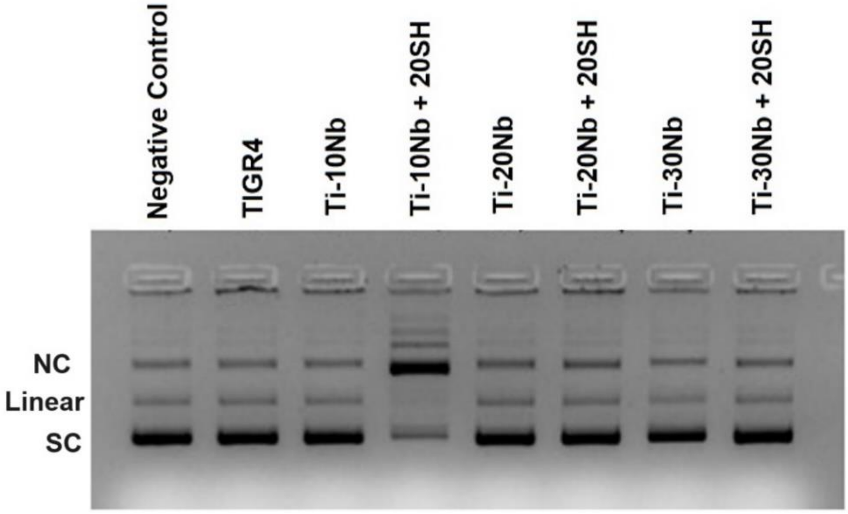

**Figure 7.6.** Plasmid-DNA interaction assay for the negative control, TIGR4, and all-porous binary Ti-xNb (x:10, 20 and 30; at.%) alloys (NC: nicked circular; SC: supercoiled).

Scanning electron microscopy showing cell morphology observation (SEM): To investigate L929 and Saos-2 cell morphologies, SEM micrographs of L929 and Saos-2 cell types planted on polished all-porous binary Ti-xNb alloys and TIGR4 were evaluated by SEM at 500X and 2500X magnifications. Here, Saos-2 cells attached to the surfaces of Ti-xNb alloy disk after 72 hours was observed (see **Fig. 7.7.**). Saos 2 cell adherence on Ti-xNb alloys was good as understood from **Fig. 7.7**.

SEM images of viable L929 and Saos-2 cells on TiGR4 and all-porous binary Ti-xNb (x: 10, 20 and 30; at.%) alloys for one day and seven days with 2500X and 500X magnifications are given in **Fig. 7.8.** The existence of viable L929 cell lines suspended on the substrate was normal because L929 cell lines came detached from the surface by becoming round during the division. On the other hand, smooth morphological images of Saos-2 cells on the substrates were seen that were connected by cytoplasmic extensions, and the Saos-2 cells were also well spread. As foreseen, the surface roughness of the highly porous binary Ti-xNb alloys with an average general porosity of 56% was higher than those of low porous binary Ti-xNb alloys with an average general porosity of 24%. However, because the surface roughness of the low and highly porous Ti-xNb (x: 10, 20 and 30; at.%) was quite high, there were no big differences between the cell attachment and proliferation of Saos-2 and L929 cells. In conclusion, L929 and Saos-2 cells were well attached to the surface of the all-porous binary Ti-xNb alloys, which revealed that good integration with the substrate was achieved for both low and highly porous binary Ti-xNb alloys.

Unlike vanadium, nickel and aluminium added for alloying Ti-6Al-4V, the most commonly used implant material, niobium in a titanium matrix, did not adversely affect cell growth and proliferation. Based on the results, niobium can be safely employed as an alloyant element. As a result, in vitro biocompatibility of all-porous binary Ti-xNb alloys did not induce toxic or allergic response for L929 and Saos-2 cell lines, indicating that adding the niobium element to the titanium matrix would not cause cytotoxicity.

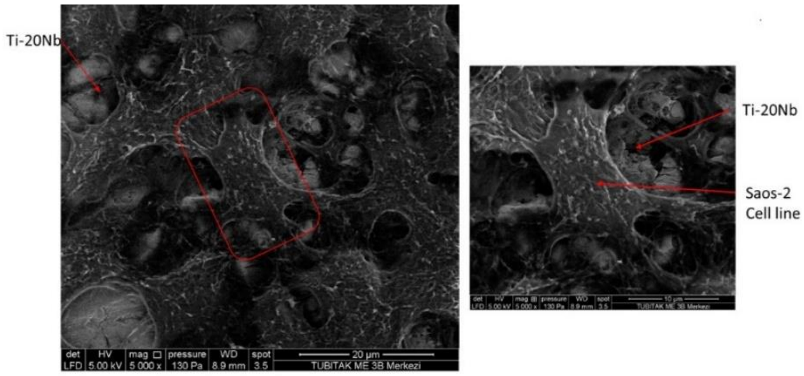

**Figure 7.7.** SEM images of Saos-2 cells seeded on Ti-xNb alloy disk and incubated for 72 hours.

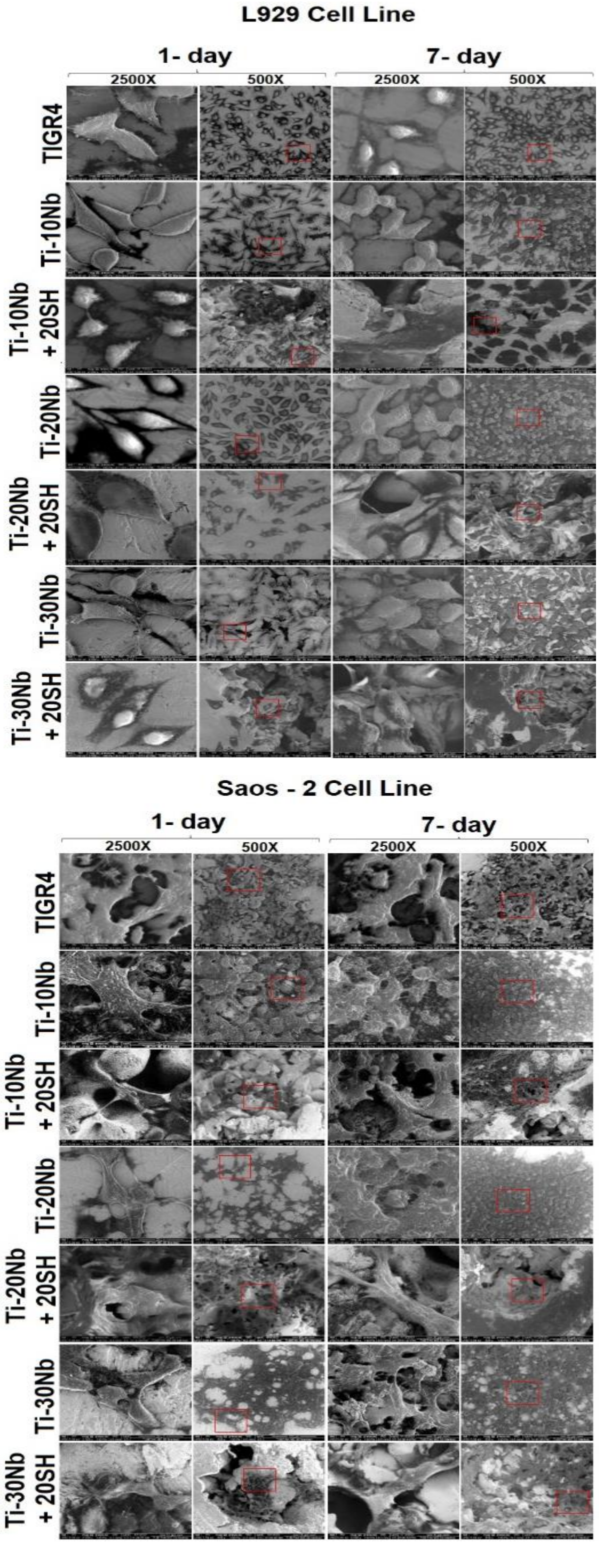

**Figure 7.8.** SEM images of viable L929 and Saos-2 cells on TiGR4 and all-porous binary Ti-xNb (x: 10, 20 and 30; at.%) alloys for one day and seven days with 2500X and 500X magnifications.

### 7.1.2. In Vitro Analysis of Binary Titanium-Zirconium Alloys

Cytotoxicity assay extract method: The cell viability of L929 and Saos-2 exposed to the low and highly porous binary Ti-20Zr alloys, DMEM, and the reference TiGR4 extracts for one day, three days and seven days is presented in **Fig. 7.9.** ($p < 0.05$)**.** All examined binary Ti-20Zr alloys did not exhibit cytotoxic effects at tested conditions. The cell viability upon exposure to the extracts of the examined all-porous binary Ti-20Zr alloys was found to be 86% to 99% for L929 and 82% to 93% for Saos-2 cell lines. Unexpectedly, the highest L929 cell viability rate of 99% was observed in low porous binary Ti-20Zr alloy with general porosity of 22% for seven days, while the lowest L929 cell viability rate of 76.5% was found in highly porous binary Ti-20Zr alloy with general porosity of 43% for one day. On the other hand, the maximum Saos-2 cell viability rate of 84.78% was determined in the highly porous binary Ti-20Zr alloy with general porosity of 43% for three days, while the minimum rate of 79.42% was found in the highly porous binary Ti-20Zr alloy with general porosity of 43% for three days. These findings demonstrated that all-porous binary Ti-20Zr alloys for incubation periods of one day, three days and seven days were bio-safe and the use of zirconium and its combination with the 20 wt.% space holders did not improve the potential of the alloy as an orthopaedic biomaterial.

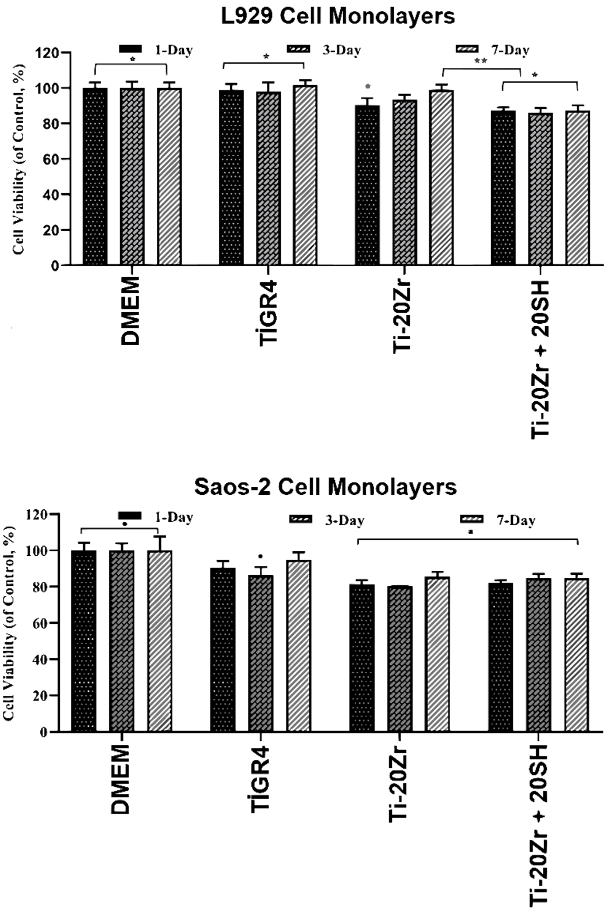

**Figure 7.9.** The cell viability of L929 and Saos-2 exposed to the extracts of DMEM, TiGR4, and all-porous binary Ti-20Zr (at.%) alloys for one day, three days and seven days measured by MTT assay (data represent mean ± SD, n = 3. for $p < 0.05$).

The proportion of formazan crystals show the intensity of living cell lines on the substrate and it is widely employed to determine calculate number of living cells. To confirm qualitative cell viability results, the images of the live cells upon formation of the formazan salt with violet colour upon low and highly porous binary Ti-20Zr alloys are presented in **Fig. 7.10**. Black spots on the optical images were showing densification of the L929 and Saos 2 cell line, while grey areas was classified as substrate. The L929 and Saos 2 cell lines grown on the low and highly porous binary Ti-20Zr alloys, were spread to a great extent and intimately attached to surfaces an almost comparable manner to that of TiGR4 and DMEM. The Saos-2 cells exhibited less spreading patterns compared to that of L929 counterparts. Nevertheless, the optical images demonstrated that L929 and Saos-2 cells cultured in the extract of low and highly binary Ti-20Zr alloys grew well. Further, the L929 and Saos-2 cells grown on the all-porous binary Ti-20Zr alloys were spread to a great extent. When the incubation times of one day, three days and seven days were compared, an increase in the number of cells was determined, which qualitatively revealed the cell viability. Therefore, this finding suggested good cytocompatibility for all-porous binary Ti-20Zr alloys.

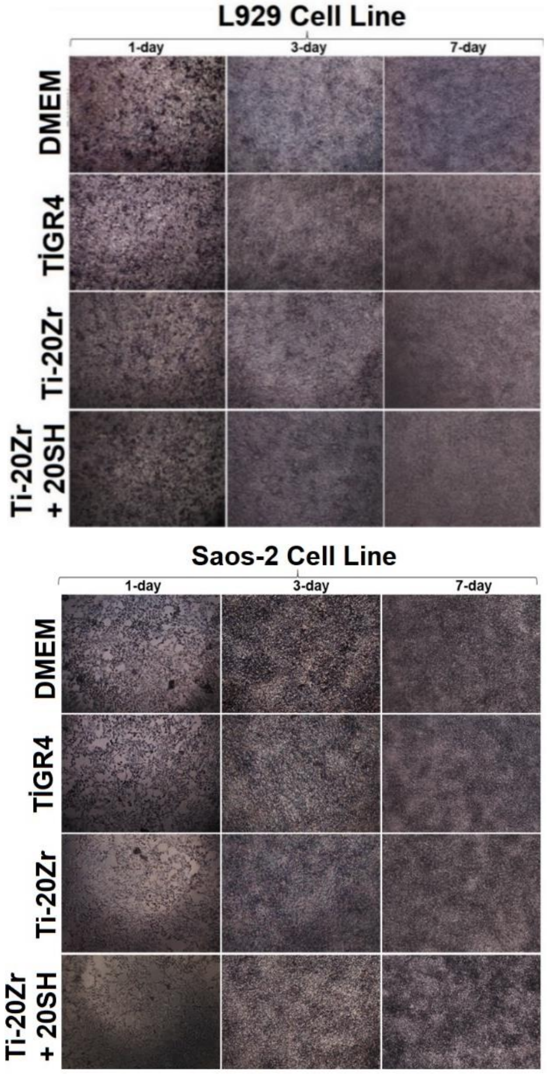

**Figure 7.10.** Images of violet formazan crystals occurring due to the activity of viable L929 and Saos-2 cells upon exposure to the extracts of DMEM, TiGR4 and all-porous binary Ti-20Zr (at.%) alloys for one day, three days and seven days with 10X magnification.

Live-dead viability extract method: The viability of L929 and Saos-2 cell lines were evaluated by means of a Live-dead viability extract method, in which the formation of green fluorescence is a direct significance of the proportion of living cells. The fluorescent images indicated that intense green fluorescence refers to living cells, while red fluorescence was linked to dead cells. In addition to the calorimetric MTT assay, the cell viability of L929 and Saos-2 were qualitatively observed after 24 hours of treatment with the all-porous binary Ti-20Zr alloys and the controls (see **Fig. 7.11.**). The fluorescence images of L-929 and Saos-2 cell types cultured for one day, three days and seven days in the extracts of low and highly porous binary Ti-20Zr alloys, DMEM, and TIGR4 increased with incubation times. This indicated outstanding cell growth, confirming that all-porous binary Ti-20Zr alloys had high metabolic activity for all incubation times.

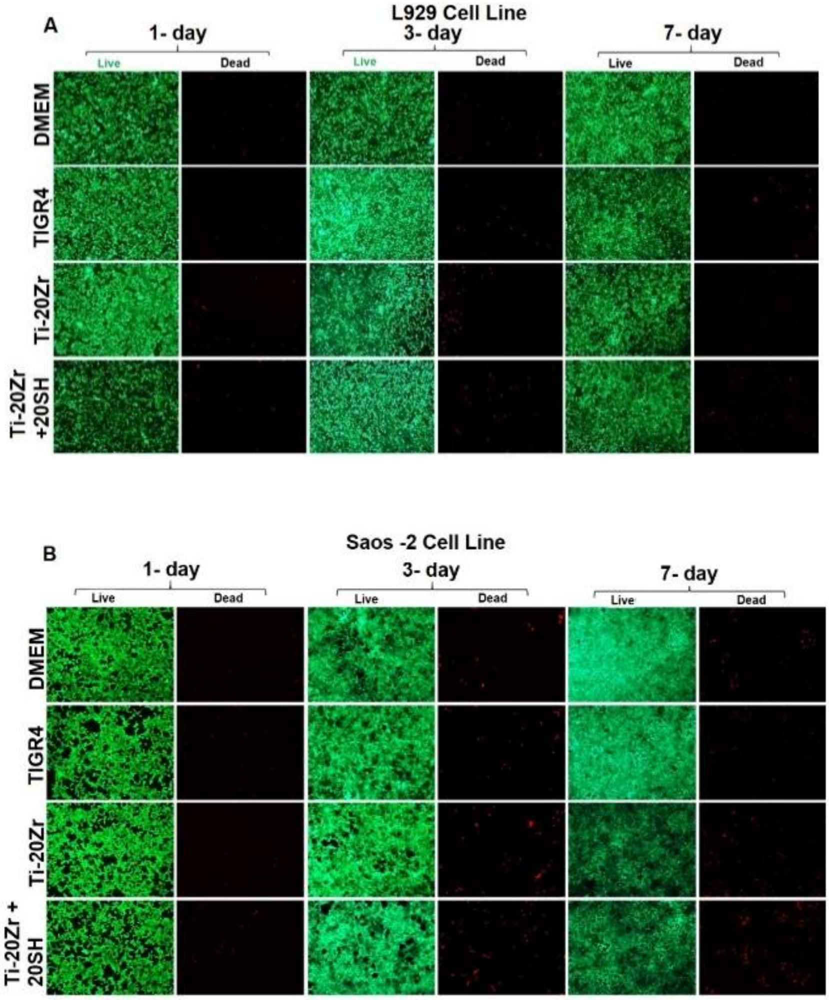

**Figure 7.11.** The images of L929 cells and Saos-2 cells upon exposure to the extracts of DMEM, TiGR4 and all-porous binary Ti-20Zr (at.%) alloys for one day, three days and seven days were taken by fluorescence microscope with 10X magnification. Green fluorescent calcein (ex/em ~495 nm/~515 nm) was retained in the live cells and red fluorescent Ethidium homodimer, EthD-1 (ex/em ~495 nm/~635 nm) bound to the nucleic acids in the membrane-damaged dead cells.

Fibronectin adsorption: L929 and Saos-2 cell proliferation, migration, and tissue integration on the low and highly porous binary Ti-20Zr alloys were examined by measuring the adsorption potential of fibronectin protein on their surfaces with the ELISA (see **Fig. 7.12.**). The low porous binary Ti-20Zr alloy exhibited much less fibronectin adsorption capacity than the reference material TiRG4 and another alloy ($p < 0.05$). As seen from the **Fig. 7.12**, higher porosity led to high fibronectin absorption since pores increased the penetration of fibronectin.

Additionally, TIGR4 reference showed better fibronectin adsorption than low and highly porous binary Ti-Zr alloys.

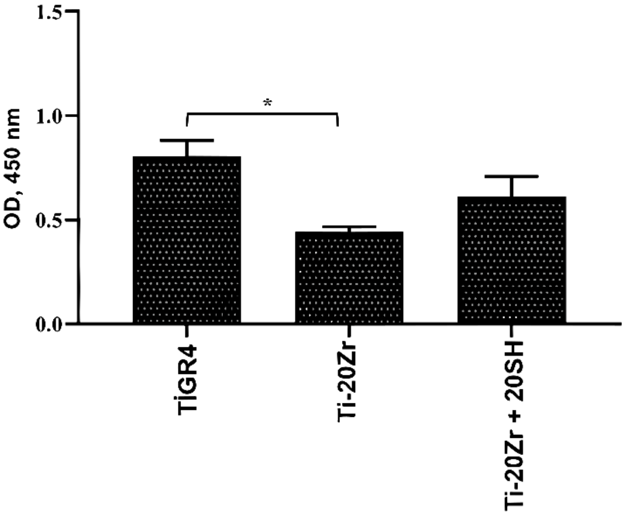

**Figure 7.12.** Adsorption of fibronectin on TIGRA and all-porous Ti-20Zr (at.%) binary alloy disks after two hours of incubation at 37°C in a 5% $CO_2$ atmosphere (data represent mean ± SD, n = 3 for $p<0.05$).

Plasmid-DNA interactions: A plasmid-DNA interaction assay was performed to compare the negative control group and TİGR4 material during long-term interaction with the tissues (see **Fig. 7.13.**). The band achieved in this thesis were labelled as NC: Nicked circular, SC: supercoiled, $ddH_2O$ was served as negative control. The plasmid-DNA interaction of the alloy extracts was examined, and low porous Ti-20Zr alloys exhibited nicked circular DNA plasmid form, while highly porous Ti-20Zr alloys displayed supercoiled DNA plasmid form that can occur naturally including negative control group and TiGR4 reference. The low porous binary Ti-20Zr alloys exhibited the same pattern compared with that of the biocompatible TiGR4 reference and negative control. Also, highly porous binary Ti-20Zr alloy did not show genotoxic effect. Consequently, the results confirmed no induced genotoxic potential. Plasmid-DNA all-porous binary Ti-20Zr alloy interaction assay also demonstrated good biocompatibility of the developed alloys. None of the tested alloys caused DNA fragmentation, which proved the non-genotoxicity of the alloys.

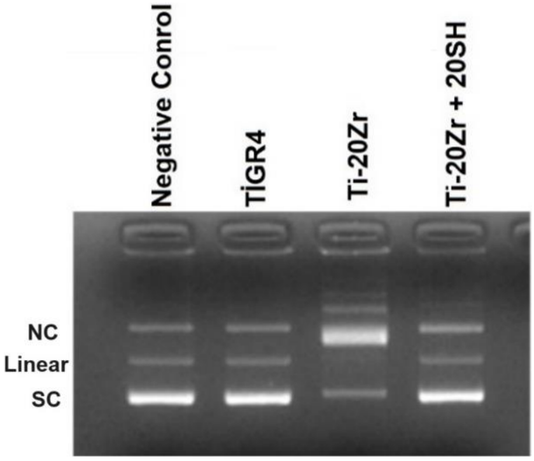

**Figure 7.13.** Plasmid-DNA interaction assay for the negative control, TIGR4, and all-porous binary Ti-20Zr (at.%) alloys (NC: Nicked circular, SC: supercoiled).

Scanning electron microscopy showing cell morphology: SEM images of Saos-2 cells seeded on Ti-20Zr alloy disk is given in **Fig. 7.14.** Accordingly, Saos-2 cell adherence on Ti-20Zr alloy was in good level due to porous structure. SEM micrographs of L929 and Saos-2 cells seeded on polished low and highly porous binary Ti-20Zr alloys and TIGR4 are given in **Fig. 7.15.** No dramatic morphological alterations of L929 and Saos-2 cell types for one day and seven days were observed. This finding showed that the general porosity of both low and highly porous Ti-20Zr binary alloys provided adequate sites for cell growth. Moreover, adherences of L929 cell line exposure to the extracts of all-porous alloys were better than those of the Saos-2 cell line. In conclusion, the biocompatibility in vitro of low and highly porous binary Ti-20Zr alloys was judged to be good.

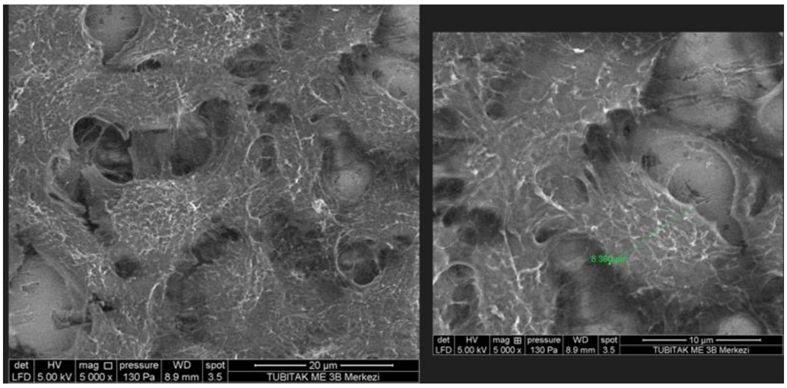

**Figure 7.14.** SEM images of Saos-2 cells seeded on Ti-20Zr alloy disk and incubated for 72 hours.

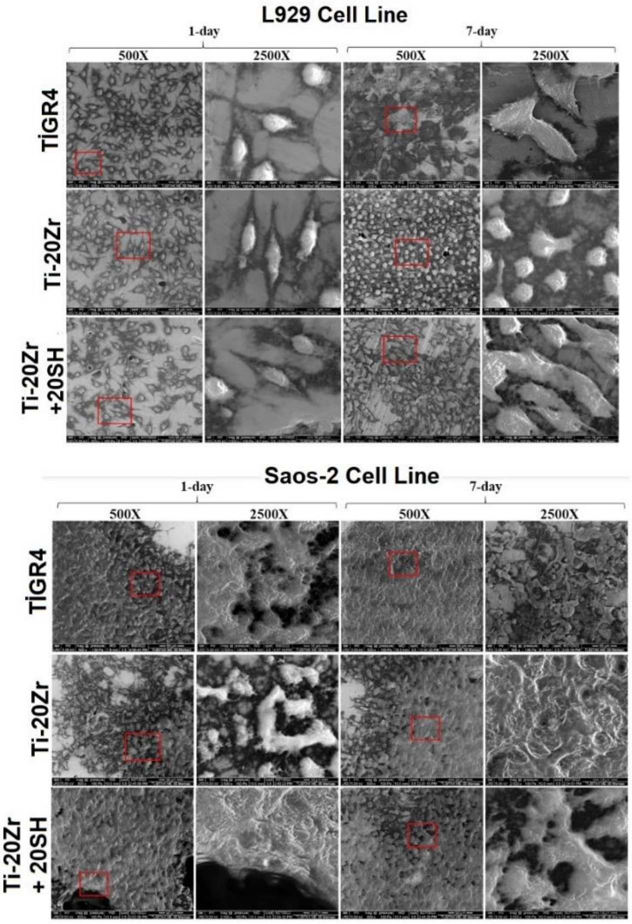

**Figure 7.15.** SEM images of viable L929 and Saos-2 cells on TiGR4 and all-porous binary Ti-20Zr (at.%) alloys for one day and seven days with 2500X and 500X magnifications.

### 7.1.3. In Vitro Analysis of Ternary Titanium-Niobium-Zirconium Alloys

Cytotoxicity assay extract method: The cell viability of L929 and Saos-2 exposed to the low and highly porous ternary Ti-xNb-10Zr alloys, DMEM, and the reference TiGR4 extracts for one day, three days and seven days is reported in **Fig. 7.16** ($p < 0.05$)**.** Based on the results achieved from the cytotoxicity assessment, the low and highly porous ternary Ti-xNb-10Zr alloys did not lead to allergic or toxic effects and exhibited good viability of L929 and Saos-2 cell types. Further, all incubation times studied showed good L929 and Saos-2 cell viability, which was a good indication for implantology. The cell viability upon exposure to the extracts of the examined low and highly porous ternary Ti-xNb-10Zr alloys was found to be 77% to 97% for L929 and 72% to 80% for Saos-2 cell lines, which revealed that they had significant differences in cell viability. The maximum L929 cell viability rate of 97.02% was found in the low porous ternary Ti-10Nb-10Zr alloy with general porosity of 21% for seven days, while the minimum rate of 76.96% was observed in the highly porous ternary Ti-10Nb-10Zr alloy with general porosity of 50% for one day. On the other hand, the highest Saos-2 cell viability rate of 79.89% was found in the low porous ternaryTi-20Nb-10Zr alloy with general porosity of 25%

for one day, while the lowest rate of 72.48% was observed in the highly porous ternary Ti-20Nb-10Zr alloy with general porosity of 56% for three days. According to these results, increasing the niobium concentration from 10% to 20% in titanium-zirconium mixtures resulted in a decrease in L929 cell viability and an improvement in Saos-2 cell viability for all-porous ternary Ti-xNb-10Zr alloys.

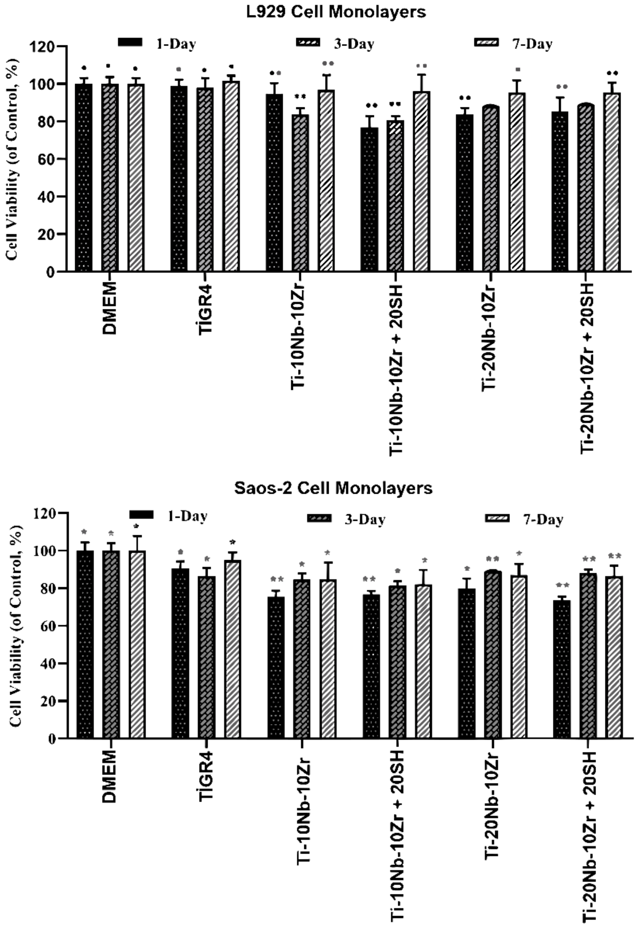

**Figure 7.16.** The cell viability of L929 and Saos-2 exposed to the extracts of DMEM, TiGR4 and all-porous ternary Ti-xNb-10Zr (x: 10 and 20; at.%) alloys for one day, three days and seven days, measured by MTT assay (data represent mean ± SD, n = 3 for $p < 0.05$).

The images of the violet formazan crystals occurring due to the activity of viable L929 and Saos-2 cells upon exposure to the extracts were taken under an optical microscope. The results of the MTT assay were obtained from quantitative optical density (OD) values and were statistically analysed. At the same time, the images of the live cells upon formation of the formazan salt with violet colour upon low and highly porous ternary Ti-xNb-10Zr alloys are given in **Fig. 7.17**. The dark area on the optical images is important since it shows the number of viable cells in the alloys. According to the images of the violet formazan crystals, cell growth of L929 and Saos-2 on surfaces and inside the pores increased for all incubation times, suggesting that all-porous ternary Ti-xNb-10Zr alloys were favourable for the use of orthopaedic biomaterial.

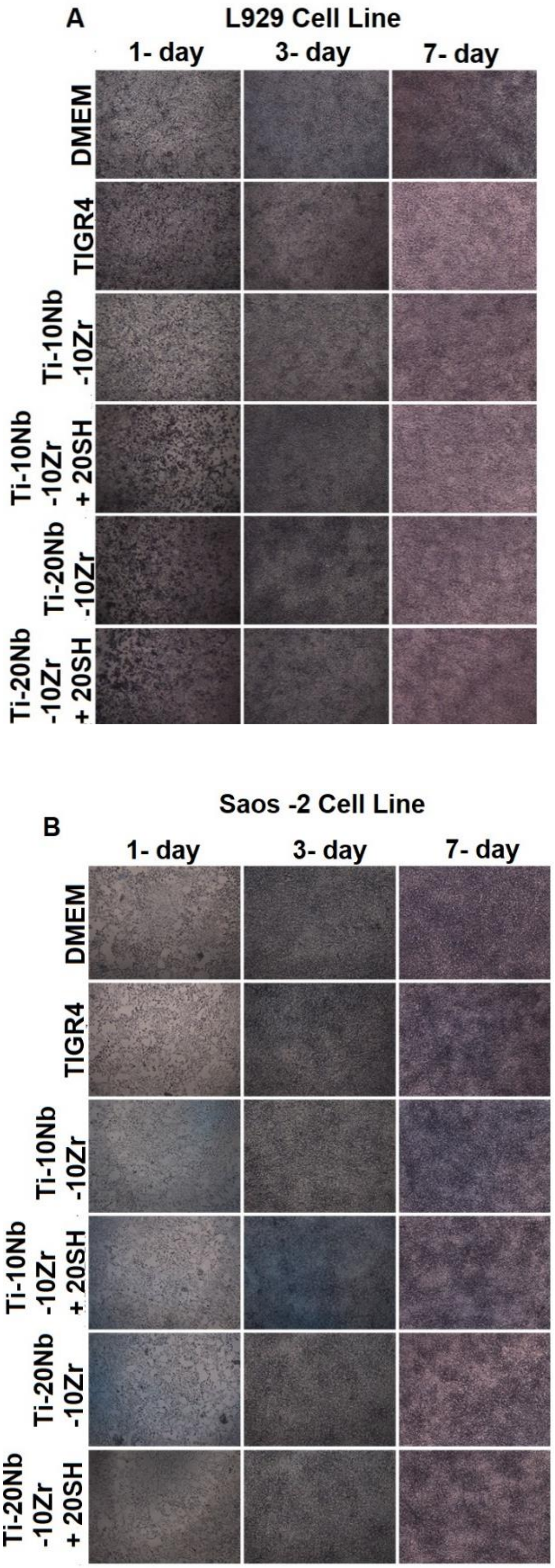

**Figure 7.17.** The images of violet formazan crystals occurring due to the activity of viable L929 and Saos-2 cells upon exposure to the extracts of DMEM, TiGR4 and all-porous ternary Ti-xNb-10Zr (x:10 and 20; at.%) alloys for one day, three days and seven days with 10X magnification.

Live-dead viability extract method: L929 and Saos-2 cells were exposed to the low and highly porous Ti-xNb-10Zr ternary alloy extracts for one day, three days and seven days. The fluorescent agents were then added to observe the live and dead cells. In addition to the calorimetric MTT assay, the cell viability of L929 and Saos-2 were qualitatively observed after 24 hours of treatment with all-porous ternary Ti-xNb-10Zr alloys and the controls. Green fluorescent calcein (ex/em ~495 nm/~515 nm) corresponded to live cells, while red fluorescent ethidium homodimer, EthD-1 (ex/em ~495 nm/~635 nm) showed the dead cells (see **Fig. 7.18.**). The fluorescence images of the low and highly porous ternary Ti-xNb-10Zr alloys were compared to those of the control groups in the wells for one day, three days and seven days. The cell viability and proliferation of L929 and Saos-2 after one day and seven days of incubation were also qualitatively demonstrated with an intensive green fluorescent appearance. Low and highly porous Ti-xNb-10Zr alloys were found to be biocompatible as compared to the control, DMEM, and the reference material TiGR4. In conclusion, all incubation times showed good L929 and Saos-2 cell viability.

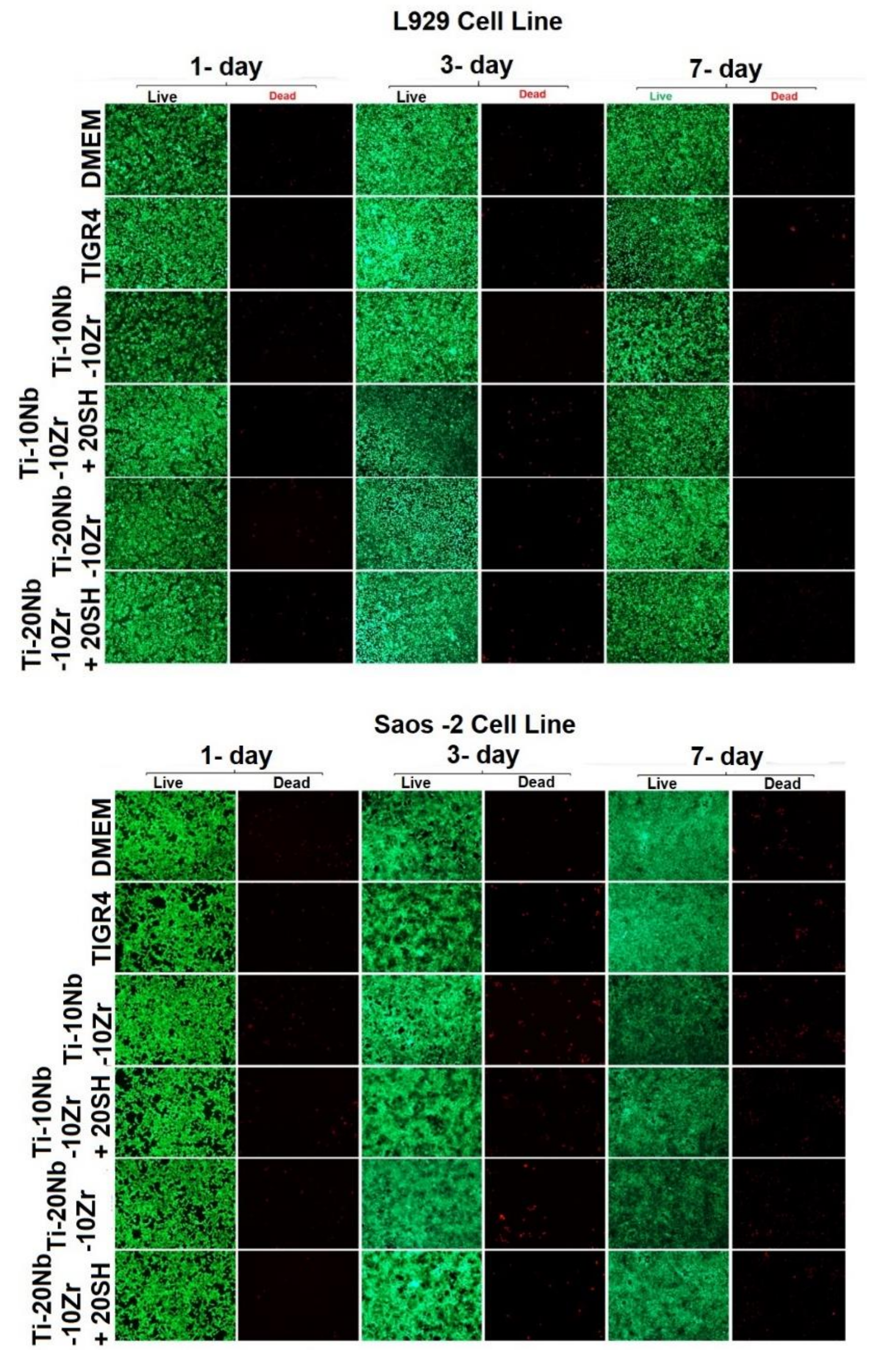

**Figure 7.18.** The images of L929 cells and Saos-2 cells upon exposure to the extracts of DMEM, TiGR4 and all-porous ternary Ti-xNb-10Zr (x: 10 and 20; at.%) alloys for one day, three days and seven days were taken by fluorescence microscope with 10X magnification. Green fluorescent calcein (ex/em ~495 nm/~515 nm) was retained in the live cells and red fluorescent Ethidium homodimer, EthD-1 (ex/em ~495 nm/~635 nm) bound to the nucleic acids in the membrane-damaged dead cells.

Fibronectin adsorption: L929 and Saos-2 cell proliferation, migration and tissue integration on all-porous ternary Ti-xNb-10Zr alloys were examined by measuring the adsorption potential of fibronectin protein on their surfaces with the ELISA (see **Fig. 7.19.**). The results showed that the addition of a space holder agent and increasing the niobium concentration from 10% to 20% enhanced the fibronectin adsorption capacity. However, this situation was related to higher general porosity of the alloy. Further, highly porous ternary Ti-20Nb-10Zr alloys exhibited even better fibronectin absorption than the reference material ($p < 0.05$).

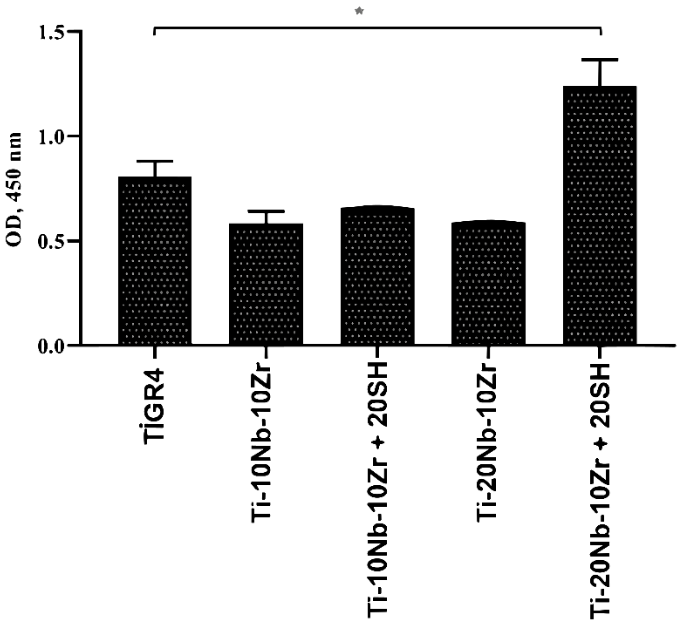

**Figure 7.19.** Adsorption of fibronectin on TIGRA4 and all-porous ternary Ti-xNb-10Zr (x:10, and 20; at.%) alloy disks after two hours of incubation at 37°C in a 5% $CO_2$ atmosphere (data represent mean ± SD, n = 3 for p<0.05).

Plasmid-DNA interactions: Pure plasmid DNA was incubated with extracts of negative control, TIGRA4 and all-porous ternary Ti-xNb-10Zr alloys in the absence of any external agents, and the migration pattern alteration was then detected by agarose gel electrophoresis. Pure plasmid DNA is composed of supercoiled (SC) and nicked circular (NC) forms. The results revealed that the incubation with the extracts of the examined low and highly porous ternary Ti-xNb-10Zr alloys caused no detectable change in the intensity of the SC and NC bands and was comparable to those obtained for the TiGR4 reference (see **Fig. 7.20.**). This behaviour confirmed that no induced genotoxic potential was due to the incubation of plasmid DNA in the sample extracts. In addition, this response was consistent with that of the negative control (ddH2O) and thereby no subsequent DNA smear was detected.

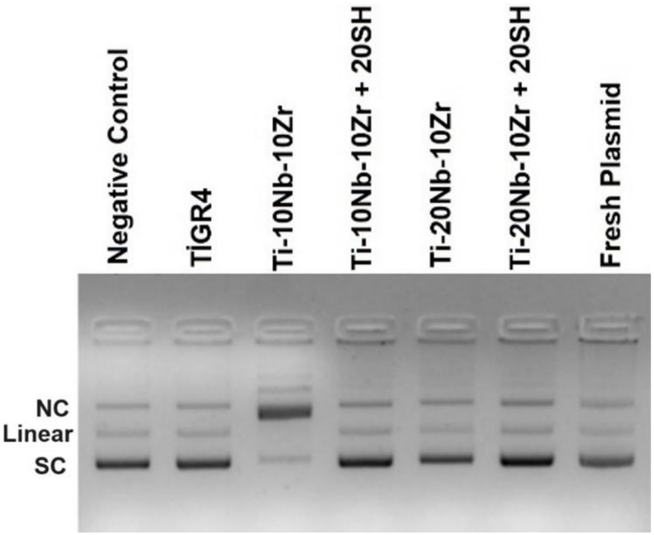

**Figure 7.20.** Plasmid-DNA interaction assay for the negative control, TIGR4, and all-porous ternary Ti-xNb-10Zr (x:10, and 20; at.%) alloys (NC: Nicked circular, SC: supercoiled).

Morphology observation of cells: To investigate the cell morphology, L929 and Saos-2 cells were seeded on the developed low and highly porous ternary Ti-xNb-10Zr alloy discs and the cell images were taken with SEM on Day 1 and Day 7 (see Fig. **7.21.**). The low and highly porous ternary Ti-xNb-10Zr alloys with an average general porosity of 23% and 53%, respectively, promoted adequate sites for biological fixation. Therefore, as seen in **Fig. 7.21**., L929 and Saos-2 cell lines were well spread on all-porous ternary Ti-xNb-10Zr alloys. Cell adherence of L929 and Saos-2 cells on the low and highly porous ternary Ti-xNb-10Zr alloys were observed as extended cytoplasmic processes (pseudopodia) into the pores. In conclusion, multiple colonies of L929 and Saos-2 cell types were found on all-porous ternary Ti-xNb-10Zr alloys.

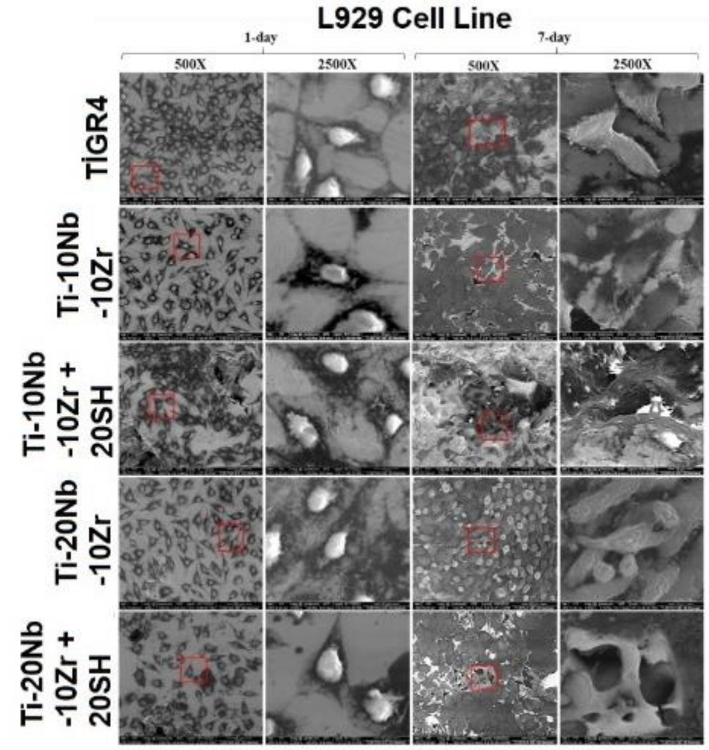
L929 Cell Line

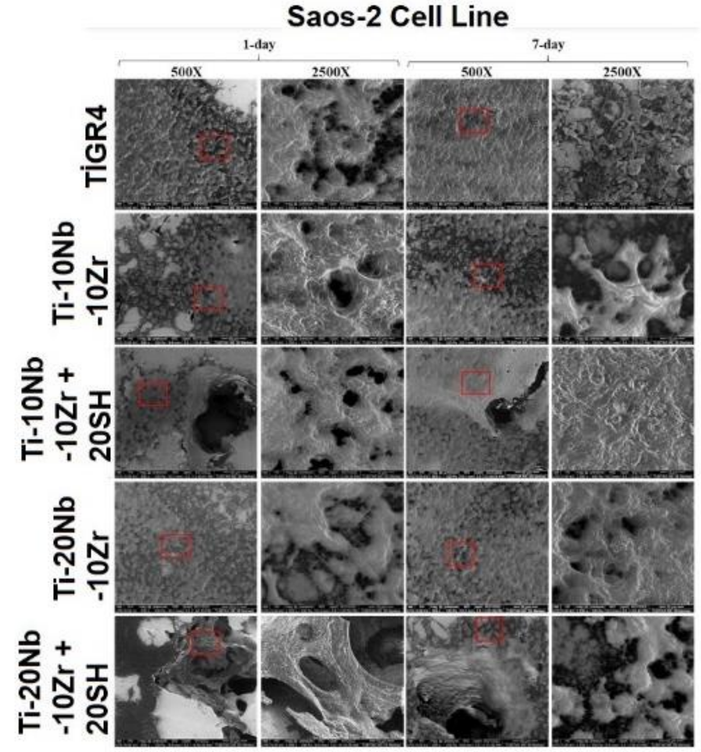
Saos-2 Cell Line

**Figure 7.21.** SEM images of viable L929 and Saos-2 cells on the reference TiGR4 and all-porous ternary Ti-xNb-10Zr (x: 10 and 20; at.%) alloys for one day and seven days with 2500X and 500X magnifications.

## 7.2. Discussion

In this thesis, the mechanically characterised manufactured Ti-xNb, Ti-20Zr, and Ti-xNb-10Zr alloys were also characterised biologically following ISO 10993. The results demonstrated the good biocompatibility of tested alloys examining cell viability and proliferation, cell morphology, genotoxicity, and cell adherence potentials, which are essential for promoting tissue healing and integration. The cell viability of the cell lines used in the experiment increased with increasing incubation time. However, noted that the relationship between incubation time and cell viability may vary according to the type of cell viability assay utilised. Therefore, we could not say that incubation time had a positive effect on the Saos 2 and L929 cell line viabilities. The treatment of highly porous Ti-xNb, Ti-20Zr and Ti-xNb-10Zr alloys compared with low porous alloys decreased the cell viability of L929 cell line on the 1-day and 3-day but not on the 7-day application. This may be due to cells adhering to the rough surface and migrating into the porous structure.

Other research stated that cell attachment and spreading on the substrate are good indicators showing the level of cytotoxicity and cell viability (Mandal et al., 2019; Han et al., 2020). Cellular responses such as migration, proliferation or specific physiological activity to the substrate may be varied depending on test conditions and cell type used. In the SEM analysis, both cell lines (Saos 2 and L929) moved towards the porous regions and proliferated highly in these regions. At this point, it could be said that the effect of general porosity on the SEM morphology of Saos 2 and L929 cell lines was generally positive.

Protein adsorption may occur after the implantation of biomaterial within a biological environment and is one of the key determinants of the responses of cells to the material surface (Barberi et al., 2022). The results showed that adding niobium played a minimal role on the fibronectin adsorption of the alloys studied in this thesis, but general porosity of the alloys had major effects on the fibronectin adsorption. Especially, for highly porous tested alloys, fibronectin adsorption level increased since fibronectin protein absorption was greater on rough surfaces. It was concluded that fibronectin adsorption values of the highly porous Ti-xNb, Ti-20Zr and Ti-xNb-10Zr alloys were better than that of low porous tested alloys.

The increase in niobium concentration resulted in no significant change in L929 cell viability among different period of the treatments. The increase in niobium concentration resulted in increase in Saos-2 cell viability within the different period of the treatments. It could be explained that the Saos-2 cell line might have sensitive metabolic activity to the niobium metals, which may induce the cell proliferation. In addition to these, niobium concentration might change the surface characteristics of the alloys. Regarding biological characteristics of niobium, it is nontoxic and allergy-free metal, indicting acceptable biocompatibility and osteoconductivity. In this study, the increased level of niobium might induce much more mitochondrial activity, cell proliferation, fibroblast adsorption potential of biomaterial surfaces. In the previous work resulted in similar finding's that the comparative study on the biological performance of niobium, titanium, and stainless steel revealed that there were much more mitochondrial activity and cell proliferation on niobium compared to the others.

Some studies on Ti-Nb-Zr alloys stated that biocompatibility of Ti-15Nb and Ti-15Zr using Saos-2 and mouse calvaria-derived MC3T3-E1 subclone 14 pre-osteoblast cells confirmed our results of cell viability and morphology (Li et al., 2009; Zhang et al., 2020). In another study, the investigation of Ti-25Nb and Ti-13Nb-13Zr alloys resulted in good adhesion and proliferation in rabbit and human bone-marrow-derived mesenchymal cells (Bigi et al., 2007; Xu et al., 2013). In addition to these findings, Falanga et al. reported that cellular proliferation and adherence in Ti-Nb samples were induced more than the Ti-40 (grade 2 Titanium alloy) (Falanga et al., 2019). In another study, confocal microscope images of Saos-2 cells grown on titanium binary alloys revealed that Ti-15Nb and Ti-15Zr induced cell attachment and proliferation, which was also observed in our study (Li et al., 2009). Bigi et al. demonstrated that MSCs cultured onto hydroxyapatite-coated Ti-6Al-4V and Ti-13Nb-13Zr alloys observed mainly elongated fibroblast-like cells and more round osteoblastic cells, respectively (Bigi et al., 2007). They reported that Ti-13Nb-13Zr caused no adverse effects, as confirmed in our study. Our findings are consistent with the previous findings of such increased fibronectin adsorption and cell adhesion and proliferation on Ti-24Nb-4Zr-8Sn compared to Ti-6Al-4V alloy (Liu et al., 2018). One mechanism of protein adsorption was the electrostatic interaction between proteins and the material surface. Mahundla et al. reported that cell proliferation, adhesion and fibronectin adsorption on Ti-34Nb-25Zr alloys were observed less than on Ti-6Al-4V alloys. This could be due to the high level of Nb and Zr content and the absence of a space holder agent, compared to our results (Mahundla et al., 2019).

In this thesis low and highly porous Ti-xNb, Ti-20Zr, and Ti-xNb-10Zr alloys were fabricated successfully. Optical images revealed that sintering temperature selected in this study was appropriate for generating micro porosity inside the alloys. However, adding space holder agent was crucial factor to create macro porosity. Therefore, pore size and distribution of the alloys with space holder agent were much greater than that of the alloys without space holder agent, which played a significant role on the enhancing cell viability and cell adherence.

EDS results showed that macro porosity made diffusion between particles difficult due to the fact that pathways for diffusion increased in the highly porous Ti-xNb, and Ti-xNb-10Zr alloys.

Therefore, homogeneity of the low porous Ti-xNb, and Ti-xNb-10Zr alloys was better than that of highly porous Ti-xNb, and Ti-xNb-10Zr alloys. Proportion of primary niobium phase (undissolved niobium) in highly porous Ti-xNb, and Ti-xNb-10Zr alloys was higher that of low porous Ti-xNb, and Ti-xNb-10Zr alloys. However, this was not a crucial factor for in-vitro analysis because titanium, niobium and zirconium were biocompatible for human body.

XRD analysis indicated that low and highly porous Ti-xNb, and Ti-xNb-10Zr alloys exhibited the α-Ti + β-Ti phases with primary niobium phase, while low and highly porous binary Ti-20Zr alloys displayed the hcp α-Ti phase and some distorted hcp α'-Ti phase due to zirconium dissolved in the titanium matrix. Having different phase constituent of the alloys did not affected the cell viability and other cellular activities.

However, having different phase structure is crucial for mechanical test as mechanical properties of the α-Ti is different from those of the β-Ti. For instance, β-Ti has more ductility than α-Ti. Therefore, the mechanical test of the alloys having similar porosity levels were different from each other due to their phase structures. Ultimate compressive strength of the low porous binary Ti-10Nb alloy (having 20% porosity) was saved as 1295 MPa, while that of the low porous Ti-30Nb (having 23% porosity) was measured as 618 MPa. This finding showed that formation of β-Ti on the low and highly porous Ti-xNb and Ti-xNb-10Zr alloys played significant role on the reducing mechanical performances of the alloys, which is essential for implantology as risk of stress shielding effect reduces. On the other hand, adding space holder agent was more effective than phase structure of the alloys achieved in this thesis. As mentioned earlier, adding space holder agent created macro porosity inside the alloys, which deteriorates the mechanical performances of the alloys. Ultimate compressive strength for low porous binary Ti-20Zr alloy was 1376 MPa, while that for highly porous binary Ti-20Zr alloys was found as only 356 MPa. This finding supported that compressive strength properties of the alloys achieved in this thesis was dramatically affected by porosity level. Also, higher porosity level had a positive effect on the cell attachment and protein absorption, which was consistent with SEM micrographs showing cell attachment on the surface of the alloys.

Based on literature reports, there is a close relationship between corrosion performances and in vitro analysis. In this thesis, corrosion performances of the alloys achieved in this study was agreement with in vitro analysis. Low and highly porous Ti-xNb, Ti-20Zr, and Ti-xNb-10Zr alloys exhibited good corrosion performances and acceptable biocompatible features. The conclusion was that the fabricated alloys might be good candidates as implant materials that need to stay in the body for a long time.

# Chapter 8. Conclusions and Future Work

## 8.1. Conclusions

This thesis aims to overcome the drawbacks of the above-mentioned problems by producing Ti-xNb (x: 10, 20, and 30; at.%), Ti-20Zr (at.%), Ti-xNb-10Zr (x: 10, and 20; at.%) alloys with different porosities used as orthopaedic biomaterial that can mimic the bone structure. Microstructural analysis was performed by using various methods including scanning electron microscopy, energy dispersive spectroscopy, electron backscatter diffraction, and x-ray diffraction. Corrosion resistance was assessed via electrochemical polarization tests, while mechanical behaviour was determined by uniaxial compressive tests. In vitro studies such as cell viability and proliferation, adhesion potential, and genotoxicity were examined by performing MTT assay, fibronectin adsorption, and plasmid-DNA interaction assay. Based on the results obtained, the following facts were determined.

The powder metallurgy method combined with the space holder technique was appropriate to produce Ti-xNb, Ti-20Zr and Ti-xNb-10Zr alloys with differing porosities.

The alloys studied could be divided into low and high porous categories, with porosities ranging from 21% to 29% and 43% to 58%, respectively.

The addition of a space holder agent effectively adjusted the porosity characteristics of the alloys achieved.

The phase constituent of the all-porous Ti-20Zr alloys was classified as the mixture of the predominant hcp α phase and some distorted hcp α phases, whereas that of the all-porous Ti-xNb and Ti-xNb-10Zr alloys were the bcc β-Ti phases with some hcp α-Ti phases and the primary niobium phase.

Adding a space holder did not considerably affect the phase constituents of the alloys achieved in this thesis.

EDS peaks for the low and highly porous Ti-xNb, Ti-20Zr, and Ti-xNb-10Zr alloys were comprised of Ti-Kβ, Ti-Kα and some Nb-L. No other peak belonging to undesired elements was found in the microstructures.

The ultimate compressive strengths of low porous alloys were in a range of 1276 MPa to 1019 MPa; those of highly porous alloys ranged between 356 MPa and 48 MPa. As foreseen, porosities dramatically diminished the mechanical performance of the alloys.

Potentiodynamic polarisation revealed that alloys fabricated in this thesis had good corrosion behaviours, protecting corrosion attacks in HBSS.

The alloys achieved in this study displayed good biocompatibility (≥70% cell viability) as required for the use of orthopaedic biomaterial.

The fibronectin adsorption of the alloys revealed that highly porous alloys and increased niobium compositions increased their protein adsorption and consequently induced cell adherence and proliferation.

Microscopic examination of L929 and Saos-2 cell lines on highly porous alloys increased cell adherence and proliferation at a high density due to migration of the pores when compared to the cell's morphology via SEM analysis on low porous alloys and the reference TiGR4 alloy.

## 8.2. Suggestions and Future Work

Based on the results obtained from this thesis, the following topics can be examined in the future.

Powder metallurgy combined with the space holder technique used in this work is an efficient way to produce the alloys with porosities without changing phase constituents. However, other alternative production methods, which reflect better the properties of natural bone, can be employed to produce same alloys with porosity.

It can be given a detailed description of how hot isostatic pressing (HIP) or other advanced compaction techniques affects the biomechanical properties of porous Ti-xNb, Ti-20Zr, and Ti-xNb-10Zr alloys used as implant.

The role of how different manufacturing processes or designs affect the biomechanical properties of porous Ti-xNb, Ti-20Zr, and Ti-xNb-10Zr alloys used as implant can be studied. More appropriate mould design can mimic bone structure (higher porosity inside, lower porosity outside). In this way, the interior of the alloys can be obtained with a porosity of 70% to 90%, and the outer layer with a porosity of 1% to 30%.

Bend strength, tensile strength, torsional testing, fatigue test, hardness test, and wear test can be performed on the all-porous alloys obtained in this thesis, which are important indicators showing the service life of the alloys when implanted.

Differing thermal treatments can be applied to the all-porous alloys achieved to generate different combinations of α-Ti and β-Ti phases.

The shape memory effect for Ti-xNb and Ti-xNb-10Zr alloys can be determined by differential scanning calorimetry and thermal gravimetric analysis.

In vivo biocompatibility (animal test) is also recommended to see the response of the all-porous alloys achieved in this work. It is believed that these tests, which were carried out within a multidisciplinary study group, will help to convert the developed porous alloys into a product such as knee prostheses, dental implants and hip joints.

The all-porous alloys produced in this study can be coated with appropriate chemicals to improve their antibacterial properties; thus, such alloys efficiently promote the formation and spread of bone cells.

The factors affecting the healing time between implant and new bone formation after surgery can be accurately determined by further biological assessments.

More information on the stability of porous Ti-xNb, Ti-20Zr, and Ti-xNb-10Zr alloys used as implant can be gathered through long-term clinical tests.

The aesthetic results in different patient groups can be examined.

## References

Abdelrhman, Y., Gepreel, M. A. H., Kobayashi, S., Okano, S., & Okamoto, T. (2019). Biocompatibility of new low-cost (α+ β)-type Ti-Mo-Fe alloys for long-term implantation. Materials Science and Engineering: C, 99, 552-562.

Abrahamsson, I., Berglundh, T., Linder, E., Lang, N. P., & Lindhe, J. (2004). Early bone formation adjacent to rough and turned endosseous implant surfaces: an experimental study in the dog. Clinical oral implants research, 15(4), 381-392.

Adamczyk, J., & Opiela, M. (2004). Influence of the thermo–mechanical treatment parameters on the inhomogeneity of the austenite structure and mechanical properties of the Cr–Mo steel with Nb, Ti, and B microadditions. Journal of Materials Processing Technology, 157, 456-461.

Adamovic, D., Ristic, B., & Zivic, F. (2018). Review of existing biomaterials—method of material selection for specific applications in orthopedics. Biomaterials in Clinical Practice, 47-99.

Agrawal, R., Kumar, A., Mohammed, M. K., & Singh, S. (2023). Biomaterial types, properties, medical applications, and other factors: a recent review. *Journal of Zhejiang University-SCIENCE A*, 1-16.

Ahmed Y M, Sahari KSM, Ishak M and Khidhir B A (2014). Titanium and its alloy: International Journal of Science and Research 3 1351-1361.

Ahmed, Hebatalrahman. (2005). Titanium data base part1.

Ak, H.D. (2014) The effect of sintering conditions on the properties of AISI 304L and AISI 316L austenitic stainless steels produced by powder metallurgy method, Master dissertation, İstanbul Technical University.

Alabort, E., Tang, Y. T., Barba, D., & Reed, R. C. (2022). Alloys-by-design: A low-modulus titanium alloy for additively manufactured biomedical implants. *Acta Materialia*, *229*, 117749.

Albrektsson, T., & Johansson, C. (2001). Osteoinduction, osteoconduction and osseointegration. European spine journal, 10(2), S96-S101.

Al-Qureshi, H. A., Galiotto, A., & Klein, A. N. (2005). On the mechanics of cold die compaction for powder metallurgy. Journal of Materials Processing Technology, 166(1), 135-143.

An, Y. B., Oh, N. H., Chun, Y. W., Kim, Y. H., Park, J. S., Choi, K. O., ... & Lee, W. H. (2005). Surface characteristics of porous titanium implants fabricated by environmental electro-discharge sintering of spherical Ti powders in a vacuum atmosphere. Scripta materialia, 53(8), 905-908.

Anas, S., Khan, M. Y., & Pabla, B. S. (2023). Orthopaedic application of biomaterials: A study. In *Innovative Processes and Materials in Additive Manufacturing* (pp. 269-281). Woodhead Publishing.

Angelo, P. C., Subramanian, R., & Ravisankar, B. (2022). *Powder metallurgy: science, technology and applications*. PHI Learning Pvt. Ltd.

Antunes, R. A., Salvador, C. A. F., & Oliveira, M. C. L. D. (2018). Materials selection of optimized titanium alloys for aircraft applications. Materials Research, 21.

Anusavice, K. J., Shen, C., & Rawls, H. R. (Eds.). (2012). Phillips' science of dental materials. Elsevier Health Sciences.

Ardhy, S., Affi, J., & Yetri, Y. (2023). Improvement in Bioactivity Properties of Hydroxyapatite Coated Ti-6Al-4V ELI with Addition of Zirconium Oxide for Orthopaedic Implant. *Journal of Biomimetics, Biomaterials and Biomedical Engineering*, *59*, 81-89.

Arifvianto, B., Leeflang, M. A., & Zhou, J. (2016). Characterization of the porous structures of the green body and sintered biomedical titanium scaffolds with micro-computed tomography. Materials Characterization, 121, 48-60.

Aşık, E. E., & Bor, Ş. (2015). Fatigue behaviour of Ti–6Al–4V foams processed by magnesium space holder technique. Materials Science and Engineering: A, 621, 157-165.

Aydoğmuş, T. (2010). Processing and characterization of porous titanium nickel shape memory alloys.

Babu, B., Jayaram, R. S., & Muthukumar, P. S. A (2022) Basic Overview of Composite Materials and Some of their Biomedical Engineering Applications.

Bai, Y., Deng, Y., Zheng, Y., Li, Y., Zhang, R., Lv, Y., ... & Wei, S. (2016). Characterization, corrosion behavior, cellular response, and in vivo bone tissue compatibility of titanium–niobium alloy with low Young's modulus. Materials Science and Engineering: C, 59, 565-576.

Baker, H. (1992). Alloy phase diagrams. ASM handbook, 3, 2-80.

Balazic, M., Kopac, J., Jackson, M. J., & Ahmed, W. (2007). Titanium and titanium alloy applications in medicine. International Journal of Nano and Biomaterials, 1(1), 3-34.

Baldissera, M. R., Rios, P. R., Hein, L. R. O., & Sandim, H. R. Z. (2011). Three-dimensional characterization of pores in Ti-6Al-4V alloy. Materials research, 14, 102-106.

Banerjee, D., & Williams, J. C. (2013). Perspectives on titanium science and technology. Acta Materialia, 61(3), 844-879.

Barberi, J. A. C. O. P. O., Mandrile, L., Napione, L., Giovannozzi, A. M., Rossi, A. M., Vitale, A., ... & Spriano, S. (2022). Albumin and fibronectin adsorption on treated titanium surfaces for osseointegration: An advanced investigation. *Applied Surface Science*, *599*, 154023.

Bazhin, A. V., Kahnert, S., Kimpfler, S., Schadendorf, D., & Umansky, V. (2010). Distinct metabolism of cyclic adenosine monophosphate in regulatory and helper CD4+ T cells. Molecular immunology, 47(4), 678-684.

Berglundh, T., Abrahamsson, I., Albouy, J. P., & Lindhe, J. (2007). Bone healing at implants with a fluoride-modified surface: an experimental study in dogs. Clinical Oral Implants Research, 18(2), 147-152.

Bersuker, I. B. (2010). Electronic structure and properties of transition metal compounds: introduction to the theory. John Wiley & Sons.

Bhattarai, S. R., Khalil, K. A. R., Dewidar, M., Hwang, P. H., Yi, H. K., & Kim, H. Y. (2008). Novel production method and in-vitro cell compatibility of porous Ti-6Al-4V alloy disk for hard tissue engineering. Journal of Biomedical Materials Research Part A: An Official Journal of The Society for Biomaterials, The Japanese Society for Biomaterials, and The Australian Society for Biomaterials and the Korean Society for Biomaterials, 86(2), 289-299.

Bidaux, J. E., Closuit, C., Rodriguez-Arbaizar, M., Zufferey, D., & Carreño-Morelli, E. (2013). Metal injection moulding of low modulus Ti–Nb alloys for biomedical applications. Powder Metallurgy, 56(4), 263-266.

Bigi, A., Nicoli-Aldini, N., Bracci, B., Zavan, B., Boanini, E., Sbaiz, F., ... & Cortivo, R. (2007). In vitro culture of mesenchymal cells onto nanocrystalline hydroxyapatite-coated Ti13Nb13Zr alloy. *Journal of Biomedical Materials Research Part A*, *82*(1), 213-221.

Biologydictionary.net Editors. "Bone Cells." Biology Dictionary, Biologydictionary.net, 11 May. 2021, https://biologydictionary.net/bone-cells/

Black, J., & Hastings, G. (Eds.). (2013). Handbook of biomaterial properties. Springer Science & Business Media.

Bordbar, H., Yousefi, A. A., & Abedini, H. (2017). Production of titanium tetrachloride (TiCl4) from titanium ores: A review. Polyolefins Journal, 4(2), 149-173.

Bottino, M. C., Coelho, P. G., Henriques, V. A., Higa, O. Z., Bressiani, A. H., & Bressiani, J. C. (2009). Processing, characterization, and in vitro/in vivo evaluations of powder metallurgy processed Ti-13Nb-13Zr alloys. Journal of Biomedical Materials Research Part A: An Official Journal of The Society for Biomaterials, The Japanese Society for Biomaterials, and The Australian Society for Biomaterials and the Korean Society for Biomaterials, 88(3), 689-696.

Boyan, B. D., Hummert, T. W., Dean, D. D., & Schwartz, Z. (1996). Role of material surfaces in regulating bone and cartilage cell response. Biomaterials, 17(2), 137-146.

Boyer, R., Welsch, G., & Collings, E. W. (1994). ASM Materials Properties Handbook: Titanium Data Sheets. The Materials Information Society: Materials Park, OH, USA.

Bozzolo, G., Noebe, R. D., & Abel, P. B. (Eds.). (2007). Applied computational materials modeling: theory, simulation and experiment. Springer Science & Business Media.

Bram, M., Stiller, C., Buchkremer, H. P., Stöver, D., & Baur, H. (2000). High-porosity titanium, stainless steel, and superalloy parts. Advanced engineering materials, 2(4), 196-199.

Brandt, J. M., Guenther, L., O'brien, S., Vecherya, A., Turgeon, T. R., & Bohm, E. R. (2013). Performance assessment of femoral knee components made from cobalt–chromium alloy and oxidized zirconium. The Knee, 20(6), 388-396.

Bronzino, J. D. (2000). Biomedical Engineering Handbook 2 (Vol. 2). Springer Science & Business Media.

Bronzino, J. D., & Peterson, D. R. (2014). Biomedical engineering fundamentals. CRC press.

Brunette, D. M., Tengvall, P., Textor, M., & Thomsen, P. (2001). Titanium in medicine: material science, surface science, engineering, biological responses and medical applications (p. 232). Berlin: Springer.

Cacciamani, G., Riani, P., & Valenza, F. (2011). Equilibrium between MB2 (M= Ti, Zr, Hf) UHTC and Ni: a thermodynamic database for the B–Hf–Ni–Ti–Zr system. Calphad, 35(4), 601-619.

Çakmak, Ö., Mehmet, K. A. Y. A., ANNAÇ, E., & Mustafa, K. Ö. M. (2022). İmplantasyon Uygulamaları İçin Toz Metalurjisi ile Üretilen Ti-16Nb-4Sn Alaşımının Mikroyapı ve Biyouyumluluk Özelliklerinin İncelenmesi. Gazi Mühendislik Bilimleri Dergisi, 8(1), 29-40.

Calderon Moreno, J. M., Popa, M., Ivanescu, S., Vasilescu, C., Drob, S. I., Neacsu, E. I., & Popa, M. V. (2014). Microstructure, mechanical properties, and corrosion resistance of Ti-20Zr alloy in undoped and NaF doped artificial saliva. Metals and Materials International, 20(1), 177-187.

Callister, W. D., & Rethwisch, D. G. (2011). Chap. 15 Characteristics, Applications and Processing of Polymers. Materials Science and Engineering 8th Ed (8th ed.). John Wiley & Sons (Asia) Pte Ltd.

Cannella, V., Altomare, R., Chiaramonte, G., Di Bella, S., Mira, F., Russotto, L., ... & Guercio, A. (2019). Cytotoxicity evaluation of endodontic pins on L929 cell line. *BioMed Research International*, *2019*.

Cetin, Y., Ibrahim, A. M. H., Gungor, A., Yildizhan, Y., Balog, M., & Krizik, P. (2020). In-vitro evaluation of a partially biodegradable TiMg dental implant: The cytotoxicity, genotoxicity, and oxidative stress. *Materialia*, *14*, 100899.

Cetin, Y., Sahin, M. G., & Kok, F. N. (2021). Application potential of three-dimensional silk fibroin scaffold using mesenchymal stem cells for cardiac regeneration. *Journal of Biomaterials Applications*, *36*(4), 740-753.

Chang, I., & Zhao, Y. (Eds.). (2013). Advances in powder metallurgy: properties, processing and applications. Elsevier.

Chang, J. H., Liu, J. F., Sun, Y. S., Wu, C. P., Huang, H. H., & Han, Y. (2017). Mesoporous surface topography promotes bone cell differentiation on low elastic modulus Ti–25Nb–25Zr alloys for bone implant applications. Journal of Alloys and Compounds, 707, 220-226.

Chen, Q., & Thouas, G. A. (2015). Metallic implant biomaterials. Materials Science and Engineering: R: Reports, 87, 1-57.

Chen, X., Liao, Q., Gong, M., & Fu, Q. (2023). Corrosion Performances of Selective Laser Melting Ti6Al4V Alloy in Different Solutions. *Metals*, *13*(2), 192.

Chopra, D., Jayasree, A., Guo, T., Gulati, K., & Ivanovski, S. (2022). Advancing dental implants: Bioactive and therapeutic modifications of zirconia. *Bioactive Materials*, *13*, 161-178.

Choubey, A., Basu, B., & Balasubramaniam, R. (2005). Electrochemical behavior of Ti-based alloys in simulated human body fluid environment. Trends in Biomaterials & Artificial Organs, 18(2), 64-72.

Connors, J. P., Stelzer, J. W., Garvin, P. M., Wellington, I. J., & Solovyova, O. (2022). The Role of the Innate Immune System in Wear Debris-Induced Inflammatory Peri-Implant Osteolysis in Total Joint Arthroplasty. *Bioengineering*, *9*(12), 764.

Cordeiro, J. M., & Barão, V. A. (2017). Is there scientific evidence favouring the substitution of commercially pure titanium with titanium alloys for the manufacture of dental implants. Materials Science and Engineering: C, 71, 1201-1215.

Cordeiro, J. M., Beline, T., Ribeiro, A. L. R., Rangel, E. C., da Cruz, N. C., Landers, R., ... & Barão, V. A. (2017). Development of binary and ternary titanium alloys for dental implants. Dental Materials, 33(11), 1244-1257.

Couto, B. A. D. A., Fernandes, J. C. H., Saavedra-Silva, M., Roca, H., Castilho, R. M., & Fernandes, G. V. D. O. (2023). Antisclerostin Effect on Osseointegration and Bone Remodeling. *Journal of Clinical Medicine*, *12*(4), 1294.

Cui, Y., Li, Y., Luo, K., & Xu, H. (2010). Microstructure and shape memory effect of Ti–20Zr–10Nb alloy. Materials Science and Engineering: A, 527(3), 652-656.

Curtin, J., Wang, M., & Sun, H. (2017). Factors affecting the release of titanium into human serum. International Journal of Oral and Maxillofacial Surgery, 46, 94.

Cvijović-Alagić, I., Cvijović, Z., Mitrović, S., Panić, V., & Rakin, M. (2011). Wear and corrosion behaviour of Ti–13Nb–13Zr and Ti–6Al–4V alloys in simulated physiological solution. Corrosion science, 53(2), 796-808.

Danewalia, S. S., & Singh, K. (2021). Bioactive glasses and glass–ceramics for hyperthermia treatment of cancer: state-of-art, challenges, and future perspectives. Materials Today Bio, 10, 100100.

Darvell, B. W. (2018). Materials science for dentistry. Woodhead publishing.

de Oliveira, C. S. S., Griza, S., de Oliveira, M. V., Ribeiro, A. A., & Leite, M. B. (2015). Study of the porous Ti35Nb alloy processing parameters for implant applications. Powder Technology, 281, 91-98.

Degischer, H. P., & Kriszt, B. (2002). Handbook of cellular metals (Vol. 71). Wiley-VCH, Weinheim.

Demirci, S., Dikici, T., Tünçay, M. M., Dalmış, R., Kaya, N., Kanbur, K., ... & Güllüoğlu, A. N. (2022). Investigation of surface-modified EBM printed Ti-6Al-4V alloys for biomedical applications. *Surfaces and Interfaces*, *34*, 102372.

DEMİREL, M. (2012). Ortopedide alternatif kemik biyo-greftlerinin üretimi ve in vivo/in vitro biyouyumluluk-biyomekanik analizleri/The production of bone bio-grafts and in vivo/in vitro biocompatibility-bio mechanical analysis.

Dikici, T. (2016). Investigation of the mechanical properties of micro and nano structured titanium oxide films produced on titanium implant for biomedical applications (Doctoral dissertation).

Dinu, M., Franchi, S., Pruna, V., Cotrut, C. M., Secchi, V., Santi, M., ... & Vladescu, A. (2018). Ti-Nb-Zr system and its surface biofunctionalization for biomedical applications. In Titanium in Medical and Dental Applications (pp. 175-200). Woodhead Publishing.

Donachie, M. J. (2000). Titanium: a technical guide. ASM international.

dos Santos, G. A. (2015). Tecnologia dos Materiais Metálicos: Propriedades, Estruturas e Processos de Obtenção. Saraiva Educação SA.

Du, P., Xiang, T., Cai, Z., & Xie, G. (2022). The influence of porous structure on the corrosion behavior and biocompatibility of bulk Ti-based metallic glass. *Journal of Alloys and Compounds*, *906*, 164326.

Edosa, O. O., Tekweme, F. K., & Gupta, K. (2022). A review on the influence of process parameters on powder metallurgy parts. *Engineering and Applied Science Research*, *49*(3), 433-443.

Ehtemam-Haghighi, S., Liu, Y., Cao, G., & Zhang, L. C. (2016). Influence of Nb on the β→ α ″martensitic phase transformation and properties of the newly designed Ti–Fe–Nb alloys. Materials Science and Engineering: C, 60, 503-510.

Eisenbarth, E., Velten, D., Müller, M., Thull, R., & Breme, J. (2004). Biocompatibility of β-stabilizing elements of titanium alloys. Biomaterials, 25(26), 5705-5713.

Elden, E. (2016). Production of metallic biomaterials by vacuum arc melting method and investigation of their properties, (Master dissertation), Dokuz Eylül University.

Elfghi, M.A. (2020). Mechanical properties of powder metallurgy (Ti-6Al-4V) alloy manufactured with hot isostatic pressing (doctoral dissertation).

engh Jr, C. A., Young, A. M., Engh Sr, C. A., & Hopper Jr, R. H. (2003). Clinical consequences of stress shielding after porous-coated total hip arthroplasty. Clinical Orthopaedics and Related Research®, 417, 157-163.

Esen, Z. (2007). Production and characterization of porous titanium alloys.

Esen, Z., & Bor, Ş. (2011). Characterization of Ti–6Al–4V alloy foams synthesized by space holder technique. Materials Science and Engineering: A, 528(7-8), 3200-3209.

Eurostat (2022) Policy. Available at [http://epp.eurostat.ec.europa.eu/statistics_explained/index.php/Mortality_and_life_expectancy_statistics](http://epp.eurostat.ec.europa.eu/statistics_explained/index.php/Mortality_and_life_expectancy_statistics) (Accessed: 26 december 2022).

Falanga, A., Laheurte, P., Vahabi, H., Tran, N., Khamseh, S., Saeidi, H., ... & Mozafari, M. (2019). Niobium-treated titanium implants with improved cellular and molecular activities at the tissue–implant interface. *Materials*, *12*(23), 3861.

Fojt, J., Joska, L., & Málek, J. (2013). Corrosion behaviour of porous Ti–39Nb alloy for biomedical applications. Corrosion science, 71, 78-83.

Franca, C. M., de Souza Balbinot, G., Cunha, D., Saboia, V. D. P. A., Ferracane, J., & Bertassoni, L. E. (2022). In-vitro models of biocompatibility testing for restorative dental materials: from 2D cultures to organs on-a-chip. *Acta Biomaterialia*.

Froes, F. H., Mashl, S. J., Hebeisen, J. C., Moxson, V. S., & Duz, V. A. (2004). The technologies of titanium powder metallurgy. Jom, 56(11), 46-48.

Fujii, T., Murakami, R., Kobayashi, N., Tohgo, K., & Shimamura, Y. (2022). Uniform porous and functionally graded porous titanium fabricated via space holder technique with spark plasma sintering for biomedical applications. *Advanced Powder Technology*, *33*(6), 103598.

Gao, X., He, R. X., Yan, S. G., & Wu, L. D. (2011). Dermatitis associated with chromium following total knee arthroplasty. The Journal of arthroplasty, 26(4), 665-e13.

Gasik, M. M., & Yu, H. (2009). Phase Equilibria and Thermal Behavior of the Biomedical Ti-Nb-Zr Alloy. na.

Geetha, M., Singh, A. K., Asokamani, R., & Gogia, A. K. (2009). Ti based biomaterials, the ultimate choice for orthopaedic implants–a review. Progress in materials science, 54(3), 397-425.

Geetha, M., Singh, A. K., Gogia, A. K., & Asokamani, R. (2004). Effect of thermomechanical processing on evolution of various phases in Ti–Nb–Zr alloys. Journal of Alloys and Compounds, 384(1-2), 131-144.

Gerdemann, S. J. (2001). TITANIUM: Process Technologies. Advanced materials & processes, 159(7), 41-41.

German, R. M. (2005). Powder metallurgy and particulate materials processing: the processes, materials, products, properties and applications (pp. 20-56). Princeton: Metal powder industries federation.

Gibon, E., Amanatullah, D. F., Loi, F., Pajarinen, J., Nabeshima, A., Yao, Z., ... & Goodman, S. B. (2017). The biological response to orthopaedic implants for joint replacement: Part I: Metals. Journal of Biomedical Materials Research Part B: Applied Biomaterials, 105(7), 2162-2173.

Gibson, L. J. (2000). Mechanical behavior of metallic foams. Annual Review of Materials Research, 30, 191.

Gibson, L. J., Ashby, M. F., & Harley, B. A. (2010). Cellular materials in nature and medicine. Cambridge University Press.

Gogia, A. K. (2005). High-temperature titanium alloys. Defence Science Journal, 55(2), 149-173.

Goncalves, A. D., Balestri, W., & Reinwald, Y. (2020). Biomedical implants for regenerative therapies. Biomaterials.

González-Gualda, E., Baker, A. G., Fruk, L., & Muñoz-Espín, D. (2021). A guide to assessing cellular senescence in vitro and in vivo. *The FEBS journal*, *288*(1), 56-80.

Goodhew, P. J., Humphreys, J., & Beanland, R. (2000). Electron microscopy and analysis. CRC press.

Gottlow, J., Dard, M., Kjellson, F., Obrecht, M., & Sennerby, L. (2012). Evaluation of a new titanium-zirconium dental implant: a biomechanical and histological comparative study in the mini pig. Clinical implant dentistry and related research, 14(4), 538-545.

Götz, H. E., Müller, M., Emmel, A., Holzwarth, U., Erben, R. G., & Stangl, R. (2004). Effect of surface finish on the osseointegration of laser-treated titanium alloy implants. Biomaterials, 25(18), 4057-4064.

Gou, J., Wang, Z., Hu, S., Shen, J., Tian, Y., Zhao, G., & Chen, Y. (2020). Effects of trace Nb addition on microstructure and properties of Ti–6Al–4V thin-wall structure prepared via cold metal transfer additive manufacturing. *Journal of Alloys and Compounds*, *829*, 154481.

Groover, M. P. (2020). Fundamentals of modern manufacturing: materials, processes, and systems. John Wiley & Sons.

Guerra, C., Sancy, M., Walczak, M., Martínez, C., Ringuedé, A., Cassir, M., ... & Aguilar, C. (2020). Effect of added porosity on a novel porous Ti-Nb-Ta-Fe-Mn alloy exposed to simulated body fluid. Materials Science and Engineering: C, 111, 110758.

H. M. King, "Ilmenite:," A black iron titanium oxide mineral. The primary ore of titanium, source of titanium dioxide, 21 December 2015. [Online]. Available: https://geology.com/minerals/ilmenite.shtml. [Accessed 11 May 2020].

Ha, Y., Ma, X., Li, S., Li, T., Li, Z., Qian, Y., ... & He, C. (2022). Bone microenvironment-mimetic scaffolds with hierarchical microstructure for enhanced vascularization and bone regeneration. *Advanced Functional Materials*, *32*(20), 2200011.

Hallab, N. J., Anderson, S., Stafford, T., Glant, T., & Jacobs, J. J. (2005). Lymphocyte responses in patients with total hip arthroplasty. Journal of Orthopaedic Research, 23(2), 384-391.

Han, M. K., Kim, J. Y., Hwang, M. J., Song, H. J., & Park, Y. J. (2015). Effect of Nb on the microstructure, mechanical properties, corrosion behavior, and cytotoxicity of Ti-Nb alloys. Materials, 8(9), 5986-6003.

Han, X., Ji, X., Zhao, M., & Li, D. (2020). Mg/Ag ratios induced in vitro cell adhesion and preliminary antibacterial properties of TiN on medical Ti-6Al-4V alloy by Mg and Ag implantation. *Surface and Coatings Technology*, *397*, 126020.

Hao, Y. L., Li, S. J., Sun, S. Y., Zheng, C. Y., & Yang, R. (2007). Elastic deformation behaviour of Ti–24Nb–4Zr–7.9 Sn for biomedical applications. Acta biomaterialia, 3(2), 277-286.

Hao, Y. L., Li, S. J., Sun, S. Y., Zheng, C. Y., Hu, Q. M., & Yang, R. (2005). Super-elastic titanium alloy with unstable plastic deformation. Applied Physics Letters, 87(9), 091906.

Heinl, P., Müller, L., Körner, C., Singer, R. F., & Müller, F. A. (2008). Cellular Ti–6Al–4V structures with interconnected macro porosity for bone implants fabricated by selective electron beam melting. Acta biomaterialia, 4(5), 1536-1544.

Henriques, V. A. R., Campos, P. P. D., Cairo, C. A. A., & Bressiani, J. C. (2005). Production of titanium alloys for advanced aerospace systems by powder metallurgy. Materials Research, 8, 443-446.

Henriques, V. A. R., Galvani, E. T., Petroni, S. L. G., Paula, M. S. M., & Lemos, T. G. (2010). Production of Ti–13Nb–13Zr alloy for surgical implants by powder metallurgy. Journal of materials science, 45(21), 5844-5850.

Hernandez, J. L., & Woodrow, K. A. (2022). Medical Applications of Porous Biomaterials: Features of Porosity and Tissue‐Specific Implications for Biocompatibility. *Advanced Healthcare Materials*, *11*(9), 2102087.

Ho, W. F., Chen, W. K., Wu, S. C., & Hsu, H. C. (2008). Structure, mechanical properties, and grindability of dental Ti–Zr alloys. Journal of materials science: Materials in medicine, 19(10), 3179-3186.

Ho, W. F., Cheng, C. H., Pan, C. H., Wu, S. C., & Hsu, H. C. (2009). Structure, mechanical properties and grindability of dental Ti–10Zr–X alloys. Materials Science and Engineering: C, 29(1), 36-43.

Hon, Y. H., Wang, J. Y., & Pan, Y. N. (2003). Composition/phase structure and properties of titanium-niobium alloys. *Materials transactions*, *44*(11), 2384-2390.

Hong, T. F., Guo, Z. X., & Yang, R. (2008). Fabrication of porous titanium scaffold materials by a fugitive filler method. Journal of materials science: materials in medicine, 19(12), 3489-3495.

Hoppe, V., SzymczykZiółkowska, P., Rusi ´nska, M., Dybała, B., Poradowski, D., Janeczek, M. (2021). Assessment of mechanical, chemical, and biological properties of Ti-Nb-Zr alloy for medical applications. Materials, 14, 126-144.

Hoppe, V., Szymczyk-Ziółkowska, P., Rusińska, M., Dybała, B., Poradowski, D., & Janeczek, M. (2020). Assessment of mechanical, chemical, and biological properties of Ti-Nb-Zr alloy for medical applications. *Materials*, *14*(1), 126.

Hsu, H. C., Wu, S. C., Sung, Y. C., & Ho, W. F. (2009). The structure and mechanical properties of as-cast Zr–Ti alloys. Journal of alloys and Compounds, 488(1), 279-283.

https://www.lenntech.com/periodic/elements/zr.htm#:~:text=Zirconium%20is%20a%20very%20strong,hardness%20is%20similar%20to%20copper.

Hudecki, A., Kiryczyński, G., & Łos, M. J. (2019). Biomaterials, definition, overview. In *Stem cells and biomaterials for regenerative medicine* (pp. 85-98). Academic Press.

Ijaola, A. O., Akamo, D. O., Damiri, F., Akisin, C. J., Bamidele, E. A., Ajiboye, E. G., ... & Asmatulu, E. (2022). Polymeric biomaterials for wound healing applications: a comprehensive review. *Journal of Biomaterials Science, Polymer Edition*, *33*(15), 1998-2050.

Ikeda, M., Komatsu, S. Y., Sowa, I., & Niinomi, M. (2002). Aging behavior of the Ti-29Nb-13Ta-4.6 Zr new beta alloy for medical implants. Metallurgical and Materials Transactions A, 33(3), 487-493.

Ikehata, H., Nagasako, N., Furuta, T., Fukumoto, A., Miwa, K., & Saito, T. (2004). First-principles calculations for development of low elastic modulus Ti alloys. Physical Review B, 70(17), 174113.

Imwinkelried, T. (2007). Mechanical properties of open-pore titanium foam. Journal of biomedical materials research Part A, 81(4), 964-970.

Industry Experts, Inc (2022) Policy. Available at http://www.linkedin.com/company/industry-experts/orthopedic-implants-a-global-market-overview- 504642/product Accessed: 30 december 2022).

James, W. B. (2015). Powder Metallurgy Methods and Applications, vol. 7. ASM International.

Jazayeri, H. E., Rodriguez-Romero, M., Razavi, M., Tahriri, M., Ganjawalla, K., Rasoulianboroujeni, M., ... & Tayebi, L. (2018). The cross-disciplinary emergence of 3D printed bioceramic scaffolds in orthopedic bioengineering. Ceramics International, 44(1), 1-9.

Jensen, T. H. L., & Figure, M. D. (2009). Development of a novel biomaterial–a nanotechnological approach. Dan Med Bull, 56, 215.

Ji, S., Gu, Q., & Xia, B. (2006). Porosity dependence of mechanical properties of solid materials. Journal of Materials Science, 41(6), 1757-1768.

Jonitz-Heincke, A., Tillmann, J., Klinder, A., Krueger, S., Kretzer, J. P., Høl, P. J., ... & Bader, R. (2017). The impact of metal ion exposure on the cellular behavior of human osteoblasts and PBMCs: In vitro analyses of osteolytic processes. Materials, 10(7), 734.

Ju, J., Feng, Y., Li, H., Wu, R., & Wang, B. (2022). An approach towards utilization of water-quenched blast furnace slag for recovery of titanium, magnesium, and aluminum. *Journal of Environmental Chemical Engineering*, *10*(4), 108153.

Kang, L., & Yang, C. (2019). A review on high-strength titanium alloys: microstructure, strengthening, and properties. Advanced Engineering Materials, 21(8), 1801359.

Karasevskaya, O. P., Ivasishin, O. M., Semiatin, S. A., & Matviychuk, Y. V. (2003). Deformation behavior of beta-titanium alloys. Materials Science and Engineering: A, 354(1-2), 121-132.

Kargozar, S., Singh, R. K., Kim, H. W., & Baino, F. (2020). “Hard” ceramics for “Soft” tissue engineering: Paradox or opportunity?. Acta biomaterialia, 115, 1-28.

Kariya, S., Umeda, J., Ma, Q., & Seiichi, K. (2018). Ductility improvement mechanism of pure titanium with excessive oxygen solid solution via rapid cooling process. Nippon Kinzoku Gakkaishi/Journal of the Japan Institute of Metals, 82(10), 390-395.

Katz, J. L. (1980). Anisotropy of Young's modulus of bone. Nature, 283(5742), 106-107.

Kaur, M., & Singh, K. (2019). Review on titanium and titanium based alloys as biomaterials for orthopaedic applications. Materials Science and Engineering: C, 102, 844-862.

Kaya, M., Yakuphanoğlu, F., Elibol, E., & Köm, M. (2019). Microstructure characterization and biocompatibility behaviour of TiNbZr alloy fabricated by powder metallurgy. Materials Research Express, 6(12), 126560.

Kennedy, A. (2012). Porous metals and metal foams made from powders. Powder Metallurgy, 2, 31-46.

Kevenlik, O.F. (2013). Production of SiC reinforcement Al 2014 matrix composite by powder metallurgy method and investigation of its mechanical properties, Master dissertation, University of Kırıkkale

Kim, J. I., Kim, H. Y., Inamura, T., Hosoda, H., & Miyazaki, S. (2005). Shape memory characteristics of Ti–22Nb–(2–8) Zr (at.%) biomedical alloys. Materials Science and Engineering: A, 403(1-2), 334-339.

Kim, K. M., Kim, H. Y., & Miyazaki, S. (2020). Effect of Zr content on phase stability, deformation behavior, and Young’s modulus in Ti–Nb–Zr alloys. Materials, 13(2), 476.

Klinder, A., Seyfarth, A., Hansmann, D., Bader, R., & Jonitz-Heincke, A. (2018). Inflammatory response of human peripheral blood mononuclear cells and osteoblasts incubated with metallic and ceramic submicron particles. Frontiers in Immunology, 9, 831.

Kljajević, L., Matović, B., Nenadović, S., Baščarević, Z., Cvetićanin, N., & Devečerski, A. (2011). Fabrication of ZrC/SiC, ZrO2/SiC and ZrO2 powders by carbothermal reduction of ZrSiO4. Processing and Application of Ceramics, 5(2), 103-112.

Kobayashi, E., Matsumoto, S., Doi, H., Yoneyama, T., & Hamanaka, H. (1995). Mechanical properties of the binary titanium-zirconium alloys and their potential for biomedical materials. Journal of biomedical materials research, 29(8), 943-950.

Kohavi, D., Badihi Hauslich, L., Rosen, G., Steinberg, D., & Sela, M. N. (2013). Wettability versus electrostatic forces in fibronectin and albumin adsorption to titanium surfaces. *Clinical oral implants research*, *24*(9), 1002-1008.

Kokubo, T., & Yamaguchi, S. (2009). Novel bioactive titanate layers formed on Ti metal and its alloys by chemical treatments. Materials, 3(1), 48-63.

Kondoh, K. (Ed.). (2012). Powder metallurgy. BoD–Books on Demand.

Krebs, R. E. (2006). The history and use of our earth's chemical elements: a reference guide. Greenwood Publishing Group.

Krishna, R. (2022). Titanium-Based Alloys with High-Performance: Design and Development. *Titanium Alloys-Recent Progress in Design, Processing, Characterization, and Applications*.

Kükürtcü, B. (2008). Biyoaktif cam ve cam-seramik malzemelerin üretimi ve yapay vücut sıvısı içerisindeki davranımlarının incelenmesi (Doctoral dissertation, Fen Bilimleri Enstitüsü).

Kunčická, L., Kocich, R., & Lowe, T. C. (2017). Advances in metals and alloys for joint replacement. Progress in Materials Science, 88, 232-280.

Kusano, T., Seki, T., Higuchi, Y., Takegami, Y., Osawa, Y., & Ishiguro, N. (2018). Preoperative canal bone ratio is related to high-degree stress shielding: a minimum 5-year follow-up study of a proximally hydroxyapatite-coated straight tapered titanium femoral component. The Journal of Arthroplasty, 33(6), 1764-1769.

Lang, N. P., Matinlinna, J. P., & Matinlinna, J. P. (2013). Handbook of Oral Biomaterials.

Lee, B., Lee, T., Lee, Y., Lee, D. J., Jeong, J., Yuh, J., ... & Lee, C. S. (2014). Space-holder effect on designing pore structure and determining mechanical properties in porous titanium. Materials & Design, 57, 712-718.

Lee, C. M., Ju, C. P., & Chern Lin, J. H. (2002). Structure–property relationship of cast Ti–Nb alloys. Journal of Oral rehabilitation, 29(4), 314-322.

Lee, M. H., Kim, K. B., Han, J. H., Eckert, J., & Sordelet, D. J. (2008). High strength porous Ti–6Al–4V foams synthesized by solid state powder processing. Journal of Physics D: Applied Physics, 41(10), 105404.

Lee, T., Mathew, E., Rajaraman, S., Manivasagam, G., Singh, A. K., & Lee, C. S. (2015). Tribological and corrosion behaviors of warm-and hot-rolled Ti-13Nb-13Zr alloys in simulated body fluid conditions. International journal of nanomedicine, 10(Suppl 1), 207.

Lee, W. H., & Hyun, C. Y. (2007). Fabrication of fully porous and porous-surfaced Ti-6Al-4V implants by electro-discharge-sintering of spherical Ti-6Al-4V powders in an one-step process. Journal of materials processing technology, 189(1-3), 219-223.

Leyens, C., & Peters, M. (Eds.). (2003). Titanium and titanium alloys: fundamentals and applications. John Wiley & Sons.

Li, B. Y., Rong, L. J., Li, Y. Y., & Gjunter, V. E. (2000). Synthesis of porous Ni–Ti shape-memory alloys by self-propagating high-temperature synthesis: reaction mechanism and anisotropy in pore structure. Acta materialia, 48(15), 3895-3904.

Li, C., & Zhu, Z. (2006). Dynamic Young's modulus of open-porosity titanium measured by the electromagnetic acoustic resonance method. Journal of Porous materials, 13(1), 21-26.

Li, D., Wang, C., Li, Z., Wang, H., He, J., Zhu, J., ... & Chen, X. (2018). Nano-sized Al2O3 particle-induced autophagy reduces osteolysis in aseptic loosening of total hip arthroplasty by negative feedback regulation of RANKL expression in fibroblasts. Cell Death & Disease, 9(8), 1-15.

Li, J., Yang, H., Wang, H., & Ruan, J. (2014). Low elastic modulus titanium–nickel scaffolds for bone implants. Materials Science and Engineering: C, 34, 110-114.

Li, S., Choi, M. S., & Nam, T. H. (2021). Phase stability of the amorphous phase and non-equilibrium phase in a β Ti-Zr-based shape memory alloy. Scripta Materialia, 195, 113721.

Li, W., Liou, F., Newkirk, J., Taminger, K. M. B., & Seufzer, W. J. (2017). Investigation on Ti6Al4V-V-Cr-Fe-SS316 multi-layers metallic structure fabricated by laser 3D printing. Scientific reports, 7(1), 1-14.

Li, X., Wang, C. T., Zhang, W. G., & Li, Y. C. (2009). Properties of a porous Ti—6Al—4V implant with a low stiffness for biomedical application. Proceedings of the Institution of Mechanical Engineers, Part H: Journal of Engineering in Medicine, 223(2), 173-178.

Li, Y. C., Wong, C., Xiong, J. Y., Hodgson, P., & Wen, C. E. (2009). In vitro cytotoxicity of binary Ti alloys for bone implants. In *Materials Science Forum* (Vol. 618, pp. 295-298). Trans Tech Publications Ltd.

Li, Y. H., Chen, N., & Zhang, H. L. (2018). Powder sintering and characterization of biomedical porous tinb alloy. Dig J Nanomater Bios, 13, 491-498.

Li, Y. H., Chen, R. B., Qi, G. X., Wang, Z. T., & Deng, Z. Y. (2009). Powder sintering of porous Ti–15Mo alloy from TiH2 and Mo powders. Journal of alloys and compounds, 485(1-2), 215-218.

Li, Y., Yang, C., Zhao, H., Qu, S., Li, X., & Li, Y. (2014). New developments of Ti-based alloys for biomedical applications. Materials, 7(3), 1709-1800.

Limmer, A., & Wirtz, D. C. (2017). Osteoimmunology: influence of the immune system on bone regeneration and consumption. Zeitschrift für Orthopädie und Unfallchirurgie, 155(03), 273-280.

Lin, Y. C., Huang, J., He, D. G., Zhang, X. Y., Wu, Q., Wang, L. H., ... & Zhou, K. C. (2019). Phase transformation and dynamic recrystallization behaviors in a Ti55511 titanium alloy during hot compression. *Journal of Alloys and Compounds*, *795*, 471-482.

Liu, C. F., Lee, T. H., Liu, J. F., Hou, W. T., Li, S. J., Hao, Y. L., ... & Huang, H. H. (2018). A unique hybrid-structured surface produced by rapid electrochemical anodization enhances bio-corrosion resistance and bone cell responses of β-type Ti-24Nb-4Zr-8Sn alloy. *Scientific reports*, *8*(1), 6623.

Liu, Q., Meng, Q., Guo, S., & Zhao, X. (2013). α′ Type Ti–Nb–Zr alloys with ultra-low Young's modulus and high strength. Progress in Natural Science: Materials International, 23(6), 562-565.

Liu, S., Huang, P., Zhou, Y., Zhang, S., & Wang, Y. (2023). A review of the different fabrication techniques of porous Mg structures considering the effect of manufacturing parameters on corrosion rate and mechanical properties in the bio application. *Journal of Materials Science*, 1-24.

Liu, X., Chen, S., Tsoi, J. K., & Matinlinna, J. P. (2017). Binary titanium alloys as dental implant materials—a review. Regenerative biomaterials, 4(5), 315-323.

Luo, S. D., Song, T., Lu, S. L., Liu, B., Tian, J., & Qian, M. (2020). High oxygen-content titanium and titanium alloys made from powder. *Journal of Alloys and Compounds*, *836*, 155526.

Lütjering, G., & Williams, J. C. (2007). Titanium matrix composites (pp. 367-382). Springer Berlin Heidelberg.

Ma, G., Di, T., Song, C., Niu, F., Lu, J., & Wu, D. (2022). Phase transformation mechanism and mechanical properties of Ti-45Al-8Nb alloy prepared by directed laser deposition. *Materials Characterization*, *193*, 112256.

Madehow (2022) Policy. Available at http://www.madehow.com/Volume-7/Titanium.html (Accessed: 26 december 2022).

Magone, K., Luckenbill, D., & Goswami, T. (2015). Metal ions as inflammatory initiators of osteolysis. Archives of orthopaedic and trauma surgery, 135(5), 683-695.

Mahundla, M. R., Matizamhuka, W. R., Machaka, R., Yamamoto, A., & Shongwe, M. B. (2019, October). Biocompatibility Study of Ti-based Alloys Fabricated by Spark Plasma Sintering. In *IOP Conference Series: Materials Science and Engineering* (Vol. 655, No. 1, p. 012021). IOP Publishing.

Maity, J., & Sharma, A. (2023). A novel analytical approach to ascertain hardenability of plain carbon steel. *Philosophical Magazine*, *103*(5), 407-434.

Majumdar, D. D., Sahu, S., Mondal, D. P., Roychowdhury, A., Jha, A. K., & Ghosh, M. (2023). Microstructural Analysis and Corrosion Behavior of a Titanium Cenosphere Composite Foam Fabricated by Powder Metallurgy Route. *ChemistrySelect*, *8*(12), e202203581.

Majumdar, J. D., & Manna, I. (2015). Laser surface engineering of titanium and its alloys for improved wear, corrosion and high-temperature oxidation resistance. In Laser Surface Engineering (pp. 483-521). Woodhead publishing.

Majumdar, P., Singh, S. B., & Chakraborty, M. (2008). Elastic modulus of biomedical titanium alloys by nano-indentation and ultrasonic techniques—A comparative study. Materials Science and Engineering: A, 489(1-2), 419-425.

Makurat-Kasprolewicz, B., & Ossowska, A. (2023). Recent advances in electrochemically surface treated titanium and its alloys for biomedical applications: A review of anodic and plasma electrolytic oxidation methods. *Materials Today Communications*, 105425.

Málek, J., Hnilica, F., Veselý, J., Smola, B., Bartáková, S., & Vaněk, J. (2012). The influence of chemical composition and thermo-mechanical treatment on Ti–Nb–Ta–Zr alloys. Materials & Design, 35, 731-740.

Manam, N. S., Harun, W. S. W., Shri, D. N. A., Ghani, S. A. C., Kurniawan, T., Ismail, M. H., & Ibrahim, M. H. I. (2017). Study of corrosion in biocompatible metals for implants: A review. Journal of Alloys and Compounds, 701, 698-715.

Mandal, S., Das, V. V., Debata, M., Panigrahi, A., Sengupta, P., Rajendran, A., ... & Basu, S. (2019). Study of pore morphology, microstructure, and cell adhesion behaviour in porous Ti-6Al-4V scaffolds. *Emergent Materials*, *2*, 453-462.

Massalski, T. B., Murray, J. L., Bennett, L. H., & Baker, H. (2017). Binary Alloy Phase Diagrams (American Society for Metals, Metals Park, Ohio, 1986). Vol. I, 1100.

Matsumoto, H., Watanabe, S., & Hanada, S. (2006, November). Strengthening of low Young's modulus beta Ti-Nb-Sn alloys by thermomechanical processing. In Proceedings of the Materials and Processes for Medical Devices Conference (MPMD 06) (pp. 9-14). ASM International.

Matuła, I., Dercz, G., Zubko, M., Maszybrocka, J., Jurek-Suliga, J., Golba, S., & Jendrzejewska, I. (2020). Microstructure and porosity evolution of the ti–35zr biomedical alloy produced by elemental powder metallurgy. Materials, 13(20), 4539.

Medvedev, A. E., Molotnikov, A., Lapovok, R., Zeller, R., Berner, S., Habersetzer, P., & Dalla Torre, F. (2016). Microstructure and mechanical properties of Ti–15Zr alloy used as dental implant material. journal of the mechanical behavior of biomedical materials, 62, 384-398.

Mendes, M. W., Ágreda, C. G., Bressiani, A. H., & Bressiani, J. C. (2016). A new titanium based alloy Ti–27Nb–13Zr produced by powder metallurgy with biomimetic coating for use as a biomaterial. Materials Science and Engineering: C, 63, 671-677.

Metal pages, (2022) Policy. Available at http://www.metal pages.com/metalprices/titanium/ (Accessed: 26 december 2022).

Misch, C. E. (2004). Dental implant prosthetics-E-book. Elsevier Health Sciences.

Mishchenko, O., Ovchynnykov, O., Kapustian, O., & Pogorielov, M. (2020). New Zr-Ti-Nb alloy for medical application: development, chemical and mechanical properties, and biocompatibility. *Materials*, *13*(6), 1306.

Moffat, D. L., & Kattner, U. R. (1988). The stable and metastable Ti-Nb phase diagrams. Metallurgical Transactions A, 19(10), 2389-2397.

Moharamzadeh, K., Brook, I. M., & Van Noort, R. (2009). Biocompatibility of resin-based dental materials. Materials, 2(2), 514-548.

Mondal, D. P., Patel, M., Jain, H., Jha, A. K., Das, S., & Dasgupta, R. (2015). The effect of the particle shape and strain rate on microstructure and compressive deformation response of pure Ti-foam made using acrowax as space holder. Materials Science and Engineering: A, 625, 331-342.

Morrison, R. J., Kashlan, K. N., Flanangan, C. L., Wright, J. K., Green, G. E., Hollister, S. J., & Weatherwax, K. J. (2015). Regulatory considerations in the design and manufacturing of implantable 3D-printed medical devices. Clinical and translational science, 8(5), 594-600.

Moses, P. G., Janotti, A., Franchini, C., Kresse, G., & Van de Walle, C. G. (2016). Donor defects and small polarons on the TiO2 (110) surface. Journal of Applied Physics, 119(18), 181503.

Murphy, C. M., Haugh, M. G., & O'brien, F. J. (2010). The effect of mean pore size on cell attachment, proliferation and migration in collagen–glycosaminoglycan scaffolds for bone tissue engineering. *Biomaterials*, *31*(3), 461-466.

Mutlu, I. (2013). Sinter-coating method for the production of TiN-coated titanium foam for biomedical implant applications. Surface and Coatings Technology, 232, 396-402.

Myer, K. (Ed.). (2003). *Standard handbook of biomedical engineering and design*.

Nag, S., Banerjee, R., & Fraser, H. L. (2005). Microstructural evolution and strengthening mechanisms in Ti–Nb–Zr–Ta, Ti–Mo–Zr–Fe and Ti–15Mo biocompatible alloys. Materials Science and Engineering: C, 25(3), 357-362.

Nagaram, A. B., & Ebel, T. (2016). Development of Ti-22Nb-Xzr using metal injection moulding for biomedical applications. In Key Engineering Materials (Vol. 704, pp. 334-342). Trans Tech Publications Ltd.

Nakai, M., Niinomi, M., & Oneda, T. (2012). Improvement in fatigue strength of biomedical β-type Ti–Nb–Ta–Zr alloy while maintaining low Young's modulus through optimizing ω-phase precipitation. Metallurgical and Materials Transactions A, 43(1), 294-302.

Nasiłowska, B., Skrzeczanowski, W., Bombalska, A., & Bogdanowicz, Z. (2023). Laser Emission Spectroscopy of Graphene Oxide Deposited on 316 Steel and Ti6Al4V Titanium Alloy Suitable for Orthopedics. *Materials*, *16*(7), 2574.

Nazari, K. A., Nouri, A., & Hilditch, T. (2015). Mechanical properties and microstructure of powder metallurgy Ti–xNb–yMo alloys for implant materials. Materials & Design, 88, 1164-1174.

Niinomi, M. (2002). Recent metallic materials for biomedical applications. Metallurgical and materials transactions A, 33(3), 477-486.

Niinomi, M. (2010). Trend and present state of titanium alloys with body centered structure for biomedical applications. Tetsu-To-Hagane/Journal of the Iron and Steel Institute of Japan, 96(11), 661-670.

Niinomi, M., Hattori, T., Kasuga, T., & Fukui, H. (2006). Titanium and its alloys, Encyclopedia of Biomaterials and Biomedical Engineering.

Niu, W., Bai, C., Qiu, G., & Wang, Q. (2009). Processing and properties of porous titanium using space holder technique. Materials Science and Engineering: A, 506(1-2), 148-151.

Nouri, A., Chen, X., Li, Y., Yamada, Y., & Hodgson, P. D. (2008). Synthesis of Ti–Sn–Nb alloy by powder metallurgy. Materials Science and Engineering: A, 485(1-2), 562-570.

Nuilek, K. (2020). Investigation the effect of activation and exfoliation on carbon nanosheets properties (Doctoral dissertation).

Nytimes (2010) Policy. Available at http://www.nytimes.com/2010/04/03/business/03ortho.html?_r=1&pagewanted=all (Accessed: 26 december 2022).

Omran, B. A. (2020). *Nanobiotechnology: a multidisciplinary field of science* (pp. 145-184). Cham: Springer.

Oppenheimer, S., & Dunand, D. C. (2010). Solid-state foaming of Ti–6Al–4V by creep or superplastic expansion of argon-filled pores. Acta materialia, 58(13), 4387-4397.

Orr, A. W., Helmke, B. P., Blackman, B. R., & Schwartz, M. A. (2006). Mechanisms of mechanotransduction. Developmental cell, 10(1), 11-20.

Orthopedic network news, vol. 33, how an orthopaedic implant is made, Mendenhall Associates Inc

Ou, K. L., Weng, C. C., Lin, Y. H., & Huang, M. S. (2017). A promising of alloying modified beta-type Titanium-Niobium implant for biomedical applications: Microstructural characteristics, in vitro biocompatibility and antibacterial performance. Journal of Alloys and Compounds, 697, 231-238.

Ozturk, F., Ece, R. E., Polat, N., & Koksal, A. (2011). Tensile Properties of Titaniuni Alloys at Various Strain Rates.

Pan, Y., Zhang, J., Wu, X., Yang, Y., Kuang, F., Zhang, C., ... & Lu, X. (2023). Grain growth kinetics and densification mechanism of Ti/CaB6 composites by powder metallurgy pressureless sintering. *Journal of Alloys and Compounds*, 168686.

Pandey, A. K., Gautam, R. K., & Behera, C. K. (2022). Microstructure, mechanical strength, chemical resistance, and antibacterial behavior of Ti–5Cu–x% Nb biomedical alloy. *Biomedical Materials*, *17*(4), 045022.

Paris, V., & Mousavinasab, S. (2022). High-performance lubricants in powder compaction: An overview of their benefits. *Materials Today: Proceedings*.

Park, J. B., & Kim, Y. K. (2014). Metallic biomaterials. In Biomedical Engineering Fundamentals (pp. 505-526). CRC Press.

Pilliar, R. M. (1987). Porous-surfaced metallic implants for orthopedic applications. Journal of biomedical materials research, 21(A1 Suppl), 1-33.

Pina, S., Rebelo, R., Correlo, V. M., Oliveira, J. M., & Reis, R. L. (2018). Bioceramics for osteochondral tissue engineering and regeneration. Osteochondral tissue engineering, 53-75.

Prakash, C., Singh, S., Ramakrishna, S., Królczyk, G., & Le, C. H. (2020). Microwave sintering of porous Ti–Nb-HA composite with high strength and enhanced bioactivity for implant applications. Journal of Alloys and Compounds, 824, 153774.

Prakoso, A. T., Basri, H., Adanta, D., Yani, I., Ammarullah, M. I., Akbar, I., ... & Kamarul, T. (2023). The effect of tortuosity on permeability of porous scaffold. *Biomedicines*, *11*(2), 427.

Pushp, P., Dasharath, S. M., & Arati, C. (2022). Classification and applications of titanium and its alloys. *Materials Today: Proceedings*, *54*, 537-542.

Qin, P., Liu, Y., Sercombe, T. B., Li, Y., Zhang, C., Cao, C., ... & Zhang, L. C. (2018). Improved corrosion resistance on selective laser melting produced Ti-5Cu alloy after heat treatment. ACS Biomaterials Science & Engineering, 4(7), 2633-2642.

Qu, W., Sun, X., Yuan, B., Xiong, C., Zhang, F., Li, Y., & Sun, B. (2016). Microstructures and phase transformations of Ti-30Zr-xNb (x= 5, 7, 9, 13 at.%) shape memory alloys. Materials Characterization, 122, 1-5.

Quan, R., Yang, D., Yan, J., Li, W., Wu, X., & Wang, H. (2009). Preparation of graded zirconia–CaP composite and studies of its effects on rat osteoblast cells in vitro. Materials Science and Engineering: C, 29(1), 253-260.

Rafandi, F. I., Firdaus, M. B., Yaqin, R. I., Kurniawan, B. A., & Hidayat, M. I. P. (2016). Pemodelan dan Fabrikasi Komposit Bermatriks Logam dengan Penguat Kalsit (CaCO3) dari Kulit Kerang untuk Sprocket Motor Komersial. Prosiding SENIATI, 106-A.

Raffa, M. L., Nguyen, V. H., Hernigou, P., Flouzat-Lachaniette, C. H., & Haiat, G. (2021). Stress shielding at the bone-implant interface: influence of surface roughness and of the bone-implant contact ratio. *Journal of Orthopaedic Research®*, *39*(6), 1174-1183.

Rajan, S. (2020). *Analysis of Microstructure Evolution and Mechanical Properties of Linear Friction Welded Titanium alloys* (Doctoral dissertation, Carleton University).

Ramakrishna, S. (2004). An introduction to biocomposites. Imperial College Press.

Rao, X., Chu, C. L., & Zheng, Y. Y. (2014). Phase composition, microstructure, and mechanical properties of porous Ti–Nb–Zr alloys prepared by a two-step foaming powder metallurgy method. Journal of the mechanical behavior of biomedical materials, 34, 27-36.

Rathor, S., & Uddanwadiker, R. (2022). A review on the effect of biomechanical aspects and the type of stability fixation on the bone fracture healing process. *Machines, Mechanism and Robotics: Proceedings of iNaCoMM 2019*, 327-335.

Revankar, G. D., Shetty, R., Rao, S. S., & Gaitonde, V. N. (2014). Analysis of surface roughness and hardness in titanium alloy machining with polycrystalline diamond tool under different lubricating modes. Materials Research, 17, 1010-1022.

Rodriguez-Contreras, A., Punset, M., Calero, J. A., Gil, F. J., Ruperez, E., & Manero, J. M. (2021). Powder metallurgy with space holder for porous titanium implants: A review. Journal of Materials Science & Technology, 76, 129-149.

Romero-Resendiz, L., Rossi, M. C., Seguí-Esquembre, C., & Amigó-Borrás, V. (2023). Development of a porous Ti–35Nb–5In alloy with low elastic modulus for biomedical implants. *Journal of Materials Research and Technology*, *22*, 1151-1164.

Ruan, J., Yang, H., Weng, X., Miao, J., & Zhou, K. (2016). Preparation and characterization of biomedical highly porous Ti–Nb alloy. Journal of Materials Science: Materials in Medicine, 27(4), 1-8.

Ryan, G., Pandit, A., & Apatsidis, D. P. (2006). Fabrication methods of porous metals for use in orthopaedic applications. Biomaterials, 27(13), 2651-2670.

Ryhänen, J. (1999). Biocompatibility evaluation of nickel-titanium shape memory metal alloy (pp. 3-44). Oulun yliopisto.

Sadeghpour, S., Abbasi, S. M., Morakabati, M., Kisko, A., Karjalainen, L. P., & Porter, D. A. (2018). On the compressive deformation behavior of new beta titanium alloys designed by d-electron method. Journal of Alloys and Compounds, 746, 206-217.

Sahoo, P., Das, S. K., & Davim, J. P. (2019). Tribology of materials for biomedical applications. In Mechanical Behaviour of Biomaterials (pp. 1-45). Woodhead Publishing.

Sakaguchi, R. L., & Powers, J. M. (2012). Craig's restorative dental materials-e-book. Elsevier Health Sciences.

Samal, P., & Newkirk, J. (2015). History of powder metallurgy. ASM Handbook, 7, 3-8.

Sankhla, A. M., Patel, K. M., Makhesana, M. A., Giasin, K., Pimenov, D. Y., Wojciechowski, S., & Khanna, N. (2022). Effect of mixing method and particle size on hardness and compressive strength of aluminium based metal matrix composite prepared through powder metallurgy route. journal of materials research and technology, 18, 282-292.

Santos, D. R. D., Henriques, V. A. R., Cairo, C. A. A., & Pereira, M. D. S. (2005). Production of a low young modulus titanium alloy by powder metallurgy. Materials Research, 8, 439-442.

Sargeant, A., & Goswami, T. (2006). Hip implants: paper V. Physiological effects. Materials & design, 27(4), 287-307.

Savio, D., & Bagno, A. (2022). When the total hip replacement fails: A review on the stress-shielding effect. *Processes*, *10*(3), 612.

Seal, B. L., Otero, T. C., & Panitch, A. (2001). Polymeric biomaterials for tissue and organ regeneration. Materials Science and Engineering: R: Reports, 34(4-5), 147-230.

Sebastián, E., Murciano, A., De Aza, P. N., & Velasquez, P. (2023). Synthesis of 3D porous ceramic scaffolds obtained by the sol-gel method with surface morphology modified by hollow spheres for bone tissue engineering applications. *Ceramics International*, *49*(3), 4393-4402.

Seetharaman, S. (2005). Fundamentals of metallurgy. Cambridge: Woodhead Publishing Limited and Maney Publishing.

Seo, B., Park, H. K., Park, C. S., & Park, K. (2023). Effect of alloying elements on corrosion properties of high corrosion resistant titanium alloys in high concentrated sulfuric acid. *Materials Today Communications*, *34*, 105131.

Sherif, E. S. M., Bahri, Y. A., Alharbi, H. F., Ijaz, M. F., & Alnaser, I. A. (2022). Influence of Tantalum Addition on the Corrosion Passivation of Titanium-Zirconium Alloy in Simulated Body Fluid. *Materials*, *15*(24), 8812.

Sing, S. L. (2022). Perspectives on additive manufacturing enabled beta-titanium alloys for biomedical applications. *International Journal of Bioprinting*, *8*(1).

Slokar, L., Matković, T., & Matković, P. (2012). Comparison of microstructural characteristics for biomedical Ti (70, 80 at.%)-Cr-Mo and Ti (70, 80 at.%)-Nb-Zr alloys. Tehnički glasnik, 6(2), 178-182.

Slokar, L., Štrkalj, A., & Glavaš, Z. (2019). Synthesis of Ti-Zr alloy by powder metallurgy. Engineering Review: Međunarodni časopis namijenjen publiciranju originalnih istraživanja s aspekta analize konstrukcija, materijala i novih tehnologija u području strojarstva, brodogradnje, temeljnih tehničkih znanosti, elektrotehnike, računarstva i građevinarstva, 39(1), 115-123.

Soyler M. (2007) Powder metallurgy and applications, Master dissertation, Gebze Technical University.

Stern, M., & Geary, A. L. (1957). Electrochemical polarization: I. A theoretical analysis of the shape of polarization curves. Journal of the electrochemical society, 104(1), 56.

Stratton-Powell, A. A., Pasko, K. M., Brockett, C. L., & Tipper, J. L. (2016). The biologic response to polyetheretherketone (PEEK) wear particles in total joint replacement: a systematic review. Clinical Orthopaedics and Related Research®, 474(11), 2394-2404.

Subedi, M. M. (2013). Ceramics and its Importance. Himalayan Physics, 4, 80-82.

Sudhakar, K. V., & Wood, E. (2016). Superplastic grade titanium alloy: comparative evaluation of mechanical properties, microstructure, and fracture behavior. Journal of Materials, 2016.

Sumitomo, N., Noritake, K., Hattori, T., Morikawa, K., Niwa, S., Sato, K., & Niinomi, M. (2008). Experiment study on fracture fixation with low rigidity titanium alloy. Journal of Materials Science: Materials in Medicine, 19(4), 1581-1586.

Sun, F., Hao, Y. L., Nowak, S., Gloriant, T., Laheurte, P., & Prima, F. (2011). A thermo-mechanical treatment to improve the superelastic performances of biomedical Ti–26Nb and Ti–20Nb–6Zr (at.%) alloys. Journal of the mechanical behavior of biomedical materials, 4(8), 1864-1872.

Sweeney, M. R. (2006). Review of: Clinical Aspects of Dental Materials: Theory, Practice, and Cases.

Takeda, O., Uda, T., & Okabe, T. H. (2014). Rare earth, titanium group metals, and reactive metals production. In Treatise on process metallurgy (pp. 995-1069). Elsevier Ltd.

Tammas-Williams, S., Withers, P. J., Todd, I., & Prangnell, P. B. (2017). The influence of porosity on fatigue crack initiation in additively manufactured titanium components. Scientific reports, 7(1), 7308.

Tanji, A., Fan, X., Sakidja, R., Liaw, P. K., & Hermawan, H. (2022). Niobium addition improves the corrosion resistance of TiHfZrNbx high-entropy alloys in Hanks' solution. *Electrochimica Acta*, *424*, 140651.

Te Riele, H., Michel, B., & Ehrlich, S. D. (1986). Are single-stranded circles intermediates in plasmid DNA replication?. *The EMBO journal*, *5*(3), 631-637.

Thouas, G. A. (2015). Metallic implant biomaterials. Mater Sci Eng R Reports, 87, 1-57.

Tirrell, M., Kokkoli, E., & Biesalski, M. (2002). The role of surface science in bioengineered materials. Surface Science, 500(1-3), 61-83.

Titanium alloy-mechanical properties https://www.kobelco.co.jp (https://www.kobelco.co.jp/english/titan/files/details.pdf )

Titanium and Titanium Dioxide, USGS Mineral Commodity Summaries, January 2020 and January 2022, https://www.explainthatstuff.com/titanium.html

Tiwary, A., Kumar, R., & Chohan, J. S. (2022). A review on characteristics of composite and advanced materials used for aerospace applications. *Materials Today: Proceedings*, *51*, 865-870.

Torres-Sanchez, C., Al Mushref, F. R. A., Norrito, M., Yendall, K., Liu, Y., & Conway, P. P. (2017). The effect of pore size and porosity on mechanical properties and biological response of porous titanium scaffolds. Materials Science and Engineering: C, 77, 219-228.

Tüfekci, M., Özkal, B., Maharaj, C., Liu, H., Dear, J. P., & Salles, L. (2023). Strain-rate-dependent mechanics and impact performance of epoxy-based nanocomposites. *Composites Science and Technology*, *233*, 109870.

Tuncer, N., Arslan, G., Maire, E., & Salvo, L. (2011). Influence of cell aspect ratio on architecture and compressive strength of titanium foams. Materials Science and Engineering: A, 528(24), 7368-7374.

Vermes, C., Roebuck, K. A., Chandrasekaran, R., Dobai, J. G., Jacobs, J. J., & Glant, T. T. (2000). Particulate wear debris activates protein tyrosine kinases and nuclear factor κB, which down-regulates type I collagen synthesis in human osteoblasts. Journal of Bone and Mineral Research, 15(9), 1756-1765.

Vicente, F. B., Correa, D. R., Donato, T. A., Arana-Chavez, V. E., Buzalaf, M. A., & Grandini, C. R. (2014). The influence of small quantities of oxygen in the structure, microstructure, hardness, elasticity modulus and cytocompatibility of Ti-Zr alloys for dental applications. Materials, 7(1), 542-553.

W. Nicholson, J. (2020). Titanium alloys for dental implants: A review. *Prosthesis*, *2*(2), 11.

Wang, B., Ruan, W., Liu, J., Zhang, T., Yang, H., & Ruan, J. (2019). Microstructure, mechanical properties, and preliminary biocompatibility evaluation of binary Ti–Zr alloys for dental application. Journal of Biomaterials Applications, 33(6), 766-775.

Wang, J. C., Liu, Y. J., Qin, P., Liang, S. X., Sercombe, T. B., & Zhang, L. C. (2019). Selective laser melting of Ti–35Nb composite from elemental powder mixture: Microstructure, mechanical behavior and corrosion behavior. Materials Science and Engineering: A, 760, 214-224.

Wang, M., Xu, P., & Lei, B. (2023). Engineering multifunctional bioactive citrate-based biomaterials for tissue engineering. *Bioactive Materials*, *19*, 511-537.

Wang, X. H., Li, J. S., Rui, H. U., Kou, H. C., & Lian, Z. H. O. U. (2013). Mechanical properties of porous titanium with different distributions of pore size. Transactions of Nonferrous Metals Society of China, 23(8), 2317-2322.

Wang, X., Li, Y., Lin, J., & Hodgson, P. D. (2008). Effect of heat-treatment atmosphere on the bond strength of apatite layer on Ti substrate. Dental Materials, 24(11), 1549-1555.

Wen, C. E., Mabuchi, M., Yamada, Y., Shimojima, K., Chino, Y., & Asahina, T. (2001). Processing of biocompatible porous Ti and Mg. Scripta materialia, 45(10), 1147-1153.

Wen, C. E., Yamada, Y., & Hodgson, P. D. (2006). Fabrication of novel TiZr alloy foams for biomedical applications. Materials Science and Engineering: C, 26(8), 1439-1444.

Wen, C. E., Yamada, Y., Shimojima, K., Chino, Y., Hosokawa, H., & Mabuchi, M. (2002). Novel titanium foam for bone tissue engineering. Journal of materials research, 17(10), 2633-2639.

Wheeler, K. R., Karagianes, M. T., & Sump, K. R. (1983). Porous titanium alloy for prosthesis attachment. In Titanium alloys in surgical implants. ASTM International.

Willett, W., Skerrett, P. J., & Giovannucci, E. L. (2017). Eat, drink, and be healthy: the Harvard Medical School guide to healthy eating. Simon and Schuster.

Williams, D. F. (2008). On the mechanisms of biocompatibility. Biomaterials, 29(20), 2941-2953.

Willie, B. M., Yang, X., Kelly, N. H., Merkow, J., Gagne, S., Ware, R., ... & Bostrom, M. P. (2010). Osseointegration into a novel titanium foam implant in the distal femur of a rabbit. Journal of Biomedical Materials Research Part B: Applied Biomaterials: An Official Journal of The Society for Biomaterials, The Japanese Society for Biomaterials, and The Australian Society for Biomaterials and the Korean Society for Biomaterials, 92(2), 479-488.

Witte, F., Fischer, J., Nellesen, J., Crostack, H. A., Kaese, V., Pisch, A., ... & Windhagen, H. (2006). In vitro and in vivo corrosion measurements of magnesium alloys. Biomaterials, 27(7), 1013-1018.

Wojnar, L., Dąbrowski, J. R., & Oksiuta, Z. (2001). Porosity structure and mechanical properties of vitalium-type alloy for implants. Materials characterization, 46(2-3), 221-225.

Wu, J., Tan, X., An, X., Zhang, J., Guo, Y., Liu, J., ... & Wang, Q. (2022). Development of biomedical Ti-Nb-Zr-Mn alloys with enhanced mechanical properties and corrosion resistance. *Materials Today Communications*, *30*, 103027.

Wu, M. H., Lee, M. H., Wu, C., Tsai, P. I., Hsu, W. B., Huang, S. I., ... & Li, Y. Y. (2022). In vitro and in vivo comparison of bone growth characteristics in additive-manufactured porous titanium, nonporous titanium, and porous tantalum interbody cages. *Materials*, *15*(10), 3670.

Wu, T., Blawert, C., Serdechnova, M., Karlova, P., Dovzhenko, G., Wieland, D. F., & Zheludkevich, M. L. (2022). Formation of plasma electrolytic oxidation coatings on pure niobium in different electrolytes. *Applied Surface Science*, *573*, 151629.

Xia, D., Chen, J., Zhang, Z., & Dong, M. (2022). Emerging polymeric biomaterials and manufacturing techniques in regenerative medicine. *Aggregate*, *3*(5), e176.

Xiang, C., Zhang, Y., Li, Z., Zhang, H., Huang, Y., & Tang, H. (2012). Preparation and compressive behavior of porous titanium prepared by space holder sintering process. Procedia Engineering, 27, 768-774.

Xu, J., Weng, X. J., Wang, X., Huang, J. Z., Zhang, C., Muhammad, H., ... & Liao, Q. D. (2013). Potential use of porous titanium–niobium alloy in orthopedic implants: preparation and experimental study of its biocompatibility in vitro. *PloS one*, *8*(11), e79289.

YALÇIN, C. (2012). Effect of thermal aging on physical properties of NiMnGa alloy and the x-ray microtomograph analysis.

Yang, G., & Zhang, T. (2005). Phase transformation and mechanical properties of the Ti50Zr30Nb10Ta10 alloy with low modulus and biocompatible. Journal of Alloys and Compounds, 392(1-2), 291-294.

Yang, S. Y., Ren, W., Park, Y., Sieving, A., Hsu, S., Nasser, S., & Wooley, P. H. (2002). Diverse cellular and apoptotic responses to variant shapes of UHMWPE particles in a murine model of inflammation. Biomaterials, 23(17), 3535-3543.

Yetim, A. F. (2009). Nitridation behavior of Ti6Al4V and AISI316L stainless steel (also used as a biomaterial) alloy with plasma, and the comparison of this with Ti-Dlc thin film deposition (Doctoral dissertation, Ph. D. thesis, Atatürk University Graduate School of Natural and Applied Sciences, Erzurum).

Yılmaz, E., Gökçe, A., Findik, F., & Gülsoy, H. Ö. (2017). Characterization of biomedical Ti-16Nb-(0–4) Sn alloys produced by powder injection molding. Vacuum, 142, 164-174.

Yılmaz, E., Gökçe, A., Findik, F., & Gulsoy, H. Ö. (2018). Assessment of Ti–16Nb–xZr alloys produced via PIM for implant applications. Journal of Thermal Analysis and Calorimetry, 134(1), 7-14.

Yilmaz, E., Gökçe, A., Findik, F., & Gülsoy, H. Ö. (2018). Powder Metallurgy Processing of Ti-Nb Based Biomedical Alloys. Acta Physica Polonica A, 134(1), 278-280.

You, L., & Song, X. (2012). A study of low Young′ s modulus Ti–Nb–Zr alloys using d electrons alloy theory. Scripta Materialia, 67(1), 57-60.

Zahir, A., Mahmood, U., Nazir, A., Hussain, T., & Abid, S. (2022). Biomaterials for medical and healthcare products. In *Medical Textiles from Natural Resources* (pp. 43-86). Woodhead Publishing.

Zhang, H., Wang, C., Pyczak, F., Ebel, T., & Liu, X. A new kind of biomedical Ti-Mn-Nb alloy. *physica status solidi (a)*.

Zhang, J., Wang, H., Yang, S., Xing, X., Shu, X., & Jin, X. (2018). Corrosion and wear properties of biomedical Ti-Zr-based alloys. Materials and Corrosion, 69(12), 1703-1712.

Zhang, X., & Williams, D. (Eds.). (2019). *Definitions of biomaterials for the twenty-first century*. Elsevier.

Zhang, Y., Sun, D., Cheng, J., Tsoi, J. K. H., & Chen, J. (2020). Mechanical and biological properties of Ti–(0–25 wt%) Nb alloys for biomedical implants application. *Regenerative biomaterials*, *7*(1), 119-127.

Zhao, D., Chang, K., Ebel, T., Qian, M., Willumeit, R., Yan, M., & Pyczak, F. (2013). Microstructure and mechanical behavior of metal injection molded Ti–Nb binary alloys as biomedical material. Journal of the mechanical behavior of biomedical materials, 28, 171-182.

Zhao, Q., Ueno, T., & Wakabayashi, N. (2023). A review in titanium-zirconium binary alloy for use in dental implants: Is there an ideal Ti-Zr composing ratio?. *Japanese Dental Science Review*, *59*, 28-37.

Zheng, J., Xia, R., Sun, C., Yaqoob, N., Qiu, Q., Zhong, L., ... & Huijben, M. (2023). Fast and Durable Lithium Storage Enabled by Tuning Entropy in Wadsley–Roth Phase Titanium Niobium Oxides. *Small*, 2301967.

Zheng, Y., Sun, H., Yan, L., Pang, X., & Gao, K. (2023). Effect of Aging Time on Crack Initiation Mechanism of Precipitation Hardening Stainless Steel in Very High Cycle Fatigue Regime. *International Journal of Fatigue*, 107522.

Zhou, J., Cui, Z., Zhang, B., Kundu, T., & Sevostianov, I. (2023). The effect of porosity on the elastic properties of cortical bone and ultrasound propagation. *International Journal of Engineering Science*, *182*, 103772.

Zhu, X., Serati, M., Mutaz, E., & Chen, Z. (2022, June). True Triaxial Testing of Anisotropic Solids. In *56th US Rock Mechanics/Geomechanics Symposium*. OnePetro.

Zhuravleva, K. (2014). Porous ß-type Ti-Nb alloy for biomedical applications.